Photoactive TiO_2 Coatings by Suspension Plasma Spraying

Hediyeh Khatibnezhad

A Thesis

In the Department

of

Mechanical, Industrial and Aerospace Engineering

Presented in Partial Fulfillment of the Requirements For the Degree of

Doctor of Philosophy (Mechanical Engineering) at

Concordia University

Montreal, Quebec, Canada

April 2023

CONCORDIA UNIVERSITY
School of Graduate Studies

CONCORDIA UNIVERSITY

School of Graduate Studies

This is to certify that the thesis prepared

By: Hediyeh Khatibnezhad

Entitled: **Photoactive TiO_2 Coatings by Suspension Plasma Spraying**

And submitted in partial fulfillment of the requirements for the degree of

Doctor of Philosophy (Mechanical Engineering)

Complies with the regulations of the University and meets the accepted standards with respect to originality and quality.

Signed by the final examining committee:

_____ Chair
Dr. Anjali Awasthi

_____ External Examiner
Dr. Shrikant Joshi

_____ Examiner
Dr. Fariborz Haghighat

_____ Examiner
Dr. Ali Dolatabadi

_____ Examiner
Dr. Martin Pugh

_____ Thesis Supervisor
Dr. Christian Moreau

Approved by: _____
Dr. Muthukumaran Packirisamy, Graduate Program Director

04/20/2023: _____
Dr. Martin Pugh, Dean of Faculty

ABSTRACT

Photoactive TiO_2 Coatings by Suspension Plasma Spraying

Hediyeh Khatibnezhad, PhD

Concordia University, 2023

Recently the advantages of titanium dioxide (TiO_2), as one of the most recognized photocatalysts for the degradation of organic compounds in wastewater, have prompted a great deal of research. However, its unsatisfactory efficiency caused by the large bandgap of TiO_2 and high recombination rate of photo-generated e^-/h^+ has limited its application. Thermal spray processes as environmentally friendly technologies appear as a versatile and rapid processing approach compatible with industrial production. Suspension plasma spray (SPS) deposition could be used to obtain TiO_2 deposits with an effective photoactive performance to decompose organic compounds and antiviral applications. Furthermore, TiO_2 coatings with various degrees of sub-stoichiometric oxidation can be achieved with plasma spray deposition.

In this project, coatings with different anatase phase contents were produced. The results show no direct correlation between anatase content and the photocatalytic activity of as-sprayed coatings due to their unique microstructure and the presence of oxygen vacancies. In comparison, anatase phase positively enhanced the photocatalytic activity in the post-treated coatings with similar coating characteristics and oxygen contents.

Moreover, oxygen vacancy presented an influential role in improving the photocatalytic activity of sub-stoichiometric TiO_{2-x} coatings produced by SPS. The energy levels introduced by oxygen vacancies and Ti^{3+} ions in TiO_2 lattice sites decreased the bandgap energy and shifted the absorption edge to visible light. The energy levels can also improve the charge carriers' lifetime by acting as traps for electrons and holes. Results showed that the photocatalytic activity of as-sprayed sub-stoichiometric TiO_{2-x} coatings was 2-3 times higher than that of post-treated stoichiometric TiO_2 coatings.

Further studies on the cerium-doped TiO_2 showed SPS-SPPS technique as a promising method for doping TiO_2. However, results revealed the importance of adding an optimum amount of dopant to reach the highest photoactivity. Moreover, a nanocomposite of TiO_2- CeO_2 can help photocatalytic activity. Otherwise, sub-micron CeO_2 particles in the composite matrix could cover the active surface of TiO_2 particles and decrease the photocatalytic efficiency.

Finally, the antiviral performance of the coatings was assessed. The results show that thermally sprayed coatings can introduce a potentially cost-effective solution to produce efficient antiviral high-touch coatings for indoor/ outdoor applications.

DEDICATION

Dedicated to the loves of my life, my beloved parents, Rezvan and Mohsen, my beautiful daughter, Liana, and my wonderful husband, Armin, for their endless love and encouragement.

ACKNOWLEDGMENTS

First and foremost, I would like to express my sincere gratitude to my thesis supervisor, Prof. Christian Moreau, for his continuous guidance, encouragement, support, and patience during the course of my Ph.D. program. Thank you for giving me the privilege to be a part of your group and work with you and learn from not only your immense knowledge but also from your inspiring life lessons, commitment, creativity, and compassion over the course of this research.

I am grateful to Dr. Robin Drew and Dr. Mamoun Medraj from Concordia University, Dr. Gwenaël Chamoulaud and Dr. Galyna Shul from Université du Québec à Montréal (UQAM), Philippe Plamondon and Josianne Lefebvre from Polytechnique Montréal University for giving me permission to use the facilities in their laboratories. I would like to thank Concordia University's research staff, particularly Robert Oliver, Mazen Samara, and Dmytro Kevorkov, and administrative staff, including Leslie Hosein and Arlene Zimmerman.

I am grateful to thank Dr. Fabian Ambriz-Vargas, Elnaz and Morvarid, my great colleagues, who helped me through the difficulties of the research with their help, support, and commitment.

I wish to thank Dr. Fadhel Ben Ettouil, who supported me thoroughly with his knowledge and experience. Fadhel, thank you for always being available, helping me with the experiments, and answering all my questions patiently.

I would like to express great appreciation to Dr. Ali Dolatabadi and Dr. Pantcho Stoyanov for their constant motivation, encouragement, and support. Dr. Dolatabadi and Dr. Stoyanov, many thanks for all your guidance; I have greatly benefited from your help and support.

I am thankful to all group members who participated in the "Covid Alliance Project" to investigate the antiviral activity of thermally sprayed coatings. Special thanks to Dr. David Kwan from Concordia University, Dr. Chen Liang from McGill University, and Dr. Maurice Ringuette from the University of Toronto for their valuable support for the antiviral tests and their interpretation. Special thanks to Dr. Rogerio Lima, Dr. Jörg Oberste-Berghaus from National Research Council Canada, Murray Pearson from HATCH, Steve Beaudin from Metal7, and Alan Burgess from SprayWerx Technologies for their continuous support, assistance, and guidance they put into the "Covid Alliance project" which presented in chapter 7 of my thesis.

I am greatly thankful to my great friends at Concordia University and the entire Thermal Spray Laboratory group members including Tahmineh, Sadaf, Navid, Saeed, Amit, Masiar, Mahdi, Farzam, Peyman, Maryam, Anahita, Ali, Hamideh, Golnoush. Thank you for being such a helpful and great team.

I would like to thank my thesis committee members, Dr. Fariborz Haghighat, Dr. Ali Dolatabadi, Dr. Martin Pugh, and Dr. Shrikant Joshi for taking the time to review my work, asking insightful questions, and challenging questions and giving me constructive comments and suggestions.

I extend my appreciation to the Natural Sciences and Engineering Research Council of Canada (NSERC) and MITACS for the financial support of the project.

A special thanks to my amazing husband, Armin, and my little angel, Liana, for their endless understanding, patience, and encouragement. Armin and Liana, I am so lucky to share my life with you. Without you, this achievement would not have been possible.

Last but not least, my most heartfelt thanks go to my parents, Rezvan and Mohsen, my brother Hesam, and my sister-in-law Afsaneh, for supporting me with their unconditional love and ever-lasting support and for believing in me every single step of my journey.

CONTRIBUTION OF AUTHORS

This thesis is written in a manuscript-based format. Chapters 1, 2, 3, and 8 are the introduction, literature review, experimental methods, and conclusions of the thesis, respectively. The thesis includes coauthored works in Chapters 4, 5, 6, and 7 that were reprinted from papers published or submitted to scientific journals. The contribution of each coauthor is described below:

Chapter 4:

H. Khatibnezhad, F. Ambriz-Vargas, F. Ben Ettouil, C. Moreau*, Role of phase content on the photocatalytic performance of TiO_2 coatings deposited by suspension plasma spray, Journal of the European Ceramic Society 42 (2022) 2905–2920.

* Corresponding author

H. Khatibnezhad worked on the literature review, planning, and methodology, performed all SPS coating experiments, post-treatments, and collected the data. She conducted all characterization tests, analyses, and discussions about the results and wrote the original draft, and review & editing the manuscript. F. Ambriz-Vargas helped the first author during the investigation and writing the manuscript. F. Ben Ettouil assisted with the preparation of samples. C. Moreau supervised the research and revised the manuscript.

Chapter 5:

H. Khatibnezhad, F. Ambriz-Vargas, F. Ben Ettouil, C. Moreau*, An investigation on the photocatalytic activity of sub-stoichiometric TiO_{2-x} coatings produced by suspension plasma spray, journal of the European Ceramic Society 41 (2020) 544-556.

* Corresponding author

H. Khatibnezhad worked on the literature review, planning, and methodology, performed all SPS coating experiments, post-treatments, and collected the data. She conducted all characterization tests, analyses, and discussions about the results and wrote the original draft, and review & editing the manuscript. F. Ambriz-Vargas helped the first author during the investigation and writing the manuscript. F. Ben Ettouil assisted with the preparation of samples. C. Moreau supervised the research and revised the manuscript.

Chapter 6:

H. Khatibnezhad, F. Ben Ettouil, C. Moreau*, Photoactive Ce-doped TiO_2 and CeO_2-TiO_2 composite coatings deposited by suspension/solution plasma spray, submitted to the journal of the Materials Research Bulletin.

* Corresponding author

H. Khatibnezhad worked on the literature review, planning, and methodology, performed all SPS and SPPS coating experiments, and collected the data. She conducted all characterization tests, analyses, and discussions about the results and wrote the original draft, and review & editing the manuscript. F. Ben Ettouil assisted with the preparation of samples. C. Moreau supervised the research and revised the manuscript.

Chapter 7:

H. Khatibnezhad[1], E. Aleebrahim[1], M. M. Bajgiran, F. Ben Ettouil, M. Solomon, S. Sagan, S. Beaudin, J. Oberste-Berghaus, R. S. Lima, C. Liang, C. Moreau*, Antiviral Properties of Thermal

Sprayed Coatings Against Human Coronaviruses HCoV-229E, ready to be submitted to the scientific journal.

[1] These authors contributed equally.

* Corresponding author

This study was part of the collaborative research work among the members of the Green-SEAM NSERC Strategic Network (Concordia University, McGill University, University of Toronto, National Research Council of Canada, Metal 7 Inc., Hatch, and SprayWerx) funded through NSERC and Mitacs. The first two authors were responsible for performing methodology, investigation, formal analysis, visualization, writing the original draft, and the following review & editing of the paper. C. Moreau supervised the research and revised the manuscript. The rest of the authors assisted with the preparation of samples (APS and S-HVOF coatings) and helped the authors during the investigation and writing the manuscript.

Table of Contents

List of Figures

List of Tables

Nomenclature

Al_2O_3	Alumina
APS	Atmospheric Plasma Spray
ATR-FTIR	Attenuated Total Reflectance-Fourier transform infrared spectroscopy
BSE	Back-scattered electron
C	Concentration
CB	Conduction band
Ce	Cerium
CeO_2	Cerium oxide
Cu_2O	Copper oxide
CVD	Chemical Vapor Deposition
D_{10}	10% of particles are this particle size
D_{50}	50% of particles are this particle size
D_{90}	90% of particles are this particle size
e^-	Electron
EDS/EDX	Energy Dispersive X-ray Spectroscopy
Eg	Bandgap
FE-SEM	Field Emission Scanning Electron Microscopy
h^+	hole
$OH_f^\bullet$	Free hydroxyl radical
$OH_s^\bullet$	Surface-bound hydroxyl radicals
$^\bullet HO$	Hydroxyl radicals
K	rate constant of the pseudo-first-order reaction
MB	Methylene Blue
$O_2^{-\bullet}$	Superoxides ions
PCO	Photocatalytic oxidation
PFU	Plaque Forming Units
PVP	Polyvinylpyrrolidone
R^2	Correlation coefficient
Ra	Arithmetic mean height of the surface on a line (μm)
RLU	Relative Luminescence Unit
ROS	reactive oxygen species
SARS	Severe acute respiratory syndrome
SE	Secondary electron
SEM	Scanning Electron Microscopy
S-HVOF	Suspension High-Velocity Oxygen Fuel
SLPM	Standard liter per minute
SPPS	Solution Precursor Plasma Spray
SPS	Suspension Plasma Spray
TGA	Thermogravimetric analysis
TiO_2	Titanium dioxide, titania
T_m	Melting point
UV	Ultraviolet
UV-vis	UV/vis absorption spectroscopy
VB	Valence band
WHO	World Health Organization
Wt. %	Weight percent
XPS	X-ray photoelectron spectroscopy
XRD	X-ray diffraction

Chapter 1. Introduction

1.1 Background

Nowadays, water and air contamination are serious forms of pollution, and their damaging effects on human health and the biosphere can be irreparable [1][2]. As the main part of industrial wastewater, synthetic dyes are widely used by manufacturing industries in huge quantities. The colored effluents might also endanger aquatic life by reducing the dissolved oxygen level and blocking sunlight penetration, and their potential to produce carcinogenic substances is of concern. It indicates the importance of treating colored wastewater before releasing them into different water bodies [3]. Different techniques, such as coagulation [4], electrochemical/ sedimentation processes [5] and adsorption [6][7], have been proposed for water purification. However, these approaches might produce a new kind of pollution which need some expensive post-treatment.

Novel strains of respiratory tract infections have initiated human pandemics and caused extensive disease, death, and disruption, for decades. After Severe Acute Respiratory Syndrome (SARS) coronavirus and Middle East Respiratory Syndrome (MERS) coronavirus, the most recent pandemic caused by the novel human coronavirus disease (COVID-19) has raised worldwide attention towards public health over the past two decades [8]. Over 627 million cases of infection of coronavirus disease (COVID-19), including around 6.5 million deaths, were reported by the World Health Organization (WHO) by November 2022 [9].

Therefore, removing pollutants and viruses from our environment has received increasing attention in the scientific world. Photocatalytic oxidation (PCO) is considered an effective approach to remove organic compounds in aqueous solutions in the presence of a semiconductor photocatalyst and UV light [10]. It is a technique in which mostly sunlight (contains around 5% UV light) is utilized for the decomposition and removal of organic poison compounds and harmful gases from water and air and for the conversion of solar energy to electric power with the production of hydrogen [11][12][13].

Titanium dioxide (TiO_2) is an abundant, low-cost, chemically stable, and non-toxic material. TiO_2, as one of the most researched semiconductor materials, shows excellent technological properties and has extensive applications such as photocatalysts, dye-sensitized solar cells, sensor devices, membranes, and paints [14][15]. It also has attracted ever-growing worldwide attention for antipathogenic applications [16][17][18][19]. The powerful oxidizing potential of TiO_2 was revealed in late 1960 when Fujishima and Honda were working on photo-electrochemical (PEC) solar cells at the University of Tokyo [20]. There are many advantages of the photocatalysis process, some of which are the possibility of (i) using it in various media: gaseous phase (for air purification) and aqueous solutions (for rectifying water), (ii) utilizing renewable and pollution-free solar energy for photocatalysis for environmental remediation, (iii) reducing secondary wastes in the process due to efficient mineralization [20].

1.2 TiO_2 limitation

Among advanced oxidation processes, TiO_2 photocatalysis showed an excellent ability to mineralize various organic pollutants in wastewater and polluted air using solar energy. However, its application is limited for two main reasons; large bandgap (anatase ~3.2 eV and rutile ~3 eV) and low photo-quantum efficiency [21][22]. The former restricts TiO_2 application under UV light to absorb a small fraction of sunlight (<5%) that meets its bandgap energy [23]. The latter is caused by the high recombination rate of photo-generated electron-hole pairs, which reduces the photocatalyst efficiency. When charge carriers recombine before moving to the photocatalyst's surface, there are no more charges to start the reaction [24]. Therefore, some modifications are needed to activate TiO_2 photocatalyst under visible light to utilize a more significant portion of the solar spectrum and to improve its efficiency by increasing the charge carrier lifetime.

In photocatalysis, the higher the surface area, the better the photocatalyst's efficiency since more spots would be available to degrade pollution. In this regard, TiO_2 nano powder photocatalyst has shown to be an efficient photocatalyst. However, after the photocatalysis reaction, powder recovering processes from the treated water raised economic and safety concerns. This problem can be overcome by using TiO_2 films, while the resulting surface area reduction could be compensated by producing nano- and micro-structured TiO_2 coatings [21].

1.3 Research objectives

Some modification methods and chemical additives have been investigated in recent decades to increase the photocatalytic activity of TiO_2 under visible light irradiation as the main part of the solar spectrum. From the critical literature review, numerous works have been done to activate TiO_2 coating using the most common methods, such as sol-gel and CVD. However, it is still challenging to develop coatings in industrial scale-up. In the last decades, thermal spray processes as environmentally friendly technology appear as a versatile and rapid processing approach where the large surface area coverage and fast deposition rate make this deposition process compatible with large-scale industrial production. To the best of our knowledge, among the research studies on the thermally sprayed TiO_2 coatings, there is a lack of studies on the effect of doped/self-doped TiO_2 due to its challenging limitations, such as short residence time and reaction time. Moreover, the role of the crystalline phase as one of the most important parameters affecting photocatalytic activity has not been comprehensively reviewed for thermally sprayed TiO_2 coatings. Furthermore, there is not any systematic work to study the overall performance of thermal spray technology in producing cost-effective antiviral coatings for possible future pandemics.

The main objective of this research study is a comprehensive investigation to develop thermally sprayed photoactive coatings under visible light, as follows:

- A process map to clarify the role of the phase content of the SPS coatings on their photocatalytic properties.
- A comprehensive study about the effect of oxygen deficiencies on the photocatalytic properties of sub-stoichiometric TiO_{2-x} coatings obtained by SPS
- An investigation of the photocatalytic efficiency of TiO_2 coatings by introducing cerium dopants into TiO_2 lattice.
- A comprehensive study on the antiviral activity of TiO_2 coatings and its composites.

1.4 Thesis organization

This thesis includes eight chapters, and each chapter is briefly explained.

Chapter 1 (introduction) This chapter introduces the water purification problem, a brief background of TiO_2 application, its limitations, and the research objectives of this study.

Chapter 2 (Literature review) This chapter provides the basic principle of photocatalytic oxidation, its applications and limitations. Afterwards, some affecting parameters on the TiO_2 photocatalytic efficiency are reviewed. Parameters like crystalline phase, the amount of catalyst, the concentration of pollutant, light intensity and irradiation time were investigated. Subsequently, TiO_2 modification strategies were explained. Moreover, this chapter presents thermal spraying processes. Suspension plasma spraying (SPS), solution precursor plasma spray (SPPS), atmospheric plasma spraying (APS), and suspension-high velocity oxygen fuel (SHVOF) methods that are used in this research are briefly described. Finally, TiO_2 photocatalysts produced by thermal spraying processes were reviewed.

Chapter 3 (Experimental procedures) This chapter presents the experimental methodology, starting materials, post-treatments, characterization methods and analysis instruments. The experimental methodology for photocatalytic and antiviral evaluation was explained in detail.

Chapter 4 (Paper 1) shows a systematic work to present the influential role of anatase phase on the photocatalytic activity of TiO_2 coatings obtained by suspension plasma spraying.

Chapter 5 (Paper 2) provides a systematic work to present the influential role of oxygen vacancies (as self-dopant) on the optical properties and photocatalytic activity of sub-stoichiometric TiO_{2-x} coatings obtained by suspension plasma spraying.

Chapter 6 (Paper 3) The photocatalytic performance of cerium-doped TiO_2 and CeO_2-TiO_2 coatings produced by Suspension plasma spray (SPS)/ solution precursor plasma spray (SPPS) and SPS was evaluated.

Chapter 7 (Paper 4) The role of the different thermal spray processes in producing TiO_2, Cu_2O, TiO_2-Cu_2O and TiO_2-Al_2O_3 antiviral coatings was investigated. The human common cold coronavirus, HCoV-229E, was used as a surrogate for SARS-CoV-2 to investigate the antiviral activity of the coatings in a containment level-2 laboratory.

Chapter 8 (Conclusion and future work) summarizes this research work's main outcomes, conclusions and contributions. Finally, some recommendations for future work are provided.

Chapter 2. Literature review

2.1 Mechanism of photocatalysis

Nowadays, water and air contamination are serious forms of pollution, and their damaging effects on human health and biosphere can be irreparable [1][2]. Therefore, removing pollutants from our environment has been receiving increasing attention in the scientific world. Organic dyes, as a recognized source of pollution released by the dye industry into waste-water, are widely used as a test pollutant [25]. Many traditional techniques are used for dye removal from waste-water, some of which are filtration, adsorption, coagulation, sedimentation, and treatment with ozone. However, these ways may produce a new kind of pollution that needs some expensive post-treatment [3][26][27].

Photocatalysis is a technique that has brought about some advantages compared with conventional methods by decomposition and removal of organic poison compounds and harmful gases from water and air under irradiation of light. Therefore, a photocatalyst is a material that can absorb light to produce photo-generated electron-hole pairs, which allow chemical transformations of participants and create its chemical composition after each cycle of such interactions [28][29].

The characterization of the absorption spectrum of the photocatalyst is important to determine whether the optical activation is possible under sunlight. Many biocompatible semiconductors are used as photocatalysts, including TiO_2, ZnO, SnO_2, and CeO_2. They can produce charge carriers under light irradiation with sufficient short wavelengths. Not only do they play a crucial role in environmental remediation, but also they can be used as photovoltaic materials to prevent fogging of the glass and in the electronic industry (Fig. 2.1) [30][31][32][33]. Over the last few decades, TiO_2 has appeared as one of the most important photocatalysts, which can operate at room temperature in a cleaner, safer, and more effective way [34].

Figure 2. 1 Possible applications of metal oxides [33].

2.2 TiO_2 as a photocatalyst

Photocatalysis is defined as an advanced oxidation process (AOP). The mechanism consists of generating electron-hole pairs through exciting electrons from the valence to the conduction bands by absorption of photons of equal or larger energy than the bandgap energy. The photo-generated electron-hole pairs can migrate to the surface of TiO_2, where they are trapped by oxygen molecules and adsorbed water to generate highly oxidizing radical species, such as hydroxyl radicals ($^{\bullet}HO$) and superoxides ($O_2^{-\bullet}$) ions (Fig. 2.2) [35]. This process involves decomposing the organic material (like organic dyes as a test pollutant) and even mineralizing the intermediates into harmless products, mostly carbon dioxide and water. There are many advantages of the photocatalysis process, some of which are the possibility of (i) using it in various media: gaseous phase (for air purification) and aqueous solutions (for rectifying water), (ii) utilizing renewable and pollution-free solar energy for photocatalysis for environmental remediation, (iii) reducing secondary wastes in the process due to efficient mineralization [20].

The commonly postulated chain reactions occurring in the photocatalytic process are as follows [36][3]:

$$TiO_2 + h\upsilon \rightarrow e^- + h^+ \quad (2.1)$$

$$H_2O + h^+ \rightarrow {}^{\bullet}OH + H^+ \quad (2.2)$$

$$O_2 + e^- \rightarrow O_2^{-\bullet} \quad (2.3)$$

$$O_2^{-\bullet} + H^+ \rightarrow HO_2^{\bullet} \quad (2.4)$$

$$2HO_2^{\bullet} \rightarrow H_2O_2 + O_2 \quad (2.5)$$

$$H_2O_2 \rightarrow 2{}^{\bullet}OH \quad (2.6)$$

$${}^{\bullet}OH + Dye \rightarrow intermediate \rightarrow H_2O + CO_2 \quad (2.7)$$

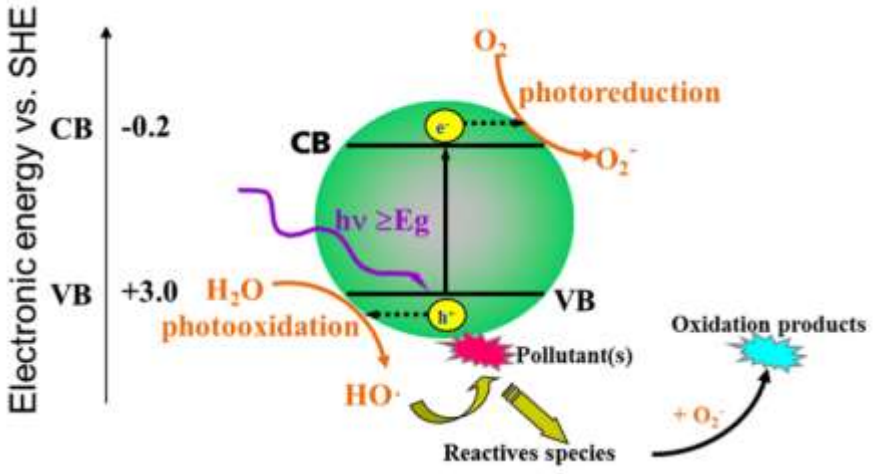

Figure 2. 2 Schematic representation of the photocatalytic mechanism [36].

2.3 Parameters affecting photocatalytic degradation of TiO_2

The photocatalytic degradation rate of organic compounds primarily depends on several parameters, which are described below.

2.3.1 Crystalline phase

The photocatalytic degradation rate of organic compounds primarily depends on the crystalline phase of TiO_2. Anatase and rutile are the two main crystalline phases of titania that anatase irreversibly transforms to rutile at a higher temperature than 600 ºC for a fine pure anatase powder. However, the reported temperature can vary in the range of 400-1200 ºC depending on factors such as particle size, surface area, atmosphere, impurities, raw materials, and processing methods [37]. The large bandgap of pure TiO_2 (3.0 for rutile and 3.2 for anatase) makes it active under UV light. It has been indicated that the phase mixture of both polymorphs shows better photocatalytic activity than single phases due to their synergistic effects [22]. Yet, for single-phased titania, the photocatalytic activity of anatase is commonly better than its rutile counterpart in all types of reaction media [22][37][38][39]. Some hypotheses have explained the reasons for the differences in the photocatalytic efficiency of anatase and rutile. Although the larger bandgap of anatase causes lower absorbance ability towards solar light, it may enhance the redox power of charge carriers and surface adsorption capacity to hydroxyl groups attributed to the different position of the conduction and valence bands and higher Fermi energy of anatase [22][36][38].

Based on the literature, in direct bandgap semiconductors, like rutile, photo-generated electrons and holes recombine directly, resulting in the emission of a photon. On the other hand, anatase, with an indirect bandgap, has a longer lifetime of photoexcited electrons and holes due to its slower recombination process. This is because a phonon is necessary for the recombination to occur, as shown in Fig. 2.3 [22][38].

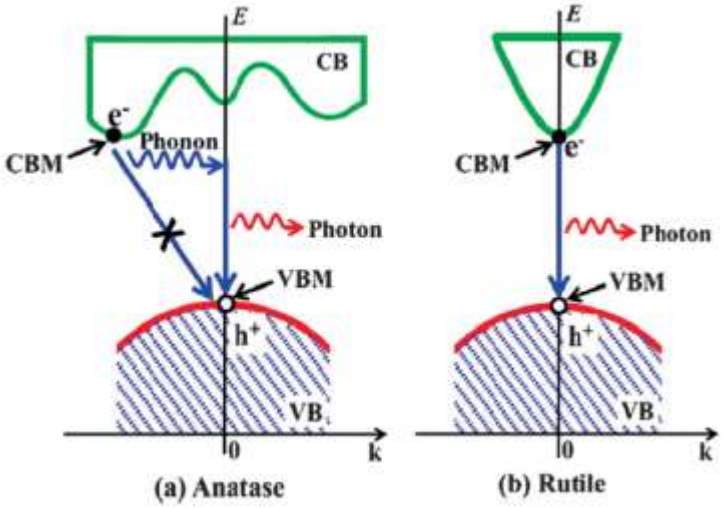

Figure 2. 3 Comparison of recombination processes of e/h within indirect gap anatase (a) and direct gap rutile (b) [38].

As a result, anatase shows a longer electron-hole lifetime and exciton diffusion length. Therefore, it is more probable for photo-generated charges to migrate from the bulk to the surface and drive surface chemical reactions that improve photocatalytic performance [22][38][40].

According to Luttrell's work [22], anatase has a higher charge diffusion length than rutile since charge carriers excited deeper in the bulk of anatase could take part in photoreactions. The larger charge diffusion length of anatase might be attributed to its longer lifetime of charge carrier and/or its higher photo-generated electron/hole mobilities.

Based on the Odling et al. [41] report, anatase shows free hydroxyl radical ($OH_f^{\bullet}$) in TiO_2/water interface that could decompose organic pollutants both at the surface and in the bulk solution for water purification, while rutile phase presents only surface-bound hydroxyl radicals ($OH_s^{\bullet}$) with the ability to degrade contaminants only at the surface of the photocatalyst during the photocatalytic reaction. That might be the reason for the higher photocatalytic activity of anatase phase than that of rutile phase.

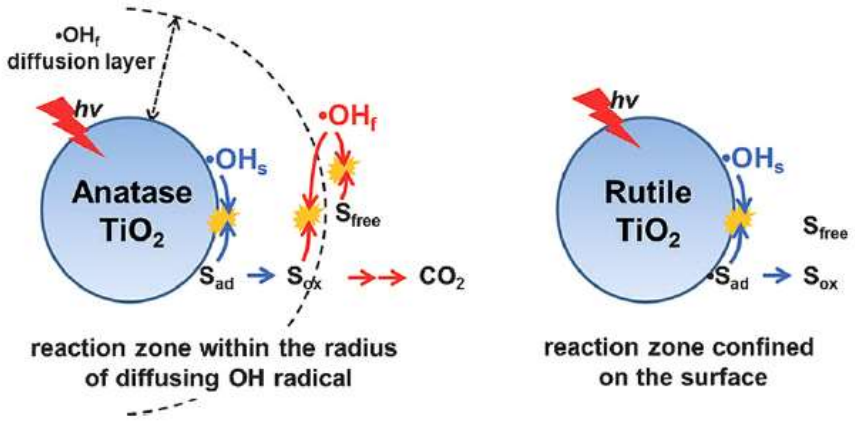

Figure 2. 4 Schematic of hydroxyl radical formation and reaction with organic substances upon rutile and anatase [41].

2.3.1.1 Anatase to rutile phase transformation

According to the literature, for pure anatase, reconstructive transformation to rutile begins in the air at 600 ºC; however, there is a range value of transition temperature of anatase to rutile between 400 ºC to 1200 ºC due to its dependency on several factors. Indeed, some parameters, like the particle size, surface area, atmosphere, heating rate, soaking time, impurities, and sample preparation, could influence the kinetics of this transition. However, it is known that the phase transformation temperature is in the range of 600 to 700 °C for a fine high-purity powder [37].

From the thermodynamic point of view, rutile is the stable phase of TiO_2 at all temperatures and pressures due to its lower free energy of formation (-889,406 kJ mol^{-1} for rutile and -883,266 kJ mol^{-1} for anatase, each at 298 K) [37][42]. However, at small particle size, anatase is more stable due to its lower surface free energy than those of rutile and brookite (1.25 J m^{-2} for anatase and 2.17 J m^{-2} for rutile at 298 K) and anatase formation is more probable according to the Eq. 2.8 [42],

$$G^o = \Delta G_f^o + A\gamma \quad (2.8)$$

Where ΔG_f^o (J mol^{-1}) is the standard free energy of formation, A (m^2 mol^{-1}), the molar surface area and γ (J m^{-2}) the surface free energy.

According to Fig. 2.5, which represents the standard free energies based on the particle spherical diameter calculated at 298 K, there is a critical particle size of 15 nm. Below this point, anatase exhibits lower standard free energy and more stability, and above rutile is the more stable phase [42].

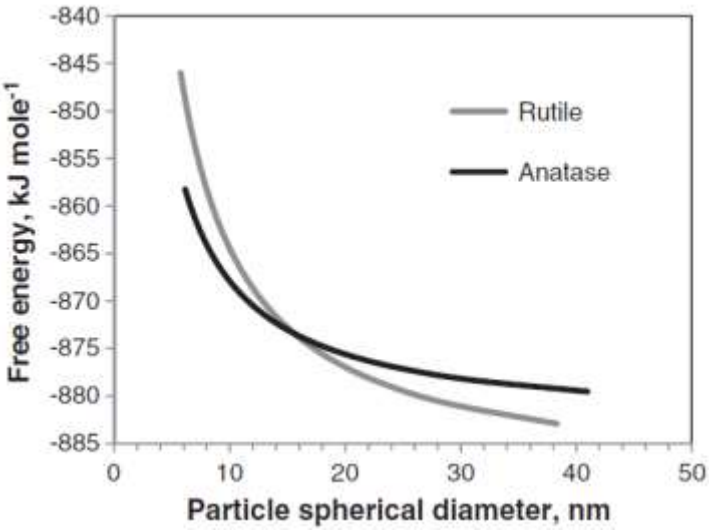

Figure 2. 5 Standard free energies for anatase and rutile at 298 K vs. spherical particle diameter [42].

Furthermore, in some coating methods like plasma spraying, metastable anatase possibly nucleates from the liquid at an undercooling temperature below 0.88 T_m, while rutile nucleates at a temperature above 0.88 T_m (1870 K) until the melting point (T_m=2130 K) [43][44][42]. In thermal spray deposition, TiO_2 solidifies under rapid quenching conditions to form both rutile and anatase [45].

2.3.2 The amount of catalyst

With increasing the catalyst concentration, photocatalytic activity improves by increasing the number of active sites. Increasing the surface means an increasing number of $^{\bullet}OH$ radicals, which can participate in the actual degradation of the dye solution. For catalysts in the form of powder, after a certain amount of catalyst, the solution becomes turbid and thus blocks the UV radiation for the reaction to proceed, which decreases the degradation of pollutants. Table 2.1 shows the effect of catalyst amount on % decolorization [3].

Table 2. 1 Effect of V_2O_5/TiO_2 on % decolorization of dye solution in the presence of UV (concentration of TB=SO=80 µM, CV=40 µM, irradiation time=20min, pH=6.1) [3].

Dye	Catalyst amount (mg/20 mL)				
	10	20	25	30	40
Toludine Blue (TB)	15	40	47	41	27
Safranin Orange (SO)	8	11	21	12	-
Crystal Violet (CV)	6.5	12	-	17	15

Reducing the particle size can also increase the surface area. For example, nano-sized TiO_2 has a more efficient ability in water purification and recycling due to its smaller size compared with bulk TiO_2. By reducing the size of the catalyst, the surface-to-volume ratio will increase [28].

2.3.3 Concentration of pollutant

Pollutant type and its concentration play an important role in photocatalytic activity. It has been reported that under the same operating conditions, the degradation rate diminishes with increasing the concentration of pollutants, and a longer irradiation time is needed to reach complete mineralization. As dye concentration increases, more organic compounds are adsorbed on the surface of titania. However a smaller number of photons can reach the catalyst surface. Hence fewer hydroxyl radicals are formed, resulting in less degradation percentage [3][46].

2.3.4 Light intensity and irradiation time

TiO_2, with its large bandgap (3.2 eV), activates mainly under light wavelengths at $\lambda<380$ nm region and therefore, the results of photocatalytic reaction vary under different wavelengths of the light source. Many studies have shown that light intensity affects dye degradation as follows; the degradation rate would increase linearly with increasing light intensity in the range of 0-20 mW/cm^2 (first order) in which electron-hole creation is predominant, and their recombination is negligible. This approves the photo-induced nature of the activation of the catalytic mechanism, with the participation of photo-generated electron holes in the reaction process. However, under moderate light intensities (25 mW/cm^2), the rate relies on the square root of the light intensity. According to the literature, shifting from Φ to $\Phi^{1/2}$ is because of the number of photo-generated holes available during the formation of the photo-generated charges. In TiO_2 as an n-type semiconductor, the photo-generated holes available in the valance band are much less than electrons in the conduction band that consists of photo-induced electrons plus n-electrons. As a result, the photo-induced holes are the rate-limiting step. At high-intensity, the dependency of the reaction rate on light intensity is reduced to zero as the electron-hole recombination increases, thereby causing a lower effect on the reaction rate [3][46][47][48]. The photocatalytic reaction rate would reduce with irradiation time (Fig. 2.6) due to the deactivation of active sites by strong byproduct deposition [3].

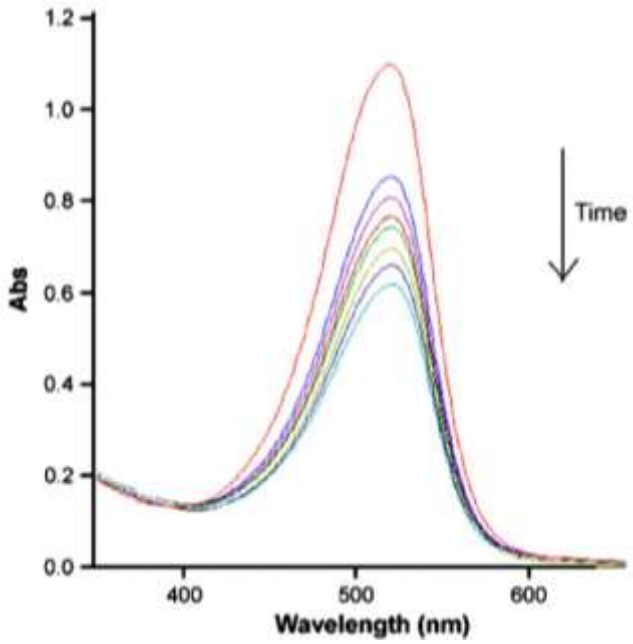

Figure 2. 6 Effect of irradiation time on % degradation of an azo dye [3].

2.4 Modifications of TiO_2 photocatalysts

Since Honda and Fujishima first found a strong oxidation and reduction power of photoexcited titanium dioxide (TiO_2) in 1972, semiconductor photocatalysts have attracted much attention, especially for environmental treatments. TiO_2 displays quite high reactivity and chemical stability under UV light (λ<380 nm), whose energy exceeds the bandgap of 3.2 eV in the anatase crystalline phase [49]. However, one of the significant problems in using TiO_2 as a catalyst is low reactivity under visible light (λ> 400 nm), which limits its application when using the main part of the solar spectrum. Moreover, it has low photo-quantum efficiency, which arises from the fast recombination of photo-generated electrons and holes. One promising method to overcome this issue is creating energy levels within the bandgap or adequately shifting the conduction band (CB) and/or the valence band (VB) so that photons of lower energy can excite electrons. These energy levels also can act as a trap for reducing the recombination rate [3]. Various strategies have been investigated to shift the absorption edge of TiO_2 into the visible region and improve its photocatalytic activity. Doping pure TiO_2 with either anions or cations is one way to sensitize TiO_2 under visible light [50].

2.4.1 Cationic dopants

Cationic-doped TiO_2 with elements such as rare earth metals, noble metals, poor metals, and transition metals have been widely studied. The metallic ions-doped TiO_2 expands the light absorption region and increases the quantum efficiency by preventing the recombination of the photo-generated electrons and holes on the conduction and valence bands, respectively [50].

However, increasing the visible light absorption is not a sufficient factor to improve the photoactivity of doped TiO_2. The concentration of doped metal ions is an important parameter which should be optimized. Above a certain amount of concentration, the photocatalytic activity reduces due to the increase in recombination. Furthermore, metal ions should be doped near the surface of TiO_2 particles to improve charge transferring. While in deep doping, metal ions probably behave as recombination centers due to the problematic transfer of photo-generated charges to the interface [51]. The transition metals that exhibit two or more oxidation states usually improve the TiO_2 photocatalytic activity. For example, iron (Fe) with different ion forms (Fe^{4+}, Fe^{3+}, and Fe^{2+}) acts as a trap for the electron-hole pairs and therefore prevents their recombination (Fig. 2.7) [52].

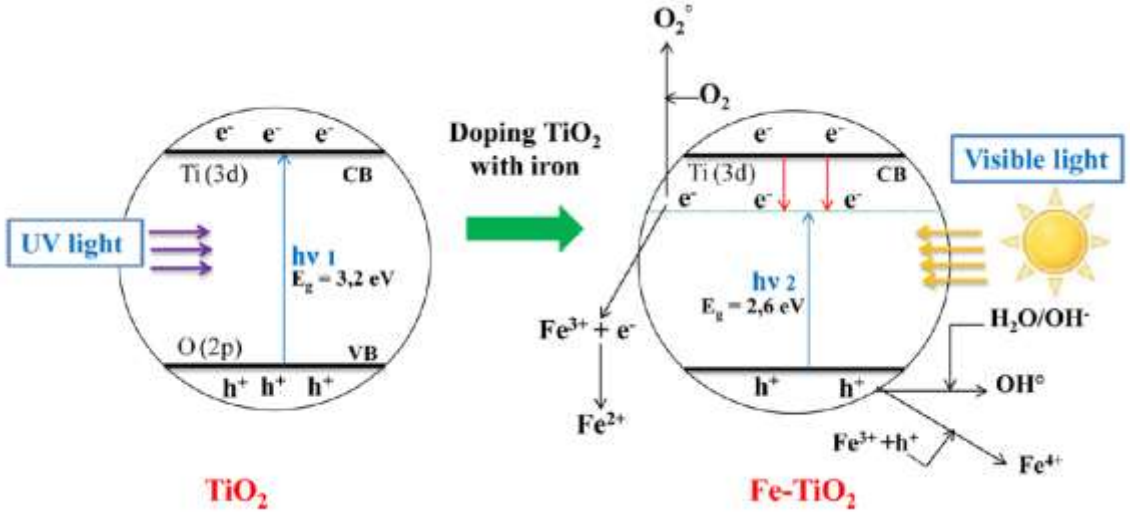

Figure 2. 7 The schematic energy level of iron doping TiO_2 [52].

2.4.1.1 Rare earth metal doping

Rare earth metals are a group of seventeen elements in the periodic table that are classified as lanthanides. These elements are not abundant in the Earth's crust, making them rare. Rare earth metals like Ce and Nd are other types of influential cationic dopants to improve catalysis due to their incompletely occupied 4f and empty 5d orbitals. It has been reported that Ce as a dopant could limit the grain size growth of TiO_2 to reduce its crystallite size and increase the specific surface area. It also can act as a trap to scavenge electrons and increase charge carrier lifetime [52][53].

Based on the literature, cerium doping could enhance the photocatalytic performance of TiO_2 by improving its optical properties and decreasing the electron/ hole recombination rate. The charge imbalance or strain induced by Ce^{3+} incorporation might create oxygen vacancy. It has been reported that Ce^{3+}/Ce^{4+} mixture and oxygen vacancies would introduce energy 4f levels just below the TiO_2 conduction band, which are responsible for more photocatalytic activity. These energy levels would decrease the bandgap to activate TiO_2 photocatalyst at a longer wavelength and inhibit charge carrier recombination by trapping them [53][54][55][56][57].

Doping TiO_2 with rare earth metal ions can enhance photocatalysis performance, yet this process may also have some drawbacks. Beyond the optimum value of the dopant, the photocatalytic activity of TiO_2 decreased, which can be attributed to the formation of deep-level energy states close to the Fermi level acting as the charge recombination centers and reducing the charge carriers' lifetime [54]. ˇStengl et al. [53] reported the optimal dosage of rare earth ions needed to get the most effective separation of photo-excited electron hole pairs to degrade Orange II dye. Based on their results, the optimum amount of rare earth dopant is 1-2 wt.% to achieve the highest activity under visible light.

It should be noted that using rare earth metals to improve PCO efficiency for industrial applications might not be cost-effective.

2.4.2 Anionic dopants

Doping with non-metals to improve the photoactivity and probability of TiO_2 catalysts for industrial application is quite a new method, which few research works have reported in the open literature. Anion doping (N, F, C, and S) shows positive effects in the redshift to the visible region and higher photocatalytic activity. Unlike metal ions (cations), their role as recombination centers might be minimized and, therefore, are more effective to enhance the photocatalytic activity. In this case, the impurity states are close to the valence band edge [46][47].

Among anionic dopants, nitrogen has been found a considerable interest, which shows a promising extension for environmental applications where the conventional TiO_2 is not used. The nitrogen species could be either a substitutional or an interstitial N atom in the TiO_2 matrix. According to Fig. 2.8, the substitutional species are mostly located just above the valence band, while the interstitial nitrogen states are present at 0.73 eV above the valence band [11][12].

Carbon doping of TiO_2 also attains a significant interest by introducing new states (C2p) above the valance band edge of titania (O2p) to narrow the bandgap. Some carbonaceous species may also form by carbon incorporation into titania lattice, which could promote the absorption of visible light. However, they might limit the photocatalytic activity of C- doped TiO_2 by covering and blocking surface active sites [58]. Moreover, C-doped TiO_2 exhibits higher surface area by inhibiting particle growth, which provides more reactive sites and improves the adsorption of more target pollutants [52][59][60].

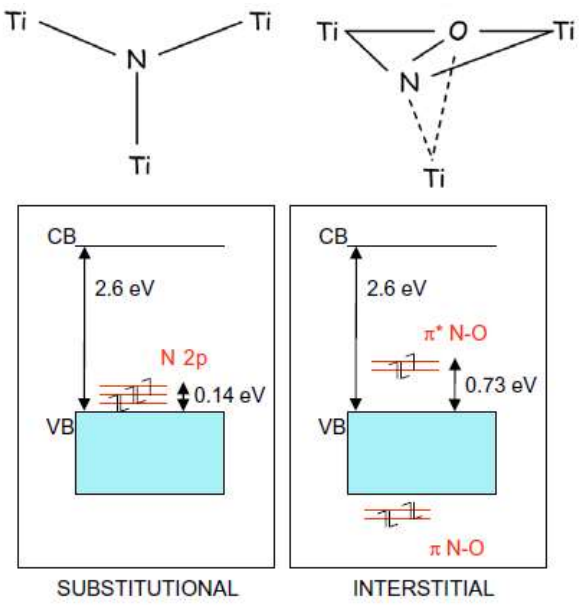

Figure 2. 8 Electronic structure substitutional and interstitial models [11].

Although the numerous advantages attained by doping TiO_2 with non-metal anions, researchers have found that the content of dopant would drop during the annealing process of synthesizing doped-TiO_2 nanopowder, thus decreasing the photoactivity under visible radiation [52][61].

2.4.3 Self-doped TiO_2

Another strategy for enhancing photocatalytic activity consists of using reduced forms of titania such as TiO_x ($x < 2$). It has been reported that sub-stoichiometric titania in the anatase phase does act as an efficient photocatalyst [62][63]. The insertion of oxygen vacancies in the anatase structure induces a band of electronic states just below the conduction band, starting to overlap with the conduction band for large vacancy concentrations. These vacancy-induced bands of electronic states are responsible for increasing the photocatalytic efficiency of the self-doped films. In sub-stoichiometric samples, the colour change to dark grey, depending on the degree of oxygen loss because of a high concentration of Ti^{3+} ions, while pure and super stoichiometric samples are fully transparent. The spectral absorption coefficient was measured in the UV-vis range (Fig. 2.9). The observed increase of optical absorption at a longer wavelength nearby to the visible region with decreasing the oxygen concentration confirmed the theoretical prediction of the creation of a new band below the conduction band [62][63][64][65]. Furthermore, oxygen vacancies in sub-stoichiometric TiO_2 dissociate water molecules and form two hydroxyl groups via H^+ transfer to neighbouring oxygen after exposure to air at room temperature [20][66][67].

Literature suggests that the existence of hydroxylation on the photocatalyst's surface is of great importance for its efficiency [36].

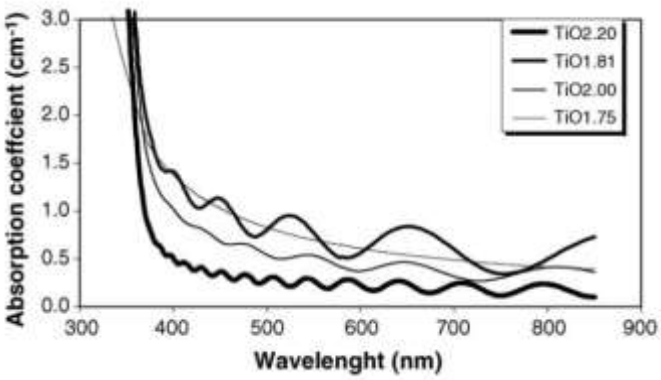

Figure 2. 9 Comparative absorptions of samples with different stoichiometry [62].

2.4.4 Composites

One approach to facilitate charge separation in the TiO_2 photocatalyst and increase its efficiency is using composite semiconductor metal oxides. It has been reported that a group of semiconductor/semiconductor or semiconductor/metal composite nanoparticles diminish the recombination rate in the semiconductor nanostructures [47][68]. CeO_2 is one of the important semiconductors with superior physical properties. The coupling between TiO_2 and CeO_2 semiconductors has been intensively investigated for the degradation of organic pollutants presenting better activity than that observed for TiO_2 and CeO_2 separately. Based on the literature, compositing TiO_2 with an optimum amount of CeO_2 nanoparticles would enhance interfacial charge separation and lower charge carrier recombination rate [69][70][71].

Additionally, coupling titania with noble metals also shows remarkable results. Noble metals, such as Ag and Au, can act as a sink for photo-induced charge carriers and promote interfacial charge-transfer processes in these composite systems, which is beneficial for maximizing the efficiency of photocatalytic reactions. Ag nanoparticles could increase the wavelength response of TiO_2 towards the visible region. These nanoparticles with a large surface area have also demonstrated promising antibacterial properties compared to bulk silver material [72][73].

2.5 TiO_2 photocatalyst applications

2.5.1 Water purification systems

Access to clean drinking water is a basic human need, the demand for which is increasing due to population growth and urban sprawl. Based on the prediction of the World Health Organization (WHO), half of the world's population will face water-stressed conditions by 2025 [41].

There are different sources of water contaminants. Textile synthetic dyes are recognized sources of pollution due to their potential carcinogenic properties and threat to aquatic life by blocking sunlight penetration and oxygen dissolution. Moreover, the natural biodegradability of these dyes is difficult. Almost 15% of the total global dye production is released into the textile effluent during the dyeing process. Therefore, it is necessary to treat the colored wastewater before releasing them into water bodies [3][74][75].

Water-soluble herbicides and antibiotics are also considered as the main pollution source for underground and surface waters. Herbicides are extensively used in the agricultural industry to increase food production and control weeds, which cause severe ecological effects on aquatic ecosystems. Antibiotics are widely used in human and veterinary medicine. They are thrown out via urine or feces to the aqueous environment with adverse effects on aquatic organisms and cannot be effectively removed by conventional water treatment process [76][77][78].

The photocatalytic process is an environmentally friendly technique that could be employed for water treatment by producing strong oxidizing radicals. TiO_2 semiconductor is considered as a great candidate for photocatalytic application. It can create considerably fewer residues or even completely degrade organic compounds from wastewater [3][76].

2.5.1.1 Degradation of Methylene Blue

Methylene blue (MB) ($C_{16}H_{18}ClN_3S$) is a water-soluble cationic dye which is widely used in the textile industry [79]. It is composed of two aromatic rings linked by a nitrogen atom, with a blue color that is highly visible in the visible light spectrum. However, it is toxic to the environment and, if not properly treated, can cause irreversible damage to ecosystems. While conventional wastewater treatment methods such as adsorption, activated carbon and flocculation are considered ineffective approaches to remove MB from the effluent, photocatalysis using TiO_2 has been studied as a potential method for its removal from wastewater [3][74][75].

Under light irradiation, TiO_2 photocatalyst would produce reactive species, such as OH radicals, which can mineralize dye molecules into smaller, nontoxic compounds such as water, carbon dioxide, and other byproducts. The smaller molecules are much less toxic to the environment and are easily broken down further by other natural processes. The byproducts formed in this process depend on the properties of the dye molecule, the intensity and wavelength of the light, the type of TiO_2 used, and the environmental conditions [3][74][75][80].

Houas et al. [74] monitored the MB degradation pathway under TiO_2/UVA irradiation system. They used UV-Vis spectroscopy and measured the total organic carbon (TOC) content of the solution. It was reported that TiO_2/UVA irradiation system could effectively remove the color of the dye. Moreover, this process could oxidize dye with almost complete mineralization of carbon, nitrogen and sulfur heteroatoms, resulting in the formation of CO_2, NH_4^+, NO_3^- and SO_4^{2-}. This mineralization process involved the oxidation of the dye molecules caused by the photocatalytic activity of TiO_2, leading to the breakdown of the dye molecules into their individual components. This study demonstrated that the TiO_2/UVA system was effective in degrading MB, making it an ideal method for the purification of diluted textile effluent [74].

2.5.2 Air purification system

In the last years, there has been an increased awareness of indoor air quality, as the pollutant levels are often higher than those encountered outdoors. Since people spend much of their time indoors, they are subjected to high levels of indoor air pollution, making it one of the top five environmental risks to human health. Indoor air can contain hazardous compounds, known as Volatile Organic Compounds (VOCs), that have been associated with a variety of adverse health effects. VOCs are a group of organic compounds that evaporate at a relatively low temperature and are typically released from many different sources, such as furniture, carpets, paint, and cleaning supplies. Heterogeneous photocatalytic oxidation (PCO) is an attractive approach for removing VOCs from the air inside buildings since it can be worked at ambient pressure and

temperature. This process involves using light energy to break down VOCs into simpler and less harmful substances, thereby improving air quality. Among various semiconductors for PCO applications, TiO_2, a cost-effective and stable photocatalyst, has been extremely effective in degrading a wide range of VOCs [81][82][83][84][85].

Moreover, TiO_2 photocatalyst can be employed to lower nitrogen oxides NO_x (NO, NO_2) and sulfur dioxide (SO_2) concentrations emitted into the atmosphere due to urbanization and industrialization. These harmful air pollutants are associated with the formation of acid rain and the greenhouse effect and can be detrimental to both human health and inner-city buildings. By using TiO_2 photocatalyst, the NO_x and SO_2 molecules will be converted into harmless compounds [86][87][88].

The application of PCO for air purification was investigated in a continuous-flow reactor. Based on the results, higher residence time would achieve by decreasing the airflow rate, which would give more VOCs the possibility of being adsorbed on the surface of the photocatalyst [82][81]. The efficiency of the PCO system also depends on the humidity level. Although water molecules are essential to produce hydroxyl radicals, high humidity levels hinder photo-oxidation by occupying the active sites by water molecules [89].

The main challenge of increasing the use of PCO technology in mechanical ventilation systems in buildings for VOCs removal is the potential production of hazardous and unwanted by-products. So PCO technology should address not only the primary pollutants but also the generated by-products in the gas phase. Therefore, PCO is better suited for low concentrations of contaminants to provide enough active sites for removing both VOCs and their intermediates [81][83].

2.5.3 Antiviral applications

Viruses and viral infections have circulated among humans for several years, causing serious problems in most people like the new human coronavirus disease 2019 (COVID-19), caused by the most novel strain of Severe Acute Respiratory Syndrome Coronavirus, SARS- Cov-2.

Compared to bacterial pathogens, viruses are smaller in size, resistant to environmental inactivation, and have different biological structures [90]. Their rigid protein shell requires intensive oxidation to be denatured. They also have a lower infectious dose of <10-10^3 particles and a higher illness risk of 10-10,000 times at the same exposure level [16]. It has been indicated that antibacterial agents do not necessarily possess antiviral activity [90]. Infectious pathogens could be transmitted either directly from person-to-person through close contact or indirectly through hand-touch contact after deposition on surfaces [91]. Healthcare facilities are mostly made of stainless-steel surfaces, which have no antimicrobial capabilities, and bacteria can attach and grow on them easily [92][93]. To inhibit indirect transmission risk, surfaces coated with intrinsic antiviral materials could be more effective than frequent cleaning of the environment [94]. Regular cleaning, particularly in public places, which could be re-infected easily, is difficult. Moreover, unintentionally missing infected parts while cleaning the surfaces may remain residuals that continue to infect [94]. To all this, the cost of the disinfectant material and manpower, and the negative influence of those materials on the environment could be added.

Recently, titanium dioxide (TiO_2) photocatalyst has attracted ever-growing attention for viral disinfection due to its exceptional mechanical and chemical resistance [16]. TiO_2 can be excited by light irradiation to produce powerful reactive species with strong oxidizing power for airborne pathogen inactivation under ambient conditions. Interaction of the virus with the

photocatalytic surface results in substantial changes in the virus structure as the virus would lose its ability to attack the host cells, as shown in Fig. 2.10 [95][17].

Copper oxide (Cu_xO) coatings also show potent antiviral activity, even under dark conditions [91][96][97]. Recent interest in visible light-sensitive Cu_xO/TiO_2 nanocomposite has been substantial due to its sustainable antiviral activity under dark conditions. A combination of copper species with photo-generated holes in the valence band of TiO_2 under light irradiation can cause membrane damage, followed by protein oxidation and DNA degradation [90][98].

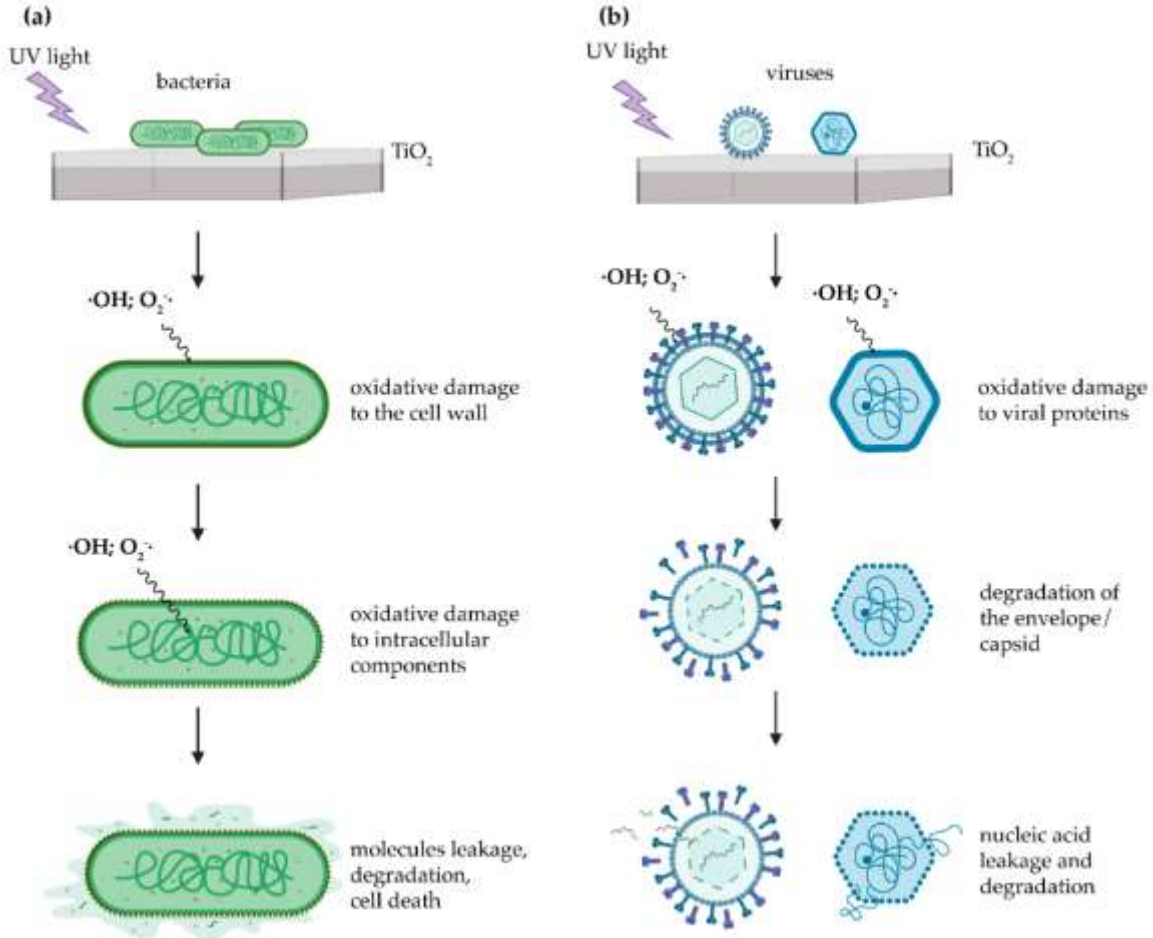

Figure 2. 10 Mechanism of TiO_2 photocatalytic inactivation of (a) bacteria and (b)viruses [99].

2.5.4 Hydrogen production

In recent decades, energy demand has particularly augmented due to urban sprawl and the industrialization of our society. Fossil fuels such as coal, oil, and natural gas are considered the primary non-renewable sources of the world's energy. However, the recent surge in fossil fuel prices and their deteriorating impact on the environment and climate change increased the necessity for environmentally friendly, renewable, and cheap energy resources to replace conventional fuels [100][101][102]. Hydrogen is recognized as an effective energy carrier and potential carbon-free fuel that can be produced in different ways, such as natural gas reforming, biomass conversion, water electrolysis, and photoelectrochemical water splitting [100][101][103]. However, only some of these techniques can produce low-carbon (green) hydrogen. Hydrogen

produced through water electrolysis is considered environmentally sustainable green hydrogen if the electricity is supplied by renewable sources like solar and wind. At this time, only 2% of the total hydrogen production is produced by water electrolysis [100]. Photoelectrochemical (PEC) water splitting has attracted ever-growing attention as a great candidate for producing H_2 fuel using specific semiconductors and sunlight energy. Several semiconductors have been studied for photocatalytic H_2 production, such as TiO_2, CuO, ZnO_2, g-C_3N_4 and WO_3 [104][105][106]. However, the large bandgap, high recombination rate, and lower surface area of these semiconductors have limited their efficiency. Based on the literature, doping, surface sensitization, using co-catalyst and PEC/PEC tandem cell are promising approaches to improve the water splitting efficiency [101][107][108][109][110].

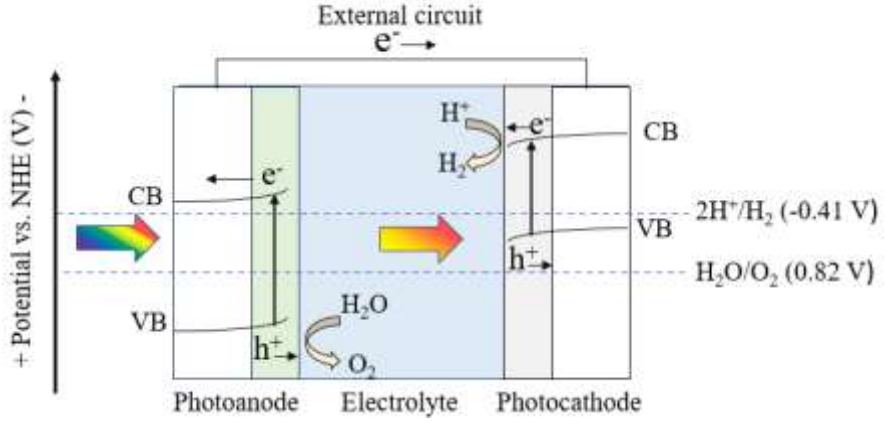

Figure 2. 11 Schematic of PEC/PEC tandem cell (Adapted from reference [108]).

2.5.5 Current industrial applications

TiO_2 photocatalysis is widely used in wastewater treatment applications due to its low cost and effectiveness. In addition, TiO_2 photocatalysis is used in industrial settings to reduce organic compounds, including pesticides, pharmaceuticals, and dyes, from wastewater.

Purifics is a company that specializes in using a commercialized photocatalytic oxidation process utilizing a TiO_2 slurry-based system to break down organic pollutants and purify water in a chemical-free process named Photo-cat. This automated system, Photo-cat®, is able to continuously recover all catalysts and runs 24/7, making its life-cycle costs much lower than traditional systems. The process works by producing reactive oxygen species (ROS) when the TiO_2 is exposed to light, breaking down pollutants into harmless products [111].

Nd-doped TiO_2 has been produced on a considerable scale in a 1000-litre reactor for use in photocatalytic self-cleaning paints, as reported by ˇStengl et al. [53].

Pilkington ActivTM glass is the first commercially available, self-cleaning glass made of a nanocrystalline TiO_2. A thin layer of TiO_2 coating with a thickness of around 15 nm is applied through a chemical vapor deposition process, resulting in a transparent, mechanically stable, photoactive coating. These coatings can be used for air and water purification and self-cleaning purposes [112].

Figure 2. 12 Purifics' TiO_2 Photo-cat® reactor for water purification [111].

2.6 Thermal spray processes

Titania nano-sized powders have a higher surface area, which is of vital benefit for photocatalytic activity. However, most of the applications of photocatalytic decomposition are reported to be carried out in aqueous media, so the powder recycling processes are troublesome. This problem can be overcome by using TiO_2 coatings. The resulting surface reduction could be compensated by producing nano- and micro-structured TiO_2 coatings [35][113]. There are many deposition techniques, which have been used for producing TiO_2 coatings such as chemical and physical vapour deposition, sol-gel and, electrophoretic deposition [114].

In recent years, thermal spray processes have emerged as an environmentally friendly, versatile, and rapid production process. The large surface area coverage and quick deposition rate of this deposition method make it suitable for large-scale industrial use. In addition, spray processes have other advantages, such as producing a wide variety of high-quality coatings and flexibility, which allow using various substrates with different shapes and sizes [114].

In thermal spray processes, multiple layers of coating are formed by molten and/or partially molten particles injected towards the substrate. Upon impinging on the substrate, the molten droplets flatten and solidify, forming splats that accumulate to build coatings with a lamellar structure (Fig. 2.13). Based on the type of energy source for heating the coating material, thermal spray methods are classified into three groups: flame spray, electric arc spray and plasma arc spray. Among different types of feedstock materials (wire, rod, powder), powder is the most common one [115][116].

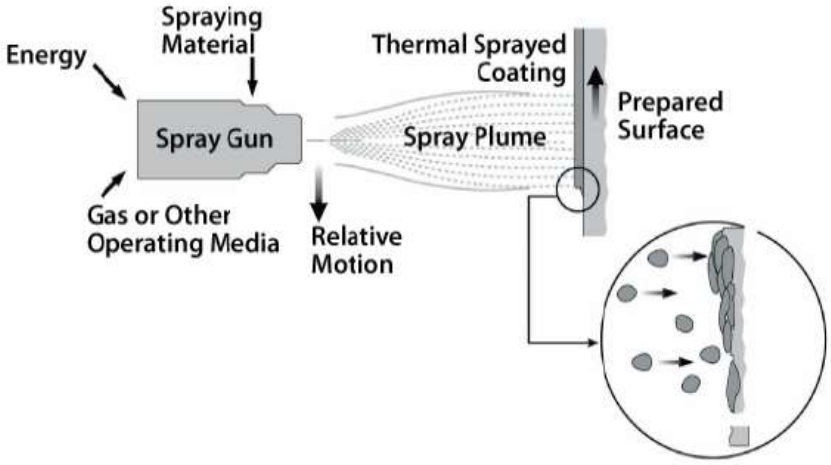

Figure 2. 13 General schematic view of thermal spray process [116].

Thermal spray techniques offer a range of temperatures and velocities which enable the deposition of a wide variety of materials, including metals, refractory alloys, ceramics, and cermets. This enables the surface morphology, microstructure and characteristics of coatings to be controlled by adjusting the spray parameters. The most common thermal spray techniques are flame spray, plasma spray, high-velocity oxygen-fuel (HVOF), and cold spray, as shown in Fig. 2.14 [115][117][118].

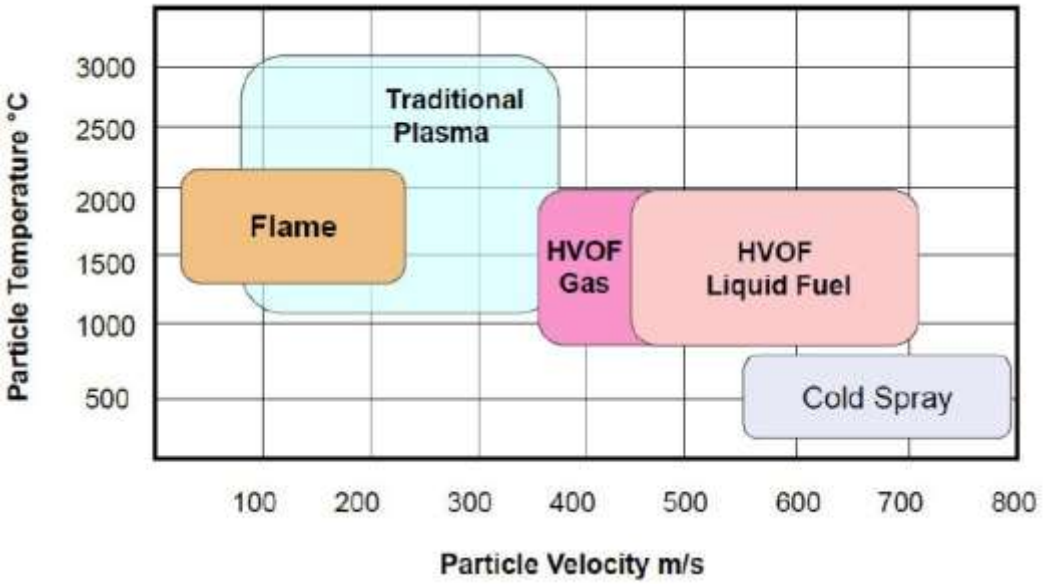

Figure 2. 14 Summary of in-flight particle temperature as a function of particle velocity for different processes [117].

Thermal spraying is mainly used to obtain TiO_2 coatings designed for electrical, mechanical, and biomedical applications, which are of high interest as economic prospects for industrial scale-up. In the last decades, thermal spraying has attracted more interest in preparing photocatalytic active titania surfaces [43].

In this study, mostly suspension and solution plasma spray were utilized to produce TiO_2 coatings. Atmospheric plasma spray (APS), and suspension high-velocity oxygen-fuel (S-HVOF) processes were used by NRC- SprayWerx and Metal7 to produce TiO_2 antiviral coatings (chapter 7 of the thesis).

2.6.1 Atmospheric plasma spraying (APS)

Among thermal spray processes, plasma spray is shown to be capable of producing microstructured functional coatings using various types of materials. Atmospheric plasma spraying (APS) is widely used to deposit a wide range of materials onto different substrates. This process utilizes a high-temperature, high-velocity plasma jet formed by passing a gas or mixture of gases (typically argon or nitrogen) through a DC current arc to heat and accelerate particles toward the substrate surface [119]. This method offers a cost-effective alternative to other surface modification techniques, making it popular in the industrial world for producing functional coatings [120]. Moreover, it has the advantage of low heat input to the substrate material, which reduces the thermal impact on the substrate and preserves its microstructure and physical properties. This technique is widely used to produce functional coatings for different applications such as resistance to wear, heat, erosion, and/or corrosion [121][122][123].

APS involves spraying relatively coarse powder particles (10 to 100 μm) that produce rather thick coatings (typically thicker than 50 μm). However, the deposition of submicron or nano-sized particles using the APS technique is very challenging. It can be explained by the particle's low momentum, which limits their penetration to the high-speed plasma jet and potential powder clogging problems in the injector [124][125].

2.6.2 Suspension plasma spraying (SPS)

Suspension Plasma Spraying (SPS) offers several advantages over conventional techniques, such as the direct use of finely dispersed powders and the production of nanostructured coatings, which is of great importance in photocatalytic activity [43]. In APS, particles smaller than 10 μm are problematic to be deposited due to their low momentum to reach the substrate and clogging problems in the powder feeder and injector. However, with SPS, a suspension of fine nanometric and/or sub-micrometric powder particles can be injected into the plasma plume [124][125].

In the SPS technique, the feedstock suspension usually contains a solvent (mostly water or ethanol), fine nanometric and/or sub-micrometric powder particles, and a dispersant material that helps stabilize the suspension. After injecting suspension into the plasma plume produced by an electric arc between an anode and a cathode, it undergoes one or multiple breakups and atomization phases. Afterward, the solvent evaporates by the plasma's heat flow, leaving powder aggregates. These clusters of fine particles, fully or partially, melt depending on the conditions and temperature and impact onto the substrate, creating splats. The liquid suspension can be injected radially or axially. A schematic SPS process with radial injection is shown in Fig. 2.15 [124][125]. A short standoff distance (between 4 to 8 cm) is needed for SPS process as smaller particles decelerate rapidly and experience extreme heating and cooling rates [115][126].

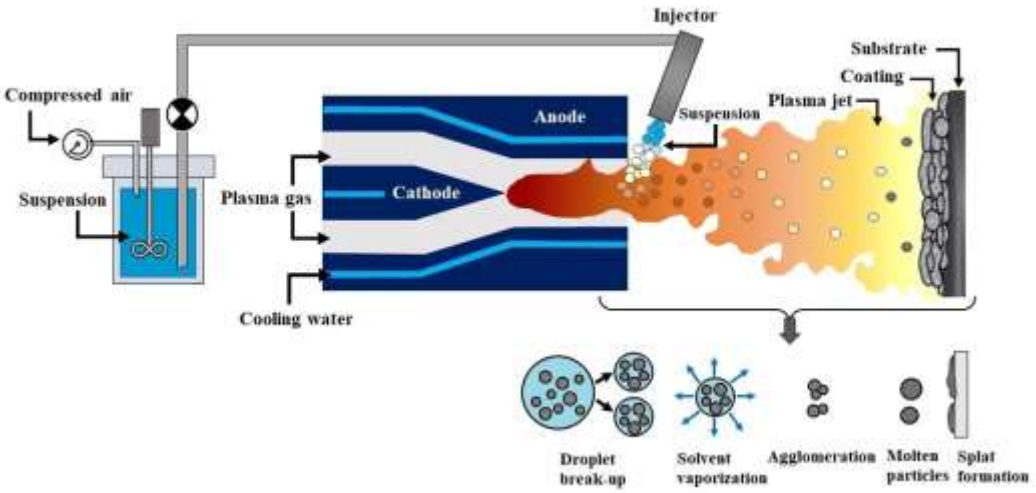

Figure 2. 15 A schematic of suspension plasma spray technique and suspension droplet evolution during its trajectory in the plasma jet [Adapted from references [125][43]].

SPS coatings are known for their unique columnar microstructure, which can be explained by the shadowing effect. This effect occurs when molten particles or droplets follow different trajectories in the plasma jet depending on their size and momentum. Fine particles with low momentum are entrained by the plasma, following trajectories parallel to the surface of the substrate and impinging at a shallow impact angle on the surface asperities. As a result, coatings grow laterally and vertically, forming a porous region by shadowing the beneath surfaces from the impact of the new particles. In contrast, the larger and heavier particles, which have higher momentum, continue on their original trajectory and impact the substrate [127][128][129][130]. Plasma-particle interaction and shadow effect are schematically presented in Fig. 2.16.

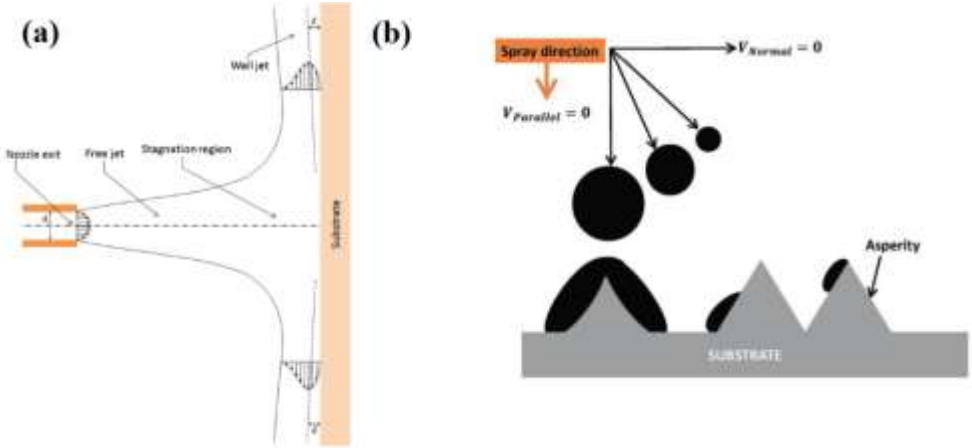

Figure 2. 16 Schematics of (a) common impinging gas-jet system [129] and (b) shadowing effect of different-size droplets impinging on the substrate asperities [130]

VanEvery et al. [131] reported that there are three potential microstructures formed by SPS coating. When the size of the suspension droplet is extremely small (< 1 μm), a columnar microstructure is formed due to the shadowing effect. For droplets with diameters between 1 to 5 μm, a feathery columnar microstructure is produced that includes some porosity bands within the columns. For droplets larger than 5 μm, the plasma flow has a less significant effect, creating a lamellar or vertically cracked structure similar to that produced by conventional APS methods.

2.6.2.1 TiO_2 coatings by SPS

Preserving the anatase phase in the hot plasma jet is a significant limitation of the thermal spray processes. Several types of research have been conducted to produce TiO_2 coatings by SPS to preserve the anatase phase in the coating as the most important TiO_2 phase for photocatalytic application. [42][43][132]. The high vaporization enthalpy of water in a water-based suspension cools the plasma jet, preventing the feedstock from fully melting and leaving particles with the same size, morphology, and crystalline phase as feedstock powder [133][134].

Moreover, the overheating and melting of anatase particles followed by fast cooling in the hot plasma jet can produce sub-stoichiometric titania by creating oxygen vacancies. Visually, the yellowish-white color of TiO_2 would shift to dark grey in TiO_{2-x}, depending on the oxygen vacancy content [135][136]. The use of hydrogen as a secondary plasma gas facilitates the reduction of the titania particles during spraying, resulting in the deposition of sub-stoichiometric TiO_2 coatings [134]. Based on the literature, hydrogen interacts with TiO_2, and both oxygen vacancy and electrons are produced, as shown in Eq. 2.9, where O_O^x is an O^{2-} ion in the oxygen lattice site, $V_{\ddot{O}}$ is an oxygen vacancy with a double positive charge, and e^- is a conduction electron [66].

$$O_O^x + H_2 \rightarrow V_{\ddot{O}} + 2e^- + H_2O \tag{2.9}$$

Consequently, Ti^{3+} ions are formed as donor doping by the electrons trapping in Ti^{4+} lattice sites [66]. The sub-stoichiometric TiO_2 exhibited a color change due to introducing a high concentration of Ti^{3+} ions. This change enabled the coating to absorb visible light more efficiently, resulting in an increased number of photo-generated charges. This was further enhanced by the new sublevel state of $[O_v \cdot Ti3^+]^+$ at the conduction band (CB) bottom of sub-stoichiometric TiO_2, which improved the charge carrier separation and modified the electron-hole transfer at the interface [137][138][139]. Operational spray parameters such as stand-off spray distance, suspension feed rate, and hydrogen flow rate play a key role in optimizing some microstructural features such as the fraction of anatase in the coatings, the crystal size, and coating thickness [132].

Based on the literature, there are limited studies dedicated to doping and/or sub-stoichiometric TiO_2 with thermal spraying processes that need more investigation. Mauer et al. [42] produced nitrogen-doped TiO_2 using SPS method by adding TiN powder to TiO_2 suspension as a feedstock. They reported the role of nitrogen doping on the absorbance of TiO_2 coatings toward the visible spectrum of light. Toma et al. [140] presented the effect of Al particles in the Al-doped TiO_2 coatings to keep the initial nanosized anatase phase of TiO_2 particles used in HVOF for sample production. Moreover, Al-doped coating presents much better photocatalytic activity than the initial agglomerated powder or even TiO_2 Degussa P25 for NO and NO_x removal from the air.

2.6.3 Solution precursor plasma spraying (SPPS)

Solution Precursor Plasma Spraying (SPPS) is a customized plasma spraying technique that produces nanoscale coatings with different crystal structures and compositions. This technique enables precise control over the final thickness and morphology of the coating, providing numerous advantages. However, feedstock material in the form of powder in the conventional plasma spray process has a particle size limit to achieve sufficient flowability. To avoid this limitation, suspension and, more recently, solution precursor thermal spraying have been developed as alternative methods. The SPPS process involves the preparation of a precursor

solution in one step with a solvent medium consisting of water, alcohol, or a combination of both, which is then sprayed onto a plasma flame. The composition of solutions at the molecular level leads to a high degree of chemical uniformity of the components. This process then progresses through a series of steps, including precipitation of the precursor, pyrolysis, sintering, melting, and solidification, forming dense solid particles from droplets [141][142][143].

Aruna et al. [142] produced TiO_2 coating using SPS and SPPS processes. TiO_2 powder and titanium isopropoxide (TIP) were used as feedstock material to prepare water-based suspension and ethanol-based solution for SPS and SPPS processes, respectively. Based on the results, SPPS-TiO_2 coatings presented higher photocatalytic activity to degrade methylene blue organic dye due to the presence of oxygen vacancy. Tejero-Martin et al. [142] also could produce Nb-doped TiO_2 coatings using Solution Precursor High-Velocity Oxy Fuel (SP-HVOF) thermal spray technology. The solution precursor contains titanium ethoxide and niobium ethoxide (dopant) dissolved on 2-isopropoxyethanol. In addition, some researchers have reported doping rare earth elements into the yttria-stabilized zirconia (YSZ) coatings through SPS/SPPS technique while rare-earth nitrates dopant precursors were dissolved in the YSZ-ethanol-based suspension before spraying. According to their results, dopants could effectively scatter phonons by introducing point defects to lower the thermal conductivity of YSZ coatings in thermal barrier applications [144][145].

2.6.4 Suspension high-velocity oxygen fuel thermal spraying (S-HVOF)

In the 1980s, the high-velocity oxy-fuel process was introduced to the commercial market. This technique mixes a fuel gas or liquid (such as hydrogen, kerosene, propylene, ethylene, or acetylene) and pure oxygen in the combustion chamber, where they are then ignited and combusted and leaves through a nozzle creating a supersonic jet. The exhausted gas passes through a converging-diverging nozzle to reach supersonic velocities ranging from 500 to 1200 m/s. Upon exiting the nozzle and entering the atmosphere, the pressure difference between the high-velocity flow and the ambient atmosphere creates shock diamonds. The feedstock material in the form of powder ranging from 5 to 45 μm can be injected into the flame using argon or nitrogen as the carrier gas. Once the powder feedstock is injected, it melts or partially melts in the flame and deposit onto the substrate to produce metal, cermet, and ceramic coatings. However, powder feedstock limits the size of the particles that can be used to reach enough flowability [115][118][143][146].

The suspension High-Velocity oxy-fuel process (S-HVOF) technique uses a modified traditional gas-fueled HVOF torch, with axial injection inside the combustion chamber, to process liquid feedstock [147]. According to Bolelli et al. research work [147], the S-HVOF process appears highly versatile, allowing for a wide range of applications. It could provide high-density and wear-resistant coatings or porous coatings containing un-melted nanoparticle agglomerates for photocatalytic activity application. This process has been shown to provide superior results compared to APS or HVOF spraying techniques.

Toma et al. [36] investigated the effect of spray parameters, such as spray distance and fuel flow rate, on the photocatalytically active TiO_2 coatings produced with S-HVOF. The results presented the significant effect of spray parameters on the characteristics of the coating like crystalline phase, microstructure, surface morphology, thickness, and surface hydroxylation, as well as the capability of the coating to absorb the light, which are important factors on the photocatalytic efficiency of TiO_2 coatings.

Chapter 3. Experimental procedures

This chapter provides an overview of the materials, systems, experimental procedures, and characterization tests that were performed for this work.

3.1 Materials

Submicron-sized titanium dioxide (TiO_2) powder (TKB Trading, Oakland-USA), Cerium (III) nitrate hexahydrate ($Ce(NO_3)_3.6H_2O$) (99%, Sigma-Aldrich, St. Louis-USA) were used as feedstock materials for chapters 4, 5, and 6. Moreover, in chapter 7 of the thesis, micron-sized TiO_2 powder (Metco 102- Metco Oerlikon, Fort Saskatchewan, Canada), nanostructured TiO_2 spray-dried powder (NEOXID T101 nano, Millidyne, Finland), copper oxide (Cu_2O) powder (PI-KEM, U.K.), aluminum oxide- 40% titanium dioxide powder (Al_2O_3- 40%TiO_2) (Amdry 6257- Metco Oerlikon, Fort Saskatchewan, Canada), and aluminum oxide- 13% titanium dioxide powder (Al_2O_3- 13%TiO_2) (Metco 130- Metco Oerlikon, Fort Saskatchewan, Canada) were used as feedstock materials to deposit antiviral coatings.

3.2 Photocatalyst preparation

3.2.1 Preparing TiO_2 coatings with various anatase phase contents

In this work, suspension plasma spraying (SPS) with different hydrogen (H_2) flow rates was utilized to deposit TiO_2 coatings with various phase contents, oxygen contents, and roughnesses. For feedstock, the suspension containing 20 wt. % commercial submicron-sized TiO_2 powder (TKB Trading, Oakland, CA) in deionized distilled water was prepared by magnetic stirring for 30 min while dispersing the powder with a 50 W sonicator. No dispersing agent was used in the suspension preparation. An Axial III^{TM} plasma torch (Northwest Mettech Corp., Canada) was used for the suspension plasma spraying (Fig. 3.1). It has the advantage of having three independent cathodes/anodes working on three power supplies that could reduce the voltage fluctuation of the plasma jet with high deposition efficiency [148]. A cooling procedure was applied using compressed air impinging on the front surface of the coating and a water-cooled substrate holder to avoid overheating of the substrate during spraying and preserve a higher anatase content in the coatings [42].

Then, we performed post-treatment processes to eliminate the influence of the morphology and oxygen content variation on the photocatalytic activity of the coatings and could determine their efficiency just based on the anatase phase content. So as-sprayed coatings were polished to reach the same roughness, followed by heat treatment at 550 °C in the air for 48 hours using an open-ended tubular furnace (Lindberg, US).

Figure 3. 1 Mettech's Axial III gun [149].

Eventually, all as-sprayed coatings and their polished heat-treated counterparts were characterized by various characterization tests. A flowchart summarizing the experimental work performed in Chapter 4 is provided below (Fig. 3.2).

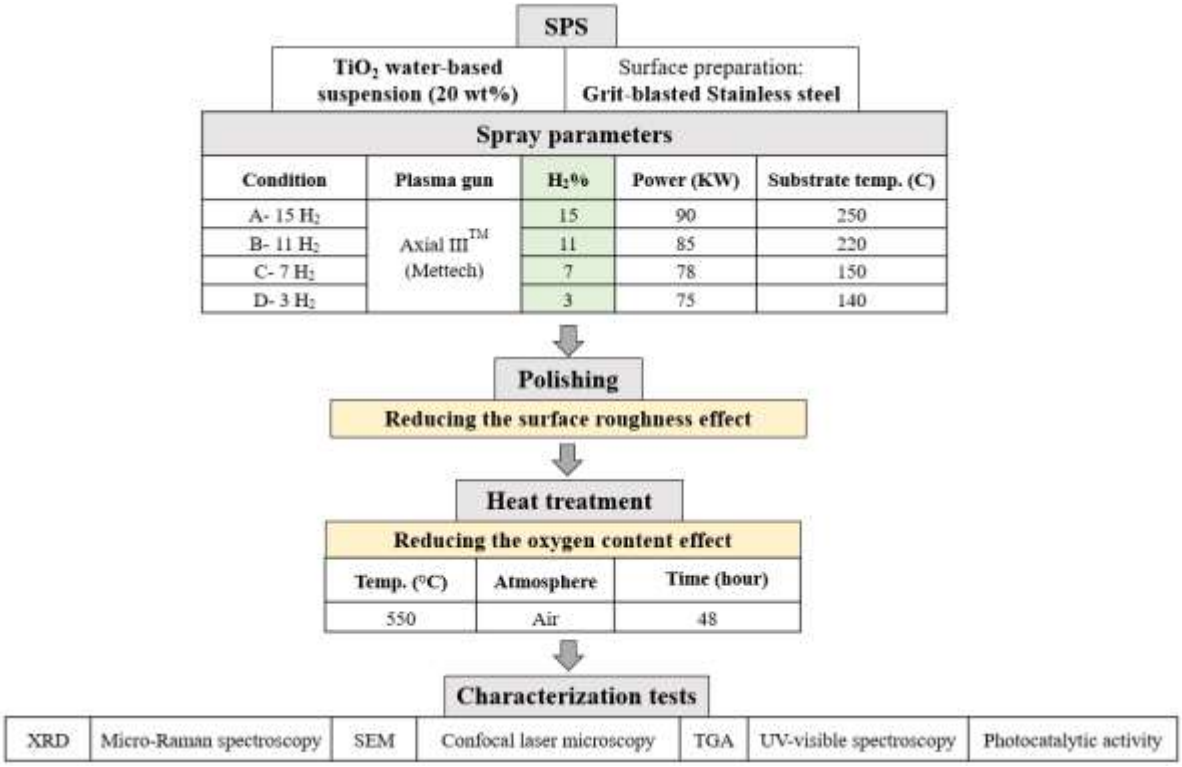

Figure 3. 2 Experimental flowchart for chapter 4.

3.2.2 Preparing sub-stoichiometric TiO_{2-x} coatings with various oxygen vacancy contents

Sub-stoichiometric TiO_{2-x} coatings were manufactured by suspension plasma spray (SPS) method with a radial 3 MB plasma torch (Oerlikon Metco, Switzerland), as shown in Fig. 3.3. 20 wt. % water-based suspension was prepared using submicron-sized TiO_2 powder (TKB Trading, Oakland, CA). Instead of playing with plasma spray parameters, which could affect all the coating characteristics, heat treatments in the air were applied at different temperatures in the range of 400-550 ºC to vary the level of oxygen vacancies. Oxygen recapturing would happen during thermal treatment raising the level of oxygen content. This was done to prevent significant changes in the

other effective parameters (such as roughness, porosity, and crystalline phase) that may influence the photocatalytic efficiency.

Figure 3. 3 3MB Plasma spray gun.

Finally, various characterization tests were performed to evaluate the role of oxygen vacancies in the photocatalytic activity of the coatings. The experimental work of chapter 5 is depicted in Fig. 3.4.

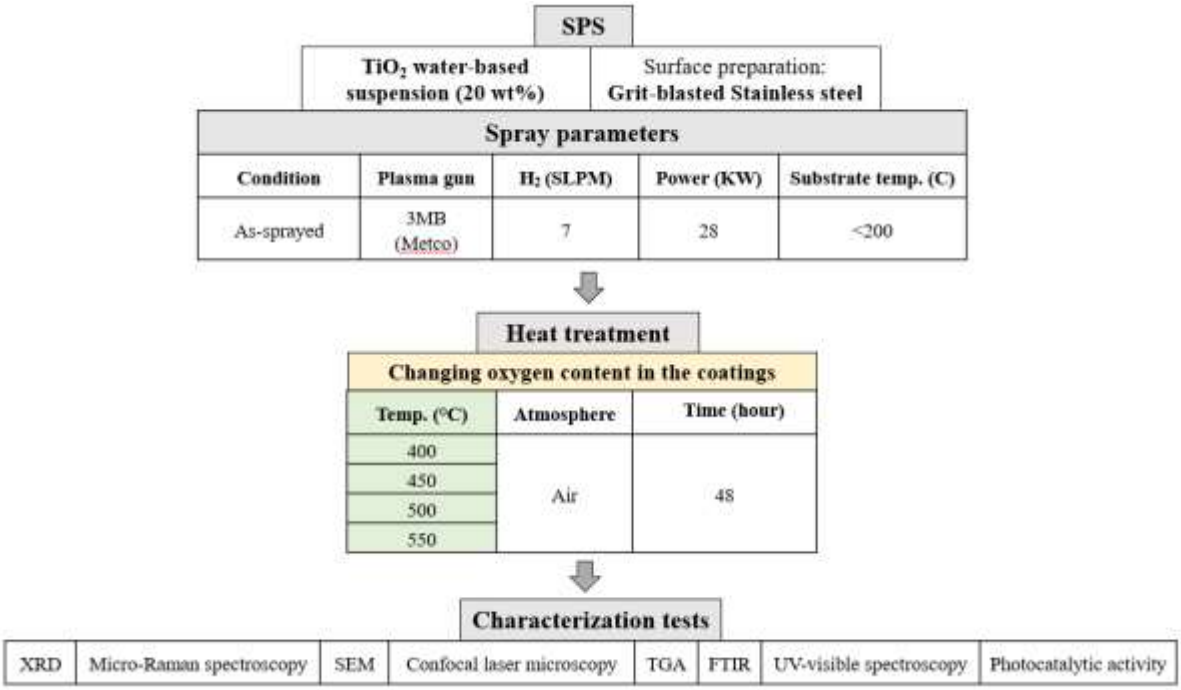

Figure 3. 4 Experimental flowchart for chapter 5.

3.2.3 Preparing Ce-doped TiO_2 and CeO_2-TiO_2 composite coatings

In this work, Ce-doped TiO_2 coatings were produced using a hybrid suspension (SPS) and solution precursor plasma spraying (SPPS) approach. CeO_2-TiO_2 composite coatings were also deposited by the SPS process. Three types of water-based suspensions with 10 wt.% solid content were prepared for the plasma spraying to produce TiO_2, Ce doped TiO_2, and TiO_2-CeO_2 composite coatings, as depicted in Fig. 3.5. TiO_2 powder (TKB Trading, Oakland, CA) was used as the source of TiO_2 for all the suspensions. To produce composite coatings of TiO_2 with CeO_2, submicron CeO_2 powder (99.9%, Sigma-Aldrich, St. Louis-USA) was used. While Cerium Nitrate (99%, Sigma-Aldrich, St. Louis-USA) dissolved in the water was utilized as a cerium precursor in Ce-doped TiO_2 coatings.

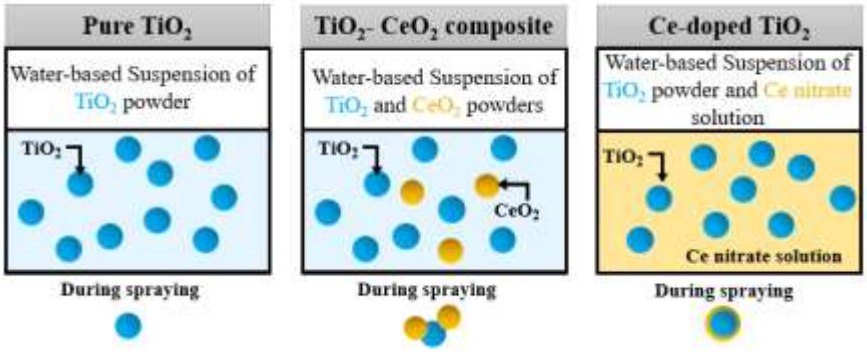

Figure 3. 5 Schematic representation of three different suspensions used to produce pure TiO_2, TiO_2-CeO_2 and Ce-doped TiO_2 coatings.

An Axial III^{TM} plasma torch (Northwest Mettech Corp., Canada) was used to deposit coatings. The axial injection has the advantage of a more uniform treatment of spray materials than the radial injection plasma torch. Coatings were produced at two different spray conditions: low power and high power. A summary of experimental work performed in chapter 6 is shown in Fig. 3.6.

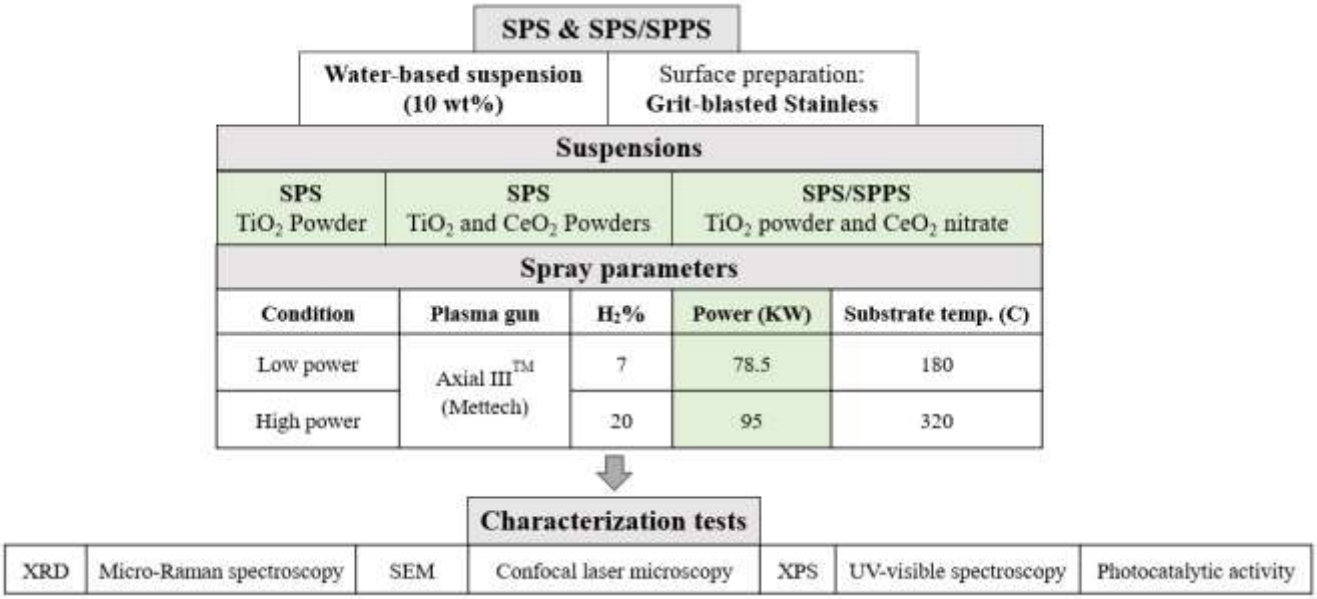

Figure 3. 6 Experimental flowchart for chapter 6.

3.2.4 Preparing antiviral coatings

In this research work, TiO_2, Cu_2O, TiO_2-Cu_2O and TiO_2-Al_2O_3 antiviral coatings were produced using different thermal spray processes, including atmospheric plasma spray (APS), suspension plasma spray (SPS), and suspension high-velocity oxygen fuel (S-HVOF). 10 wt.% water-based TiO_2 suspensions were used to deposit TiO_2 coatings by SPS and S-HVOF processes using Axial III^{TM} (Northwest Mettech Corp., Canada) and ID-Nova (Spraywerx technologies, Canada) plasma torches, respectively. The antiviral activity of coatings was investigated by different characterization tests. The experimental procedure performed in chapter 7 is shown in Fig. 3.7.

Thermal spray process

Surface preparation:
Grit-blasted Stainless steel

Spray parameters

Condition	Feedstock material	Thermal spray process	Plasma gun	Power (KW)
T1-SPS	TiO_2-TKB	SPS	Axial III^{TM}	77
T2-APS	TiO_2-Metco 102	APS	SG- 100	35
T3-APS	TiO_2-Metco 102	APS	100HE	95
T4-APS	TiO_2- NEOXID T101	APS	3MB	29
T5-SHVOF	TiO_2-TKB	S-HVOF	ID-Nova	H_2-O_2 (380-190)
C-SPS	Cu_2O	SPS	3MB	17.5
TC-SPS	Cu_2O & TiO_2-TKB	SPS	3 MB	20
A40%T-APS	Al_2O_3- 40%TiO_2 (Amdry 6257)	APS	F-4	30
A13%T-APS	Al_2O_3- 13%TiO_2 (Metco 130)	APS	100HE	65

Characterization tests

XRD	SEM	Confocal laser microscopy	Antiviral activity

Figure 3. 7 Experimental flowchart for chapter 7.

3.3 Characterization of photocatalysts

The phase identification of the TiO_2 coatings was studied using the X-ray diffraction (XRD) technique using X'Pert Pro; PANalytical (Philips, Netherlands) and D8 Advance (Bruker, USA) with Cu Kα radiation (1.5418Å) and a step size of 0.02° in a range of 20-80°. The Raman spectra of the coatings on the polished cross-sections and top surfaces were recorded using a micro-Raman spectrometer (inVia Reflex, UK) with a laser wavelength of 532 nm, objective magnification 50 x and 10 s exposure time. The surface elemental composition of the coatings was studied using an X-ray photoelectron spectroscope (XPS) (VG ESCALAB 250Xi, Thermo Fisher Scientific, USA) with an Al Kα radiation source (hυ =1486.6 eV) and a spot size of 1300 µm in diameter. The chemical stoichiometry of the as-sprayed coatings and the starting powder was

quantified using thermogravimetric analysis (TGA). TGA analysis was conducted using a thermal balance (TGA Q500/Discovery MS, TA Instruments, US) where the powders were heated at 5 °C /min in the air to 1000 °C for 90 min to re-oxidize sub-stoichiometric TiO_{2-x}. During TGA analysis, all samples were kept at 150 °C for 2 h to make them fully dried. Based on the re-oxidizing reaction of TiO_2, the quantification of oxygen atoms (x) was calculated by the sample weight increment according to Eq. 3.2 [150][151][152][153]:

$$TiO_{2-x} + \frac{x}{2} O_2 \rightarrow TiO_2 \tag{3.1}$$

$$x = \frac{\Delta w}{w_{mol}^{O}} \frac{(2W_{mol}^{O} + W_{mol}^{Ti})}{(W_0 + \Delta W)} \tag{3.2}$$

where ΔW is the weight increment, W_0 is the initial weight of the samples, W_{mol}^{O} and W_{mol}^{Ti} are the molar weight of oxygen and titanium.

The presence of adsorbed species on the sample surfaces was characterized from infrared spectra in the range of 4000-600 cm^{-1} using an ATR-FTIR (Attenuated Total Reflectance-Fourier transform infrared) spectrometer (Nicolet 6700 / Smart iTR, Thermo Scientific, US).

Top surface morphology and cross-sectioned microstructure were characterized using an ultra-high resolution cold-field emission scanning electron microscope (FE-SEM) (FESEM JSM 7600TFE, JEOL, Japan and Regulus8230, Hitachi, Japan) equipped with an energy-dispersive X-ray spectroscopy, secondary electron (SE) and backscattered electron (BSE) detectors. The three-dimensional surface topography and arithmetic average roughness (R_a) of coatings were studied using a confocal laser microscope (LEXT OLS4000, Olympus, Japan). To characterize the coating surface and cover a large enough area, 25 single images were digitally stitched together and generated 3D maps of the surfaces.

A UV-Visible-NIR spectrometer (Lambda 750, Perkin Elmer, US) was used to record the UV–Vis diffuse reflectance spectra of the coatings in the range of 340 to 600 nm. Moreover, the bandgap energy of the samples was measured based on the Tauc plot method and the following equations [36][154]:

$$\alpha h\upsilon = A(h\upsilon - E_g)^n \tag{3.3}$$

$$E_{photon}(eV) = h\nu = \frac{1239}{\lambda} \tag{3.4}$$

where α is the absorption coefficient, E_g is the bandgap calculated from the extrapolation of the straight-line portion of the $(\alpha h\nu)^{1/n}$ –hν plot, A (constant) is the slope of the linear region of the mentioned plot, λ is the wavelength, and n is 2.0 and 0.5 for indirect and direct allowed optical transitions, respectively.

3.3.1 Photocatalytic activity measurements

Organic dyes, commonly used by the dye industry and released into wastewater, are often used as a test pollutant to measure the effectiveness of photocatalytic activity in terms of pollution control [25]. In this research work, the photodegradation of TiO_2 coatings was measured by the degradation rate of methylene blue, MB ($C_{16}H_{18}ClN_3S$) when exposed to visible light. A TiO_2 sample with a surface area of 6.25 cm^2 was placed in a testing cell filled with 30 mL of MB solution with an initial concentration (C_0) and illuminated with two xenon arc lamps with an input power of 35 W each. A fan was used during the test to prevent the samples from being heated up by light

irradiation. The experimental setup is schematically shown in Fig. 3.8 (a). Sampling from the solution was taken every 30 minutes and analyzed with a UV-vis spectrophotometer (Evolution 201, Thermo Scientific, US) at a wavelength of 664 nm, which corresponds to the maximum absorbance of MB, to monitor the decomposition of the MB solution (Fig. 3.8 (b)). Before irradiation, coatings were soaked in a MB solution and left in the dark for 60 minutes, allowing the MB molecules to adsorb onto the coating surfaces. After this time, the MB concentration (C_0) was measured. Or the solution was substituted by a new 30 ml of MB solution and was placed inside the visible light setup.

The MB solution without TiO_2 coating was tested to determine the extent of degradation caused by photolysis under light irradiation. The concentration changes of MB were calculated using a pseudo-first-order kinetics equation, Eq. 3.5 [3].

$$ln\left(\frac{C_0}{C}\right) = kt \tag{3.5}$$

Where C_0 is the concentration of MB after 60 min in the dark, C is the MB concentration at each time interval, k is the apparent rate constant, and t is the irradiation time. The degradation percentage was also measured according to Eq. 3.6 [35].

$$Degradation\ (\%) = \frac{(C_0 - C)}{C_0} \times 100 \tag{3.6}$$

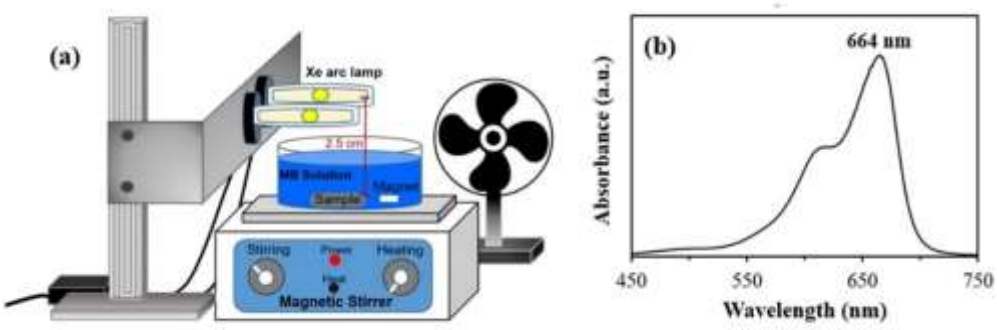

Figure 3. 8 (a) Schematic diagram of the photocatalytic setup for the visible lamp, and (b) UV-Vis absorption spectrum of the MB.

3.3.2 Antiviral activity measurement

The antiviral performance of selected coatings was assessed in a containment level 2 bio lab under UVA light (Fisher Scientific, Canada), ambient light, and dark conditions. Two UVA lamps with a wavelength of 365 nm and a power of 15 watts each were used. The UVA light intensity was reduced by decreasing the transmission to 1% using 2.0 OD UV-NIR Neutral Density Filters (88-275, Edmund Optics Inc., U.S.) to reduce the effect of UVA illumination killing the virus directly. The UVA lights and UV-NIR filters were placed approximately 7 cm and 2 cm away, respectively, from the surface of the samples, allowing for normal air circulation across the surface. The ambient light was provided using white LED lights, generally used to illuminate inside the fume hood. The intensity of the ambient light was measured at around 500 lux using a light meter (LANTEX LM-50KL, ON, Canada).

The antiviral activity of the coatings was assessed using the HCov-229E-Luc virus as a surrogate for the SARS-CoV-2 virus [155]. The HCov-229E-Luc virus contains a Luciferase

reporter gene allowing quantification of the relative amount of the viable virus in terms of Relative Luminescence Unit (RLU), determined by measuring the luminescence signal using a Luciferase assay [156].

HCoV-229E-Luc stocks containing 1000 Plaque Forming Units (PFU) were prepared in Dulbecco's Modified Eagle Medium (DMEM) containing 2% Fetal Bovine Serum (FBS). A 50 µl of the virus solution was put on the surface of the coatings. The coatings were exposed to ambient/UVA light or kept in the dark. The virus was recollected from the coating surface by pipetting 100 µL of media (Dulbecco's Modified Eagle Medium) at the coatings' surface at three-time points, 0 min, 10 min, and 20 min after exposure. A fresh coating was used for the test at each time point. The retrieved virus was then used to infect Huh7 cells in triplicates. Huh7 cells are a human epithelial liver cell line derived from hepatoma tissue, which supports HCoV-229E replication. A Renilla-Glo Luciferase Assay System (catalogue number E2720, Promega), with Perkin Elmer plate reader (Ensight, Perkin Elmer), was used to quantify the virus infection. Furthermore, a copper plate (Cu), with high antiviral activity, and a stainless steel 304 plate (S.S.) with no antiviral activity were used as positive and negative control samples, respectively [157][158].

Preface to Chapter 4.

As it was discussed in the previous chapters, one of the main objectives of this work is to perform a comprehensive study on the photoactivity of thermally sprayed TiO_2 coatings. In this chapter, the role of the crystalline phase was investigated using systematic work to show the unique properties of the as-sprayed TiO_2 coatings produced by suspension plasma spray (SPS).

Chapter 4. Role of phase content on the photocatalytic performance of TiO_2 coatings deposited by suspension plasma spray [1]

Abstract

In this work, suspension plasma spraying (SPS) with different hydrogen (H_2) flow rates was employed to produce TiO_2 coatings with various phase contents, oxygen contents, and roughnesses. To eliminate the role of the morphology and oxygen content on the photocatalytic activity, all coatings were polished to reach the same roughness followed by heat-treatment at 550 °C in air for 48 hours. Then coatings were analyzed by X-ray diffractometer (XRD), confocal laser microscope, scanning electron microscope (SEM), UV-visible spectrometer, Raman microscope, and thermogravimetric analyzer. The XRD data indicated that the percentage of anatase decreased as function of H_2 flow rates, and almost 46% of anatase transformed to rutile during SPS process at the highest H_2 flow rate. Moreover, the photocatalytic performance was evaluated by monitoring the degradation of methylene blue under visible light irradiation, and the results indicated that anatase phase positively enhances the photocatalytic activity of TiO_2 coatings.

Keywords: TiO_2, Photocatalytic activity, Suspension plasma spraying, Crystalline phase, Oxygen vacancies

4.1 Introduction

Nowadays, the accessibility of drinking water is one of the main challenges in the world. According to the World Health Organization (WHO) prediction, half of the world's population will experience water-stressed conditions by 2025 [41]. This condition raises an environmental concern to develop environment-friendly and economical water purification systems providing long-term health protection.

Photocatalysis is a technique in which light is used to decompose organic compounds from waste-water [16][11][159]. Since Honda and Fujishima first found a strong oxidation and reduction power of photoexcited titanium dioxide (TiO_2) in 1972, semiconductor photocatalysts have attracted much attention, especially for environmental treatments. TiO_2 displays relatively high reactivity and chemical stability under UV light ($\lambda<380$ nm), whose energy exceeds the bandgap of 3.2 eV in the anatase crystalline phase [49]. This mechanism consists of the generation of electron-hole pairs through the jumping of the valence band charges (electrons) into the empty energy states of the conduction band upon absorption of photons ($h\nu$). The photo-generated electron-hole pairs migrate to the TiO_2 surface, where the photogenerated holes (h^+) oxidize

[1] This chapter has been published as a peer-reviewed article in the Journal of the European Ceramic Society, Hediyeh Khatibnezhad, Fabian Ambriz-Vargas, Fadhel Ben Ettouil, Christian Moreau, *Journal of the European Ceramic Society 42 (2022) 2905-2920.*

adsorbed water or hydroxyl molecules to produce highly reactive hydroxyl radicals ($^{\bullet}OH$) while the photo-excited electrons (e^-) reduce molecular oxygen (O_2) to generate superoxide radical anions (O^{2-}). These reactive species are responsible for the photocatalytic decomposition of the organic compounds [35][150][160][161].

However, one of the significant problems in using TiO_2 as a catalyst is its low reactivity under visible light ($\lambda > 400$ nm), which limits its application for using the main part of the solar spectrum. Moreover, it has low photo-quantum efficiency, resulting from the fast recombination of photo-generated electrons and holes [162].

The photocatalytic degradation rate of organic compounds primarily depends on the crystalline phase of titania (TiO_2). Anatase and rutile are the two main crystalline phases of titania. A fine pure anatase powder would irreversibly transform to rutile at temperatures higher than 600 ºC [163]. However, the phase transition temperature could be changed from 400 to 900 °C, depending on some parameters like oxygen vacancies, impurities, and the atmosphere [164][165][37][137].

It has been reported that the phase mixture of both polymorphs shows better photocatalytic activity compared to pure phases due to the synergistic effects between them [166][22]. Yet, for single-phased titania, the photocatalytic performance of anatase is generally higher than its rutile counterpart in all types of reaction media [22][37][38][39]. Although the larger bandgap of anatase (3.0 eV for rutile and 3.2 eV for anatase) causes lower absorbance ability towards solar light, it may enhance the redox power of charge carriers and surface adsorption capacity to hydroxyl groups attributed to the different position of the conduction and valence bands and higher Fermi energy of anatase [22][36][38]. Recently, some theoretical studies have indicated that anatase exhibits an indirect bandgap. In contrast, rutile is a direct bandgap semiconductor with much faster recombination and a shorter lifetime of photoexcited electrons and holes. In the direct semiconductors, photo-generated electrons recombine directly with photo-generated holes, and a photon is emitted afterward. However, direct recombination of charge carriers in the conduction band minimum and valence band maximum is not possible in the indirect semiconductors, and a phonon is needed for recombination[22][38]. Therefore, anatase shows a longer electron-hole lifetime and exciton diffusion length that makes it more favorable for photo-generated charges to migrate from the bulk to the surface to drive surface chemical reactions and improve the photocatalytic performance [22][38][40]. Literature suggests that anatase has a higher charge carrier mobility and fastest migration of photo-generated charges from the bulk to surface due to the lightest average mass of charge carriers compared to rutile. Also, based on Luttrell's work [22], it is known that photo-generated electron-hole pairs excited deeper in the bulk could participate in photoreactions in anatase, hence, this phase has a higher charge diffusion length compared to rutile. The larger charge diffusion length of anatase may originate from its longer charge carrier's lifetime and/or its higher charge carrier mobilities.

Odling et al. [41] reported the existence of free hydroxyl radical production ($OH_f^{\bullet}$) in the TiO_2/water interface of anatase phase, while in the rutile phase only surface-bound hydroxyl radicals ($OH_s^{\bullet}$) are detected. Free hydroxyl radicals ($OH_f^{\bullet}$) could degrade organic contaminants at the surface and in the bulk solution for water purification. Whereas surface-bound radicals ($OH_s^{\bullet}$) are able to degrade pollutants only at the surface. This might be one justification for superior photocatalytic performance of anatase phase than that of rutile phase, and possibly have relevance to other photocatalytic materials and applications. Besides phase composition, there are several parameters that could affect the photocatalytic activity. In our previous work [150], sub-stoichiometric TiO_{2-x} coatings were produced by suspension plasma spraying from a water-based

suspension of anatase powder. This study clarified the influence of the oxygen vacancy concentration on the optical properties and photocatalytic activity of sub-stoichiometric TiO_{2-x} coatings. Literature suggests that oxygen deficiency induces sublevel states at the conduction band (CB) bottom of sub-stoichiometric TiO_{2-x}, which is responsible for improving the photocatalytic efficiency of coatings [138][167][139][66].

Shayegan et al. reported the critical role of the surface area in the photocatalytic performance [83]. It was indicated that the photocatalytic activity improved with increasing the catalyst's surface area by increasing the number of active sites for initiating the reaction [3][83]. Moreover, a higher density of localized states resulting from a higher surface area would be of great benefit for increasing the charge carrier lifetime of TiO_2 photocatalyst by introducing some trapping sites [37]. TiO_2 nano-sized powders have a higher specific surface area, which is of vital benefit for photocatalytic activity. However, most of the applications of photocatalytic decomposition are reported to be carried out in aqueous media, so the powder recycling processes are troublesome. This technological challenge could be overcome by using TiO_2 coatings. The resulting surface reduction could be compensated by producing nano- and micro-structured TiO_2 coatings [168][35][113].

TiO_2 coatings have been produced by various techniques; among them, thermal spray processes are of high interest as economic prospects for industrial scale-up. Spray processes have other advantages, such as producing a wide variety of high-quality coatings and flexibility, which allows using various substrates with different shapes and sizes [114]. Suspension plasma spray (SPS) can use finely dispersed powders and produce nanostructured coatings with high specific surface area, presenting several advantages over conventional techniques [43].

In this work, water-based suspension of fine TiO_2 particles was internally injected in a plasma torch to obtain photocatalytic active TiO_2 coatings with different anatase contents. After coating deposition, all samples were polished and heat-treated in the air at 550 ºC in a tubular furnace until the surface roughness and oxygen content were almost the same in all coatings. Evaluating the effect of the anatase phase on the photocatalytic activity of the suspension plasma sprayed TiO_2 coatings is the principal objective of this work by keeping constant most of the other affecting factors on the photocatalytic performance.

4.2 Experimental methodology

4.2.1 Suspension preparation

TiO_2 coatings were deposited using suspension plasma spray process. Submicron-sized titanium dioxide powder (TKB Trading, Oakland-USA) was used as a feedstock material with an average particle size of ~ 135 nm (Fig. 4.1 (a)) and a crystallography composition of pure anatase phase (Fig. 4.1 (b)). The as-received powder was suspended in deionized water to form an aqueous suspension with a solid content of 20 wt.% without adding any dispersing agent. Effective mixing was provided using a magnetic stirrer while breaking down the large agglomerates by using a sonicator. The prepared suspension demonstrated a good stability during SPS process without any detectable sedimentation. The size distribution of the particles in suspension was measured using a Spraytec unit (Malvern Instruments, UK). The results in Fig. 4.1 (c) shows a d_{50} = 0.39 µm for the suspension.

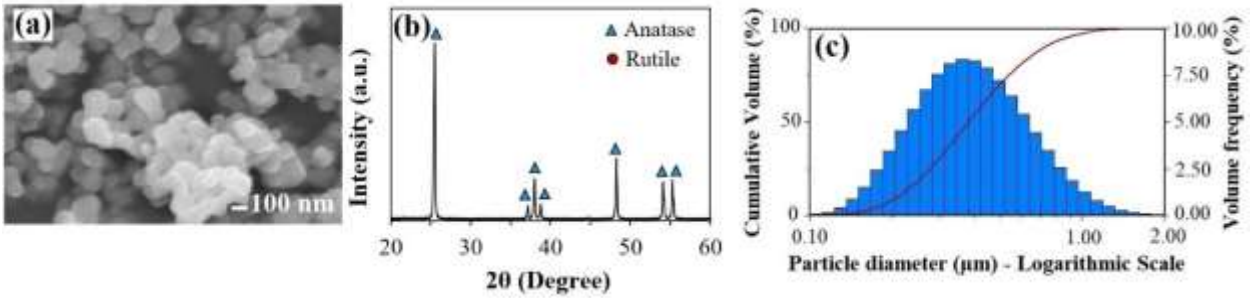

Figure 4. 1 (a) SEM micrograph and (b) XRD pattern of the feedstock TiO_2 powder, (c) particle size distribution of the water-based suspension.

4.2.2 Plasma spray processing and sample preparation

The water-based TiO_2 suspension was deposited by suspension plasma spraying using an Axial III^{TM} plasma torch (Northwest Mettech Corp., Canada) with a gas mixture of Ar, H_2, and N_2. This deposition technology combines an axial injector with an automatic suspension feed system (NanoFeed^{TM}, Northwest Mettech Corp., Canada) that ensures the correct delivery of the atomized feedstock suspension into the central core of the plasma while monitoring the suspension flow rate and density during spraying with a Coriolis flowmeter (Endress+Hauser, Canada). Moreover, the deposition system contains a plasma torch consisting of three cathodes/anodes working on three power supplies.

The TiO_2 suspension was introduced in the plasma jet through an injector with an internal diameter of 1.8 mm placed right behind the torch convergence at a feed rate of about 45 mL/min, as shown in Fig. 4.2. The spray distance for all samples was 75 mm.

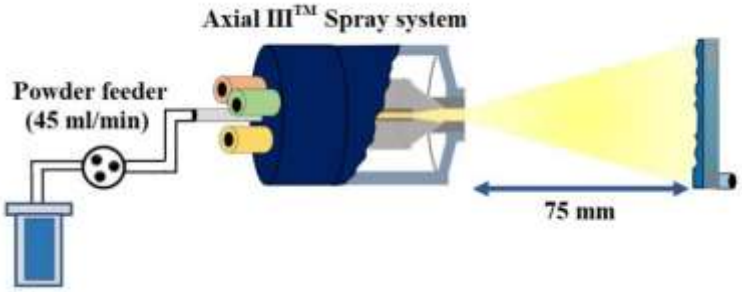

Figure 4. 2 Schematic representation of the suspension plasma spray system using an Axial III^{TM} plasma torch.

The substrates used in this study were flat 304 stainless steel coupons with dimensions of 25×25×5 mm^3. The substrate surfaces were grit-blasted by 80 grit Al_2O_3 particles to enhance adhesion properties, followed by ultrasonic cleaning in acetone to remove contamination and residues from blasting. Surface profilometry showed an average roughness R_a of 4 μm for grit-blasted substrates before deposition. Coatings were produced by 20 consecutive passes of a full spray raster with a 3 mm overlay distance with a linear torch velocity of 1 m/s. A cooling procedure was applied using a compressed air impinging on the front surface of the coating and a water-cooled substrate holder to avoid overheating of the substrate during spraying and preserve a higher anatase content in the coatings [42].

As the substrate temperature might affect the coating stoichiometry in plasma spray, a ThermoVision IR camera (A 320, FLIR, US) was used to monitor the substrate temperature during the experiment. Prior to deposition, the substrates were preheated by the plasma torch to a

temperature of 100 °C to drive off adsorbed moisture from the substrate and provide a dry surface to the first impacting particles [169]. TiO_2 coatings with different anatase contents were produced at four deposition conditions where the gas mixture ratio was the only varied parameter. Details of operating parameters are described in Table 4.1. As can be seen, the concentration of the H_2 gas used in the gas mixture has a strong influence on the plasma power gun, which affects the substrate surface temperature during the deposition process. Two groups of coatings were prepared: one in the as-sprayed condition while the coatings of the second group were polished and heat treated in air at 550 °C for 48 hours in an open-ended tubular furnace (Lindberg, US). This coating treatment was performed to reduce the potential influence of the morphology and oxygen content on the photocatalytic activity of the as-sprayed coatings. Based on our previous work [150], sub-stoichiometric TiO_{2-x} coating was reached to almost fully oxidized TiO_2 without any major phase changes after thermal treatment at 550 °C.

Table 4. 1 SPS deposition parameters for TiO_2 coatings on the stainless-steel substrates.

Conditions	Current (A)	Gas flow (SLPM)	Gas mixture			Power (kW)	Substrate temp. during the deposition (°C)
			Ar (%)	N_2 (%)	H_2 (%)		
A-15H_2	220	245	75	10	15	90	250
B-11H_2		233	78	11	11	85	220
C-7H_2		223	82	11	7	78	150
D-3H_2		213	85	12	3	75	140

4.2.3 Structural and microstructural characterization

The phase identification of the coatings was investigated by X-ray diffraction (XRD) using an X'Pert Pro; PANalytical (Philips, Netherlands) with Cu Kα radiation and in a range of 20-80° with a step size of 0.02°. Phase quantification of rutile and anatase was determined by Rietveld refinement using HighScore Plus software (Malvern PANalytical, UK). Li et al. [170] reported the existence of the preferred orientation of plasma sprayed TiO_2 coatings on different substrates. Based on the literature, Rietveld refinement is a reliable method for accurate phase composition measurements of thermal sprayed coatings by considering preferred orientation in the anisotropic thermal sprayed coatings [171].

The morphology (top surface and polished cross-section) of each film was evaluated using a field emission scanning electron microscope (FESEM JSM 7600TFE, JEOL, Japan) with an accelerating voltage of 15 kV. A confocal laser microscope (LEXT OLS4000, Olympus, Japan) was utilized to quantify the arithmetic average roughness (R_a) and surface ratio of coatings. The resulting 3D maps of the coatings' surfaces were generated by digitally stitching 25 single images (5 by 5) to cover a large enough area to be representative of the coating surface.

The phase distribution on the polished cross-section of the as-sprayed coatings before heat treatment was monitored using Raman spectrometer (Horiba, USA). This technique has been widely used as a quick method to discern the surface crystal structure of TiO_2 coatings with higher sensitivity and spatial resolution compared to XRD [150][86][172]. These measurements were conducted at room temperature using an Olympus BX-41 confocal microscope with a 50 x objective magnification (NA= 0.7), a focal spot diameter of 1.3 μm, and a hardware resolution of approximately 1 cm per pixel. A laser wavelength of 473 nm was produced by the linearly polarized Cobolt Blues 25 mW diode-pumped solid-state laser (DPSS). Moreover, the top surface Raman spotting and mapping of the coatings after heat treatment were performed by a Raman

spectrometer (inVia Reflex, UK) with a laser wavelength of 532 nm (spot size ~2 µm), objective magnification 50 x and 10 s exposure time.

4.2.4 Chemical and optical characterization

The chemical stoichiometry of the as-sprayed coatings and the starting powder was quantified using thermogravimetric analysis (TGA). Given the small size of the TGA crucible, it was necessary to perform a special sample preparation procedure to make the coatings suitable for the thermogravimetric analysis. This procedure consisted of the detachment of TiO_{2-x} coatings and turning them into powder in an agate mortar. The collected powder obtained from the coatings was analyzed by the TGA system. TGA analysis was conducted using a thermal balance (TGA Q500/Discovery MS, TA Instruments, US) where the powders were heated at 5 °C /min in air to 1000 °C for 90 min to re-oxidize sub-stoichiometric TiO_{2-x}. During TGA analysis, all samples were kept at 150 °C for 2 h to make them fully dried.

Based on the re-oxidizing reaction of TiO_2, the quantification of oxygen atoms (x) was calculated by the sample weight increment according to Eq. 4.2 [150][151][152][153]:

$$TiO_{2-x} + \frac{x}{2}O_2 \rightarrow TiO_2 \tag{4.1}$$

$$x = \frac{\Delta w}{w_{mol}^{O}} \frac{(2W_{mol}^{O} + W_{mol}^{Ti})}{(W_0 + \Delta W)} \tag{4.2}$$

where ΔW is the weight increment, W_0 is the initial weight of the samples, W_{mol}^{O} and W_{mol}^{Ti} are the molar weight of oxygen and titanium.

The bandgap energy of the as-spray coatings was calculated with the Tauc plot method using the absorption spectra obtained from a UV-Visible-NIR spectrometer (Lambda 750, Perkin Elmer, US), as shown in Eq. 4.3, and 4.4 [150][36][154] :

$$\alpha h\upsilon = A(h\upsilon - E_g)^n \tag{4.3}$$

$$E_{photon}(eV) = h\nu = \frac{1239}{\lambda} \tag{4.4}$$

where λ is wavelength, A is a constant given by the slope of the linear region in the $(\alpha h\nu)^{1/n}$ –hν plot, E_g is the optical energy gap of the material calculated from the extrapolation of the straight-line portion of the mentioned plot, and n is the characteristic of the optical transition process type, which is 2.0 and 0.5 for indirect and direct allowed optical transition, respectively.

4.2.5 Photocatalytic activity characterization

In this project, the coating's photocatalytic activity was assessed by measuring the decoloring rate of methylene blue, MB ($C_{16}H_{18}ClN_3S$) as a test pollutant according to ISO 10678:2010 [79]. In the textile industry, organic dyes are recognized source of pollution that conventional industrial treatment method cannot effectively remove them from waste-water [163][25]. First, the tested coated coupon with 2.5 x 2.5 mm^2 surface area was immersed in the 30 ml of MB solution with 2×10^{-5} M concentration for 1 hour in the dark to complete the adsorption of MB molecules on the surface of the coating. Subsequently, the solution was substituted by 30 ml of MB solution with 10^{-5} M concentration (C_0) and was placed inside the visible light setup. This setup is equipped with two xenon arc lamps with an input light power of 35 W each, and a

cooling fan was used to prevent further heating by light irradiation. The decomposition rate of MB was monitored by measuring the maximum absorbance of MB at wavelength of 664 nm every 30 min using a UV-vis spectrophotometer (evolution 201, Thermo Scientific, US).

A blank test without TiO_2 coating was performed by irradiating MB solution under visible light to evaluate the photolysis phenomenon. The rate constant of the pseudo-first-order reaction (k) and the degradation percentage was measured using Eq. 4.5 and Eq. 4.6, respectively [3][35].

$$ln\left(\frac{C_0}{C}\right) = kt \tag{4.5}$$

$$Degradation\ (\%) = \frac{(C_0 - C)}{C_0} \times 100 \tag{4.6}$$

where C_0 is the initial concentration of MB (10^{-5} M), C is MB concentration at each time interval, and t is the irradiation time.

4.3 Results and discussion

4.3.1 Structural, microstructural, and chemical composition characterization

4.3.1.1 X-ray diffraction

The XRD patterns of the TiO_2 coatings deposited at different spray conditions and the derived information are shown in Fig. 4.3 (As-sprayed) and Table 4.2, respectively. Generally, all coatings show XRD patterns with the characteristics of Bragg reflection peaks of two main phases of TiO_2, anatase, and rutile. XRD results clearly indicate the significant influence of the H_2 flow rate on the anatase content. According to Table 4.2, the anatase content decreased with increasing H_2 flow rate from 84% in Sample D-3H_2 to 56% in Sample A-15H_2. As can be seen in this table, the structural composition of all thermally sprayed coatings changed from single anatase phase (from the feedstock powder) to mixed phase of anatase combined with rutile after deposition, while anatase remains as the predominant phase in all as-sprayed coatings. To maximize anatase phase formation, the substrate temperature during deposition was minimized by using the water cooling and air cooling systems. In this work, all samples were heat-treated at 550 °C to increase the oxygen level of the sub-stoichiometric coatings to fully stoichiometric TiO_2. Based on Fig. 4.3 (Polished heat-treated) and Table 4.2, a minor phase change of anatase to rutile was observed in the heat-treated coatings.

Compared to our previous work [150], a higher anatase phase content is obtained in the current study using a high-power axial injection plasma torch, which leads to a higher in-flight particle velocity. Colmenares-Angulo et al. [45] indicated that an increase on the impact velocities, the anatase content would be increased by improving flattening/solidification rates and increasing the tendency for undercooling.

Based on the literature, rutile would be formed from equilibrium solidification, while anatase nucleation is favor in non-equilibrium solidification conditions [43][42][173][45]. During plasma spraying, anatase feedstock would either transform to rutile phase depending on the melting level of the particles [133][44] or recrystallize into anatase phase under non-equilibrium, rapid quenching conditions of spraying [45]. Mauer et al. [42] and Bannier et al. [172] showed the impact of the substrate temperature and substrate cooling on the anatase content of the plasma sprayed coatings. It has been reported that higher H_2 flow rate would increase the thermal conductivity of the plasma torch that favors the formation of rutile phase [174].

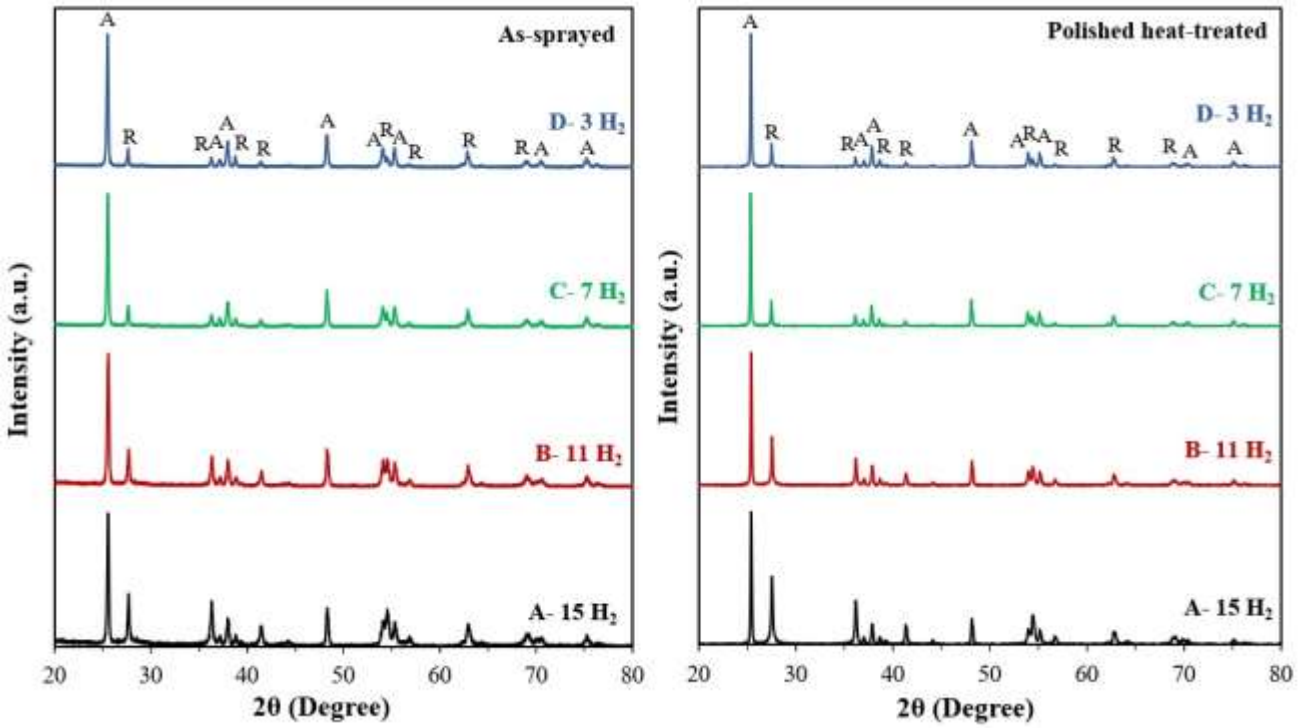

Figure 4. 3 X-ray diffraction patterns of as-sprayed TiO_2 coatings and polished heat-treated samples, where A denotes the anatase phase and R the rutile phase.

Table 4. 2 Phase content and crystallite size of the coatings derived from Fig. 4.3.

	Sample	Anatase	Rutile	Crystallite size (nm)	
				Anatase	Rutile
A-15H_2	As-sprayed	56	44	53	36
	Polished heat-treated	42	58	91	36
B-11H_2	As-sprayed	65	35	50	38
	Polished heat-treated	55	45	103	47
C-7H_2	As-sprayed	80	20	57	51
	Polished heat-treated	75	25	112	72
D-3H_2	As-sprayed	84	16	61	62
	Polished heat-treated	79	21	109	79

4.3.1.2 Coating microstructure and crystalline phase distribution

The effect of the different H_2 flow rates on the microstructure of the plasma sprayed TiO_2 coatings is presented in Figs. 4.4 and 4.5. According to the SEM micrographs of the coating top surfaces (Fig. 4.4), distinctive rounded bumps of cauliflower-like surface morphology can be observed for coatings deposited at higher H_2 flow rates (samples A-15H_2 and B-11H_2). While decreasing the secondary gas flow rate resulted in smoother surface morphologies (samples C-7H_2 and D-3H_2). The microstructure variation in the coatings can be attributed to the evolution of the suspension droplets during spraying in the plasma plume [43].

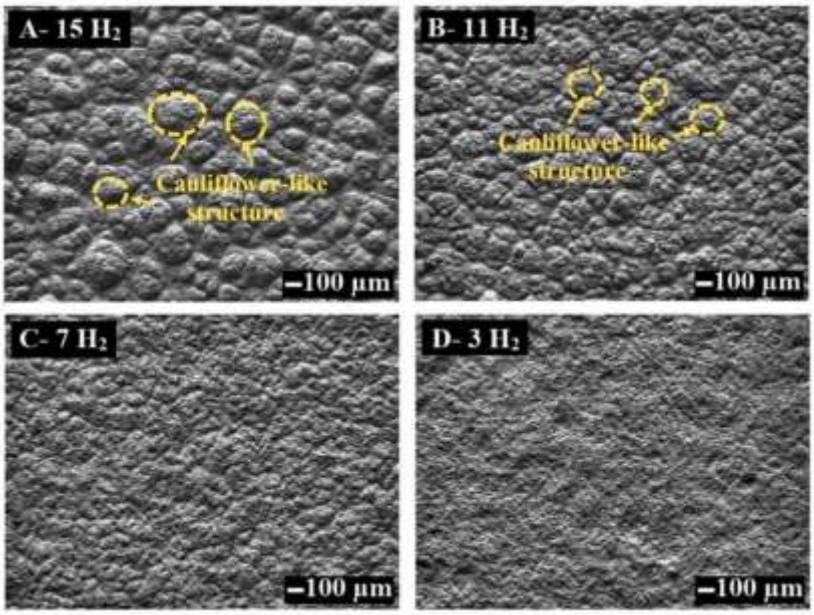

Figure 4. 4 Top surface SEM micrographs of the as-sprayed TiO_2 coatings produced at different H_2 flow rates.

Based on the cross-section micrographs (Fig. 4.5), the thickness of the as-sprayed coatings increased by increasing hydrogen flow rate of the plasma gas. In this study, the average film thickness/pass for samples A-15H_2, B-11H_2, C-7H_2, and D-3H_2 was about 11, 9, 7, and 5 µm, respectively. It could be concluded that, at a higher hydrogen flow rate, better suspension atomization might lead to higher deposition efficiency in the plasma sprayed coatings. Chen et al. [175] reported an ideal thickness of around 5 µm for TiO_2 coating to show the highest photocatalytic activity under the light wavelength of 365 nm. According to the literature, the maximum photocatalytic reaction rate was attained by complete adsorption of light in the optimum film thickness. While at lower film thicknesses, the insufficient light absorption could decrease the photoactivity. Moreover, the reaction rate would stay unchanged at higher thicknesses since the diffusional length of the photo-generated electron-hole pairs to the catalyst/liquid interface will not change [175][176]. Therefore, in the present study, the thickness variation is not expected to have any significant impact on the photocatalytic efficiency of the different coatings.

As shown in Fig. 4.5, porosity of the as-sprayed coatings increased by increasing hydrogen flow rate of the plasma gas. The relation between the microstructure and the operational parameters of plasma spray was described by Fauchais et al., especially when hydrogen is a secondary plasma gas [126]. It has been indicated that voltage fluctuations result from arc instability in plasma torch could change plasma characteristics such as velocity. Depending on the voltage fluctuation, the penetration of suspension drops would be reduced, and some partially melted particles would impact the substrate to produce porous coating [126][177]. However, it should be noted that the Axial III^{TM} plasma torch used in this study is constituted of three independent cathodes/anodes. This feature would effectively decrease voltage fluctuation in the plasma jet and allow injecting feedstock suspension right through the hottest side of the plasma jet. Consequently, lower porosity on the coatings produced at lower plasma power, like samples C-7H_2 and D-3H_2, might be attributed to the non-molten particles filled the pores after impacting onto the surface.

The micrographs illustrated in Fig. 4.5 present mechanically stable coatings firmly bonded to the substrate with a crack-free interface. Generally, all coatings are composed of a bimodal microstructure of molten and non-molten particles. Dense zones of fully melted particles appear

as the light grey areas. However, porous zones could stem from either agglomerated un-melted fine particles or large pores that can be observed as dark grey zones and black areas, respectively. As can be seen in Fig. 4.5, black zones of large pores and light grey areas of melted particles are prominent in coatings A-15H_2 and B-11H_2. However, dark grey areas of un-melted agglomerated fine particles with a size close to the starting powder are dominant in the coatings C-7H_2 and D-3H_2 that were produced at low plasma power conditions. That might be a reason explaining the large content of anatase phase present in C-7H_2 and D-3H_2 coatings since un-melted fine particles are usually attributed to anatase phase [45][178].

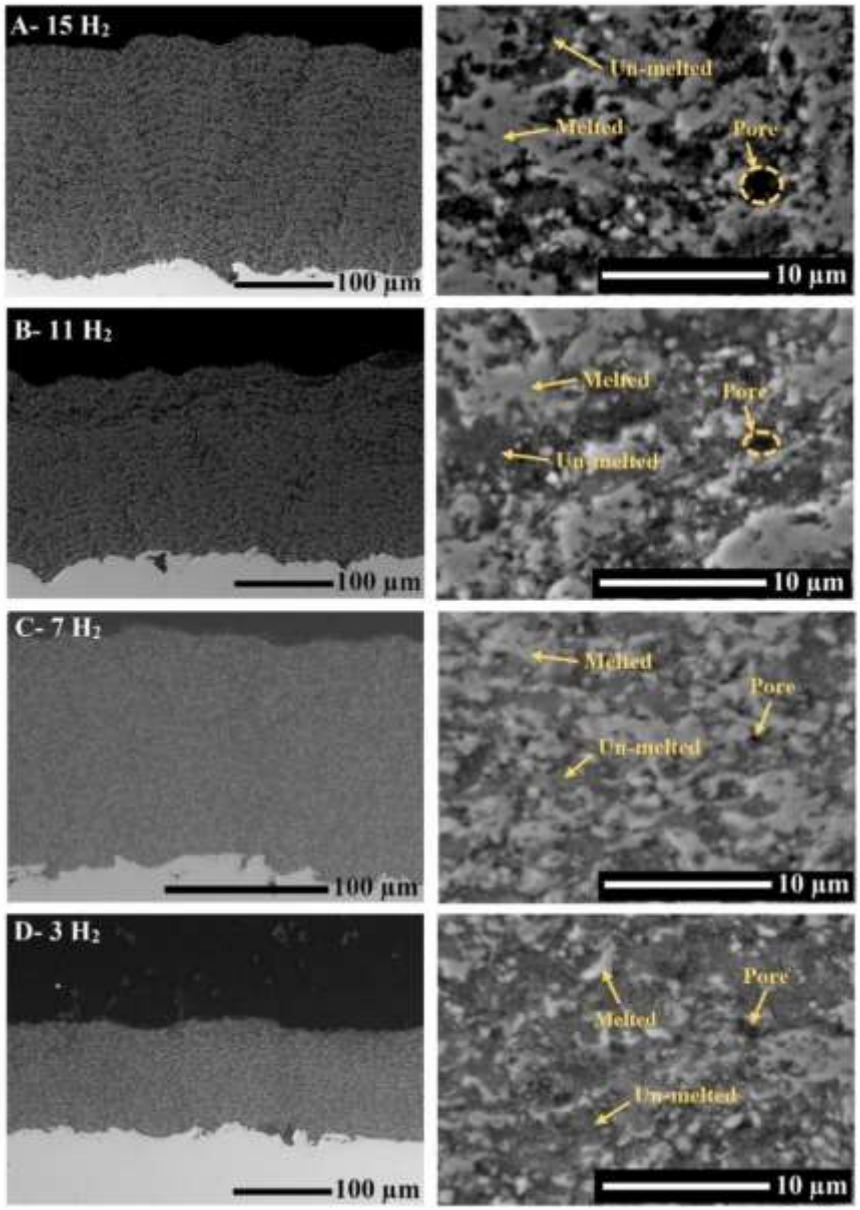

Figure 4. 5 Cross-section SEM micrographs of the as-sprayed TiO_2 coatings produced at different H_2 flow rates from lower to higher magnification, where coatings' thicknesses at different conditions are as follow: A-15H_2: 222 ± 4 µm, B-11H_2: 185 ± 5 µm, C-7H_2: 140 ± 4 µm, D-3H_2: 100 ± 3 µm.

The crystallographic phase distribution associated with the molten and non-molten areas (in Fig. 4.5) was studied by Raman spectroscopy analysis on the coatings' cross-sections of as-sprayed samples. Raman spectra of all as-sprayed coatings at these two different areas are presented in Fig. 4.6. Based on the literature, six characteristic peaks at 144, 197, 399, 513, 519, and 639 cm^{-1}, and four characteristic peaks at 143, 236, 447, and 613 cm^{-1} are considered as the fingerprints of anatase and rutile phases, respectively [114][179][180]. In Fig. 4.6, only one band was detected for the peaks located at 513 and 519 cm^{-1} due to overlapping. Although Raman result was not influenced by this overlapping because these bands were not used for phase detection.

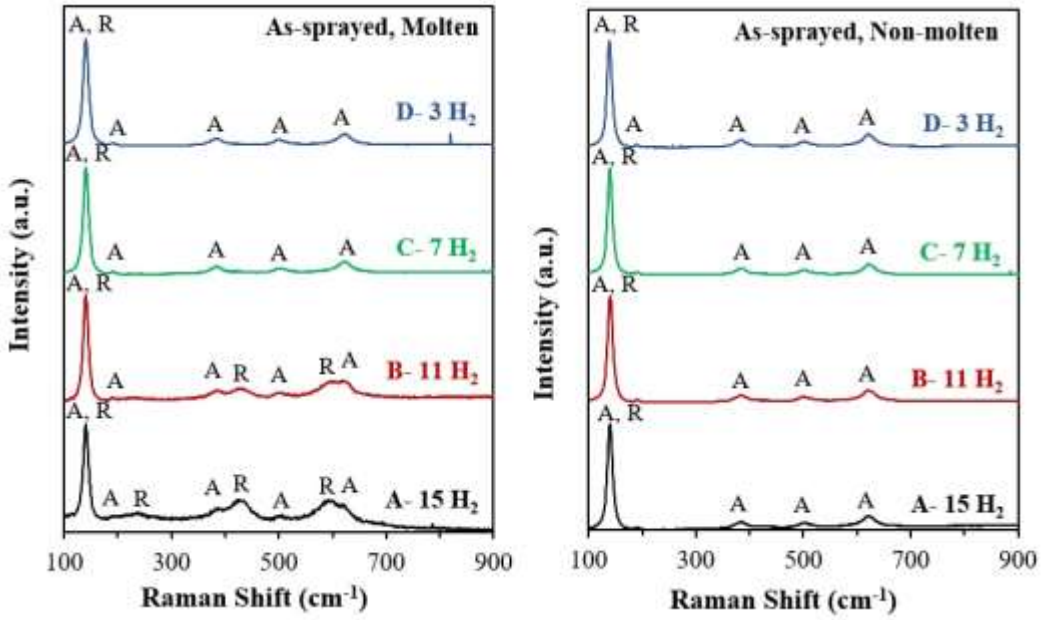

Figure 4. 6 Raman spectra results in the molten and non-molten regions on the coatings' cross-sections of as-sprayed samples deposited at different deposition parameters (as seen in Fig. 4.5), which A denotes the anatase phase and R the rutile phase.

Raman spectra of the molten particles present peaks at both anatase and rutile positions for coatings produced at higher hydrogen flow rates (A-15H_2 and B-11H_2), while coatings sprayed at lower hydrogen flow rates (C-7H_2 and D-3H_2) only show anatase peaks. Fully melted zones are typically considered as rutile phase [181]; however, metastable anatase phase can recrystallize from the liquid particles under non-equilibrium, rapid quenching conditions of thermal spraying solidification when the temperature is below 0.88 TiO_2 melting point (T_m=2130 K), as shown in Fig. 4.7 [43][42][45][44]. According to the Titanium-Oxygen phase diagram [182], the melting point of sub-stoichiometric TiO_x (x=1.95) is decreased to 2023 K.

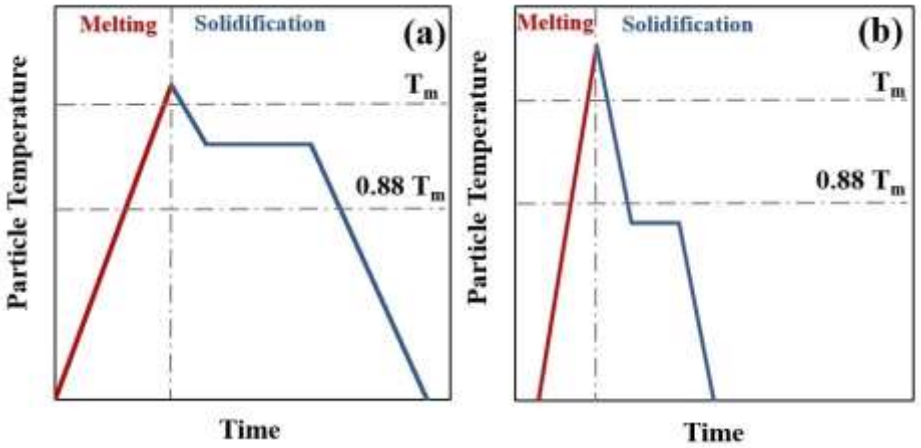

Figure 4. 7 Heating-Cooling diagrams of the feedstock powder in spraying conditions, which T_m is TiO_2 melting point (~2130 K). (a) rutile nucleation, and (b) anatase nucleation [Adapted from references [42] and [45]].

As can be seen, in all as-sprayed coatings, anatase was the only phase found in the un-melted areas, confirming that these regions did not have any crystallographic transformation during the spraying process. Based on the SEM micrographs (Fig. 4.5), the un-melted regions are basically composed of fine particles coming from starting powder that were embedded in the thermally sprayed coatings. In the water-based suspension, high vaporization enthalpy of water (2.3×10^6 J kg^{-1}) would cool down the plasma jet and leave some un-melted particles with the same size, morphology, and crystalline phase from the feedstock [183].

A more precise study on the phase distribution of anatase and rutile at the top surface of the heat-treated coatings was also investigated by Raman spectroscopy. According to Figs. 4.8, and 4.9, both Raman bands of rutile and anatase phases were observed for samples A-15H_2 and B-11H_2 that were produced at higher H_2 flow rates. While only anatase phase was detected in Raman spectra of samples C-7H_2 and D-3H_2.

Compared to XRD technique, Raman spectroscopy is considered a fast and simple method for surface crystal structure detection with a low depth of field of few micrometers (~4 μm) in a narrow spot size of about 1.5 μm. Whereas X-ray used in XRD machine for phase quantification could penetrate around 20 μm in TiO_2 coatings in a larger spot size (a few mm^2) [86][172]. As mentioned before, the diffusional length of charge carriers to the catalyst/liquid interface is about 5 μm for TiO_2 coating [175][176]. It is apparent from the literature that the photocatalytic performance of TiO_2 coating is associated with the anatase content at the surface where it is directly exposed to the pollutant and light. Although, the surface region might have a different crystalline phase than that of bulk material, especially when it is heated close to the phase transition temperatures [36][86][135][184].

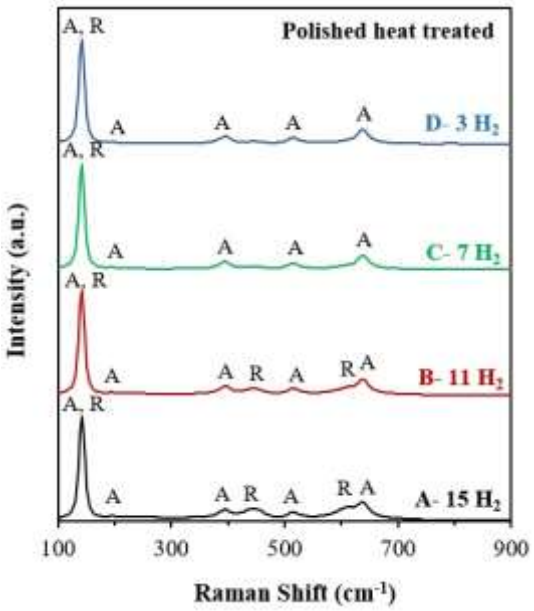

Figure 4. 8 Raman spectra results at the top surface of the polished heat-treated coatings, where A denotes the anatase phase and R the rutile phase.

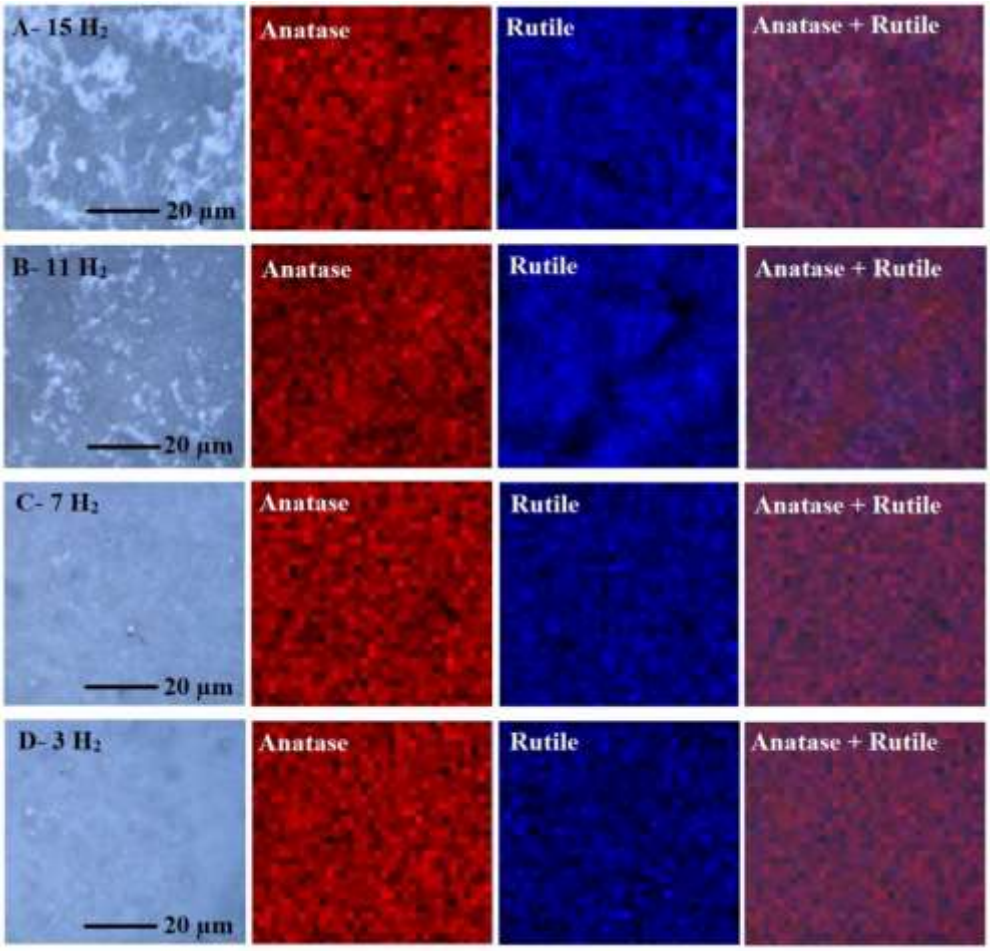

Figure 4. 9 Raman maps of the spatial distribution of characteristic Raman peaks for the polished heat-treated coatings, where red color represents anatase peak at 197 cm^{-1}, and blue color corresponds to rutile peak at 447 cm^{-1}.

4.3.1.3 Coating surface roughness

Confocal laser microscope results of all coatings before and after polishing are presented in Figs. 4.10, 4.11, and Table 4.3. As can be seen, the surface roughness and surface ratio of the as-sprayed samples increased with the increasing secondary gas flow rate of H_2. According to Figs. 4.4, and 4.10, higher surface roughness is attributed to the presence of a cauliflower-like structure that could increase surface area. In SPS, the roughness of coatings tends to increase with thickness particularly due to the shadow effect. As presented in Fig. 4.5, the higher the H_2 flow rate, the higher the thickness. This is likely the main reason why the roughness increased with increasing the H_2 flow rate.

In this work, all samples were polished to reduce the influence of roughness and surface area on the photocatalytic performance of the tested coatings, as shown in Fig. 4.11.

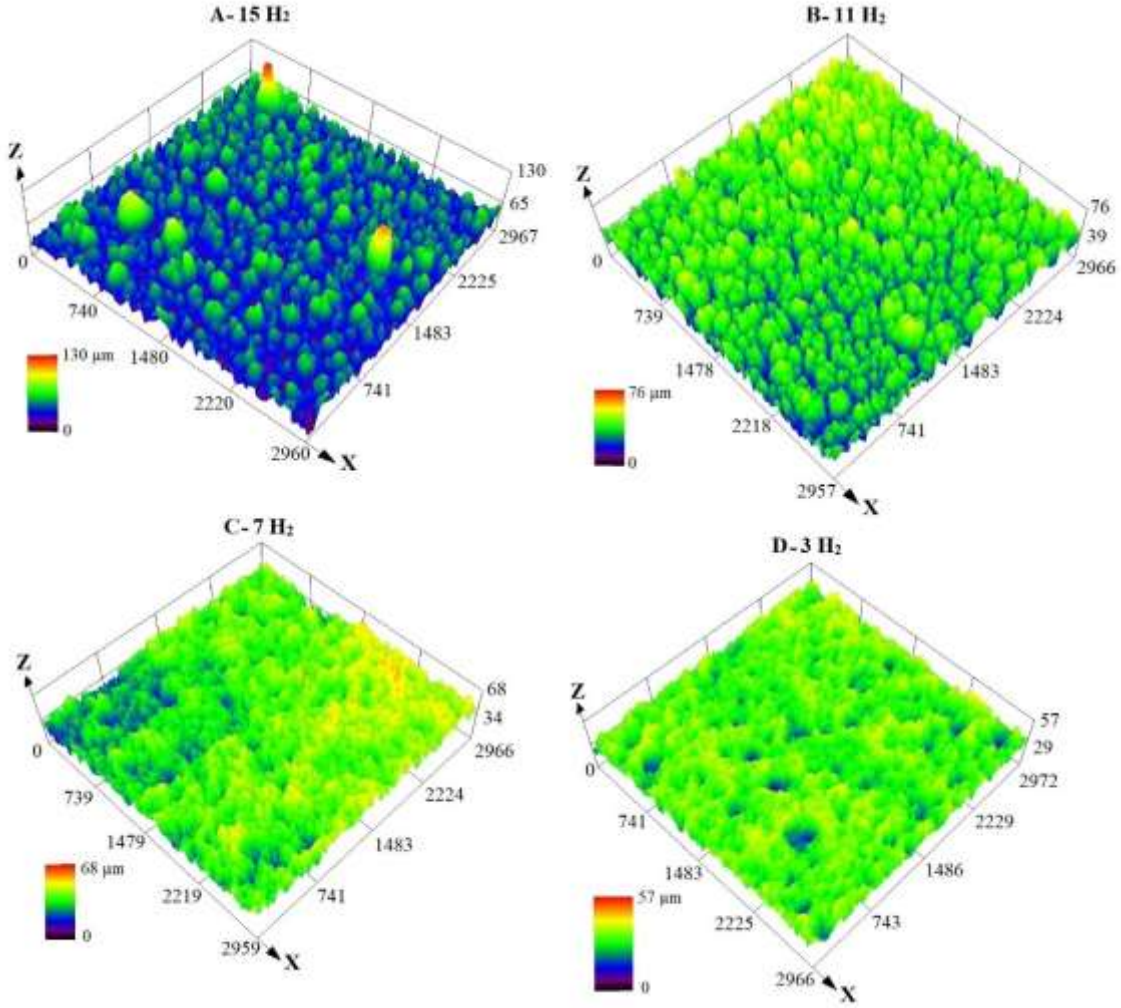

Figure 4. 10 3D images of the top surfaces of the as-sprayed coatings obtained by the confocal laser microscope.

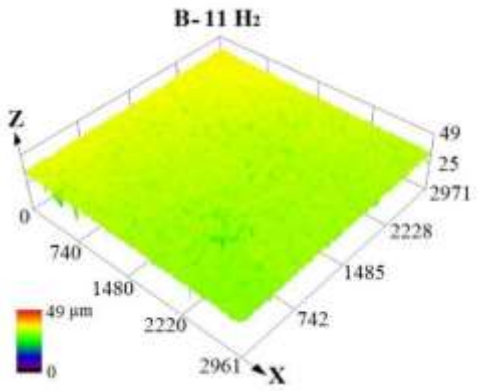

Figure 4. 11 3D images of the top surfaces of the coatings after polishing achieved by the confocal laser microscope.

Table 4. 3 Average surface roughness (R_a) of the samples before and after polishing.

Sample	Surface roughness parameter	A-15H_2	B-11H_2	C-7H_2	D-3H_2
As-sprayed	R_a (µm)	8.5 ± 0.31	5.5 ± 0.14	3.7 ± 0.07	2.9 ± 0.09
	Surface ratio	1.86	1.80	1.73	1.65
After polishing	R_a (µm)	0.96 ± 0.02	0.94 ± 0.02	0.97 ± 0.03	0.93 ± 0.007
	Surface ratio	1.39	1.41	1.43	1.39

4.3.1.4 Oxygen content measurement by TGA

TGA analysis was employed to quantify the oxygen content of the as-sprayed coatings, as shown in Fig. 4.12. The calculated stoichiometry of the coatings is provided in the figure label. Based on the results, as the hydrogen content in the plasma gas mixture varies, not only the structural and microstructural properties are affected, but also there is a deviation in the coatings' chemical stoichiometry. According to the results, samples A-15H_2 presented the lowest amount of oxygen content ($TiO_{1.945}$). While, with increasing H_2 flow rate, the oxygen vacancy content was increased in the coatings. Similar results were reported by Lee et al. [152].

It has been indicated that the intense heating of the starting TiO_2 powder in the plasma jet could favorably generate oxygen deficiency, which can be promoted by increasing hydrogen as a secondary gas in the plasma mixture due to its reductive properties. Also, the oxygen vacancy level has been associated with the in-flight particle temperature. As a result, highly stoichiometric TiO_2 starting powder would change to sub-stoichiometric TiO_{2-x} (n-type semiconductor) during plasma spraying in the as-sprayed coatings [134][45].

According to the findings of F. Millot et al. [185], oxygen vacancies could exist in sub-stoichiometric TiO_x samples with an x=1.999. Based on Fig. 4.12, TGA results presented a stoichiometry variation from $TiO_{1.945}$ to $TiO_{1.964}$. This off-stoichiometry order is enough to ensure the presence of oxygen vacancies. Additionally, Szot et al. [186] reported that for the hypothetical disorder around x= 0.0625-0.027, shear planes would be formed in [132] direction.

According to the literature, both oxygen vacancy and electrons would be produced through hydrogen/TiO_2 interaction, in which Ti^{3+} ions would be generated afterward by the electrons trapping in Ti^{4+} lattice sites [66]. Accordingly, a color shift could be observed from yellowish-white to dark-grey, depending on the amount of oxygen loss and because of Ti^{3+} ions'

concentration while pure and super stoichiometric samples are fully transparent [135] [62][63][64][65][136].

Based on our previous work [150] we concluded that in a bimodal microstructure of molten and non-molten SPS TiO_2 coatings, fully melted particles lost some oxygen during plasma spraying leading to the formation of re-solidified sub-stoichiometric titania. However, the un-melted particles, composed of particles coming from starting powder, remained stoichiometric. In the current study, both anatase and rutile were detected in samples A-15H_2 and B-11H_2, while only anatase phase was detected in the molten area of samples C-7H_2 and D-3H_2 (Fig. 4.8). As a result, both sub-stoichiometric anatase and rutile phases could be formed during the spraying process. This finding agrees with the experimental evidence demonstrated by others to show the existence of oxygen vacancies in rutile [152] and anatase phases [187]. According to the literature, there are various strategies for effectively introducing oxygen deficiency in TiO_2 based nanomaterials, such as thermal annealing in an inert gas atmosphere (vacuum or argon gas) and reducing gas environment (hydrogen gas) [188]. The stoichiometry of the as-sprayed sample produced in this work is similar to that of samples reported by Tsuyumoto et al. [189], which were annealed at 950 °C in the pure H_2 atmosphere for one hour. It indicates that plasma spraying appears a more effective, safer, and faster way to produce sub-stoichiometric TiO_{2-x}.

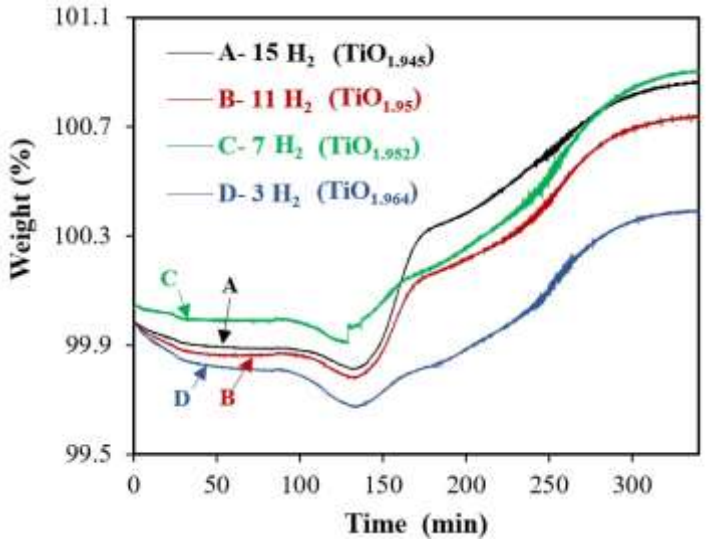

Figure 4. 12 TGA curves of the as-sprayed TiO_2 coatings obtained at different spray conditions. They were heated in the air to 1000 °C and holding at that temperature for 90 min.

Besides the TGA analysis, the intensity of the XRD peaks could provide evidence of the oxygen vacancies presented in the as-sprayed coatings. Richter et al. [190] reported that the intensity of the (101) and (111) rutile peaks is more pronounced for sub-stoichiometric samples. As shown in Fig. 4.3, the intensity of both diffraction planes increased with increasing oxygen vacancy content in the coatings produced at higher hydrogen flow rates (samples A-15H_2 and B-11H_2). Moreover, based on the literature [190], the intensity of (110) rutile peak would be increased for nearstochiometric TiO_2 samples. However, our XRD results (Fig. 4.3) showed a stronger (110) peak intensity for samples A-15H_2 and B-11H_2 with higher oxygen deficiency. This contradiction could be explained by the other aspects affecting XRD peak intensities like crystallographic texturing effects [190].

As reported in our previous work [150], as-sprayed coatings would be transformed to almost fully stoichiometric TiO_2 by oxidation after heat treating at 550 ºC for 48 hours. Fig. 4.13

is shown the coatings' color before and after heat-treatment. In as-sprayed coatings, sample A-15H_2 presented the darkest color while the color became brighter with decreasing hydrogen flow rate for sample D-3H_2, confirming the different oxygen vacancy levels produced at various spraying conditions. As can be observed, after thermal treatment, the color changed to white in all coatings suggesting that oxygen content raised in the coatings close to stoichiometric TiO_2.

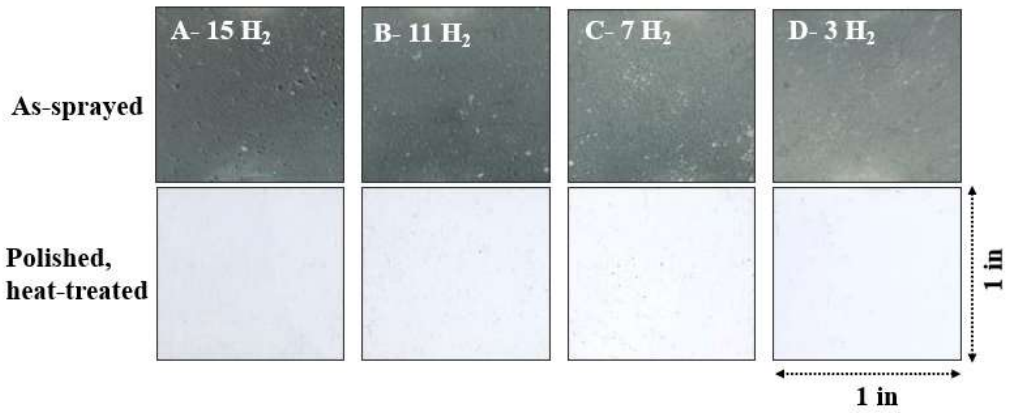

Figure 4. 13 The color difference between the as-sprayed TiO_2 coatings and polished heat-treated samples owing to oxygen recapturing.

4.3.2 Optical characterization

The UV-Vis absorption spectra of the as-sprayed coatings and after heat treatment are given in Fig. 4.14. The absorbance of the all as-sprayed coatings was shifted to higher values from that of the starting powder, whereas sample A-15H_2 showed the highest absorption in the visible range compared to the other samples produced at lower hydrogen flow rates. The results also indicated that dark grey as-sprayed coatings showed higher absorption than the thermally treated counterparts with a brighter color. As can be seen, there is less difference in the absorption and bandgap values of all heat-treated coatings.

The calculated direct and indirect bandgaps based on the UV-Vis absorption spectroscopy measurements are presented in Fig. 4.15 and Table 4.4. According to our results, bandgap energies of the as-sprayed coatings decreased as the hydrogen flow rate increased, and the lowest direct and indirect bandgaps were observed for sample A-15H_2.

The optical properties of the semiconductor are considered as one of the influencing parameters on the photocatalytic performance as its activity would be improved in the visible region by extending the light absorbance to this area [162]. A photon absorption might happen through the excitation of an electron from the filled valence band to the empty conduction band across the bandgap if the photon has an energy greater than the bandgap. This phenomenon would create a free electron and a hole in the conduction and valence band, respectively [191]. While stoichiometric TiO_2 appears as a transparent colorless material with no absorption in the visible region, oxygen vacancies in sub-stoichiometric TiO_{2-x} act as color centers to absorb visible light. Dark-grey color of the as-sprayed coatings is a good indication of the strong absorbance of the visible radiation. Generally, electron excitation by selective absorption would be the first vital step for the photocatalytic activity [138][136][191].

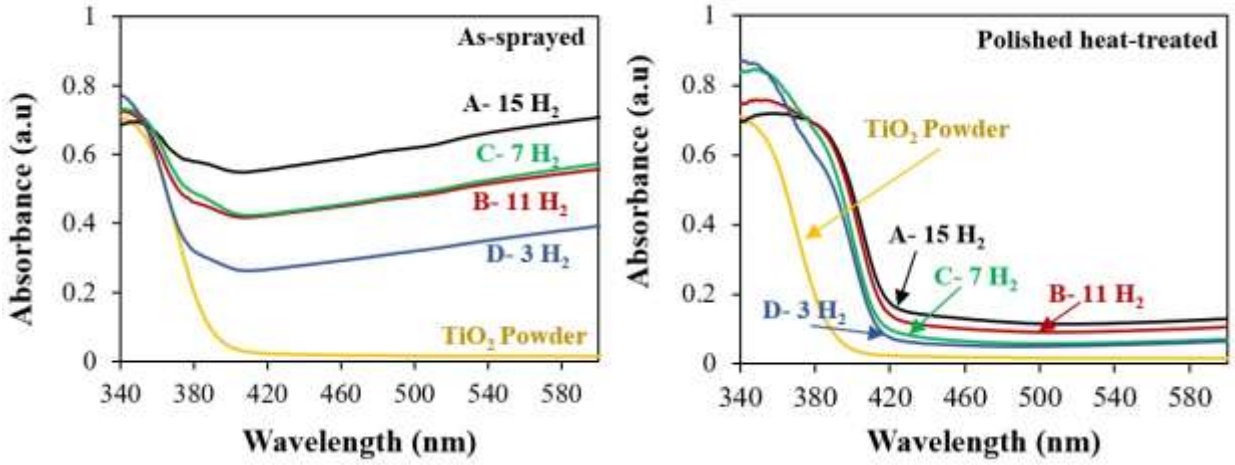

Figure 4. 14 UV-Vis absorption spectra of the as-sprayed TiO_2 coatings and polished heat-treated samples.

As reported by several authors, the bandgap value of rutile phase (E_g ~ 3.0 eV) is smaller than the anatase phase (E_g ~ 3.2 eV) [37][15][192]. Based on the literature, oxygen deficiency in TiO_2 lattice (sub-stoichiometric TiO_{2-x}) creates new energy levels below the conduction band that efficiently narrows the bandgap to be activated under visible light and enhance the photocatalytic activity [138][62][63][64][65]. The lowest direct and indirect bandgaps of sample A-15H_2 could be explained by either a higher rutile percentage with a lower bandgap or a significant oxygen vacancy content.

As explained before, the phase changes after heat-treatment were minor on all coatings while the oxygen contents were raised to fully oxidized TiO_2. Therefore, it could be concluded that oxygen vacancy concentration has a more substantial role in the optical properties of TiO_2 coatings than the crystalline phase.

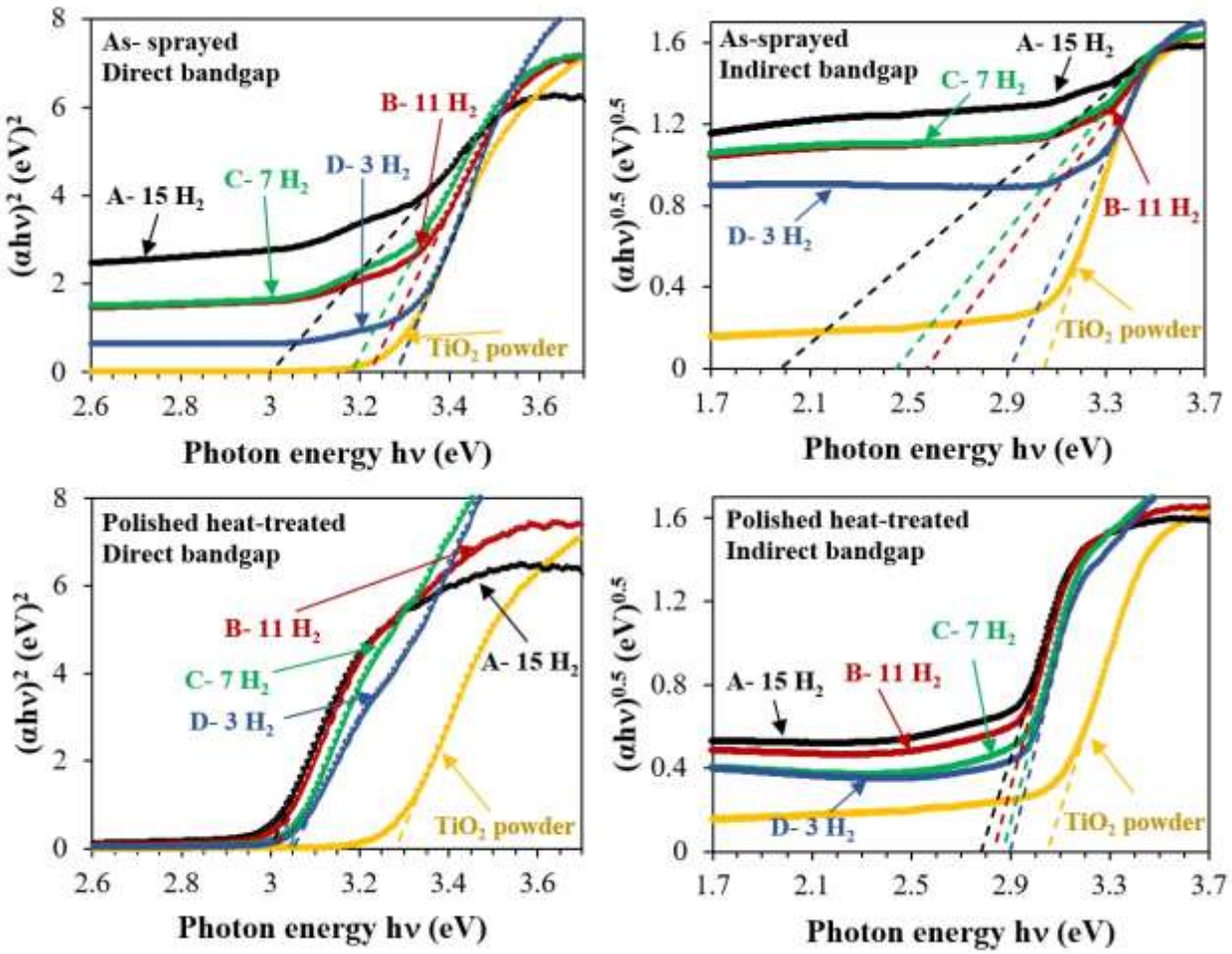

Figure 4. 15 Direct and indirect band energy diagram of the as-sprayed TiO_2 coatings obtained at different hydrogen gas concentrations and polished heat-treated samples.

Table 4. 4 Optical direct and indirect bandgaps derived from Fig. 4.15.

Condition	Bandgap		A-15H_2	B-11H_2	C-7H_2	D-3H_2	TiO_2 starting powder
As-sprayed	Direct	eV	3	3.22	3.18	3.28	3.28
		nm	413	385	389	377	377
	Indirect	eV	1.98	2.57	2.45	2.91	3.05
		nm	625	482	505	425	406
Polished heat-treated	Direct	eV	3	3.01	3.04	3.05	-
		nm	413	412	407	406	-
	Indirect	eV	2.78	2.83	2.87	2.9	-
		nm	446	437	431	427	-

4.3.3 Photocatalytic activity

The photocatalytic activity of the as-sprayed TiO_2 coatings and polished heat-treated counterparts for the degradation of methylene blue (MB) solution under a 90 min visible light illumination is plotted in Fig. 4.16. Sampling was performed every 30 min to measure the concentration change of MB during the reaction. More details on the reaction rate constant (k) and the correlation coefficient (R^2) are given in Table 4.5. Self-degradation of MB under irradiation

was performed without a coating as a benchmark, which presents minor photolysis of MB during the experiment. It can be clearly observed that all as-sprayed coatings presented higher activity than that of polished heat-treated counterparts, and the superior photocatalytic activity of ~ 95% was attained for sample C-7H_2. While after polishing and thermal treatment, sample D-3H_2 with ~ 87% MB degradation showed the best activity among other polished and heat-treated coatings.

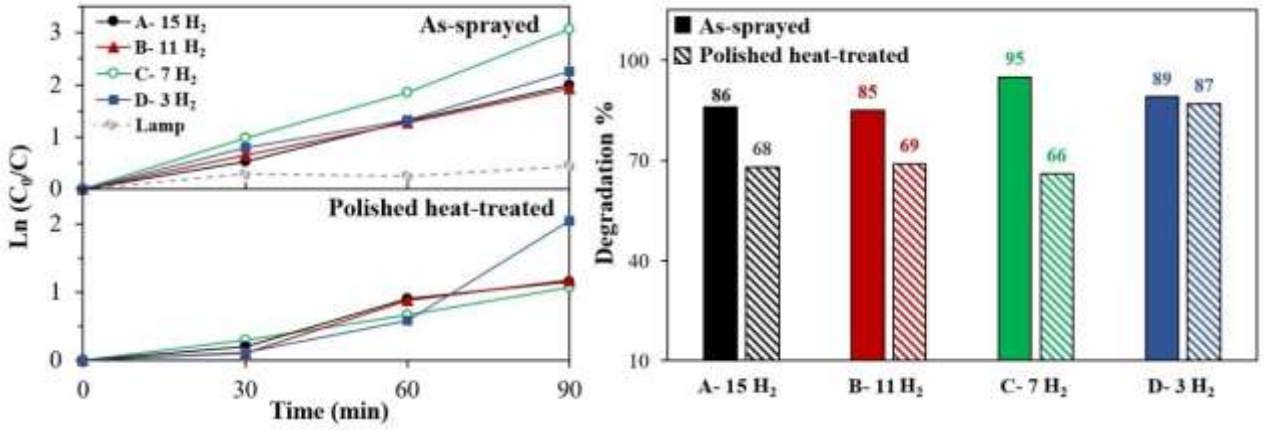

Figure 4. 16 Photocatalytic degradation of the MB solution under visible irradiation for 90 min, where C_0 is initial concentration after dark test, and C is the MB concentration at irradiation time.

Table 4. 5 Rate constant (k) of the MB solution after 90 min.

Sample	Rate constant (k) × 10^{-2} (min^{-1})		R^2	
	As-sprayed	Polished heat-treated	As-sprayed	Polished heat-treated
A-15H_2	2.2	1.1	0.99	0.94
B-11H_2	2.15	1.5	1	0.96
C-7H_2	3.3	1.2	0.99	0.99
D-3H_2	2.4	1.8	0.99	0.93

During photocatalysis, absorption of a photon with energy higher than the bandgap of TiO_2 can excite an electron from the valence to the conduction band and create an electron-hole pair. Photo-excited charge carriers would migrate to the catalyst surface to initiate reactions with the adsorbed materials at the surface. The produced oxidized radicals species such as hydroxyl radicals ($^{\bullet}HO$), and superoxide ($O_2^{-\bullet}$) ions can degrade organic compounds and mineralize the intermediates into harmless products (H_2O and CO_2) in waste-water [20][193][160][194].

The photocatalytic degradation rate of organic compounds primarily depends on several parameters, such as crystalline phase [195], TiO_2 stoichiometry [150], and surface area [28]. Nevertheless, changing the plasma spray condition (especially hydrogen content) would inevitably alter all the coating's properties, like phase content, morphology, and coating's stoichiometry. As the photocatalytic phenomenon is influenced by the coating's properties, no direct relation was observed with the photocatalytic activity of the as-sprayed coatings and their anatase content. Similar results have been reported in the other works [36][172]. In this research to study just the role of the anatase content on the photocatalytic activity of thermally sprayed coatings, all samples were polished and heat-treated at the same temperature to provide samples with the same roughness and stoichiometry. The crystalline phase is considered one of the essential factors in the photoactivity efficiency of titania coatings. Both anatase and rutile phases are tetragonal in crystal

structure containing TiO_6 octahedra shared differently in these phases and make different physical and chemical properties [37][194]. The reasons for the superior photocatalytic activity of anatase than rutile have been explained by several hypotheses, including indirect bandgap, higher charge carrier mobility, and free hydroxyl radical of anatase [41][22][38][36][40]. Although many studies have indicated that TiO_2 containing the mixture of anatase and rutile would display enhanced photocatalytic activity than that of pure phases. More precisely, the interaction between the two phases as a result of their different Fermi levels produces a synergistic effect that would reduce charge recombination [166][22][184][194][196]. For instance, Degussa (Evonik) P25, which is widely considered as a de facto standard in photocatalysis by TiO_2 consists of 80% anatase and 20% rutile [194][196][197]. In this regard, thermal spray processes are beneficial to produce TiO_2 coatings comprised of the mixture of the two phases, while the phase proportion can vary widely depending on the spray condition.

Interestingly, the phase content of samples C-7H_2 and D-3H_2 are close to Degussa P25, as discussed in XRD section. After polishing and heat treatment, a pronounced decrease in MB concentration was observed for sample D-3H_2 compared to other treated samples. It shows the significant role of the crystalline phase on the photocatalytic activity, while other influencing parameters are almost similar. Although the presence of the other affecting parameters such as higher surface area and oxygen deficiency caused an overall better photocatalytic performance of as-sprayed samples than their polished heat-treated counterparts.

4.3.3.1 Correlation between suspension plasma spray parameters and coating properties

In this research study, sub-stoichiometric TiO_{2-x} coatings were deposited at four different SPS conditions with different gas mixture proportions (Table 4.1). From the obtained results, it was observed that the concentration of the gas mixture played an important role in the coating properties and photocatalytic performance. Below, the effect of the SPS deposition parameters on the properties of the sub-stoichiometric TiO_{2-x} coatings is enlisted:

Structural and electronic properties: sub-stoichiometric TiO_{2-x} coatings deposited at four different conditions presented two crystallographic phases, anatase and rutile. As shown in Table 4.2, the higher the H_2 flow rates employed during the spraying process, the lower the anatase phase content presented in the as-sprayed coatings.
Given that the energy bandgap between rutile (E_g=3.0 eV) and anatase (E_g= 3.2 eV) phases is different, the presence of the predominant phase significantly influenced the electronic properties of the sprayed coating. As a result, as-sprayed coatings rich in anatase phase presented a higher energy bandgap (Table 4.4).

Microstructural properties: Since the concentration of H_2 in the gas mixture affects the evolution of the suspension droplets during spraying, coatings with different surface morphologies were achieved. According to Fig. 4.4, a high H_2 flow rate resulted in a large concentration of rounded bumps at the surface of sample A-15H_2, typically known as "*cauliflower-like surface morphology,*" while smoother surfaces were deposited at lower H_2 flow rates (samples C-7H_2 and D-3H_2). Moreover, there is a direct relation between the thickness of the as-sprayed coatings and H_2 flow rates. It is assumed that a higher H_2 flow rate resulted in a higher deposition efficiency in the plasma sprayed coatings.

Phase distribution: As shown in Fig. 4.5, the as-sprayed coatings were constituted of a bimodal microstructure of molten and non-molten particles. The molten regions presented both crystallographic phases (anatase and rutile), while un-melted areas were constituted of only the anatase phase. According to the results, lower plasma power resulted in coatings characterized by a larger quantity of un-melted areas with the same morphology and crystalline phase as the starting powder (D-3H_2). Contrarily, coating deposited at a higher plasma power presented a microstructure rich in molten particles (A-15H_2).

Chemical stoichiometry: The intense heating of the starting TiO_2 powder in the argon-hydrogen plasma jet has a strong effect on the coating stoichiometry. According to Fig. 4.12, stoichiometric TiO_2 powder changed to sub-stoichiometric TiO_{2-x} during plasma spraying in the as-sprayed coatings. Based on the results, the oxygen vacancy level increased by increasing the H_2 flow rate as a secondary gas in the plasma mixture with reductive properties.

Photocatalytic properties: The coating's properties were changed with the change of plasma spray parameters (especially hydrogen content), which affects the photocatalytic performance. As shown in Fig. 4.16, no direct correlation between the hydrogen flow rates and photocatalytic activity of the as-sprayed samples was found. While in the post-treated coatings with the same morphology and phase content, a better photocatalytic performance was observed for the coating produced at a lower H_2 flow rate (D-3H_2) due to the higher anatase content.

4.4 Conclusions

In this research work, the role of the crystalline phase on the photocatalytic activity of suspension plasma sprayed (SPS) TiO_2 coatings was systematically investigated. From the monitoring of the relation between plasma spraying conditions (hydrogen flow rates) and coating properties, it was concluded:

- Anatase and rutile crystallographic phases were presented in suspension plasma sprayed (SPS) TiO_{2-x} coatings, where the ratio of the phases in the as-sprayed coatings was determined by SPS gas mixture concentration. A gas mixture with low H_2 gas favors TiO_{2-x} coatings with large anatase phase concentration, while a gas mixture enriched with H_2 gas limits its concentration.
- Suspension plasma spray (Axial IIITM plasma torch) produces TiO_{2-x} coatings with a bimodal microstructure of molten and non-molten particles. The results of the SEM analysis presented the influential role of the SPS gas mixture on the coating's microstructures. Based on the results, coatings produced at lower H_2 flow rates showed a microstructure with large regions of non-molten particles (originated from unreacted feedstock powder). In comparison, coatings produced at higher H_2 flow rates presented a microstructure characterized by fully melted areas.
- Raman analysis determined from the bimodal microstructure of the coatings that molten particles present both crystallographic phases (rutile and anatase) while the un-melted regions are composed of fine particles based on anatase phase.
- An SPS gas mixture based on H_2 gas leads to oxygen deficiency on fully melted particles (during the spraying process), resulting in coatings with higher oxygen vacancy concentrations. Based on the results, the higher the hydrogen flow rates were, the higher the oxygen vacancies produced.

- Polished and heat-treated sprayed coatings did not show significant phase changes after heat treatment.
- All the coatings exhibited remarkable photocatalytic activity. However, the performance of as-sprayed coatings was significantly better than that of polished heat-treated counterparts, which might stem from the combination of phase composition and other influencing factors. While for as-sprayed coatings, no direct correlation between anatase content and their photocatalytic activity was ascertained, after polishing and heat treatment, sample D-3H_2 with the highest amount of anatase content presented the best activity.

Acknowledgments

The authors wish to acknowledge the Natural Sciences and Engineering Research Council of Canada (NSERC) for the financial support of this research through Canada Research Chairs and Discovery Grants Programs (Grant number: 950-228839).

Preface to Chapter 5.

In the previous chapter, it was demonstrated that suspension plasma spray (SPS) has the ability to produce nanostructure TiO_2 coatings with desirable oxygen vacancy and anatase phase content. Results confirmed that the combination of all the affecting parameters would define its ability to degrade the organic compounds in the as-sprayed coatings. While in post-treated coatings, anatase phase content was shown to be the desirable phase. The following chapter investigates the role of oxygen vacancy on the sub-stoichiometric TiO_2 coatings produced by SPS.

Chapter 5. An investigation on the photocatalytic activity of sub-stoichiometric TiO_{2-x} coatings produced by suspension plasma spray [2]

Abstract

To enhance the photocatalytic activity, sub-stoichiometric TiO_{2-x} films were coated on stainless steel substrates by Suspension Plasma Spraying. Because the TiO_2 particles are exposed to high temperature during deposition by plasma spray, TiO_{2-x} coating are typically produced. To achieve different levels of oxygen vacancies, as-sprayed TiO_{2-x} coatings were annealed at four different temperatures for 48 h in air. In this work, the degradation of methylene blue was performed to evaluate the photocatalytic activity under visible light. The results indicated that oxygen vacancy positively affects the photocatalytic activity of TiO_{2-x} by introducing some energy levels into the bandgap of titania. Moreover, these energy levels could act as traps for photo-excited holes and electrons, reducing the recombination rate of charges, thus improving the photocatalytic activity under the visible lamp. Additionally, coatings were analyzed by X-ray diffraction, confocal laser microscopy, scanning electron microscopy, Raman spectroscopy, thermogravimetric analysis, Fourier-transform infrared spectroscopy, and UV-visible spectroscopy.

Keywords: TiO_2, Sub-stoichiometric TiO_{2-x}, Photocatalytic activity, Suspension plasma spraying, Oxygen vacancies

5.1 Introduction

With the surge in environmental and energy-related concerns, enormous interest in semiconductor-based heterogeneous photocatalysis has prompted over the last decade [11][198]. Titanium dioxide (TiO_2) is an abundant, low-cost, chemically stable, and non-toxic material. TiO_2, as one of the most researched semiconductor materials, shows excellent technological properties and has extensive applications such as photocatalysts, dye-sensitized solar cells, sensor devices, membranes, and paints [14][15]. In photocatalysis, sunlight is used for remediation of pollutants with the degradation of highly toxic organic compounds; and for the conversion of solar energy to electric power with the production of hydrogen [11][12].

Fujishima and Honda revealed the powerful oxidizing potential of TiO_2 in the late 1960s at the University of Tokyo during their research work photo-electrochemical (PEC) solar cells [20]. Absorption of a photon with energy higher than the bandgap of TiO_2 can excite an electron from the valence to the conduction band and create an electron-hole pair which is of great

[2] This chapter has been published as a peer-reviewed article in the Journal of the European Ceramic Society, Hediyeh Khatibnezhad, Fabian Ambriz-Vargas, Fadhel Ben Ettouil, Christian Moreau, *Journal of the European Ceramic Society 41 (2021) 544-556.*

significance in producing oxidized radicals species which can degrade dyes into harmless products (H_2O and CO_2) in wastewater [20][193]. TiO_2 has three different polymorphs, anatase, rutile, and brookite. Although anatase has a larger bandgap (3.2 eV) than rutile (3 eV), it has slower recombination of photo-generated electron-hole pairs and higher adsorption affinity toward organic compounds, which makes it a desirable photocatalyst [22]. It has been indicated that anatase will irreversibly change to rutile at temperature around 600 ºC. However, the reported temperature can be varied in the range 400-1200 ºC depending on some factors such as particle size, surface area, atmosphere, impurities, raw materials and processing methods [37].

The large bandgap of TiO_2 has limited its application to regions under the illumination of UV-light which reduce its ability to use the main part of the solar spectrum [23]. Low photo-quantum efficiency caused by the high recombination rate of photo-generated electron-hole pair is considered as another main problem [24]. One promising method to overcome this issue is by creating energy levels within the bandgap to adequately shift the conduction band (CB) and/or the valence band (VB) so that photons of lower energy can excite electrons. These energy levels also can act as a trap for reducing the recombination rate [3]. It has been reported that the reduced form of titania (TiO_{2-x}) acts as an efficient photocatalyst. The insertion of oxygen vacancies in the anatase structure induces a band of electronic states just below the conduction band, starting to overlap with the conduction band for large vacancy concentrations. The moving of the optical absorption to longer wavelengths nearby to the visible region with decreasing the oxygen concentration confirmed the theoretical prediction of the creation of a new band below the conduction band. Suggesting that these vacancy-induced bands of electronic states are responsible for increasing photocatalytic properties of the TiO_{2-x} films [62][63][64][65].

TiO_2 in powder form has a prominent photocatalytic performance compared to its alternatives due to its higher surface area, which is of significance benefit for photocatalytic application. However, TiO_2 coatings are more convenient as they can be separated from the liquid or gas easily [35]. TiO_2 coatings have been produced by various techniques; among them, plasma spray deposition appears an economic process for industrial scale-up. There are other advantages, such as producing a wide variety of coatings with high quality, using a different range of particle size, and flexibility, which allows using various substrates with different shapes [114]. Suspension plasma spray (SPS) offers several advantages over conventional techniques such as the direct use of finely dispersed powders and the production of nanostructured coatings, which is of great importance in photocatalytic activity [43].

Despite all the achievements and progress in TiO_2 coatings for the photocatalytic applications, there is very limited research on the effect of oxygen deficiencies on the photocatalytic properties of the plasma-sprayed TiO_2 coatings because of its challenging limitations, and it has not been reviewed comprehensively to date. In the present work, a water-based suspension of fine TiO_2 particles was externally injected in a plasma torch to obtain photocatalytic active sub-stoichiometric titania (TiO_{2-x}) coatings. After coating deposition, heat treatments in air were applied at different temperatures in the range of 400-550 ºC to vary the level of oxygen vacancies. The main purpose of this work is to investigate the role of the oxygen deficiency on the photocatalytic activity of the suspension plasma sprayed TiO_2 coatings by keeping almost constant most of the other influencing parameters on the photocatalytic efficiency.

5.2 Materials and methodology

5.2.1 Suspension preparation and injection method

Sub-stoichiometric TiO_{2-x} coatings were manufactured by suspension plasma spray (SPS) method with a 3 MB plasma torch (Oerlikon Metco, Switzerland). For feedstock, the suspension containing 20 wt. % commercial submicron-sized TiO_2 powder (TKB Trading, Oakland, CA) in deionized distilled water was prepared by magnetic stirring for 30 min while dispersing the powder with a 50 W sonicator. No dispersing agent was used in the suspension preparation. A SEM micrograph of the starting TiO_2 powder is shown in Fig. 5.1 along with the XRD pattern, which shows anatase as the only detected phase. The particle size distribution of the aqueous suspension obtained by a Spraytec unit (Malvern Instruments, UK) was d_{10}=0.21 µm, d_{50}=0.39 µm, d_{90}=0.75 µm, is shown in Fig. 5.1.

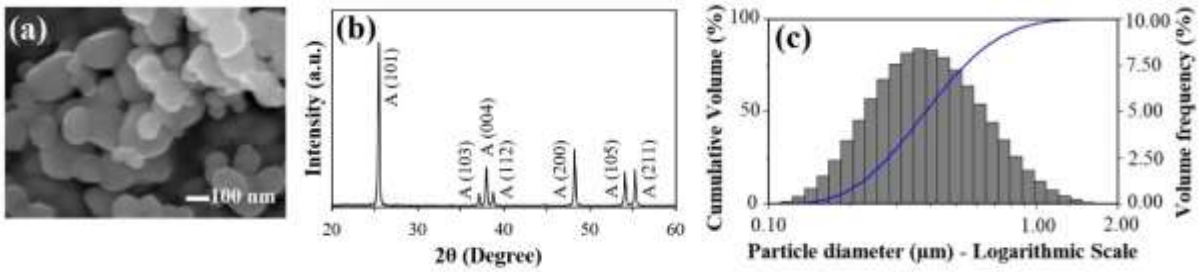

Figure 5. 1 (a) SEM micrograph and (b) XRD pattern of the feedstock TiO_2 powder, (c) particle size distribution of the aqueous suspension (d_{50}=0.39 µm) used in this study.

The water-based TiO_2 suspension was radially injected into the plasma plume using a peristaltic pump, at a feed rate of about 30 ml/min. Flat stainless steel coupons with dimensions of 25× 25× 5 mm^3 were used as substrates. Substrates were grit-blasted by 80 grit alumina particles and ultrasonically cleaned in acetone before deposition. Coatings were deposited using 40 consecutive passes of a spray raster covering the entire surface of the coupons with a linear torch velocity of 1 m/s and a 3 mm overlay distance. Details of operating parameters are summarized in Table 5.1.

Table 5. 1 SPS parameters used to deposit TiO_{2-x} coatings on the stainless steel substrates.

Plasma gun	Ar flow rate (slpm)	H_2 flow rate (slpm)	Current (A)	Power (KW)	Stand-off distance (mm)
3MB	45	7	450	28	40

Substrate temperature was monitored by A320 ThermoVision IR camera (FLIR Systems, US) during spraying. The temperature was maintained below 180 °C by using a water-cooled substrate holder coupled with an air jet directed toward the substrates during spraying. According to literature, if we could keep our substrate as cold as possible, higher anatase content would be obtained [42], and theoretically, there might be less chance for oxygen to be recaptured during passes to produce sub-stoichiometric TiO_{2-x} coatings. Moreover, for better repeatability and consistency of the experiment, a Coriolis flowmeter (Proline Promass 83, Endress+Hauser, Switzerland) was used to monitor the suspension feed rate and density of the suspension. Substrates were preheated by using the plasma torch to around 150 °C immediately prior to coating deposition. The intense heating and melting of the starting TiO_2 powder in the plasma jet could

favorably generate oxygen deficiency, which can be promoted by increasing hydrogen as a secondary gas in the plasma mixture due to its reductive properties. Also, oxygen vacancy level has been associated with the in-flight particle temperature of the particles. As a result, highly stoichiometric TiO_2 powder would change to sub-stoichiometric TiO_{2-x} (n-type semiconductor) during plasma spraying in the as-sprayed coatings. Accordingly, a color shift could be observed from yellowish-white to dark-grey, depending on the amount of oxygen loss and because of Ti^{3+} ions' concentration [62][134][135][45].

In order to obtain TiO_2 coatings with different oxygen contents, as-sprayed coatings were heat treated at various temperatures (400, 450, 500, 550 °C) in air for 48 hours in a tubular furnace. Instead of changing plasma spray condition, (especially hydrogen content) which could change all the coating's properties, we preferred to vary oxygen content by heat treatment at relatively low temperatures, to avoid major changes in the other effective parameters (porosity, crystalline phase, and etc.) on the photocatalytic efficiency.

5.2.2 Characterization and evaluation

Phase analysis of the TiO_2 coatings, before and after heat treatment, was studied by the X-ray diffraction (XRD) technique on an X'Pert Pro; PANalytical (Philips, Netherlands) with Cu Kα radiation and a step size of 0.02° in a range of 20-80°. Phase content was quantified by Rietveld refinement analysis using the Pearson's Crystal Data (PCD)-crystal structure database for inorganic compounds. For decreasing any statistical error, which may reduce our accuracy, the same coupons were used for XRD analysis before and after heat treatment. Preferred orientation is also an issue, which may lead to altered XRD relative peak intensities, so XRD precision was investigated through repeating this analysis for the one sample. A confocal laser microscope (LEXT OLS4000, Olympus, Japan) was used to study the three-dimensional surface topography and surface roughness of the coatings. The 3D maps of the surface of the coatings were generated by digitally stitching 25 single images (5 by 5) together to have enough area to be considered an average representation of the coating's surface. Amongst the different surface roughness parameters, arithmetic average surface roughness (Ra) has been widely used for measuring surface roughness. A field emission scanning electron microscope (FESEM JSM 7600TFE, JEOL, Japan) with an accelerating voltage of 15 kV and equipped with an energy dispersive X-ray spectroscopy detector (EDXS, Oxford Instruments, X-Max 80) was used to evaluate the surface morphology, microstructure and thickness of the coatings. Raman analysis on the polished coating cross-section was performed using a Raman spectrometer (inVia Reflex, UK) with a laser wavelength of 532 nm (spot size ~2 μm), objective magnification 50 x, and 10 s exposure time. The system was calibrated by using a silicon reference. After scanning the coating surface with the laser, a small fraction of the light is inelastically scattered due to the molecular vibration caused by interaction with the laser while the large part of the light is scattered elastically (Rayleigh light). These characteristic bond vibrations are used for the identification of the chemical and crystal state [86]. Measurements were conducted at a low excitation power (<10 mW) to avoid the heating effect of laser and scanning was performed from 100 to 1000 cm^{-1} wavenumber shift. Moreover, surface mapping was studied by scanning 1050 points in a 60×70 μm surface area.

To measure the stoichiometry of the starting powder and coatings, thermogravimetric analysis (TGA) was conducted by using a thermal balance (TGA Q500/Discovery MS, TA Instruments, US) while heating all samples to 1000 °C at 5 °C /min in air and holding them for 90 min to re-oxidizing sub-stoichiometric TiO_{2-x} to almost fully oxidized one. Before TGA analysis,

all samples were kept at 150 °C for 1 hour to make them fully dried. Considering the following re-oxidizing reaction [151][152][153]:

$$TiO_{2-x} + \frac{x}{2} O_2 \rightarrow TiO_2 \quad (5.1)$$

the non-stoichiometric number *x* was calculated by the sample weight increment according to Eq. 5.2 [151]:

$$x = \frac{\Delta w}{w_{mol}^{O}} \frac{(2W_{mol}^{O} + W_{mol}^{Ti})}{(W_0 + \Delta W)} \quad (5.2)$$

where ΔW is the weight increment, W_0 is the initial weight of the samples, W_{mol}^{O} and W_{mol}^{Ti} are the molar weight of oxygen and titanium.

The presence of adsorbed species on the sample surfaces was characterized from infrared spectra in the range of 4000-600 cm^{-1} using an ATR-FTIR (Attenuated Total Reflectance-Fourier transform infrared) spectrometer (Nicolet 6700 / Smart iTR, Thermo Scientific, US).

The optical absorption spectra of the starting powder and coatings in the range of 340 to 600 nm were determined with 1-nm resolution by a UV-Visible-NIR spectrometer (Lambda 750, Perkin Elmer, US) to measure the bandgap energy of the coatings according to Eqs. 5.3, and 5.4 [36][154] :

$$\alpha h\upsilon = A(h\upsilon - E_g)^n \quad (5.3)$$

$$E_{photon}(eV) = h\upsilon = \frac{1239}{\lambda} \quad (5.4)$$

where λ is wavelength, A is a constant given by the slope of the linear region in the $(\alpha h\nu)^{1/n}$ –hν plot, E_g is the optical energy gap of the material calculated from the extrapolation of the straight-line portion of the mentioned plot, and n is the characteristic of the optical transition process type, which is 2.0 and 0.5 for indirect and direct allowed optical transition, respectively.

5.2.3 Evaluation of photocatalytic activity

Organic dyes, as a recognized source of pollution released by the dye industry into wastewater, are widely used as a test pollutant for photocatalytic activity [25]. In this work, the photocatalytic performance of TiO_2 coatings was evaluated by the decoloring rate of methylene blue, MB ($C_{16}H_{18}CIN_3S$), under visible light irradiation. In this regard, one coated sample (with a surface area of 6.25 cm^2) was placed inside the testing cell containing 30 mL MB solution at an initial concentration of 2×10^{-5} M. Visible light irradiation was provided by two xenon arc lamps with an input light power of 35W each. During the test, a fan was used to avoid heating the samples by light irradiation. The schematic diagram of the experimental setup is shown in Fig. 5.2 (a). A small quantity of the solution was removed every 30 min to monitor the decomposition of MB solution by using a UV-vis spectrophotometer (evolution 201, Thermo Scientific, US) at a fixed wavelength of 664 nm related to the maximum absorbance of the MB (Fig. 5.2 (b)). Before irradiation, coatings immersed in the MB solution was kept in the dark for 60 min to complete the adsorption of MB molecules on the coating surface, after which time the MB concentration was determined as C_0. The irradiation of the MB solution without TiO_2 coating was conducted as a blank test to evaluate the degradation of the MB due to the photolysis phenomenon. The concentration changes of MB was determined by assuming pseudo first order kinetics using Eq. 5.5 [3].

$$ln\left(\frac{C_0}{C}\right) = kt \quad (5.5)$$

Where C_0 is the concentration of MB after 60 min in the dark, C is the MB concentration at each time interval, k is the apparent rate constant, and t is the irradiation time. The degradation percentage was also measured according to Eq. 5.6 [35].

$$Degradation\ (\%) = \frac{(C_0 - C)}{C_0} \times 100 \quad (5.6)$$

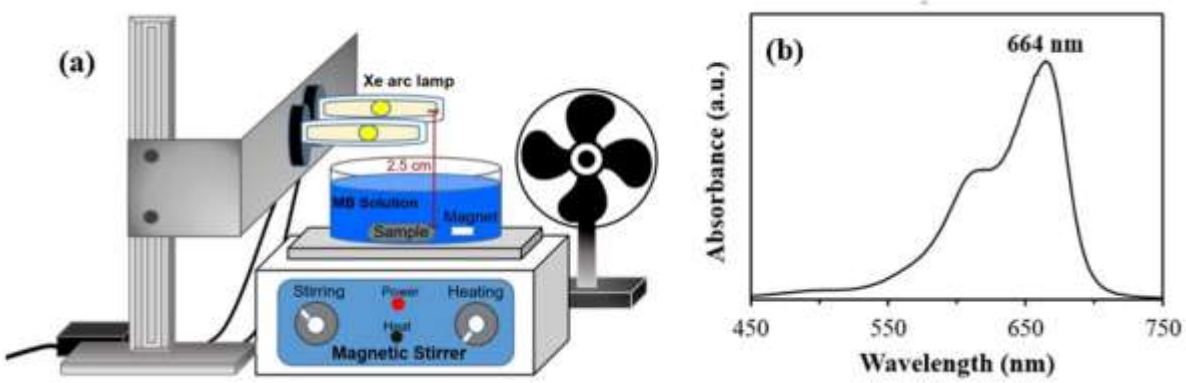

Figure 5. 2 (a) Schematic diagram of the photocatalytic setup for the visible lamp, and (b) UV-Vis absorption spectrum of the MB at 2×10^{-5} M concentration.

5.3 Results

5.3.1 Phase composition

Some previous works have reported irreversible phase transformation of TiO_2 feedstock from anatase to rutile during plasma spraying, depending on the melting level of the particles [133][44]. For the photocatalytic activity applications, the anatase phase plays an important role [134], and literature shows the relation of anatase content to the substrate temperate [42]. In order to preserve the anatase phase in the sprayed coatings, we kept the substrate temperature at a low temperature (~180 ºC) during deposition. As it can be seen in Table 5.2, the anatase content was reduced to ~30 wt% in as-sprayed coatings from 100 wt% in the starting powder.

There is a range value of transition temperatures of anatase to rutile reported in the literature due to its dependency to a number of factors. However, for a fine powder of high purity, the phase transformation temperature was reported to occur in the range of 600 to 700 °C [37] but the existence of impurities and oxygen vacancies can affect this temperature [199]. In this study, samples were heat treated at four different temperatures (400, 450, 500, 550 °C) lower than the expected transition temperature with the objective to maintain the anatase phase unchanged after thermal treatment. The XRD patterns of TiO_2 coatings in Fig. 5.3 and the derived information in Table 5.2 indicate that, after heat treatment, there is a small decrease (~2-6%) of the anatase content in the coatings. According to literature, oxygen vacancies favor phase transformation to rutile by accelerating atomic diffusion and lowering the energy required [137]. After heat treatment at higher temperatures, reabsorption of oxygen atoms into the TiO_2 lattice might cause some micro-strains, which lead to the broadening of the peaks and reducing the crystallite size.

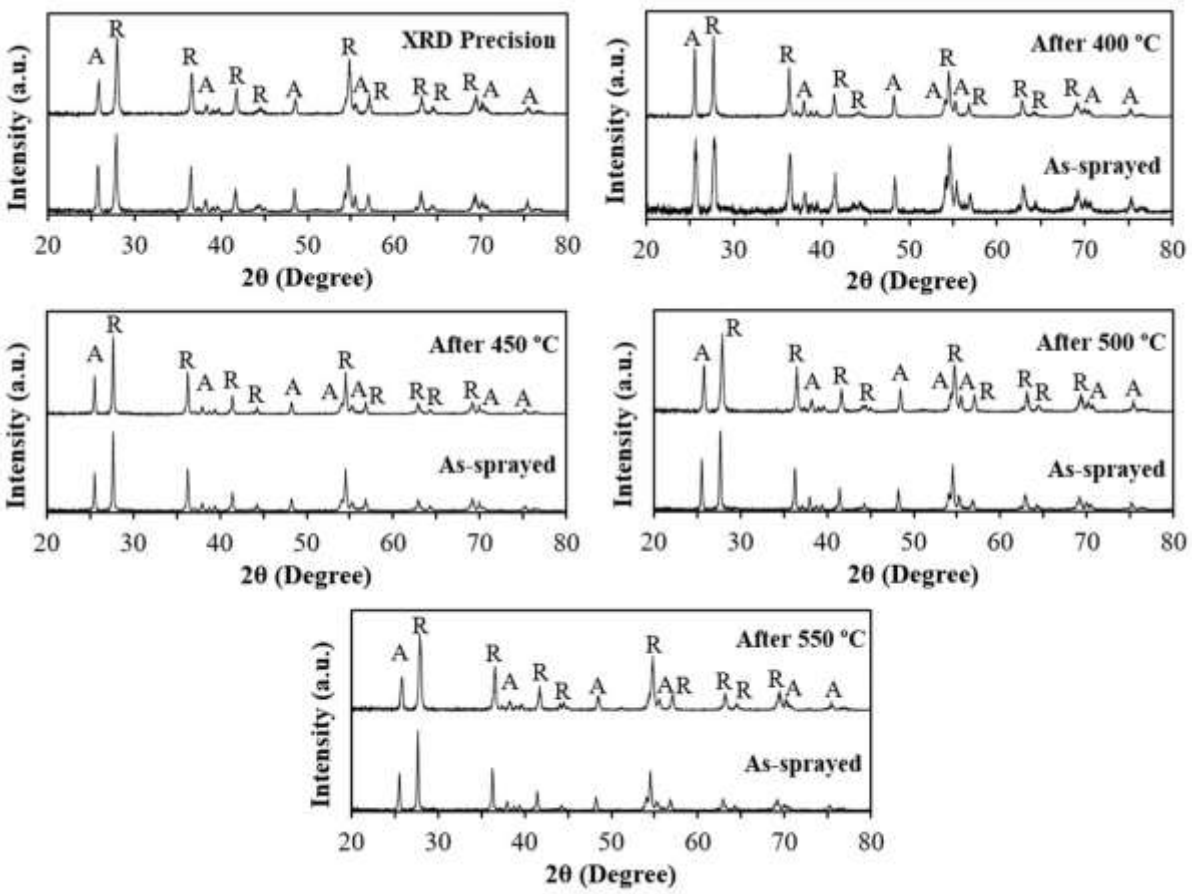

Figure 5. 3 XRD pattern of the TiO_2 coatings before and after heat treatment, where A denotes the anatase phase and R the rutile phase.

Table 5. 2 Phase content and crystallite size of the coatings, derived from Fig. 5.3.

Sample		Anatase	Rutile	Crystallite size (nm)	
				Anatase	Rutile
Precision	1	29	71	49	36
	Repeat 1	22	78	40	34
400 ºC	As-sprayed	36	64	36	31
	After 400	34	66	68	44
450 ºC	As-sprayed	27	73	64	66
	After 450	22	78	42	35
500 ºC	As-sprayed	33	67	68	62
	After 500	29	71	49	36
550 ºC	As-sprayed	29	71	62	60
	After 550	23	77	41	35

5.3.2 Coating roughness and microstructure

Based on Fig. 5.4 and Table 5.3, heat treatment at all temperatures did not have any impact on the surface roughness of the samples, as they are similar.

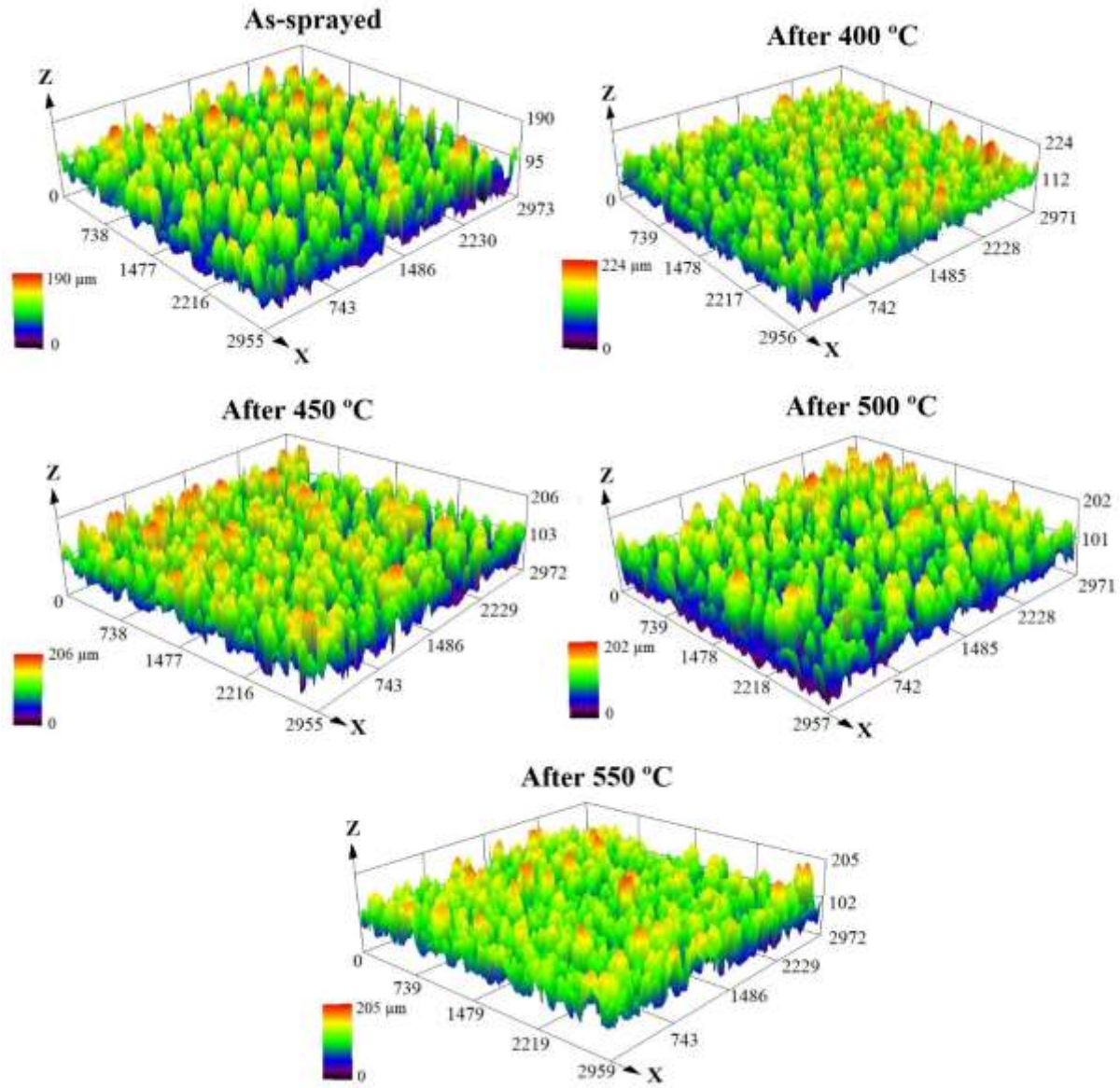

Figure 5. 4 3D images of the top surfaces of the coating achieved by the confocal laser microscope.

Table 5. 3 Arithmetic average surface roughness (R_a) of the coatings before and after heat treatment.

Surface roughness parameter	As-sprayed	After 400 ºC	After 450 ºC	After 500 ºC	After 550 ºC
R_a (µm)	23.5 ± 1.1	23.3 ± 0.9	27.0 ± 1	23.5 ± 1.3	22.4 ± 0.6

The SEM micrographs of the coating top surfaces and cross-sections before and after heat treatment are shown in Figs. 5.5 and 5.6. The coating microstructure is one of the important parameters affecting the photocatalytic activity, which remained almost unchanged after heat

treatment. In all top surface images, distinctive rounded bumps with size ranging between 50-150 μm are observed. This surface profile, so-called cauliflower-like cluster formation, can be of great benefit for photocatalytic performance by increasing the reaction area for degradation of MB solution. Cross-sectional microstructures of the coatings (Fig. 5.6) show the typical columnar structure observed in SPS coatings due to fine droplet size and their shallow impact angle (shadow effect) [127], which created some bands of porosity between the columns. Due to their small momentum, fine particles can travel almost parallel to the substrate surface by following the plasma gas flow close to the substrate. Therefore, they attach on the sides of the asperities on the surface, and coatings grow in two sides, laterally and vertically, forming a porous region by shadowing the beneath surfaces from the impact of the new particles [128]. Also, there were some vertical cracks in the coatings caused by relaxation stresses [36]. Figure 5.6 confirms that the as-sprayed coatings were firmly bonded to the stainless steel substrate with a crack free interface, but delamination happened after heat treatment at all temperatures. This delamination presumably resulted from the difference in thermal expansion coefficient between the metallic substrate and ceramic coating, which can create important thermal stress during heating and cooling in the furnace [200] ($\alpha_{\text{stainless steel}} = 18\times10^{-6}$ (K^{-1})[201], and $\alpha_{TiO2} = 9.4\times10^{-6}$ (K^{-1})[202]).

The micrographs illustrated in Figs. 5.6 and 5.7 present a bimodal microstructure, light and dark grey areas. At higher magnification (Fig. 5.8), the brighter areas appear as dense zones of fully melted particles, while darker areas are revealed to be porous filled with agglomerated un-melted or partially melted fine particles with a size close to that of the starting powder (~100 nm). Based on back-scattered electron (BSE) images and the fact that we have only titanium and oxygen in the structure, brighter and darker regions should have different mean atomic numbers, which could stem from either a significant presence of porosity or density variation. Since rutile has around 10% higher density compared to anatase, it is probable that the molten area mainly consists of rutile [203].

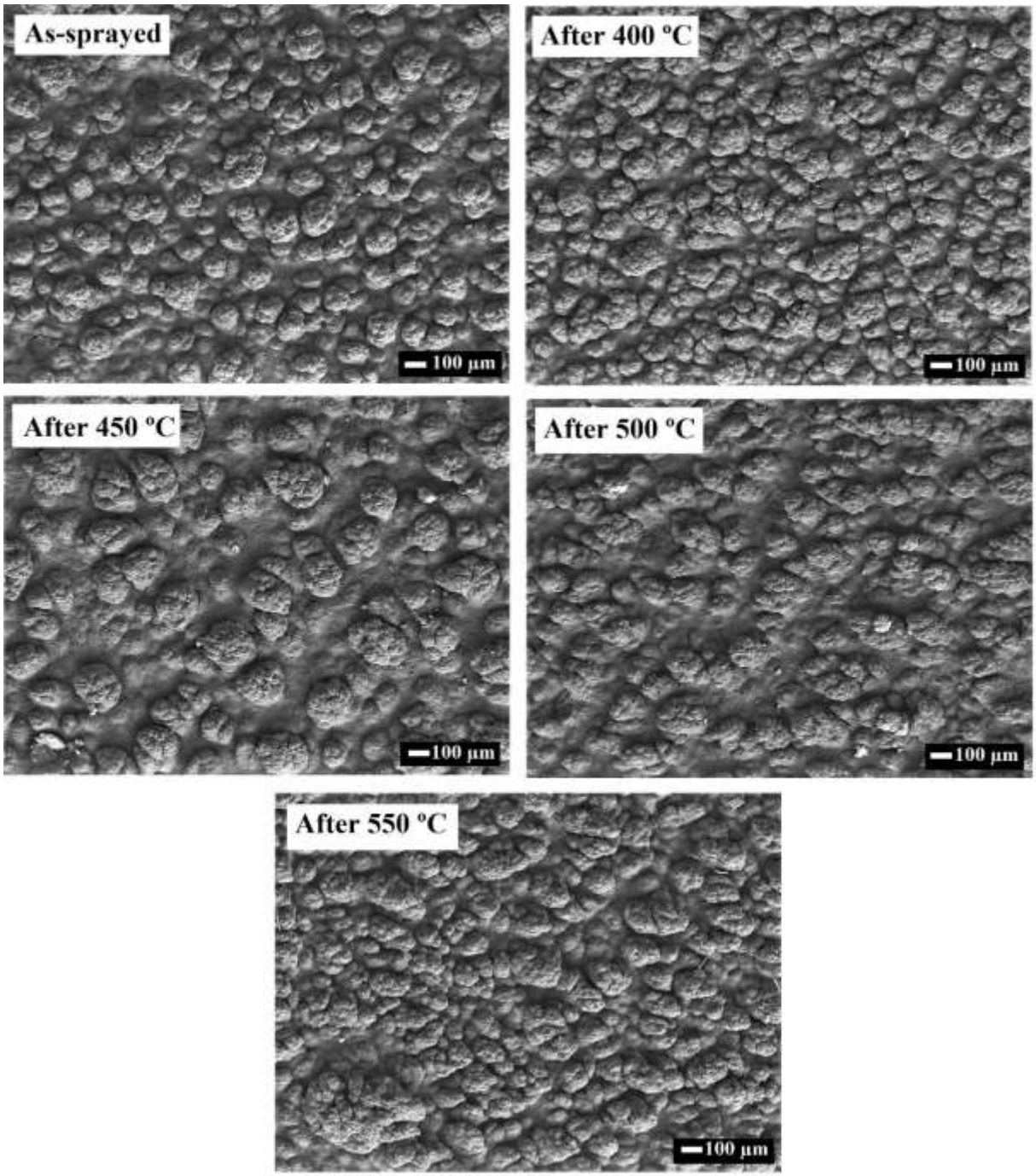

Figure 5. 5 Secondary electron (SE) FESEM micrographs of top surfaces of as-sprayed and after heat treatment coatings at different temperatures.

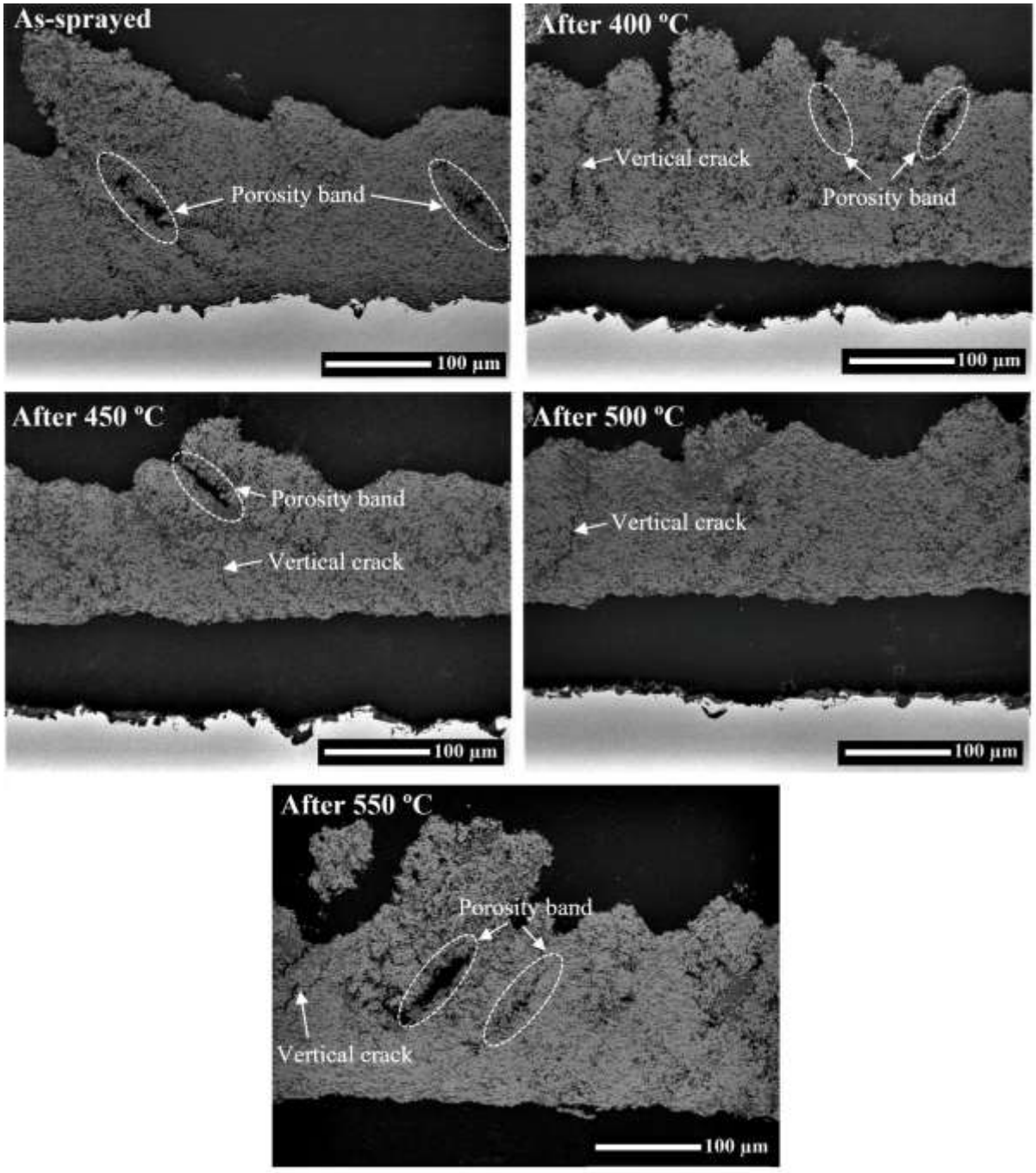

Figure 5. 6 BSE FESEM micrographs of cross-sections of as-sprayed and after heat treatment coatings at different temperatures.

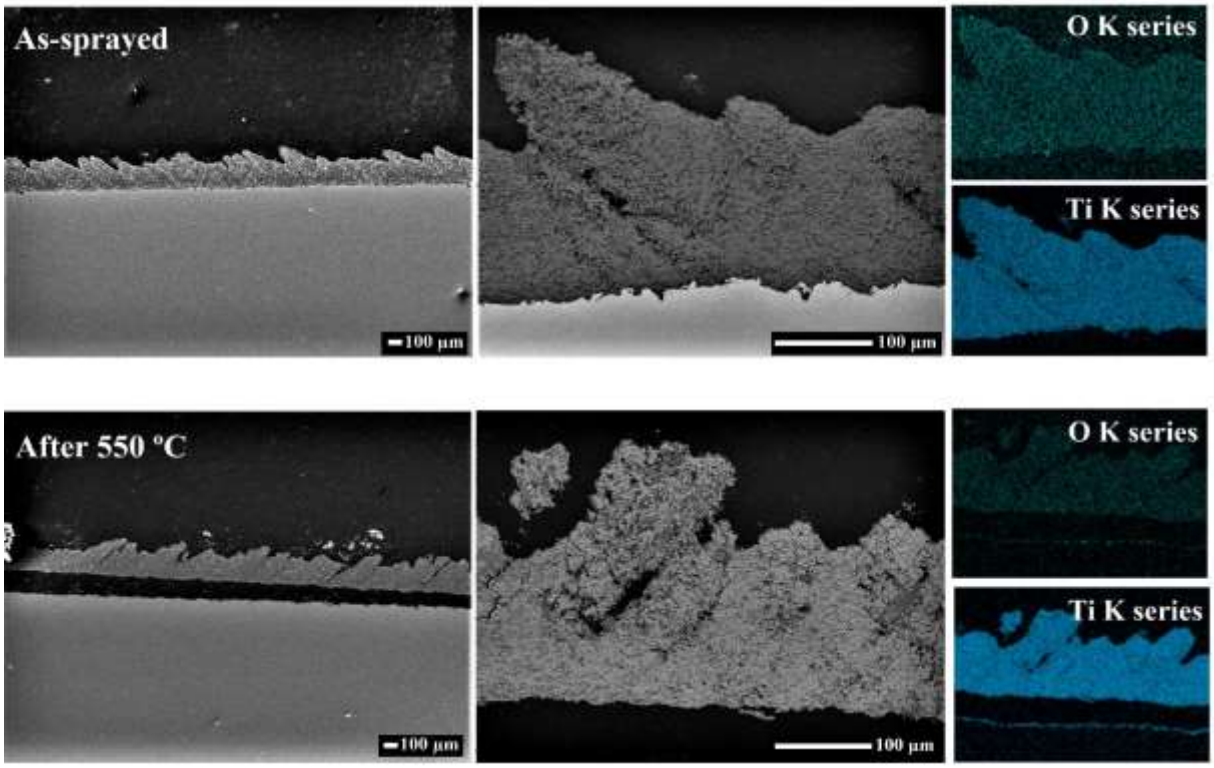

Figure 5. 7 Cross-section FESEM micrographs of as-sprayed and after 550 ºC heat treatment coatings from low to higher magnification with EDXS mapping.

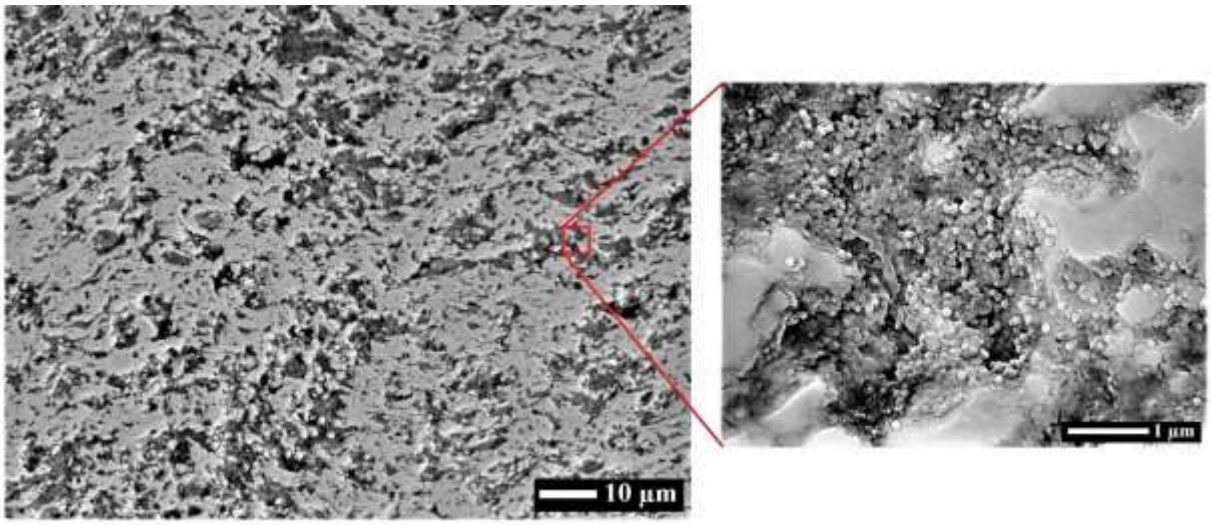

Figure 5. 8 High-magnification BSE FESEM images of molten and of non-molten areas for as-sprayed coating.

Further investigation has been performed on the selected coatings using Raman spectroscopy to identify the presence of each crystalline phase in the molten and non-molten areas. This technique is a rapid way of identifying surface crystal structure, which has been widely employed to discern anatase and rutile polymorphs in the TiO_2 coatings. It has the advantages of higher sensitivity and higher spatial resolution than XRD to indicate nanoscale phases of coatings with mapping capability [37][135][172]. Raman spectra of the bright dense and porous dark regions of as-sprayed and after 550 ºC heat treatment coatings are shown in Fig. 5.9, in which the

presence of sharp peaks is a sign of good crystalline quality. According to the literature, active modes for anatase present six peaks at 144, 197, 399, 513, 519, and 639 cm^{-1}, while rutile shows four characteristic peaks at 143, 236, 447 and 613 cm^{-1} [172][179][204]. In Fig. 5.9, there was an overlap between the peaks located at 513 and 519 $cm^{-1,}$ and Raman spectrometer presented just one band.

According to Figs. 5.9 and 5.10, dark regions in as-sprayed sample only show anatase peaks. As shown in Fig. 5.8, these dark regions are composed of small particles that have the same morphology and size than the starting powder. From these observations, it can be concluded that the dark regions are essentially composed of particles coming from starting powder that were not melted during spraying and were imbedded in the deposited coatings. The presence of these un-melted particles could be attributed to the relative high vaporization enthalpy of water as the solvent (2.3×10^6 J kg^{-1}), so the heat transfer to the particles could be reduced [183]. On the other hand, bright regions related to dense zones of fully melted particles present of both anatase and rutile phases. Although, fully melted areas are usually attributed to rutile [181], there are some anatase phases that can be formed during solidification depending on the nucleation's free energy, and interfacial energy between solid and liquid phase [44]. From the thermodynamic point of view, rutile is the stable phase of TiO_2 at all temperatures and pressures due to its lower free energy [37]. In a rapid solidification condition, rutile nucleates at a temperature above 0.88 T_m (1870 K) until the melting point (T_m=2130 K), while metastable anatase possibly nucleates from the liquid particles at an undercooling temperature below of 0.88 T_m [43][42][44]. Since in the thermal spray deposition, TiO_2 coating is formed under non-equilibrium, rapid quenching conditions [45], anatase recrystallization may occur in the molten area. The same peaks are present in the spectrum of the molten area in as-sprayed and after heat treatment coatings. However, some characteristic peaks related to rutile phase was detected in the dark grey region of after 550 ºC coating, which shows the initiation of phase transformation in these regions (Fig. 5.9). These results confirm minor phase changes after heat treatment studied by XRD analysis (section 5.3.1).

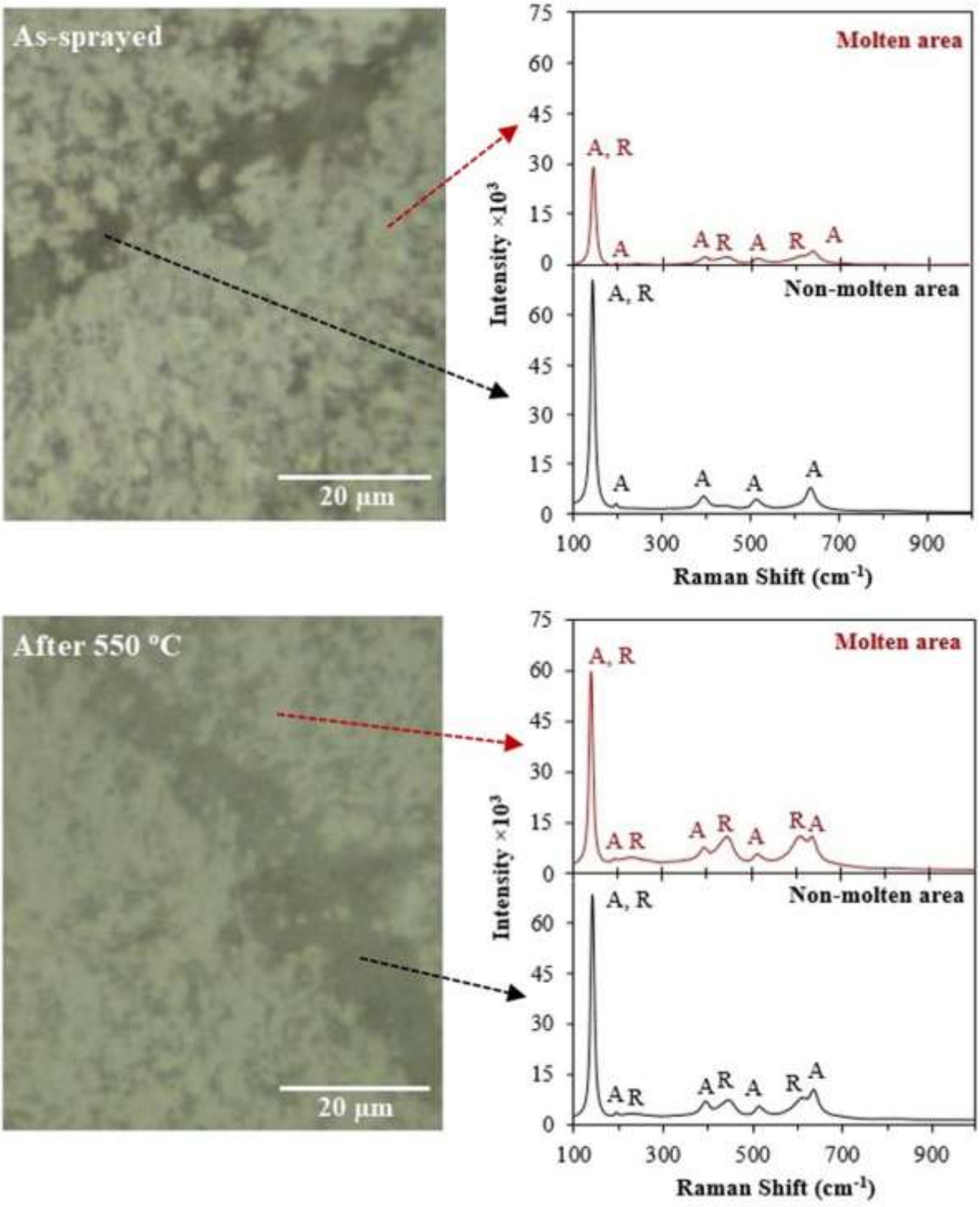

Figure 5. 9 Raman spectra results in the dark (non-molten) and bright (molten) regions for as-sprayed and after 550 ºC samples, which A denotes the anatase phase and R the rutile phase.

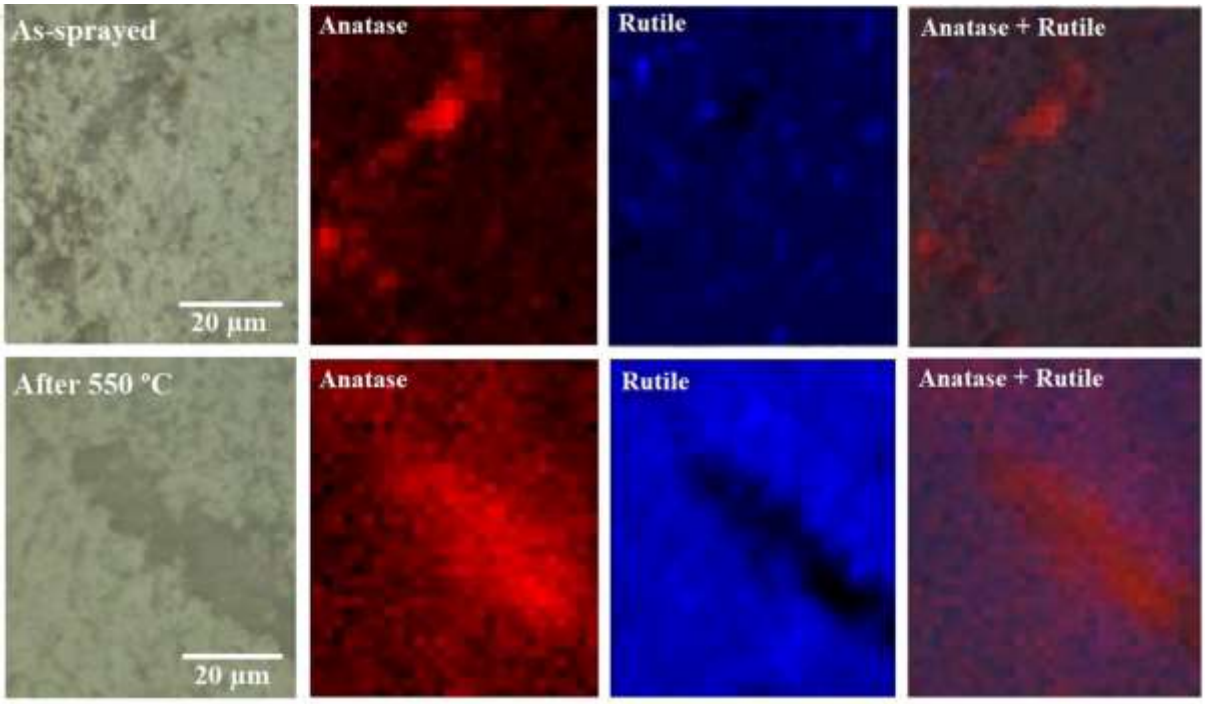

Figure 5. 10 Raman maps of the spatial distribution of characteristic Raman peaks for as-sprayed and after 550 ºC samples, where red color corresponds to anatase peak located at 197 cm^{-1}, and blue color represents rutile peak at 447 cm^{-1}.

Moreover, it has been found in several works that fully oxidized TiO_2 shows Raman peaks with higher intensity compared to sub-stoichiometric TiO_{2-x}. This attenuation of Raman peaks in TiO_{2-x} was attributed to the oxygen deficiency and not to any internal stress or grain size effects [205][206]. According to the literature, the intensity of the Raman scattered light depends on the optical properties of the material since the scattering cross-section depends on the material's optical constants [205], and physical and structural properties of the TiO_2 system that change with deviations from stoichiometric TiO_2 [207]. As seen in Figs. 5.9 and 5.10, the Raman peak intensity in the molten areas of the as-sprayed coating is much lower than after heat treatment, while there was almost no intensity change in non-molten area in the same samples. These results suggest that the fully melted particles lost some oxygen during plasma spraying leading to the formation of re-solidified sub-stoichiometric titania. Conversely, the un-melted particles found in the dark areas in the coating cross-sections remained stoichiometric. Therefore, after heat treatment at 550 ºC, the peak intensity changed only in the coating molten areas due to the recapture of oxygen during thermal treatment raising the level of oxygen content in these regions.

5.3.3 Oxygen content measurement by TGA

Figure 5.11 is shown the color shift of the coatings as sprayed and after heat treatments. The color changed from dark to light grey in coatings heated at 550 ºC due to O_2 recapturing. TGA results of TiO_2 samples are shown in Fig. 5.12 while they were heated to 1000 ºC at a rate of 5 °C /min in air and then hold that that temperature for 90 min to almost fully re-oxidize the sub-stoichiometric TiO_{2-x}. According to these results, a significant proportion of weight percentage increased during the initial heating process, and after around 300 min, the weight was almost unchanged, indicating that the heating temperature and holding time were sufficient to fully

oxidize sub-stoichiometric titania coatings. The calculated stoichiometry of the samples based on their weight gain is given in the figure legend. As can be seen, the as-sprayed sample shows the lowest amount of oxygen content ($TiO_{1.941}$), which absorbed oxygen during heat treatment to reach almost fully oxidized TiO_2 at higher temperature. The stoichiometry of the as-sprayed sample is similar to that of samples treated at 950 ºC in the pure H_2 atmosphere for 1h as reported by Tsuyumoto et al. [189] showing that plasma spraying appears a more effective, safer, and faster way to produce sub-stoichiometric TiO_{2-x}.

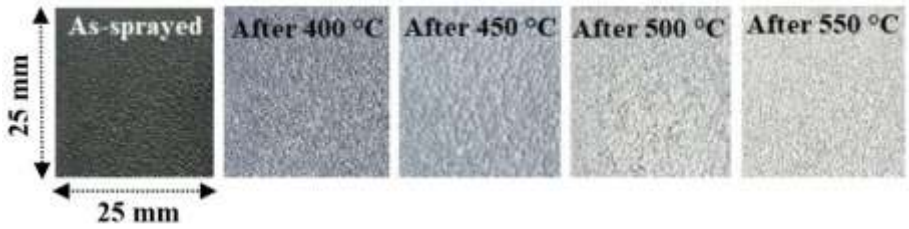

Figure 5. 11 The color change of the TiO_2 coatings before and after heat treatment due to oxygen recapture.

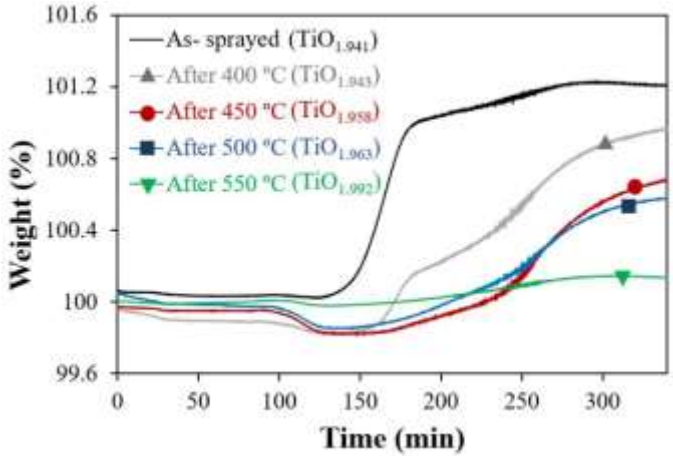

Figure 5. 12 Weight percent change during heating of TiO_2 coatings in the air to 1000 °C and holding in that temperature for 90 min. The corresponding stoichiometry for each sample is indicated in the legend.

5.3.4 Infrared spectroscopy

Figure 5.13 presents the ATR-FTIR spectra of the coatings before and after heat treatment at different temperatures in the range of 4000-600 cm^{-1}. Usually OH stretching modes related to the physisorbed molecular water show peaks located at 3400 cm^{-1}. Also, OH bending modes arise from the surface of TiO_2 and corresponds hydroxyl groups exhibit peaks located at 1600 cm^{-1}[35][208], which are negligible in our coatings. Literature suggests that the presence of weakly adsorbed water could negatively affect the photocatalytic performance of TiO_2 coatings for degradation of dye solution, while the existence of hydroxylation on the photocatalyst's surface is of great importance for its efficiency [36]. The bands detected between 2400- 2300 cm^{-1} and 3000-2800 cm^{-1} could be attributed to CO_2 molecules from the air and organic contaminants, respectively. Also, the intense broad band below 1200 cm^{-1} is assigned to Ti-O-Ti vibrations [36][183]. Fujishima et al. [20] indicated that oxygen vacancies could dissociate water molecules to produce two adsorbed OH groups per initial vacancies on the surface of the sub-stoichiometric TiO_{2-x} photocatalyst. Therefore, according to the TGA results, although we expected more intense

band related to OH groups in the ATR-FTIR spectrum of as-sprayed sample, which contains the highest amount of oxygen vacancies, all samples (before and after heat treatment) show almost the same peak intensities that could be attributed to the ATR-FTIR threshold.

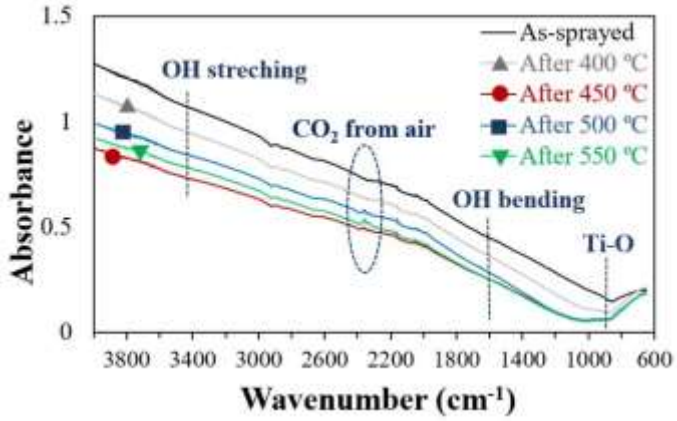

Figure 5. 13 ATR-FTIR spectra of TiO_2 coatings before and after heat treatment.

5.3.5 Optical properties

Since the photocatalytic activity strongly depends on the optical response of a semiconductor, optical properties of our samples were studied using a UV-Vis spectrophotometer. The UV-visible absorption spectra of all coatings (before and after heat treatment) and the starting TiO_2 powder are shown in Fig. 5.14. A shift of the absorption edge to the longer wavelength toward the visible range was observed for all coatings compared to the TiO_2 starting powder. In semiconductors, any absorption edge shift is attributed to a change in the bandgap [35], and these results indicate that oxygen vacancies could effectively decrease the titania bandgap. Direct and indirect bandgap of the coatings derived from extrapolating the straight-line portion of the $(\alpha h\nu)^2$-$h\nu$ and $(\alpha h\nu)^{1/2}$-$h\nu$ plots are shown in Fig. 5.14 and Table 5.4. The coatings showed different indirect band energies and almost the same direct bandgap. Among the two types of electron transitions from the valence band to the conduction band, indirect bandgap is mostly found in anatase, whereas direct bandgap is considered for rutile [38]. While, in the direct bandgap, electrons are ejected directly from the valance band maximum to the conduction band minimum; a momentum change is needed for the indirect bandgap transition resulting in an increment of the charge carrier lifetime in anatase compared to that of rutile. This longer lifetime makes anatase more efficient for photocatalytic applications as a larger number of the photo-generated electron-holes pairs are available to participate in surface reactions [22][36][38]. According to our results, there is almost no difference in the absorption of all coatings in the UV range, whereas absorption is increasing with decreasing oxygen content in the visible range. Actually, the as-sprayed sample shows the highest absorption and the smallest indirect bandgap in this region. Theoretical prediction suggested the formation of a new localized state below the conduction band resulting from the presence of oxygen vacancies in the TiO_2 lattice (considered as self-doped TiO_2), causing an effective decrease in the bandgap [138]. It also has been indicated that electron excitation from the valance band to the conduction band would be facilitated by narrowing bandgap and resulting in better photocatalytic performance [209].

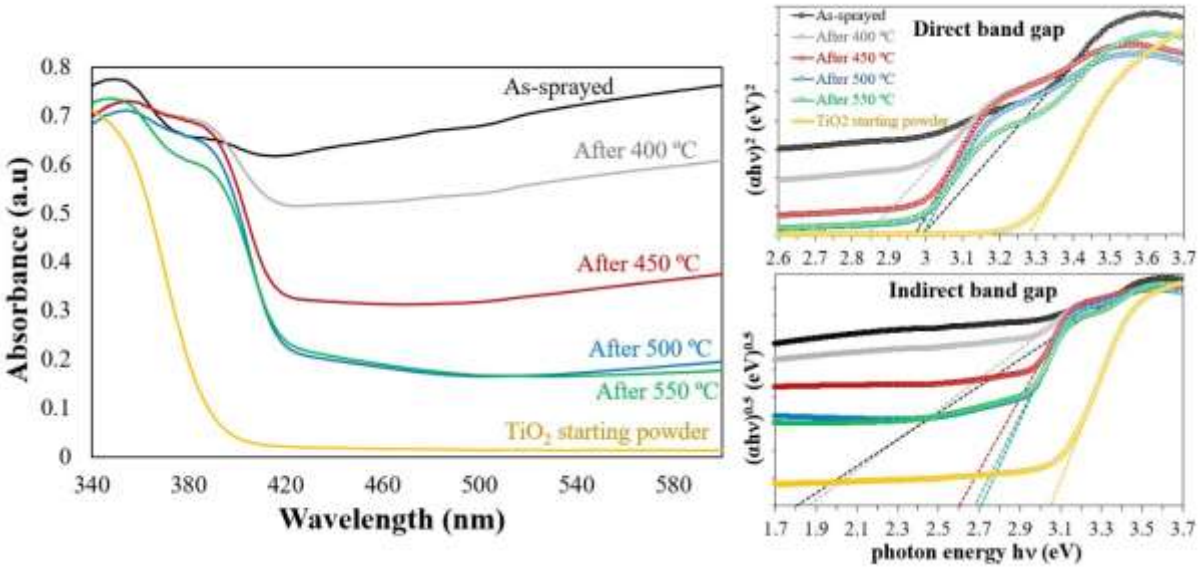

Figure 5. 14 UV-vis absorption spectra (left), and $(\alpha h\nu)^2$-hν, $(\alpha h\nu)^{1/2}$-hν plots (right) of TiO_2 coatings before and after heat treatment.

Table 5. 4 Optical direct and indirect bandgaps derived from $(\alpha h\nu)^2$-hν, $(\alpha h\nu)^{1/2}$-hν plots, respectively.

Bandgap		TiO_2 starting powder	As-sprayed	After 400 ºC	After 450 ºC	After 500 ºC	After 550 ºC
Direct	eV	3.28	3	2.85	2.97	3	2.97
	nm	377	413	434	417	413	417
Indirect	eV	3.05	1.8	1.85	2.6	2.71	2.68
	nm	406	688	669	476	457	462

5.3.6 Photocatalytic activity

The photocatalytic performance of all samples was measured by the time-dependent degradation of methylene blue (MB) under visible-light irradiation (Fig. 5.15). The value of MB degradation after 90 min, the reaction rate constant (k), and the correlation coefficient (R^2) which represents the goodness of fit of the pseudo-first-order regressions are listed in Table 5.5. A blank test without coating was done as a benchmark for evaluating the rate of self-degradation of methylene blue under irradiation, which shows minor photolysis of the MB on the experiment timetable. According to the results, it was demonstrated that the photo-degradation activity of as-sprayed sample is higher by the factor of 2-3 than that of heat-treated samples. Metha et al. [167] reported poor photocatalytic activity of the pristine TiO_2 sample for degrading aqueous solution of MB under visible light irradiation ($k \sim 5.1\times10^{-6}$ min^{-1}). While after a 30-hour heat treatment at 300 ºC in 5% H_2-Ar atmosphere, the photo-degradation rate constant k reaches the maximum 9.9 $\times10^{-3}$ min^{-1}. Wang et al. [139] produced TiO_{2-x} nanoparticles using $NaBH_4$ as a reductant in solvothermal method, then synthetized titanium dioxide nanoparticles integrated with reduced graphene oxide composite nanosheets (RGO/TiO_{2-x}). The rate constant for MB degradation under visible light was 0.00151, 0.00246, and 0.01958 min^{-1} for TiO_2, TiO_{2-x} and 0.3-RGO/TiO_{2-x}, respectively. Compared to the literature, our as-sprayed coating exhibits much better photocatalytic performance for MB degradation under visible light.

According to the literature, the photocatalytic reaction will be initiated by charge separation of photo-generated electron-holes in TiO_2 catalyst upon absorption of photons with energy larger than its bandgap. The charge carries can diffuse to the surface of the catalyst, where positive holes (h^+) in the valence band can oxidize adsorbed water or hydroxyl molecules to generate highly reactive hydroxyl radicals ($^{\bullet}OH$). Additionally, the photo-excited electrons (e^-) in the conduction band can also scavenge molecular oxygen (O_2) on the surface of the coating to produce superoxide radical anions (O^{2-}). Hydroxyl radicals with very high oxidation potential will oxidize organic pollutants to transform into CO_2 and H_2O. These active species are responsible for the photocatalytic decomposition of the organic compounds (Eq. 5.7 - 5.9) [35][160][161].

$$TiO_2 + h\nu \rightarrow e^- + h^+ \quad (5.7)$$
$$h^+ + H_2O\ (surface) \rightarrow \bullet OH + H^+ \quad (5.8)$$
$$e^- + O_2(surface) \rightarrow O_2^- \quad (5.9)$$

The photocatalytic efficiency of TiO_2 strongly depends on the light absorption ability, surface hydroxylation, and recombination rate of the photo-generated electron-hole [161]. In our case, based on the TGA and photocatalytic activity results, it is proportional to the concentration of the oxygen content in the catalyst and notable enhancement of the photocatalytic decomposition of as-sprayed sample is indicated that the oxygen vacancies in sub-stoichiometric TiO_{2-x} contributed to the photocatalytic effect. While ATR-FTIR results present almost no substantial changes with the oxygen content variation. During plasma spraying, the high spraying temperature accompanied by the reductive hydrogen as the secondary plasma gas can promote the presence of nonstoichiometric TiO_{2-x} in the as-sprayed samples [134][45]. Literature suggests that hydrogen interacts with TiO_2 and both oxygen vacancy and electrons are generated as shown in Eq. 5.10, where O_O^x is an O^{2-} ion in the oxygen lattice site, $V_{\ddot{O}}$ is an oxygen vacancy with a double positive charge, and e^- is a conduction electron [66].

$$O_O^x + H_2 \rightarrow V_{\ddot{O}} + 2e^- + H_2O \quad (5.10)$$

Ti^{3+} ions are formed subsequently by the electrons being trapped in Ti^{4+} lattice sites, which considered as donor doping [66]. The change in the color of sub-stoichiometric TiO_{2-x} as a result of a high concentration in Ti^{3+}ions [62] increased the absorption of visible light of the as-sprayed coatings by changing the bandgap; therefore a larger number of photo-generated charges could be formed in the sub-stoichiometric TiO_{2-x}. Moreover, Ti^{3+} ions introduce a new sublevel state in the form of $[O_v \cdot Ti3^+]^+$ at the conduction band (CB) bottom of sub-stoichiometric TiO_{2-x}, which favors the charge carrier separation to increase their lifetime and modify the interfacial photo-induced electron-hole transfer [138][167][139][66]. Furthermore, the oxygen vacancies in sub-stoichiometric TiO_{2-x} dissociate water molecules and form two hydroxyl groups via H^+ transfer to neighboring oxygen after exposure to air at room temperature according to Eq. 5.11[20][66][67].

$$V_{\ddot{O}} + H_2O + O_O^x \rightarrow 2(OH)_O^{\bullet} \quad (5.11)$$

Considering the above discussion, it can be deduced that oxygen vacancies are beneficial for the photocatalytic degradation reaction by the sub-stoichiometric samples, in which the MB was notably removed over the as-sprayed samples. The proposed mechanism of photo-degradation of the sub-stoichiometric TiO_{2-x} is shown schematically in Fig. 5.16.

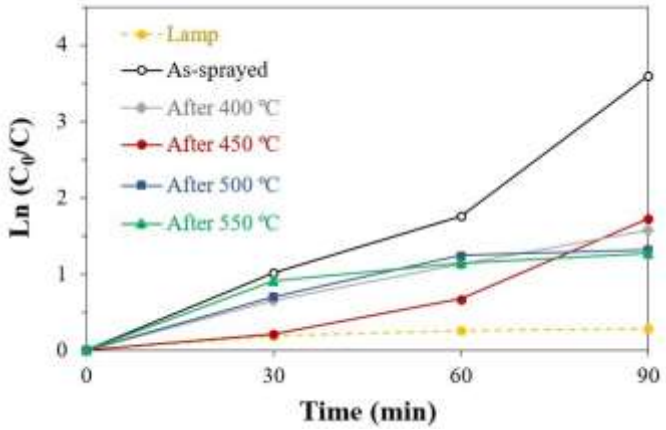

Figure 5. 15 Photocatalytic degradation of the MB solution (2×10^{-5} M) under visible irradiation, where C_0 is initial concentration after dark test, and C is the MB concentration at irradiation time.

Table 5. 5 Discoloration (%) of the MB (2×10^{-5} M) solution after 90 min, and its rate constant (k).

	As-sprayed	After 400 ºC	After 450 ºC	After 500 ºC	After 550 ºC
MB Removal after 90 min, %	97	79	82	73	71
Rate constant (k) $\times10^{-2}$, min^{-1}	3.8	1.7	1.8	1.4	1.3
Correlation coefficient (R^2)	0.96	0.99	0.90	0.91	0.82

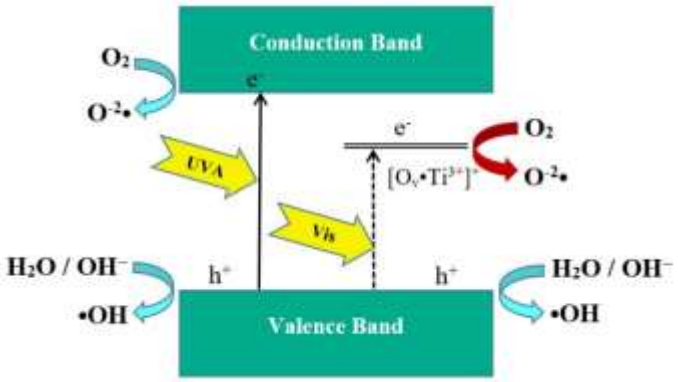

Figure 5. 16 Schematic of the proposed mechanism for the photocatalytic reaction of the stoichiometric vs. sub-stoichiometric TiO_{2-x} [Adapted from reference [138]].

5.4 Conclusion

This research investigated a comparative study on the effect of the oxygen deficiency and Ti^{3+} ions in the optical and photocatalytic performance of TiO_2 coatings produced by suspension plasma spray (SPS) on stainless steel substrates. SPS is an innovative technique to deposit sub-micron sized particles with the ability to induce non-stoichiometry and to create novel products. Coatings with different oxygen levels were generated by heat treating the as-sprayed samples at different temperatures. The higher the annealing temperature was, the more oxygen was recaptured. X-ray diffraction analysis and scanning electron microscopy of the coatings revealed no significant phase and structure difference between before and after heat treatment at 450 ºC and below. Small phase change of anatase to rutile (~2-6%) in the porous area of samples treated 550 ºC was detected by Raman analysis. Raman and thermogravimetric analyses were conducted to confirm and measure and the level of the oxygen content of samples. As expected, the variation of the optical properties as a function of the stoichiometry was evident, whereas introducing oxygen vacancies and Ti^{3+} ions in the TiO_2 lattice sites efficiently decreased the bandgap energy to lower

values and shifted the absorption edge to visible light by the formation of an $[Ov \cdot Ti^{3+}]^{+}$ between the VB and the CB of sub-stoichiometric TiO_{2-x}. Furthermore, the existence of energy level between the bandgap could promote the separation of photo-generated electrons and holes by acting as traps, leading to an enhanced photocatalytic response of the sub-stoichiometric TiO_{2-x} under visible light. According to the kinetic study, the photocatalytic process followed a pseudo-first-order pattern with a rate constant of 3.8×10^{-2} and 1.3×10^{-2} min^{-1} for the as-sprayed and after 550 ºC TiO_2 coatings with the highest and lowest oxygen deficiency, respectively. Overall, this work presented the deposition of high-efficient sub-stoichiometric TiO_{2-x} photocatalyst coatings, which have the potential to mitigate the environmental impact of the textile industry.

Acknowledgement

The authors gratefully acknowledge the financial support provided by Natural Sciences and Engineering Research Council of Canada (NSERC) through Canada Research Chairs and Discovery Grants Programs.

Preface to Chapter 6.

In the previous chapters, the role of the anatase phase content and oxygen deficiency on the suspension plasma sprayed TiO_2 coatings were investigated. It showed the ability of suspension plasma spray (SPS) to produce highly efficient sub-stoichiometric TiO_{2-x} coatings. The current chapter will try thermal spray processes to produce doped-TiO_2 coatings using a hybrid suspension (SPS) and solution precursor plasma spraying (SPPS) approach. It was challenging to produce homogenous doped-TiO_2 coating within the short residence time of plasma spraying. While using a hybrid suspension (SPS) and solution precursor plasma spraying (SPPS) techniques lead to a high degree of chemical uniformity of the components.

Chapter 6. Photoactive Ce-doped TiO_2 and CeO_2-TiO_2 composite coatings deposited by suspension/solution plasma spray [3]

Abstract

In this work, Ce-doped TiO_2 coatings were produced using a hybrid suspension (SPS) and solution precursor plasma spraying (SPPS) approach. CeO_2-TiO_2 composite coatings were also deposited by the SPS process. The photocatalytic activity of the coatings was evaluated by measuring the methylene blue degradation rate under visible light. Cerium doping and CeO_2 composite coatings were detected by X-ray diffractometer measurements and verified by energy dispersive spectroscopy mapping, Raman spectra, and X-ray photoelectron spectroscopy analysis. The hybrid SPS/SPPS technique presented a promising method to deposit doped ceramic coatings among thermal spray processes. According to the results, modifying TiO_2 coatings decreased the bandgap of TiO_2 from 3.25 to 2.3 eV using cerium dopant. However, a lower photocatalytic efficiency of TiO_2 -CeO_2 composite and Ce-doped TiO_2 coatings compared to TiO_2 could be related to the lower active surface area of TiO_2 covered by submicron CeO_2 particles and non-optimal dosage of cerium dopant, respectively.

Keywords: TiO_2, CeO_2, Photocatalytic activity, Doping, Suspension plasma spray, Solution precursor plasma spray

6.1 Introduction

Photocatalytic decomposition involves the degradation of organic contaminants to reduce environmental pollution near the surface of the photocatalyst by transforming the optical energy of the absorbed light into chemical energy for the redox reactions [20][12]. Since the strong oxidation and reduction power of photoexcited titanium dioxide (TiO_2) was discovered by Honda and Fujishima in 1972, TiO_2 has attracted ever-growing attention as a great candidate for environmental and energy applications [20][150][210]. Also, it has the advantages of high chemical stability, being abundant, low-cost, and non-toxic [211].

The crystalline phase of titania is one of the important parameters affecting photocatalytic activity. Between the two main crystalline phases of TiO_2, anatase and rutile, anatase is considered the favorable phase for photocatalytic activity. Although, it has been reported that the phase mixture of both polymorphs shows better photocatalytic activity compared to pure phases [212][166][22].

[3] This chapter is submitted to the Journal of Materials Research Bulletin, Hediyeh Khatibnezhad, Fadhel Ben Ettouil, and Christian Moreau.

Generally, a photocatalytic reaction consists of three main steps: (I) Formation of excited electron-hole pairs upon absorption of light photons; (II) migration of the photo-excited charge carriers to the surface of the semiconductor or their recombination inside the bulk material; (III) production of active hydroxyl radicals ($^{\bullet}OH$) and superoxide anions (O^{2-}) through the oxidation-reduction reaction of holes and electrons with water (or hydroxyl molecules) and oxygen molecules (O_2) on the surface. These highly reactive species can degrade organic compounds into harmless products in wastewater [20][212][160].

However, there are some limitations to TiO_2 photocatalytic activity. The large bandgap energy of TiO_2 (~ 3.0 eV for rutile and 3.2 eV for anatase) requires activation under UV light [40]. Moreover, the fast recombination of photogenerated charge carriers reduces the photo-quantum efficiency [162].

One approach to facilitate charge separation in the TiO_2 photocatalyst and enhance its efficiency is using composite semiconductor metal oxides. It has been reported that groups of semiconductor/semiconductor or semiconductor/metal composite nanoparticles diminish the recombination rate in the semiconductor nanostructures [47][68]. Based on the literature, compositing TiO_2 with an optimum amount of CeO_2 nanoparticles would enhance interfacial charge separation and lower charge carrier recombination rate [69][70][71].

Doping TiO_2 with metals or non-metal impurities is one of the most effective approaches, which has been proposed by many researchers, to reduce the bandgap energy and also decrease the recombination of photogenerated electrons and holes [52][35][213]. Cationic-doped TiO_2 with rare earth metals, noble metals, poor metals, and transition metals have been widely studied. The metallic ions-doped TiO_2 expands the light absorption region and increases the quantum efficiency by preventing the recombination of the photogenerated electrons and holes on the conduction and valence bands, respectively [50]. These dopants could introduce energy levels just below the conduction band [52]. Rare earth metals like Ce and Nd are effective cationic dopants to improve photocatalysis due to their incompletely occupied 4f and empty 5d orbitals [214][215][216]. It has been reported that Ce dopant could limit the grain size growth of TiO_2 to reduce its crystallite size and increase the specific surface area. It also can act as a trap to scavenge electrons and increase charge carrier lifetime [52][53].

Several types of research works have been conducted to produce TiO_2 coatings by thermal spray processes and mostly Suspension Plasma Spray (SPS) to produce nanostructured TiO_2 coatings with the highest amount of anatase [42][43][132]. Plasma spraying is widely used to deposit a wide range of materials onto different substrates. This process utilizes a high-temperature, high-velocity plasma jet formed by passing a gas or mixture of gases (typically argon and/or nitrogen) through a DC current arc to heat and accelerate particles toward the substrate surface. To improve the efficiency of the deposition process, a secondary gas, such as hydrogen, is added to increase the heat and momentum transfer to the spray particles [119]. With water-based suspensions of fine anatase particles, the high vaporization enthalpy of water would cool down the plasma jet. Subsequently, a higher amount of the un-melted nanosized particles would be preserved, resulting in a higher amount of anatase content in the coating [133][134]. However, there are limited studies dedicated to doping TiO_2 with thermal spraying processes because of its challenging limitations that need more investigation. Based on the literature, the so-gel process is the most studied technique to produce Ce-doped TiO_2 coatings [217][218].

Some researchers have reported doping rare earth elements into the yttria-stabilized zirconia (YSZ) coatings through SPS/SPPS technique while rare-earth nitrates dopant precursors were dissolved in the YSZ-ethanol-based suspension before spraying. According to their results,

dopants could effectively scatter phonons by introducing point defects to lower the thermal conductivity of YSZ coatings in thermal barrier applications [144][145].

In this research work, Ce-doped TiO_2 and CeO_2-TiO_2 composite coatings were produced using SPS/SPPS and SPS, respectively. The principal advantage of using SPS/SPPS for doping cerium is the possibility of developing new chemistry in the molecular-level mixing of the constituent. Moreover, there is much more possibility for ions to adsorb onto the surface of TiO_2 particles homogeneously and form the coating. To the authors' best knowledge, this is the first published work focused on Ce-doped TiO_2 using SPS/SPPS technique. Furthermore, various characterization tests were performed to confirm the presence of cerium in the coatings, such as XRD, Raman analysis, energy dispersive spectroscopy (EDS), and XPS measurements. Finally, the role of cerium doping and compositing on the optical properties and photocatalytic activity was investigated.

6.2 Experimental procedure

6.2.1 Suspension and solution preparation

Submicron-sized anatase TiO_2 powder (TKB Trading, Oakland-USA), cerium (IV) oxide (99.9%, Sigma-Aldrich, St. Louis-USA) and cerium (III) nitrate hexahydrate ($Ce(NO_3)_3.6H_2O$) (99%, Sigma-Aldrich, St. Louis-USA) were used as feedstock materials to prepare the primary solution and suspensions. Three types of water-based suspensions with 10 wt.% solid content were prepared for the plasma spraying, as shown in Table 6.1. No dispersing agent was used as the suspensions were sufficiently stable for spraying. For TiO_2 suspension, the as-received TiO_2 powder was suspended in deionized water to form an aqueous suspension. For TiO_2-CeO_2 suspension, TiO_2 powder and CeO_2 powder (10 wt.% of the solid content) were added to the deionized water. To produce Ce-doped TiO_2 suspension for the spraying, first $Ce(NO_3)_3.6H_2O$ crystals (25 wt.% of the solid content) were dissolved in water to form a solution, then the TiO_2 powder was suspended in the solution. All suspensions were effectively mixed using a magnetic stirrer as well as a sonicator to break down large agglomerates. The prepared suspensions showed good stability during spraying without any noticeable sedimentation. The size distribution of the particles in the suspensions was measured by a Spraytec unit (Malvern Instruments, UK).

Table 6. 1 Suspensions for the plasma spraying.

Samples	Suspensions	Feedstock materials		
		TiO_2 powder	CeO_2 powder	$Ce(NO_3)_3.6H_2O$
Pure TiO_2	TiO_2 (SPS)	✓	-	-
TiO_2- CeO_2 composite	TiO_2- CeO_2 (SPS)	✓	✓	-
Ce-doped TiO_2	TiO_2- Ce nitrate (SPS-SPPS)	✓	-	✓

6.2.2 Coating deposition

An Axial III^{TM} plasma torch (Northwest Mettech Corp., Canada) was used for the suspension plasma spraying. It has the advantage of having three independent cathodes/anodes working on three power supplies that could reduce the voltage fluctuation of the plasma jet with high deposition efficiency [148]. Moreover, the axial injection has the advantage of a more uniform treatment of spray materials than the radial injection plasma torch. An automatic suspension feed system (NanoFeedTM, Northwest Mettech Corp., Canada) equipped with a

Coriolis flowmeter (Endress+Hauser, Canada) was utilized to deliver the atomized feedstock suspension homogeneously into the central core of the plasma and monitor the suspension flow rate and density during spraying, respectively. The suspensions were injected into the plasma jet at a feed rate of about 30 mL/min with an atomizing gas flow rate of 15 L/min and a spray distance of 75mm. Stainless steel coupons (25×25×5 mm^3) were used as the substrate. They were grit blasted with 80 grit Al_2O_3 particles to roughen the surface ($R_a \sim 2.5$ μm) and improve the coating's adhesion to the substrate.

The substrate temperature was monitored during spraying using an A320 ThermoVision IR camera (FLIR Systems, US). An AccuraSpray 4.0 sensor (Tecnar Automation Ltd., Canada) was used to monitor the trajectory and measure the velocity of in-flight particles during spraying. A time-of-flight technique is used in the AccuraSpray system to measure particle velocity [219]. Two air amplifiers were also used to cool down the substrate during spraying and to preserve a higher anatase content in the coatings [42]. Before coating deposition, substrates were preheated by the plasma torch to around 120 °C. Coatings were produced using 20 consecutive passes of a full spray raster at two deposition conditions, low and high power. The linear torch velocity and overlay distance were 1 m/s and 3 mm, respectively. Details of operating parameters are summarized in Table 6.2, in which the gas mixture ratio was the only varied parameter. According to Table 6.2, H_2 secondary gas plays a key role in the plasma power gun and the substrate temperature during the deposition process by increasing the thermal conductivity of plasma. Based on AccuraSpray 4.0, the velocities of in-flight particles were 430 and 480 m/s for low-power and high-power conditions, respectively. It has been seen that the different suspensions did not have any impact on the particle's velocity.

Table 6. 2 SPS/SPPS deposition parameters.

Conditions	Current (A)	Gas flow (SLPM)	Gas mixture			Power (kW)	Substrate temp. during deposition (°C)	In-flight particles' velocity (m/s)
			Ar (%)	N_2 (%)	H_2 (%)			
Low power	220	223	82	11	7	78.5	~ 180	430
High power		245	70	10	20	95	~ 320	480

6.2.3 Characterization

The three-dimensional surface topography and arithmetic average roughness (R_a) of coatings were studied using a confocal laser microscope (LEXT OLS4000, Olympus, Japan). To characterize the coating surface and cover a large enough area, 25 single images were digitally stitched together and generated 3D maps of the surfaces. Top surface morphology and cross-sectioned microstructure were characterized using an ultra-high resolution cold-field emission scanning electron microscope (FE-SEM) (Regulus8230, Hitachi, Japan) equipped with an energy-dispersive X-ray spectroscopy, secondary electron (SE) and backscattered electron (BSE) detectors. The phase identification of the TiO_2 coatings was studied using the X-ray diffraction (XRD) technique using D8 Advance (Bruker, USA) with Cu Kα radiation (1.5418Å) and a step size of 0.02° in a range of 20-80°. The semi-quantitative phase analysis was measured using DIFFRACT based on the tabulated reference intensity ratio EVA software (Bruker, USA) and PDF-2 database (International Center for Diffraction Data). The crystallite sizes of the coatings (D) were estimated by the Debye-Scherrer equation (Eq. 6.1), using (101), (110) and (111) crystallographic planes for anatase, rutile and ceria, respectively [35].

$$D = \frac{K\lambda}{\beta cos\theta} \quad (6.1)$$

where λ is the wavelength of X-ray (Cu K_α) in nm, K is the constant shape factor (0.9), β is the half-peak width in radians, and θ is the Bragg angle. Lattice parameters (a, b and c) were calculated using Bragg's law with the same crystallographic planes [35][54]. The Raman spectra of the coatings on the polished cross-sections and top surfaces were recorded using a micro-Raman spectrometer (inVia Reflex, UK) with a laser wavelength of 532 nm, objective magnification 50 x and 10 s exposure time. A silicon reference was utilized for the system calibration, and measurements were performed at a low excitation power (<10 mW) to avoid the laser heating effect.

The surface elemental composition of the coatings was studied using an X-ray photoelectron spectroscope (XPS) (VG ESCALAB 250Xi, Thermo Fisher Scientific, USA) with an Al Kα radiation source (hυ =1486.6 eV) and a spot size of 1300 μm in diameter. A UV-Visible-NIR spectrometer (Lambda 750, Perkin Elmer, US) was used to record the UV–Vis diffuse reflectance spectra of the coatings in the range of 340 to 600 nm. Moreover, the bandgap energy of the samples was measured based on the Tauc plot method and the following equations [36][154]:

$$\alpha h\upsilon = A(h\upsilon - E_g)^n \quad (6.2)$$

$$E_{photon}(eV) = h\nu = \frac{1239}{\lambda} \quad (6.3)$$

where α is the absorption coefficient, E_g is the bandgap calculated from the extrapolation of the straight-line portion of the $(\alpha h\nu)^{1/n}$ –hν plot, A (constant) is the slope of the linear region of the mentioned plot, λ is the wavelength, and n is 2.0 and 0.5 for indirect and direct allowed optical transitions, respectively.

In this work, the photocatalytic activity assessment was performed by measuring the degradation rate of methylene blue, MB ($C_{16}H_{18}ClN_3S$), a representative of polluting dyestuffs in textile wastewater [25]. Figure 6.1 depicts the schematic diagram of the experimental setup designed for the photocatalytic activity assessment under visible irradiation. Visible light was provided by two 35 W Xenon lamps equipped with a cutoff filter (Edmund Optics, USA) to block UV radiation. During the test, a water bath and a fan were used to prevent heating the samples by light irradiation.

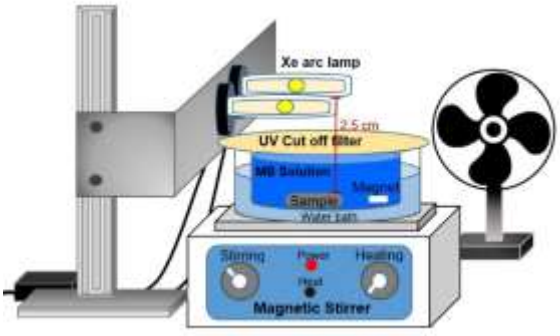

Figure 6. 1 Schematic diagram of the experimental setup.

Before starting the experiment, the coated coupons (surface area of one in^2) were immersed in 30 mL MB solution with 2×10^{-5} M concentration in the dark to achieve the adsorption/desorption equilibrium. After 60 min in the dark (C_0), the testing cell was placed inside the visible light setup. Sampling was made every 15 min to monitor the decomposition rate of MB using a UV-vis spectrophotometer (evolution 201, Thermo Scientific, US) at the maximum absorbance wavelength of MB (664 nm). The test process for the control sample was conducted on the MB solution without the coating to assess the photolysis phenomenon.

The rate constant of the pseudo-first-order reaction (k) was measured using Eq. 6.4. [3][35].

$$ln\left(\frac{C_0}{C}\right) = kt \tag{6.4}$$

where C_0 is the concentration of MB after 60 min in the dark, C is the MB concentration at each time interval, and t is the irradiation time.

6.3 Results and discussion

6.3.1 Powders and suspension characteristics

SEM micrographs and XRD patterns of TiO_2 and CeO_2 powders are shown in Fig. 6.2. Based on the XRD results, anatase and CeO_2 are the only detected phases for TiO_2 and CeO_2 powders, respectively. The particle size distributions in the aqueous suspensions are presented in Fig. 6.3. TiO_2 (SPS) and TiO_2- CeO_2 (SPS) suspensions had almost the same particle size distributions (TiO_2: d_{10}=0.2 µm, d_{50}=0.39 µm, d_{90}=0.75 µm, and TiO_2-CeO_2: d_{10}=0.24 µm, d_{50}=0.43 µm, d_{90}=0.79 µm), while larger agglomerates were formed in TiO_2- Ce nitrate suspension (d_{10}=2.9 µm, d_{50}=5.1 µm, d_{90}=8.7 µm).

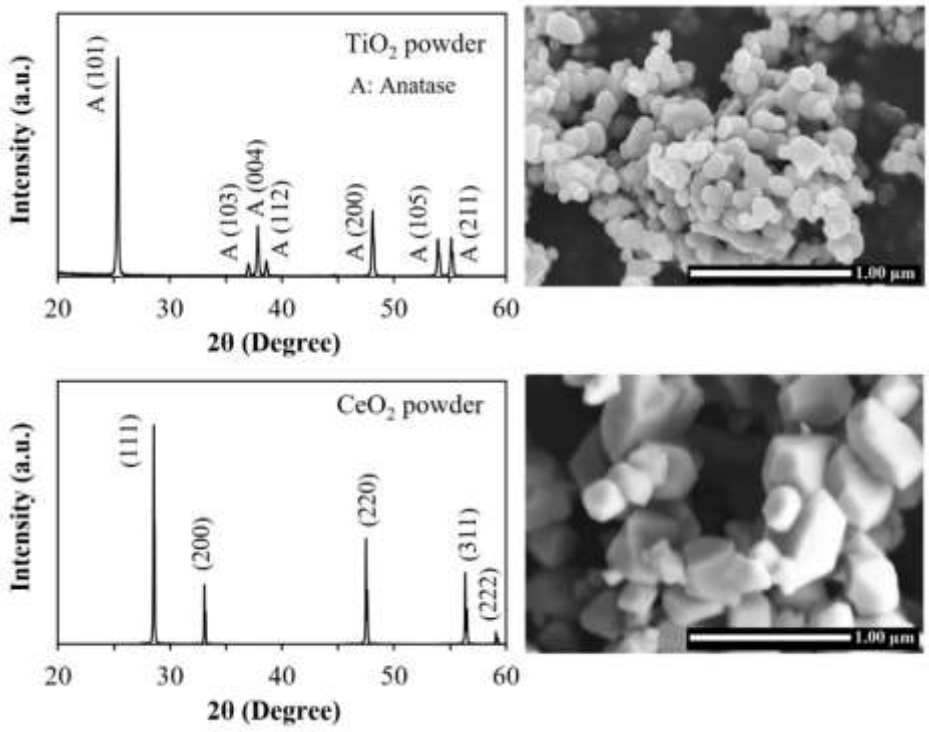

Figure 6. 2 XRD patterns and FE-SEM micrographs of the feedstock TiO_2 (top) and CeO_2 (bottom) powders.

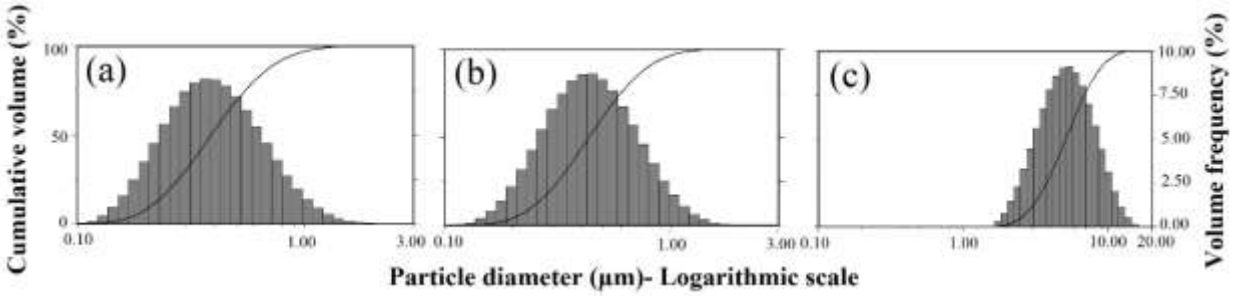

Figure 6. 3 Particle size distributions of the aqueous suspensions: (a) TiO_2 (SPS), (b) TiO_2- CeO_2 (SPS), (c) TiO_2- CeO_2 (SPS-SPPS).

6.3.2 Coating microstructures and morphology

In this work, coatings were produced at two different spray conditions: low power and high power. According to Fig. 6.4 and Table 6.3, the surface roughness increased with the increasing plasma power.

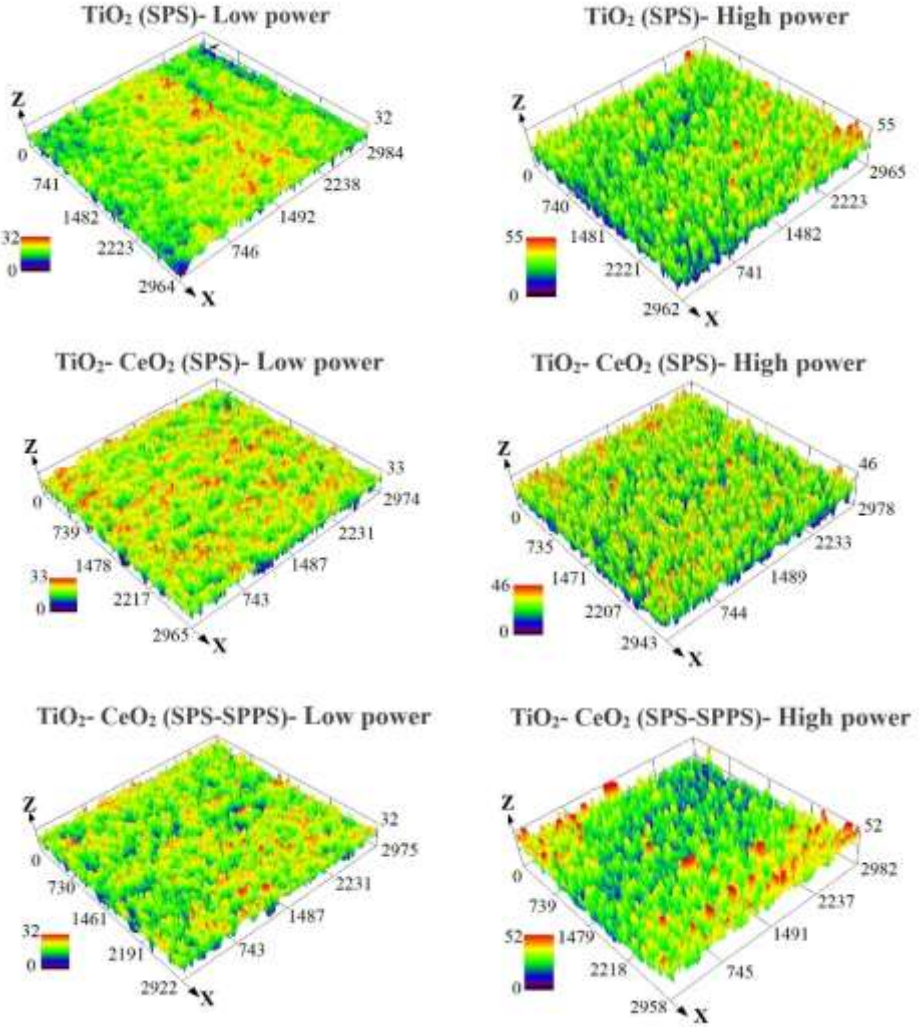

Figure 6. 4 3D images of the top surfaces of the coating attained by the confocal laser microscope.

Our previous work [212] showed that the typical cauliflower-like structure of SPS coatings would increase the roughness. It was shown that the higher the power, the greater the thickness and the surface roughness.

Table 6. 3 Arithmetic average surface roughness (R_a) of the coatings.

Sample	Surface roughness parameter- R_a (µm)		
	TiO_2 (SPS)	TiO_2- CeO_2 (SPS)	TiO_2- CeO_2 (SPS-SPPS)
Low power	2.4 ± 0.03	3.1 ± 0.03	2.7 ± 0.04
High power	4.8 ± 0.05	4.7 ± 0.05	3.5 ± 0.06

The effect of the plasma power on the microstructure of the coatings is presented in Figs. 6.5, 6.6, 6.7, and 6.8. Based on the SEM images (Fig. 6.5, 6.7 and 6.8), all coatings presented a columnar structure that was firmly bonded to the substrate with good mechanical stability. As shown in Figs. 6.5 and 6.6, spraying at low plasma power produced thinner coatings with larger areas of fine porosity. Likewise, increasing the power would improve the suspension atomization, ceramic melting and deposition efficiency.

Generally, the microstructure is made of molten and non-molten areas. At higher magnification (Fig. 6.6), dense zones formed by fully melted particles (A) appear as light grey areas. There are two types of porosities: black zones of the large pores (B) and dark grey areas of the fine porosities. Based on the results, fine porosities are found in large pores filled with either agglomerated, un-melted fine particles (C) with a size close to the starting powders or possibly in-flight re-solidified particles (D). Water solvent in the suspension would cool down the plasma jet and increase the un-melted portion in the coating. While re-solidified particles may result from the re-solidification of the melted particles before impinging onto the substrate [44][212]. The presence of water as a solvent in the suspension causes the plasma jet to cool down, resulting in a larger portion of un-melted particles in the coatings. Also, melted particles might be re-solidified in the plasma plume before being deposited on the substrate [212][44].

Backscattered electron (BSE) images of TiO_2- CeO_2 (SPS) coatings (Fig. 6.6) showed two more regions: white spots (E) and grayish-white areas (F). Since BSE signals depend on the mean atomic number of the samples [220], white and grayish-white areas of TiO_2- CeO_2 (SPS) coatings are attributed to the CeO_2 and probably TiO_2 - CeO_2 mixed oxides, respectively. It can be observed that the number of white spots decreased in the TiO_2- CeO_2 (SPS)- high power coatings indicating that there might be more mixed -oxides with spraying at high plasma power. On the other hand, no white spots related to the heavy element of cerium could be observed on the BSE images of TiO_2- CeO_2 (SPS-SPPS) coatings, suggesting that Ce was successfully doped in the coatings.

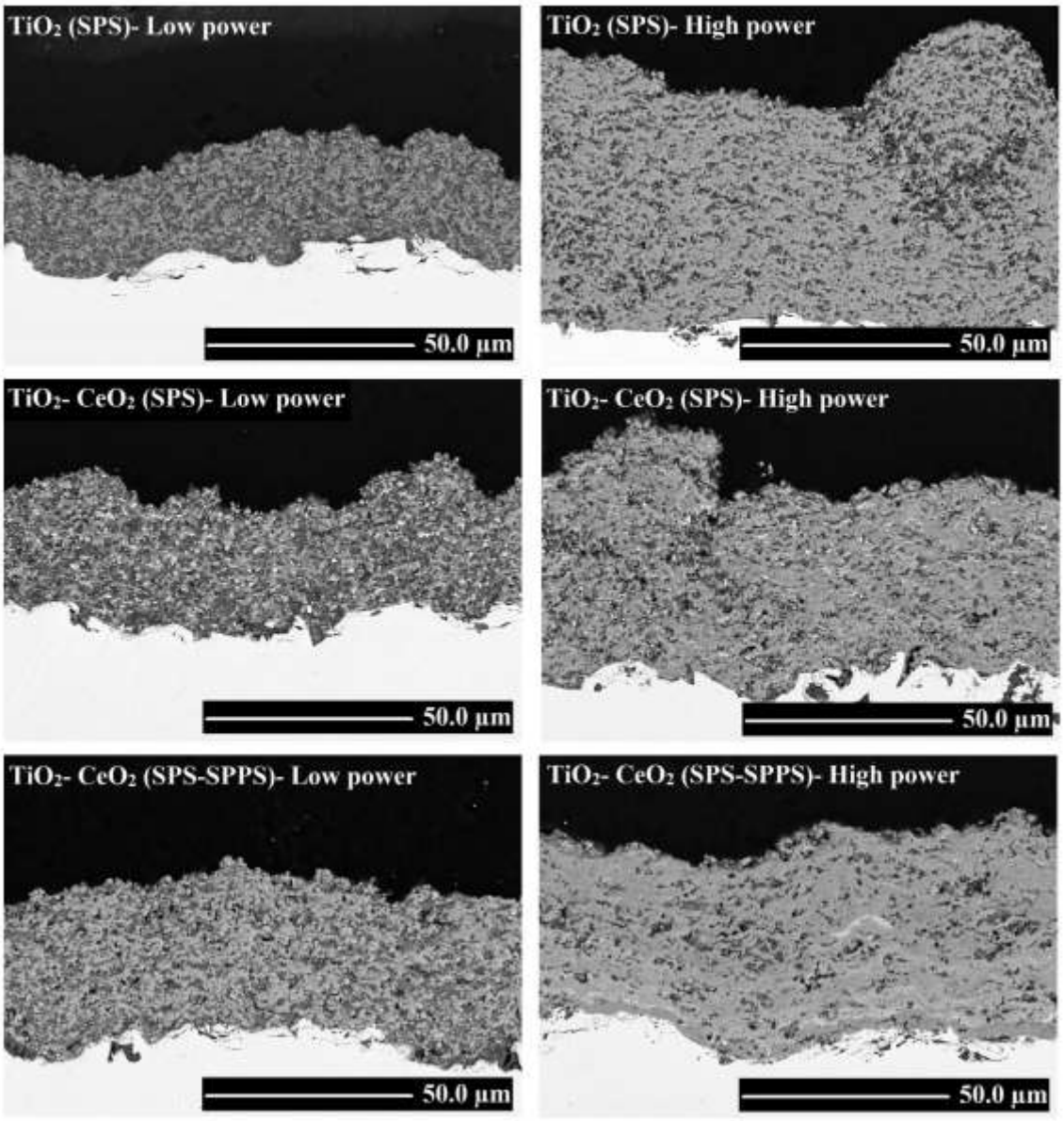

Figure 6. 5 BSE FE-SEM micrographs of coatings' cross-sections produced at two different spray conditions: low power and high power.

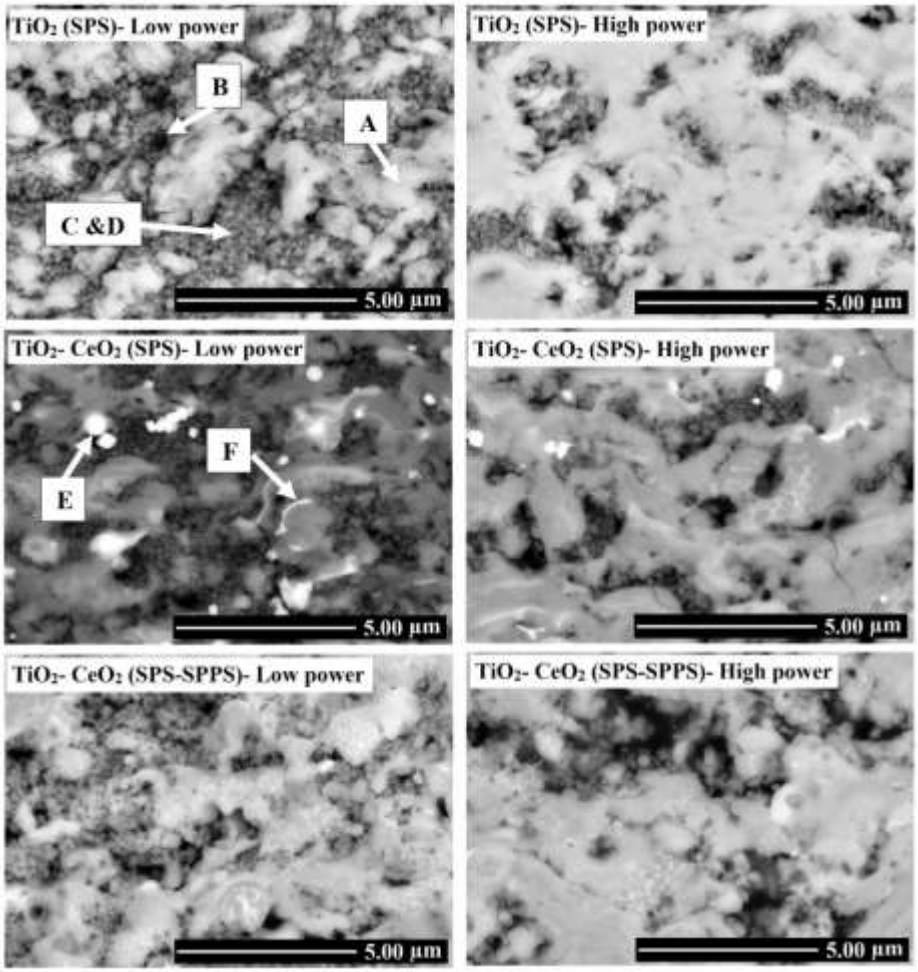

Figure 6. 6 High-magnification BSE FE-SEM images of coatings' cross-sections where (A) is fully melted particles, (B) is large pores, (C & D) are fine porosities of un-melted or re-solidified particles, (E) is CeO_2 and (F) is probably TiO_2-CeO_2 mixed oxide.

SEM top surface micrographs (Fig. 6.7) also presented a cauliflower-like surface morphology with distinctive rounded bumps for the coatings produced at high power. These results also indicated a smoother surface with low distinctive columns for TiO_2- CeO_2 (SPS-SPPS) coatings. Based on the literature, variation in the microstructure can be related to the evolution of the suspension droplets during spraying in the plasma plume [43]. In TiO_2- CeO_2 (SPS-SPPS) suspension, TiO_2 powder was suspended in the solution of water and nitric acid cerium salt. Therefore, the smoother surface of the TiO_2- CeO_2 (SPS-SPPS) coatings might be attributed to the higher suspension viscosity, larger agglomerates and, consequently, the formation of larger splats during spraying.

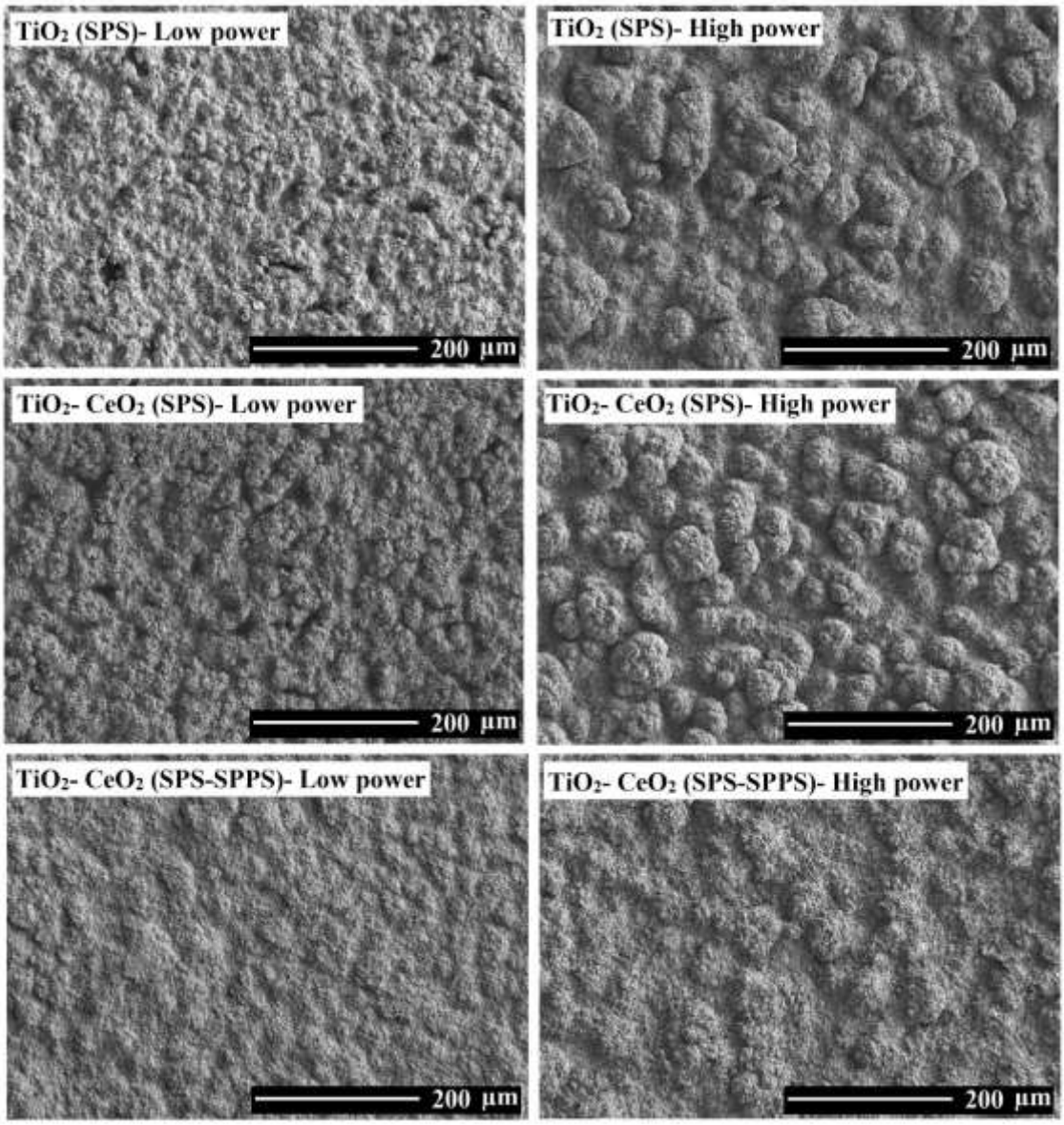

Figure 6. 7 Top surface SE FE-SEM micrographs of the coatings produced at two different spray conditions: low power and high power.

At higher magnification (Fig. 6.8), un-melted angular particles (C) and re-solidified spherical particles (D) can be clearly observed. SPS TiO_2 coatings with columnar structure and fine porosities have been found promising for providing better photocatalytic activity performance compared to atmospheric plasma spray (APS), yielding higher surface area for the photocatalytic activity [134].

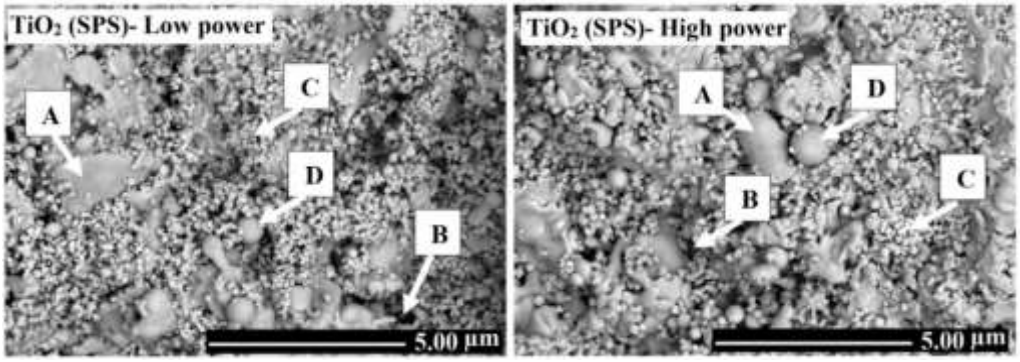

Figure 6. 8 Top surface BSE FE-SEM micrographs of the TiO_2 (SPS) coatings at a high magnification where indications are as (A) fully melted particles, (B) large pores, (C) un-melted agglomerated particles, and (D) re-solidified particles.

Further investigation was performed on the TiO_2- CeO_2 (SPS) and TiO_2- CeO_2 (SPS-SPPS) coatings to understand the distribution of the cerium element within the coating using energy dispersive spectroscopy (EDS) measurements during SEM imaging (Figs. 6.9 and 6.10). EDS mapping of TiO_2- CeO_2 (SPS) coatings presented isolated areas of cerium element in the coating, as shown in Fig. 6.9. In these coatings, there might also be some TiO_2- CeO_2 mixed oxides and Ce-doped TiO_2 areas. However, EDS mapping of TiO_2- CeO_2 (SPS-SPPS) (Fig. 6.10) did not show areas related to the isolated phase of cerium and cerium distributed throughout the coatings. These results suggested the substitutional doping of cerium into the TiO_2- CeO_2 (SPS-SPPS) coatings.

In the SPS technique, the feedstock suspension usually contains a solvent (mostly water or ethanol), and fine nanometric and/or sub-micrometric powder particles. After injecting suspension into the plasma plume produced by an electric arc between an anode and a cathode, it undergoes one or multiple breakups and atomization phases. Afterward, the solvent evaporates by the plasma's heat flow, leaving powder aggregates. These clusters of fine particles, fully or partially, melt depending on the condition and temperature and impact onto the substrate, creating splats. So doping would happen on the surface of the TiO_2 melted particles [124][125]. EDS-point analysis at different locations showed an average of 1.2 at. % cerium content. However, we noticed a non-uniform distribution of cerium doping throughout the coating that might depend on the thermal history of the spray particles and their contact with the cerium solution during spraying.

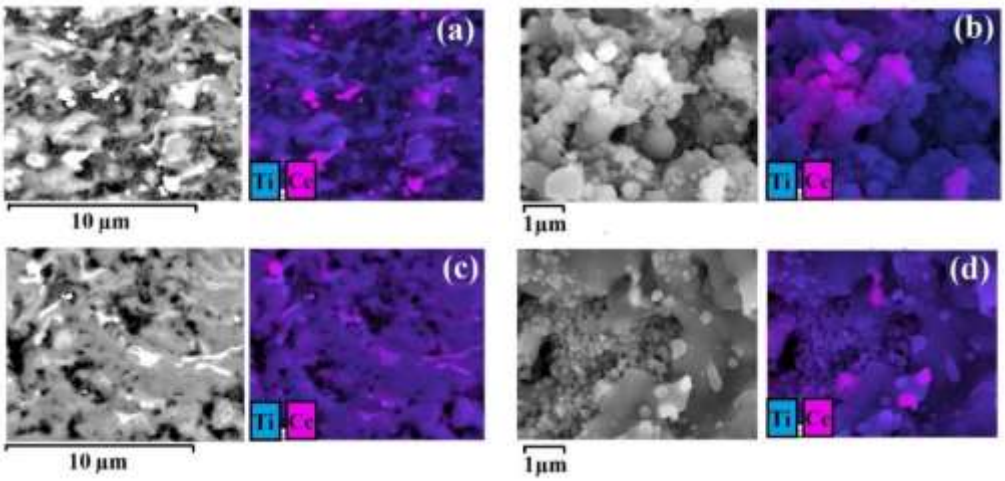

Figure 6. 9 FE-SEM-EDX mapping of the cross-sectional view (left side) and top surface view (right side) of TiO_2-CeO_2 (SPS) coatings produced at two different spray conditions: (a, b) low power, and (c, d) high power.

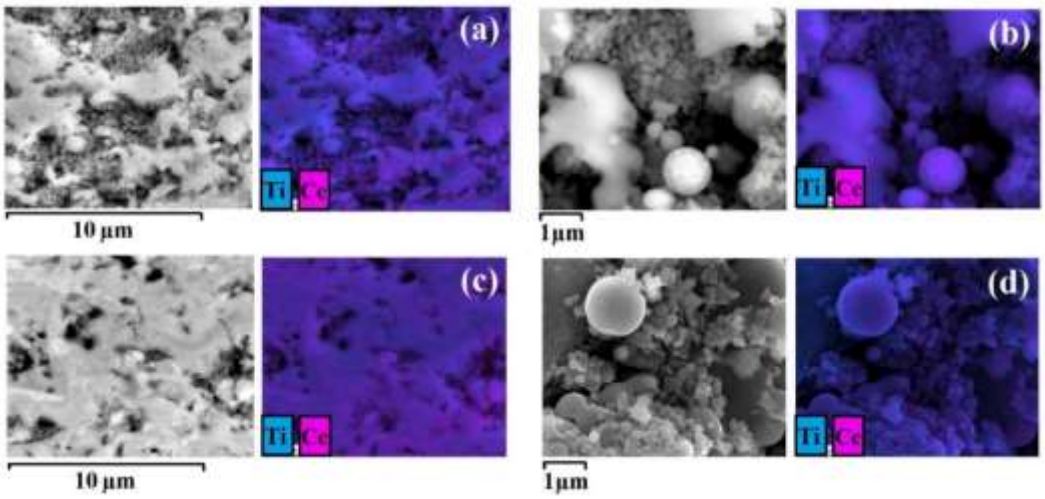

Figure 6. 10 FE-SEM-EDX mapping of the cross-sectional view (left side) and top surface view (right side) of TiO_2- CeO_2 (SPS-SPPS) coatings produced at two different spray conditions: (a, b) low power, and (c, d) high power.

6.3.3 Phase composition

The XRD patterns of the coatings and the derived information are presented in Fig. 6.11 and Table 6.4. Based on the results, a fraction of anatase phase of feedstock powder was irreversibly transformed to rutile phase during spraying in all coatings. Although, a higher content of anatase phase was maintained on the coatings produced at low plasma power. Also, low-power coatings presented higher crystallinity and lower amorphous content. As shown in FE-SEM coating cross-section images (Figs 6.5 and 6.6), low-power coatings contain a larger portion of un-melted fine particles coming from the starting powder with probably the same crystalline phase that is consistent with the higher anatase phase content in these coatings. Previous studies have also suggested that fully melted particles can either form rutile or anatase depending on the melting level of the particles and the solidification condition during spraying [133][44][45]. It has been shown that rutile is the most stable TiO_2 phase that would be formed under equilibrium solidification. While under non-equilibrium and high cooling rate conditions of SPS, anatase phase may recrystallize [42][221]. Besides, the substrate temperature is another parameter that has an influence on the anatase phase content [42][172]. In this research work, the lower substrate temperature of the low-power coatings may increase the cooling rate of the liquid droplets upon impact at the substrate or at the previously deposited particles that favor anatase nucleation in the molten areas. Moreover, more molten particles are obtained at high-power coatings that might be deposited at a relatively low temperature below the crystallization temperature and form more amorphous phases.

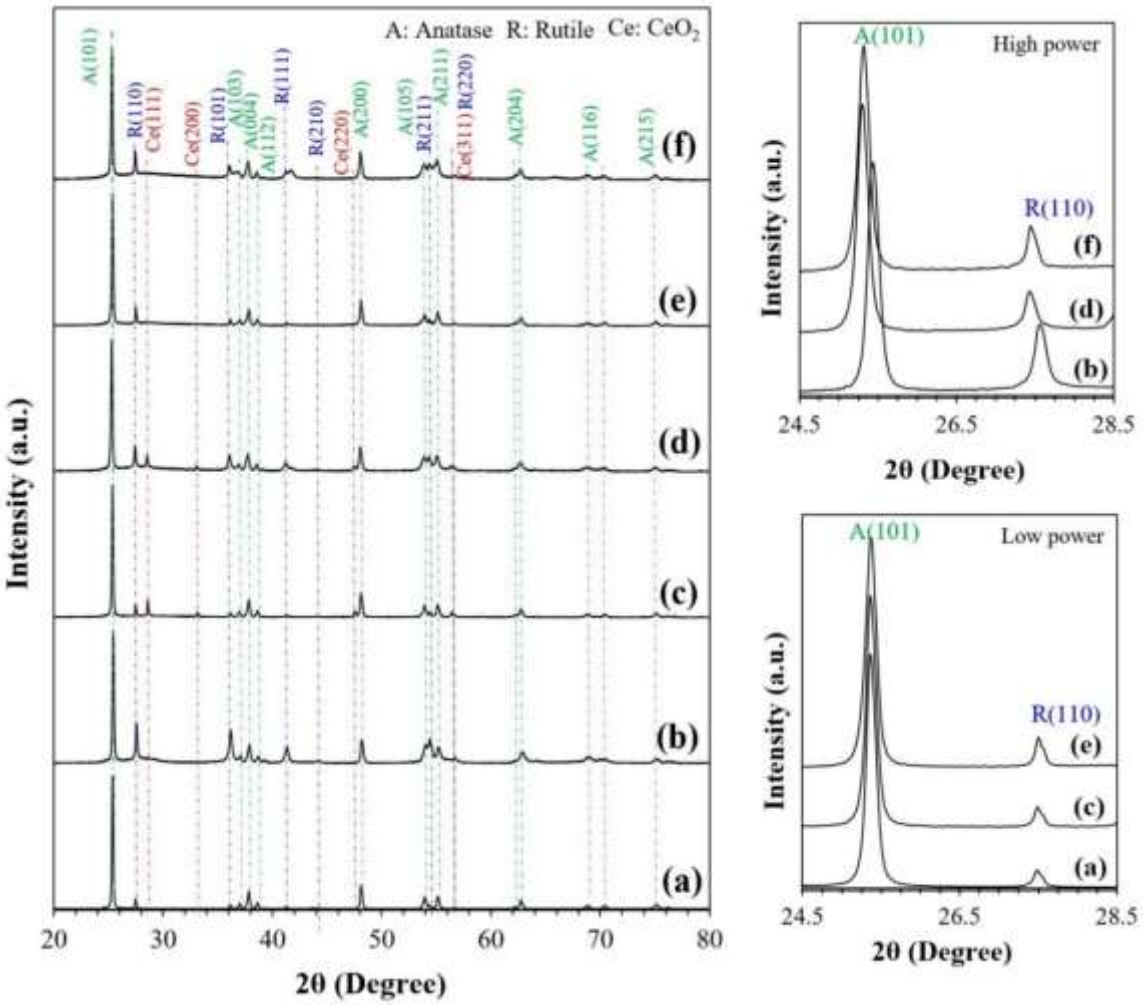

Figure 6. 11 Left side: XRD patterns of TiO_2 coatings as (a) TiO_2 (SPS)- Low power, (b) TiO_2 (SPS)- High power, (c) TiO_2- CeO_2 (SPS)- Low power, (d) TiO_2- CeO_2 (SPS)- High power, (e) TiO_2- CeO_2 (SPS-SPPS)- Low power, and (f) TiO_2- CeO_2 (SPS-SPPS)- High power. Right side: XRD shift of the most intense anatase and rutile peaks.

Table 6. 4 Phase content and crystallinity percentage of the coatings derived from Fig. 6.11.

Sample		Anatase (wt%)	Rutile (wt%)	CeO_2 (wt%)	Crystallinity (%)
TiO_2 (SPS)	Low power	89.5	10.5	-	87.2
	High power	59.5	40.5	-	73.1
TiO_2- CeO_2 (SPS)	Low power	53	8	39	78.4
	High power	53.5	19	27.5	69.3
TiO_2- CeO_2 (SPS-SPPS)	Low power	78.5	21.5	-	68.3
	High power	68.5	31.5	-	63

XRD results showed the presence of CeO_2 crystalline phase in the TiO_2-CeO_2 (SPS) coatings. While no ceria characteristic peaks were found in the XRD patterns of TiO_2- CeO_2 (SPS-

SPPS) coatings, indicating that cerium was successfully doped into the lattice of TiO_2 [53][222]. The crystalline sizes, lattice parameters and cell volumes of coatings were also calculated and summarized in Table 6.5. As can be seen, the crystallite size of the high-power coatings decreased compared to their low-power counterparts. Also, anatase and rutile unit cell volumes of high-power TiO_2- CeO_2 (SPS) and TiO_2- CeO_2 (SPS-SPPS) coatings increased in comparison to high-power TiO_2 (SPS) coating. Based on the XRD patterns, some peak shifts of anatase and rutile characteristic peaks were seen for the high-power TiO_2- CeO_2 (SPS) and TiO_2- CeO_2 (SPS-SPPS) coatings than high-power TiO_2 (SPS) coating. Literature suggests that crystallite size would decrease with increasing microstrain, presented by XRD peak broadening [223]. So, higher oxygen vacancy content induced at higher plasma power [212] might increase the microstrain and reduce the apparent crystallite size. Moreover, cerium doping can increase the interplanar spacing and cell volume of the coatings due to the larger ionic radius of Ce^{4+} and Ce^{3+} (0.103 nm and 0.09, respectively) than that of Ti^{4+} (0.068 nm). It has been shown that doping might change the position of the XRD peaks [53][54][222][143]. Figure 6.11 shows the peak shifting of high-power TiO_2- CeO_2 (SPS) and TiO_2- CeO_2 (SPS-SPPS) coatings compared to TiO_2 (SPS).

Table 6. 5 Crystallite size, cell parameters a and c, and cell volume of the coatings derived from XRD results.

Sample		Crystallite size (nm)		Unit cell parameter					
				Anatase			Rutile		
		Anatase	Rutile	a (Å)	c (Å)	Cell Volume (Å^3)	a (Å)	c (Å)	Cell Volume (Å^3)
TiO_2 (SPS)	Low power	80.4	111	3.781	9.418	134.66	4.586	2.956	62.18
	High power	62.4	65.6	3.777	9.314	132.86	4.574	2.952	61.78
TiO_2- CeO_2 (SPS)	Low power	79	121.6	3.781	9.413	134.60	4.585	2.957	62.16
	High power	66.3	87.4	3.786	9.523	136.51	4.596	2.961	62.53
TiO_2- CeO_2 (SPS-SPPS)	Low power	69.7	117.2	3.781	9.405	134.44	4.583	2.956	62.10
	High power	64.1	94.7	3.785	9.491	135.93	4.593	2.961	62.46

Micro-Raman spectrometer was used to investigate the presence of each crystalline phase in the melted and un-molten areas. Raman spectra of the coatings are displayed in Figs. 6.12, 6.13, and 6.14. Accordingly, Raman peaks at 144, 197, 399, 513, and 639 cm^{-1} are assigned to the anatase crystalline phase. While the Raman spectrum of the rutile phase is located at 143, 236, 447 and 613 cm^{-1}. Moreover, CeO_2 fluorite type presents a band at 463 cm^{-1} [179][204][69]. The Raman results of the cross-sectioned coatings presented only the characteristic signals of the anatase phase in the un-melted zones, confirming that these areas have the same crystallographic phases as the starting powder, which were shown in SEM micrographs as well (Fig. 6.6). At the same time, rutile characteristic bands were detected in the melted areas. Moreover, CeO_2 peaks were only found in the un-melted areas of TiO_2- CeO_2 (SPS) coatings produced at two powers (Fig. 6.12). Based on the results, all samples presented a slight peak shift from 144 cm^{-1} to 142 cm^{-1} due to oxygen vacancy or lattice defect [54], as shown in Fig. 6.13. All low-power coatings presented the same position of the main peak at 142 cm^{-1}. However, at high power, the peak

position of the melted area of the TiO_2- CeO_2 (SPS) and TiO_2- CeO_2 (SPS-SPPS) coatings slightly shifted to a higher wavenumber side (Fig. 6.13). The peak shift indicates small TiO_2 structural deformation probably due to the cerium doping [224].

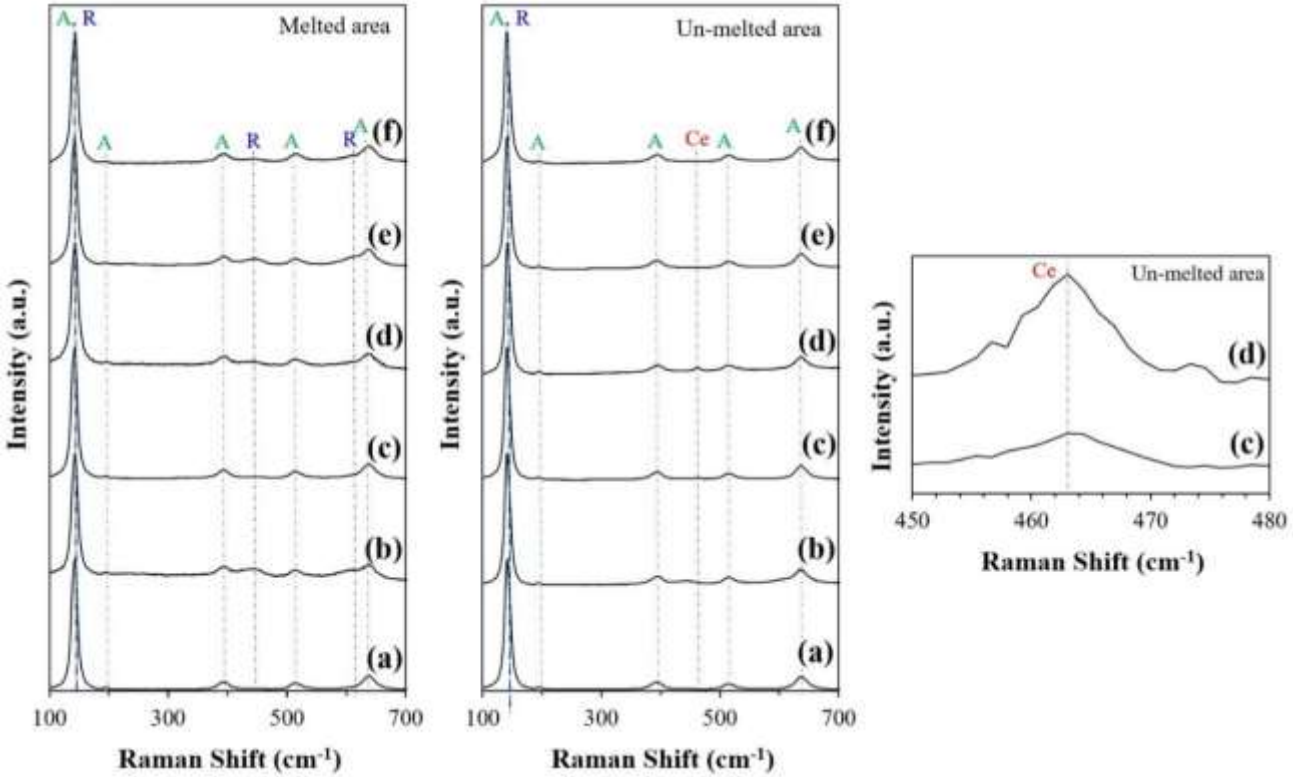

Figure 6. 12 Left side and middle: Raman spectra result in the melted and un-melted regions on the cross-sections of TiO_2 coatings as (a) TiO_2 (SPS)- Low power, (b) TiO_2 (SPS)- High power, (c) TiO_2- CeO_2 (SPS)- Low power, (d) TiO_2- CeO_2 (SPS)- High power, (e) TiO_2- CeO_2 (SPS-SPPS)- Low power, and (f) TiO_2- CeO_2 (SPS-SPPS)- High power, which A denotes the anatase phase and R the rutile phase. Right side: detail of the most intense ceria peak for TiO_2- CeO_2 (SPS) samples produced at low and high power.

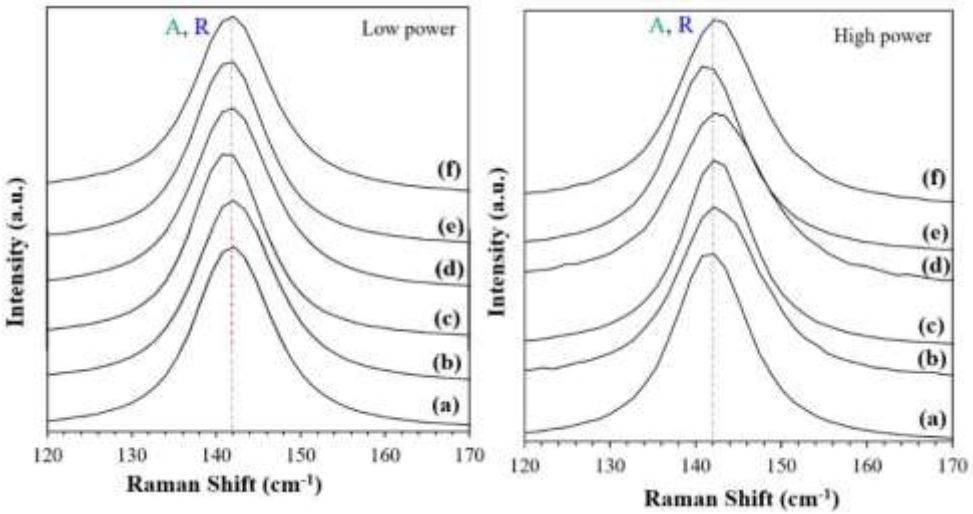

Figure 6. 13 Raman shift of the main TiO_2 band of the coatings' cross-sections produced at different powers as (a) TiO_2 (SPS)- un-melted area, (b) TiO_2 (SPS)- melted area, (c) TiO_2- CeO_2 (SPS)- un-melted area, (d) TiO_2- CeO_2 (SPS)- melted area, (e) TiO_2- CeO_2 (SPS-SPPS)- un-melted area and (f) TiO_2- CeO_2 (SPS-SPPS)- melted area.

As the photocatalytic reaction takes place on the surface, a Raman analysis was also performed on the coatings' top surfaces to investigate the phase distribution of the surface. According to Fig. 6.14, anatase was the only phase detected for low-power coatings. Though, coatings produced at high power presented rutile characteristic peaks. In addition, CeO_2 peaks were detected in the TiO_2- CeO_2 (SPS) coatings.

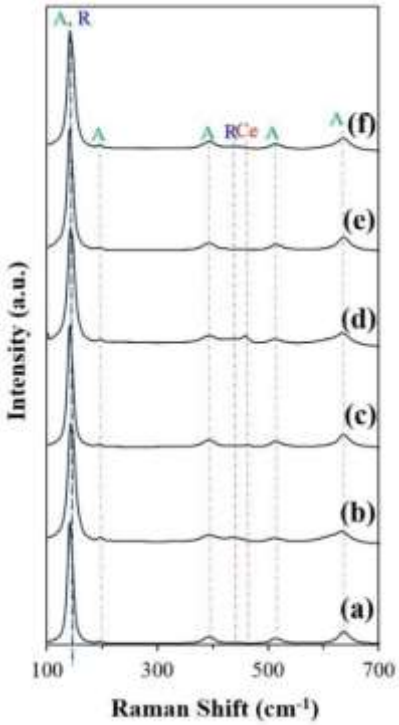

Figure 6. 14 Raman spectra results at the top surface of coatings as (a) TiO_2 (SPS)- Low power, (b) TiO_2 (SPS)- High power, (c) TiO_2- CeO_2 (SPS)- Low power, (d) TiO_2- CeO_2 (SPS)- High power, (e) TiO_2- CeO_2 (SPS-SPPS)- Low power, and (f) TiO_2- CeO_2 (SPS-SPPS)- High power, which A denotes the anatase phase and R the rutile phase.

6.3.4 XPS analysis

All coatings were characterized by XPS to determine the chemical state and surface elemental composition. According to the XPS survey spectrum (Fig. 6.15), Ti 2p, O 1s, and C 1s elements are obviously observed in the coatings. Moreover, cerium element was seen in the TiO_2- CeO_2 (SPS) and TiO_2- CeO_2 (SPS-SPPS) coatings.

The high-resolution Ti 2p XPS spectra (Fig. 6.16 left) of the coatings showed two main peaks of Ti^{4+} at 459 eV and 464.5 attributed to the Ti $2p_{3/2}$ and Ti $2p_{1/2}$, respectively [57][82][56]. Minor peaks at lower binding energies of 456.8 eV and 458.1 eV confirmed the presence of Ti^{3+} or TiO_2 suboxide for the coatings containing cerium as a dopant and TiO_2- CeO_2 composite coatings [35].

Figure 6.16 depicts high-resolution O 1s XPS spectra of coatings (middle graph). The peaks located at 530.3 eV, 531.9 eV and 532.8 eV are ascribed to the O^{2-} ions in the metal oxide crystal structure (Ti-O bonds), the bridge oxygen on the surface, and Ti-OH of TiO_2, respectively [56]. In addition, the small peak at 528.1 eV corresponding to TiO_2 suboxide or Ce-O bonds is also observed in CeO_2 (SPS) and TiO_2- CeO_2 (SPS-SPPS) coatings.

The Ce 3d high-resolution spectra of the TiO_2- CeO_2 (SPS) and TiO_2- CeO_2 (SPS-SPPS) coatings are displayed in Fig. 6.16 (right) and labelled as $3d_{5/2}$ and $3d_{3/2}$ spin-orbital. The results show that the mixture of both Ce^{3+} and Ce^{4+} states is presented in the coatings. However, Ce^{3+} diffraction peaks were not detected by XRD patterns in Fig. 6.11, indicating its low content. Ce 3d data extracted from Fig. 6.16 are tabulated in Table 6.6 [222][225][226].

Based on our previous results [150][212], TiO_2 coatings deposited by SPS were sub-stoichiometric, and a thermogravimetric analysis was performed to measure the oxygen vacancy level. Although in this work, no peak related to Ti^{3+} or suboxide TiO_2 was found for the TiO_2 (SPS) coatings that could be attributed to the XPS detection limit [225]. These results indicated the presence of reduced cerium states (Ce^{3+}) in TiO_2-CeO_2 (SPS) and TiO_2-CeO_2 (SPS-SPPS) coatings. It creates additional oxygen vacancies above the XPS detection limit to maintain charge neutrality [225].

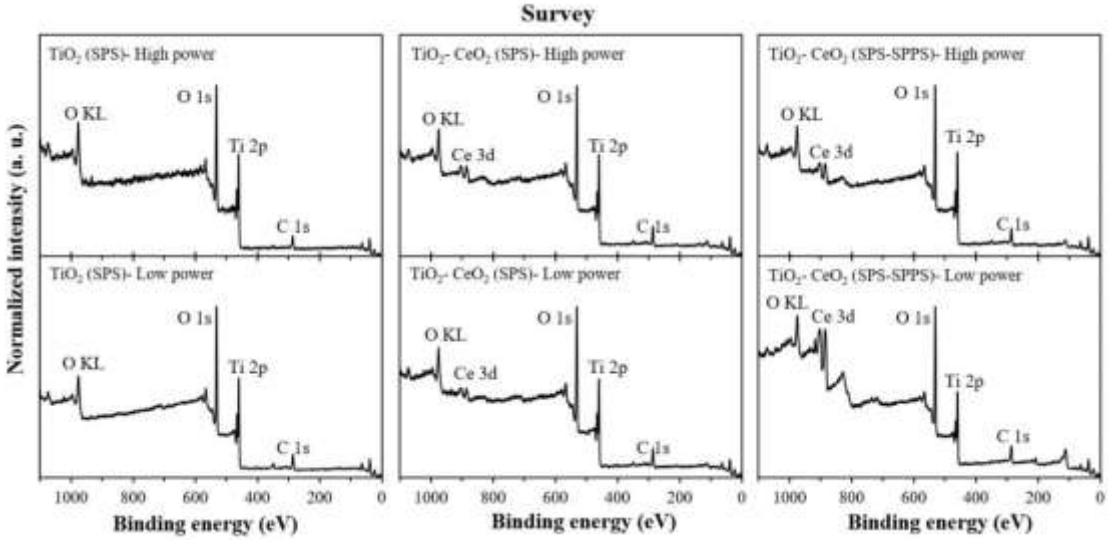

Figure 6. 15 XPS survey spectra of the top surface of coatings.

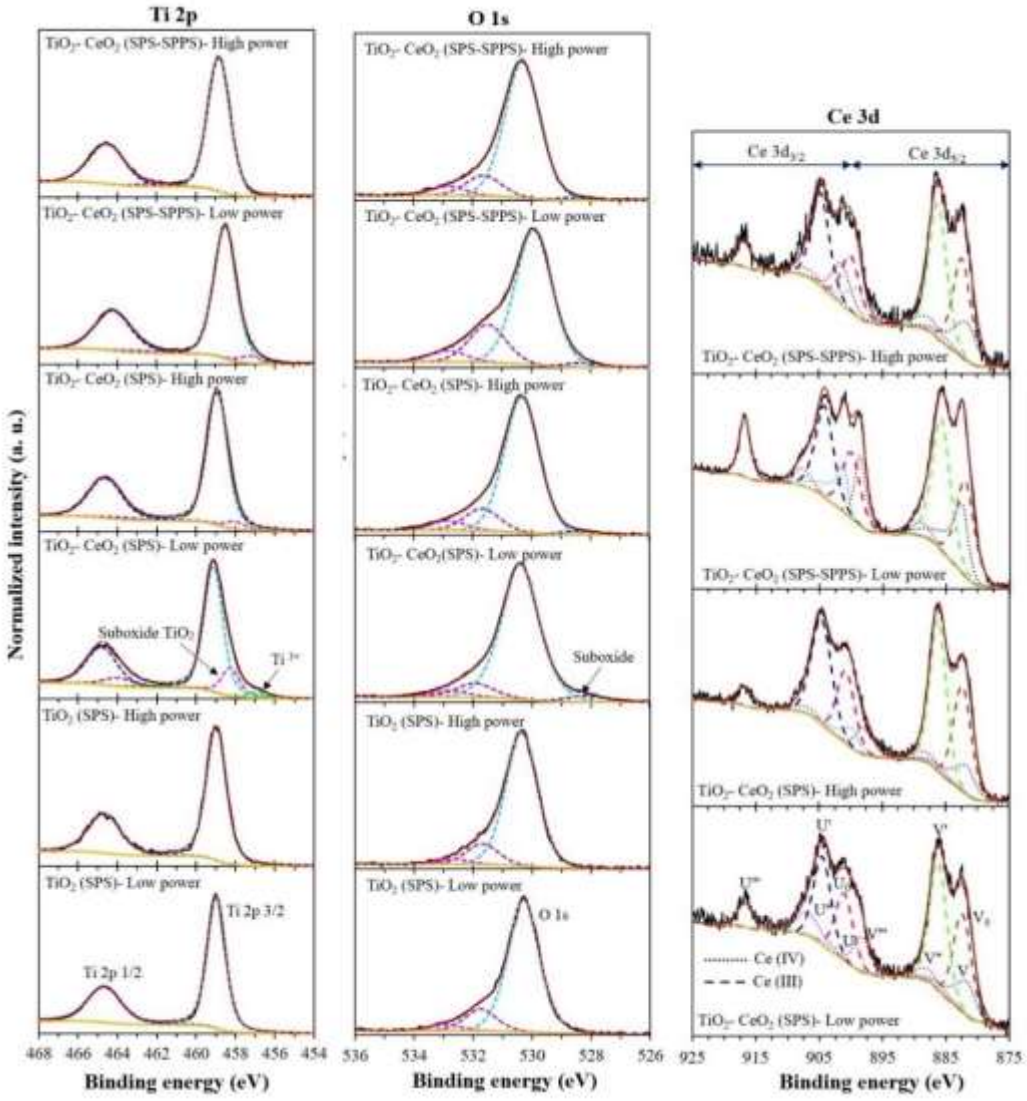

Figure 6. 16 High-resolution XPS spectra of Ti 2p, O 1s, and Ce 3d of the top surface of coatings.

Table 6. 6 XPS Data of Ce 3d peaks of TiO_2- CeO_2 (SPS) and TiO_2- CeO_2 (SPS-SPPS) coatings.

Sample	Power	Ce $3d_{5/2}$					Ce $3d_{3/2}$				
		V_0	V	V'	V''	V'''	U_0	U	U'	U''	U'''
		Ce (III)	Ce (IV)	Ce (III)	Ce (IV)	Ce (IV)	Ce (III)	Ce (IV)	Ce (III)	Ce (IV)	Ce (IV)
TiO_2- CeO_2 (SPS)	Low	882.2	881.5	885.8	887.7	897.8	900.7	899	904.3	906.7	916.2
	High	882	881.5	885.9	887.8	897.3	900.4	899.5	904.2	906.6	916.2
TiO_2- CeO_2 (SPS-SPPS)	Low	881.6	882.2	885.5	888.5	898.3	899.5	901.3	904.6	907.3	916.6
	High	882.1	881.4	886	887.8	901.2	899.8	899.7	904.5	906.7	916.5

6.3.5 Optical properties

A UV-Vis spectrophotometer was utilized to investigate the optical properties and light sensitivities of the coatings. Figure 6.17 shows the UV-Vis absorption spectra of the coatings. It has been shown that all high-power coatings presented higher visible light absorption compared to low-power coatings. Among high-power coatings, it was observed that the band edge position of

TiO_2- CeO_2 (SPS) and TiO_2- CeO_2 (SPS-SPPS) coatings shifted to a longer wavelength compared to TiO_2 (SPS) coating. Moreover, low-power coatings containing cerium showed higher absorption in the visible range in comparison with TiO_2 (SPS) coating. The absorption edge shifting in high-power coatings indicates their bandgap narrowing [35][70].

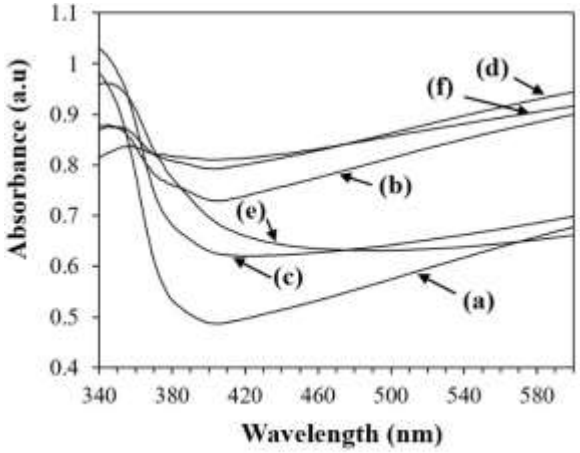

Figure 6. 17 UV-Vis absorption spectra of coatings as (a) TiO_2 (SPS)- Low power, (b) TiO_2 (SPS)- High power, (c) TiO_2- CeO_2 (SPS)- Low power, (d) TiO_2- CeO_2 (SPS)- High power, (e) TiO_2- CeO_2 (SPS-SPPS)- Low power, and (f) TiO_2- CeO_2 (SPS-SPPS)- High power.

Direct and indirect bandgap energies of the coatings determined from the intercept of the tangent to the $(\alpha h\nu)^2$-hν and $(\alpha h\nu)^{1/2}$-hν plots are given in Fig. 6.18 and summarized in Table 6.7. The results confirmed that the bandgap of the high-power coatings, and more specifically, TiO_2- CeO_2 (SPS) and TiO_2- CeO_2 (SPS-SPPS) coatings containing cerium decreased, which might be derived from either the existence of oxygen vacancy or the presence of cerium as a dopant/ composite in the TiO_2 structure. The role of the oxygen vacancy in optical properties and photocatalytic activity of the TiO_2 coatings was studied entirely in our previous works [150][212]. Literature suggests that the plasma spraying technique using H_2 secondary gas could produce sub-stoichiometric TiO_{2-x} coatings, while the higher the hydrogen flow rates, the higher the oxygen vacancy content [150][212][45]. The formation of new energy levels below the conduction band of the sub-stoichiometric TiO_{2-x} could effectively decrease the bandgap to be activated under visible light [138][63][65]. In addition, these energy levels within the sub-stoichiometric TiO_{2-x} bandgap can act as traps, helping to separate photo-generated electrons and holes. This feature can improve the material's photocatalytic efficiency when exposed to visible light [150][138][167][139][66].

Moreover, several works indicated the influential role of cerium doping in improving light utilization efficiency [54][225]. It has been suggested that unoccupied 4f states below the conduction band introduced by cerium doping are responsible for higher visible light absorption and lower bandgap of the Ce-doped TiO_2 samples [55]. Additionally, Jiang et al. [70] and Fan et al. [69] reported the bandgap narrowing of TiO_2- CeO_2 composite as a result of the formation of the TiO_2 and CeO_2 heterojunction.

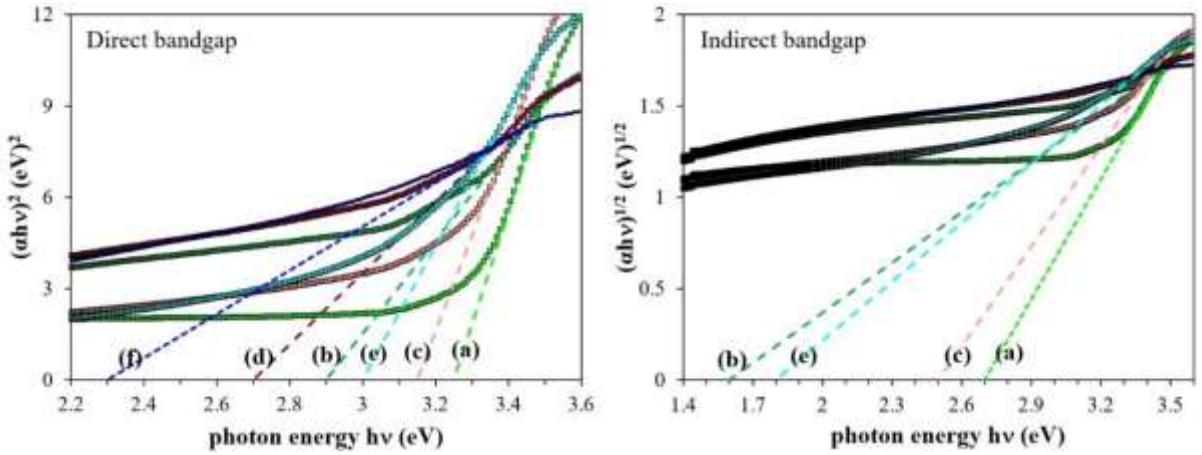

Figure 6. 18 Direct and indirect band energy diagram of coatings as (a) TiO_2 (SPS)- Low power, (b) TiO_2 (SPS)- High power, (c) TiO_2- CeO_2 (SPS)- Low power, (d) TiO_2- CeO_2 (SPS)- High power, (e) TiO_2- CeO_2 (SPS-SPPS)- Low power, and (f) TiO_2- CeO_2 (SPS-SPPS)- High power.

Table 6. 7 Calculated direct and indirect bandgap energies for coatings.

Bandgap		TiO_2 (SPS)		TiO_2- CeO_2 (SPS)		TiO_2- CeO_2 (SPS-SPPS)	
		Low power	High power	Low power	High power	Low power	High power
Direct	eV	3.25	2.9	3.15	2.7	3	2.3
	nm	381	427	393	459	413	539
Indirect	eV	2.7	1.6	2.5	-	1.8	-
	nm	459	774	496	-	688	-

6.3.6 Photocatalytic properties

The photocatalytic activity of the coatings was evaluated by the time-dependent photodegradation of methylene blue (MB) under visible-light irradiation. The reaction rate constants (k) obtained from the slopes of the graph ln (C_0 / C) versus irradiation time represent the photocatalytic activity of TiO_2 coatings, as shown in Fig. 6.19. A blank test without TiO_2 sample was measured as a benchmark to evaluate MB photolysis under light exposure. As illustrated in Fig. 6.19, TiO_2 (SPS) coatings presented the highest activity compared to TiO_2 coatings doped with cerium or composited with CeO_2.

In the photocatalysis process of TiO_2, electron-hole pairs are generated by ejecting electrons from the valence to the conduction band when it is illuminated with photon energy higher than its bandgap. Electrons and holes might be either recombined in bulk and on the surface of the photocatalyst or trapped on the surface and produce active radials (superoxide anions and hydroxyl radicals) to degrade organic compounds into harmless products [150][54]. The following reactions are suggested for TiO_2-CeO_2 nanocomposite as below [71]:

$$TiO_2 + h\nu \rightarrow e^- + h^+ \quad (6.5)$$

$$e^- + Ce^{4+} \rightarrow Ce^{3+} \quad (6.6)$$

$$Ce^{3+} + O_2 \rightarrow Ce^{4+} + O_2^{-*} \quad (6.7)$$

$$h^+ + H_2O\ (surface) \rightarrow OH^* + H^+ \quad (6.8)$$

$$O_2^{-*} + 4H^+ \rightarrow 2OH^* \quad (6.9)$$

$$Adsorbed\ MB + OH^* \rightarrow \text{Degraded products} \rightarrow H_2O + CO_2 \quad (6.10)$$

Based on the literature, compositing TiO_2 with CeO_2 could enhance its photocatalytic activity by improving the separation of the photogenerated charge carriers [69]. As depicted in Fig. 6.20 (a) in TiO_2-CeO_2 nanocomposite, electrons in the conduction band (CB) of CeO_2 inject into the CB of TiO_2 due to the lower energy. Likewise, holes in the valence band (VB) of TiO_2 transfer to the CeO_2 valence band [69][71]. It has been indicated that adding an optimum amount of CeO_2 nanoparticles could enhance the photocatalytic activity in the TiO_2-CeO_2 nanocomposite as a result of the effective interfacial charge separation and lower charge carrier recombination rate [69][70][71]. Based on the photocatalytic activity results and SEM images (Figs. 6.19 and 6.9), the lower activity of TiO_2- CeO_2 (SPS) composite coatings could be explained by covering TiO_2 active surface with inert submicron CeO_2 particles, as schematically shown in Fig. 6.20 (b). Therefore, lower electron-hole pairs would be generated upon light irradiation, suppressing their degradation ability.

According to the literature, cerium doping would improve photocatalytic activity by reducing the bandgap and improving charge carrier lifetime. It has been reported that Ce^{3+} incorporation might create charge imbalance or strain that could form oxygen vacancy. The presence of Ce^{3+}/Ce^{4+} mixture and oxygen vacancies would induce unoccupied 4f energy levels just below the TiO_2 conduction band, which could reduce bandgap and suppress the electron-hole recombination (Fig. 6.20 (c)) [53][54][55][56][57]. However, an optimum dosage of dopant is needed to improve photoactivity. Makdee et al. [54] reported the deleterious effect of cerium doping on the photocatalytic activity of TiO_2 upon increasing the cerium content. This can be explained by the formation of deep-level energy states close to the Fermi level that act as the charge recombination centers to decrease the charge carriers' lifetime, as depicted in Fig. 6.20 (d). Based on the XPS results (section 6.3.4), a higher amount of oxygen vacancies was induced in the coatings containing cerium which might be the reason of the lower photocatalytic activity of the cerium-doped coatings (TiO_2- CeO_2 (SPS-SPPS)). These results indicate that the optimum cerium content is needed to improve the photocatalytic efficiency.

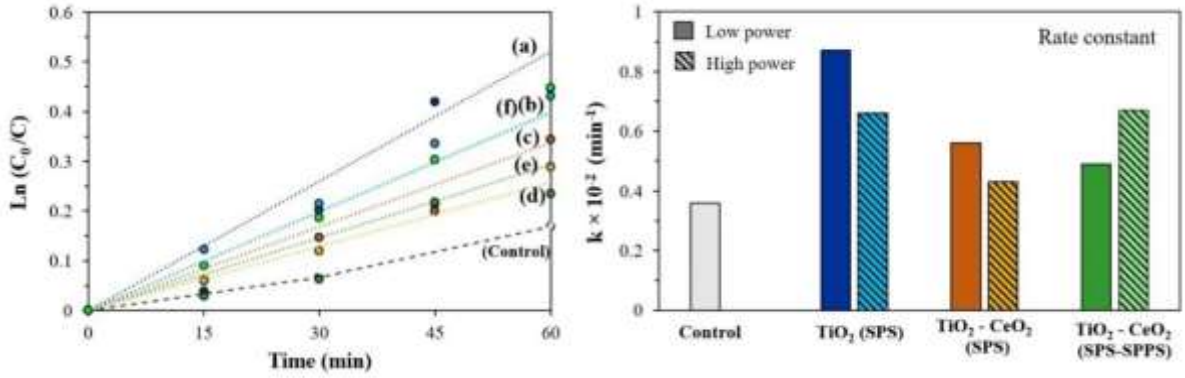

Figure 6. 19 Left side: Photocatalytic degradation of the MB solution under visible irradiation (C_0: initial concentration after dark test, C: MB concentration at irradiation time); Right side: Pseudo-first order rate constant of the degradation of MB by coatings as(a) TiO_2 (SPS)- Low power, (b) TiO_2 (SPS)- High power, (c) TiO_2- CeO_2

(SPS)- Low power, (d) TiO_2- CeO_2 (SPS)- High power, (e) TiO_2- CeO_2 (SPS-SPPS)- Low power, and (f) TiO_2- CeO_2 (SPS-SPPS)- High power.

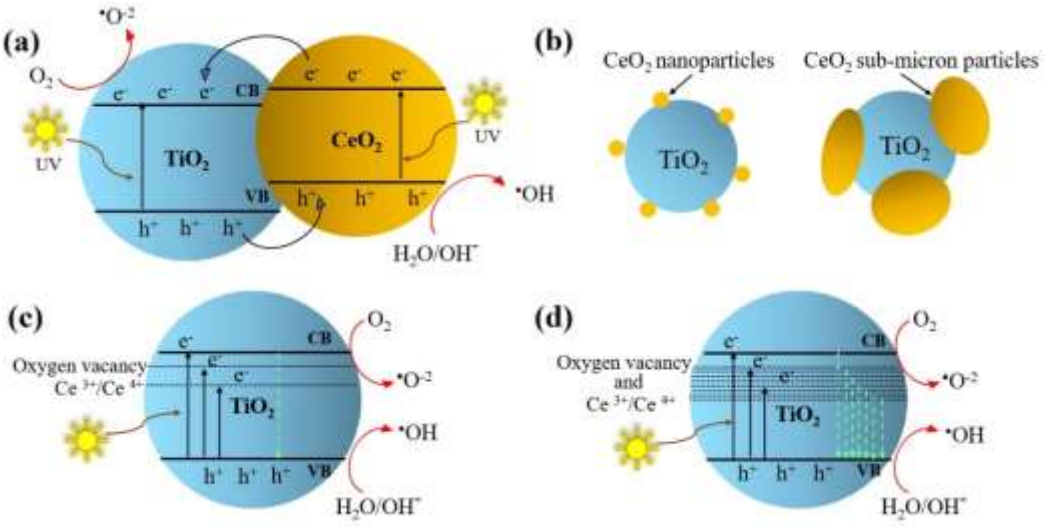

Figure 6. 20 (a) Schematic representation of the proposed photocatalytic mechanism of TiO_2- CeO_2 composite, (b) schematic of TiO_2- CeO_2 nanocomposite and TiO_2-CeO_2 composite of sub-micron powders (Adapted from references [69][71]), (c) schematic representation of the proposed photocatalytic mechanism of Ce-doped TiO_2 at the optimum amount of dopant, (d) and at higher dosage of cerium dopant (Adapted from references [54]).

6.4 Conclusion

In this research work, TiO_2- CeO_2 composite (TiO_2- CeO_2 (SPS)) and Ce-doped TiO_2 coatings (TiO_2- CeO_2 (SPS-SPPS)) have been deposited by suspension plasma spraying (SPS) and suspension/solution precursor plasma spraying (SPS-SPPS) techniques at different conditions and the influence of the cerium on optical and photocatalytic properties of TiO_2 coatings were investigated. The existence of the cerium dopant was confirmed by EDS mapping, XRD peaks and Raman peak shifting. Moreover, XPS analysis confirms the presence of Ce ions in the form of a mixture between Ce^{3+} and Ce^{4+}, indicating the formation of higher oxygen vacancies in Ce-doped and CeO_2 composite coatings. The experimental UV-Vis results indicate that cerium doping or CeO_2 composite with TiO_2 could effectively move the absorbance edge of TiO_2 coatings toward the visible range. However, pure TiO_2 coating (TiO_2 (SPS)) presented better photocatalytic activity. Sub-micron CeO_2 particles in the composite matrix covered the active surface of TiO_2 particles and decreased the photocatalytic efficiency of the coatings. Additionally, the lower photocatalytic activity of the Ce-doped TiO_2 coatings can be explained by the formation of the deep-level point defects (such as oxygen vacancy) originating from a not optimal dosage of dopant that could increase the recombination rate of photogenerated charge carriers. In the current study, the SPS-SPPS method has shown a promising technique for doping TiO_2 while further investigation is needed to optimize the dopant concentration and improve its uniformity in the coating by changing the suspension concentration and plasma spray parameters, respectively.

Acknowledgement

This study was financially supported by the Natural Sciences and Engineering Research Council of Canada (NSERC) through Canada Research Chairs and Discovery Grants Programs.

Preface to Chapter 7.

In previous chapters, highly active TiO_2 coatings were produced and the ability of plasma spray technique to create doped-TiO_2 coatings was shown. In the current chapter, a practical approach was utilized to investigate the overall performance of thermal spray technology in the perspective of protecting public health against the viral transmission such as human coronavirus disease (COVID-19) and improve antiviral surface technologies for possible future pandemics minimizing risks to individuals and public health.

Chapter 7. Antiviral properties of thermal sprayed coatings against human coronaviruses HCoV-229E [4]

Abstract

For decades, novel viral strains of respiratory tract infections have caused human pandemics and initiated widespread illnesses, deaths, and disruptions. The recent Coronavirus disease 2019 (COVID-19) outbreak caused by SARS-CoV-2 virus has raised an urgent need to develop novel antiviral coatings as one of the potential solutions to mitigate the transmission of viral pathogens. Titanium dioxide (TiO_2) is considered an excellent candidate for viral disinfection under light irradiation, with the potential to be activated under visible light for indoor applications. This research assessed the antiviral performance of thermally sprayed TiO_2 coatings under UVA and ambient light. We also report the antiviral performance of TiO_2 composites with other oxides, such as Cu_2O and Al_2O_3, produced by SPS, APS, and suspension HVOF techniques. To evaluate the antiviral performance of the above coatings in a containment level-2 laboratory, a human common cold coronavirus, HCoV-229E, was initially used as a relevant surrogate for SARS-CoV-2. Coatings were also analyzed using SEM and XRD and were classified based on their surface roughness, porosity, and phase composition. Collectively, our data indicate that thermal sprayed TiO_{2-x} coatings serve as a promising antipathogenic solution for indoor applications on highly touched surfaces and in ventilation systems. Moreover, the versatile and scalable thermal spray technology makes this process compatible with industrial production.

Keywords: TiO_2; Cu_2O; Photoactivity; Contact-Killing; Antiviral Coatings; Thermal spray; Human Coronaviruses HCoV-229E; COVID-19

7.1 Introduction

As of March 2020, the widespread and rapid increase of the novel human coronavirus disease (COVID-19), which causes severe acute respiratory syndrome (SARS) named SARS-CoV-2, has raised worldwide attention towards public health. The World Health Organization reported in early November 2022 over 627 million cases of infection, including over 6.5 million deaths, due to the COVID-19 pandemic [8][9]. After SARS coronavirus and Middle East Respiratory Syndrome (MERS) coronavirus, this is the third highly pathogenic human coronavirus that was spread over the past two decades [8].

Vaccination against SARS-CoV-2 has been developed since 2020, with acceptable success [227]. However, vaccination cannot prevent the emergence of new variants. Infectious pathogens could be transmitted either directly from close person-to-person contact or indirectly through hand-

[4] This chapter is to be submitted as an article to the scientific Journal. Hediyeh Khatibnezhad, Elnaz Aleebrahim, Morvarid Mohammadian Bajgiran, Fadhel Ben Ettouil, Megan Solomon, Selena Sagan, Steve Beaudin, Jörg Oberste-Berghaus, Rogerio S. Lima, Chen Liang, Christian Moreau

touch contact after deposition on surfaces [91]. Based on the literature, airborne transmission of SARS-CoV-2 virus was the main transmission route [228], but previous studies revealed that the highly contagious COVID-19 virus could remain infectious for days on some surfaces [91]. To inhibit the risk of indirect transmission of infections, coated surfaces with intrinsic antiviral materials could be more effective than frequent cleaning of the environment. Regular cleaning in public places is costly, and re-contamination may occur. An incomplete cleaning process or ineffective cleaning agents may also leave viral residues that may continue to contaminate surfaces [94][229]. Moreover, respiratory disease symptoms such as coughing and mucus production would contaminate the cleaned surfaces frequently and increase the risk of virus transmissions [8]. Healthcare facilities are mostly made of stainless-steel surfaces as a common material due to its corrosion resistance and clean appearance. However, stainless steel has no antimicrobial capabilities and bacteria can attach and grow on them easily [92][93]. Thus, developing highly efficient, low-cost, and environmentally friendly antiviral coatings as one of the potential solutions to mitigate the transmission of viral diseases seems a reasonable solution. The antimicrobial properties of various metals, particularly copper and silver, have been extensively studied and documented [230]. The COVID-19 pandemic caused a surge in research interest in copper due to its ability to deactivate viruses, which is directly related to the amount of copper in the surface of the alloy. However, using copper-based materials on a large scale during a pandemic could pose risks of toxicity and environmental issues [231].

Since the antibacterial properties of titanium dioxide (TiO_2) photocatalyst was reported by Matsunaga et al. in 1985 [232], TiO_2 has attracted ever-growing worldwide attention for antipathogenic applications due to its unique mechanical and chemical resistance [16][17][18][19]. TiO_2 can be excited by light irradiation to produce powerful reactive oxygen species (ROS) with strong oxidizing power for airborne pathogen inactivation under ambient conditions. Interaction of the virus with the photocatalytic surface results in substantial changes in the virus structure, leading to the loss of the ability of the virus to attack host cells [17][95].

Among the two main crystalline phases of TiO_2, the anatase phase presented the highest activity for photoactive applications. However, previous reports have shown the synergistic effects of the mixture of anatase and rutile phases that could enhance the photoactivity of TiO_2 photocatalyst [92][212][166][22]. Furthermore, based on the literature, increasing the surface area could also improve the photoactivity of TiO_2 photocatalysts by increasing the active sites for reaction initiation and decreasing the charge carrier's recombination rate by introducing some trapping sites [3][83][37].

Alumina could be utilized with TiO_2 to improve the mechanical properties of TiO_2 coatings [233][234]. Among different alumina phases, the stable corundum phase (α-Al_2O_3) presents high chemical stability, high electrical resistance, and good thermal and mechanical properties [177].

Copper oxide (Cu_2O) coatings also show potent antiviral activity, even under dark conditions [91][96][97]. Recent interest in visible light-sensitive Cu_2O-TiO_2 nanocomposite has been substantial due to its sustainable antiviral activity under dark conditions. Cu_2O-TiO_2 nanocomposite is desirable for indoor environmental remediation applications and also exhibits strong antiviral activity under dark conditions during the night when indoor light instruments are switched off [90][98]. These coatings would be less susceptible to viral contamination and can minimize the spread of the viruses.

TiO_2 films and coatings have been fabricated by various techniques; however, introduction into the market of antiviral coatings relies on the capability of the coating deposition technique for mass production. Thermal spray technology appears as a versatile and rapid processing approach

where the large surface area coverage and fast deposition rate (up to hundreds of microns in a couple of minutes) make this deposition process compatible with the industry [92][235][121]. Spray processes have other advantages, such as the flexibility of producing a wide variety of high-quality coatings on substrates with different shapes and sizes [114]

Based on our previous work [212][150], thermally sprayed sub-stoichiometric TiO_{2-x} coatings presented remarkable photocatalytic performance under visible light. These coatings were deposited using the suspension plasma spray (SPS) process. The results indicated the effect of the oxygen deficiency and Ti^{3+} ions on decreasing the bandgap energy and shifting the absorption edge to the visible light range [150].

In this research work, TiO_2, Cu_2O, TiO_2-Cu_2O and TiO_2-Al_2O_3 antiviral coatings were produced using different thermal spray processes, including atmospheric plasma spray (APS), suspension plasma spray (SPS), and suspension high-velocity oxygen fuel (S-HVOF). Eventually, the human common cold coronavirus, HCoV-229E, was used as a surrogate for SARS-CoV-2 to investigate the antiviral activity of the coatings in a containment level-2 laboratory.

7.2 Experimental procedure

7.2.1 Preparation of antiviral coatings

Submicron-sized titanium dioxide (TiO_2) powder (TKB Trading, Oakland-USA), micron-sized TiO_2 powder (Metco 102- Metco Oerlikon, Fort Saskatchewan, Canada), nanostructured TiO_2 spray-dried powder (NEOXID T101 nano, Millidyne, Finland), copper oxide (Cu_2O) powder (PI-KEM, U.K.), aluminum oxide- 40% titanium dioxide powder (Al_2O_3- 40%TiO_2) (Amdry 6257- Metco Oerlikon, Fort Saskatchewan, Canada), and aluminum oxide- 13% titanium dioxide powder (Al_2O_3- 13%TiO_2) (Metco 130- Metco Oerlikon, Fort Saskatchewan, Canada) were used as feedstock materials to deposit coatings. SEM micrographs of the feedstock powders are shown in Fig. 7.1.

Different thermal spray processes were applied to produce the antiviral coatings on the grit-blasted 304 stainless steel coupons (1-inch diameter). Details of operating parameters are summarized in Tables 7.1 and 7.2. Five different types of TiO_2 coatings were produced to provide various microstructure, roughness, porosity, and anatase phase contents. 10 wt.% water-based TiO_2 suspensions without any dispersing agent were used as a feedstock material to deposit T1-SPS and T5-SHVOF coatings by suspension plasma spray (SPS) and suspension high-velocity oxygen fuel (S-HVOF) processes. Axial III^{TM} (Northwest Mettech Corp., Canada) and ID-Nova (Spraywerx technologies, Canada) plasma torches were applied for producing T1-SPS and T5-SHVOF coatings, respectively. ID-Nova HVOF spray torch is a new technology to spray the interior sections of the components. T2-APS, T3-APS, and T4-APS TiO_2 coatings were deposited by atmospheric plasma spray (APS) using S.G.- 100 (Praxair, USA), 100HE (Progressive Surface, USA), and 3 M.B. (Oerlikon Metco, Switzerland) plasma guns.

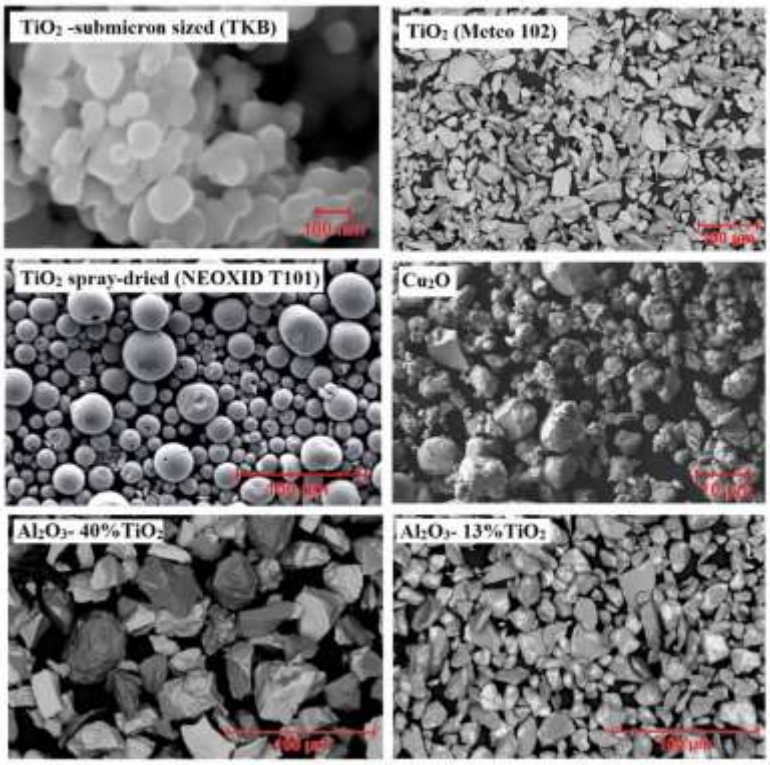

Figure 7. 1 SEM micrographs of the feedstock powders. Note: SEM micrographs of TiO_2 powder (Metco 102), Al_2O_3- 40%TiO_2, and Al_2O_3- 40%TiO_2 are taken from the data sheets provided by Metco Oerlikon.

Cu_2O and TiO_2- Cu_2O (75% TiO_2 – 25% Cu_2O) coatings were deposited by SPS method with a 3 MB plasma torch. 10 wt.% ethanol-based suspensions containing a small quantity of polyvinylpyrrolidone (PVP) (Sigma-Aldrich, Oakville, Canada) (5 wt.% corresponding to the solid content) as a dispersing agent were used to deposit C-SPS and TC-SPS coatings. A roller mill was utilized for suspensions for five days to increase the homogeneity and break down large agglomerates. The particle size distribution of the suspensions was measured by a Spraytec unit (Malvern Instruments, U.K.), as shown in Fig. 7.2.

Table 7. 1 Thermal spray deposition parameters.

Sample	Feedstock material	Thermal spray process	Plasma gun	Powder feed rate (g/min)	Suspension feed rate (mL/min)	Current (A)	Spray distance (mm)	Power (kW)
T1-SPS	TiO_2-TKB	SPS	Axial III^{TM}	-	30	220	75	77
T2-APS	TiO_2-Metco 102	APS	SG- 100	25	-	1000	100	35
T3-APS	TiO_2-Metco 102	APS	100HE	100	-	400	115	95
T4-APS	TiO_2- NEOXID T101	APS	3MB	20	-	500	75	29
T5-SHVOF	TiO_2-TKB	S-HVOF	ID-Nova	-	36.5	-	30	H_2-O_2 (380-190)
C-SPS	Cu_2O	SPS	3MB	-	35	500	50	17.5
TC-SPS	Cu_2O & TiO_2-TKB	SPS	3 M.B.	-	35	500	50	20
A40%T-APS	Al_2O_3- 40%TiO_2 (Amdry 6257)	APS	F-4	30	-	480	120	30
A13%T-APS	Al_2O_3- 13%TiO_2 (Metco 130)	APS	100HE	90	-	260	115	65

Table 7. 2 Primary and secondary gas flow rates for plasma sprayed coatings (SPS and APS coatings)

Sample	Ar flow rate (L/min)	Secondary gas flow rate (L/min)		
		H_2	He	N_2
T1-SPS	Gas flow (SLPM): 223, Gas mixture (%): Ar: 82/ N_2: 11/ H_2: 7			
T2-APS	42.7	-	27.4	-
T3-APS	85	66	-	66
T4-APS	40	8	-	-
C-SPS	50	-	10	-
TC-SPS	50	1	-	-
A40%T-APS	40	8	-	-
A13%T-APS	86	56	-	56

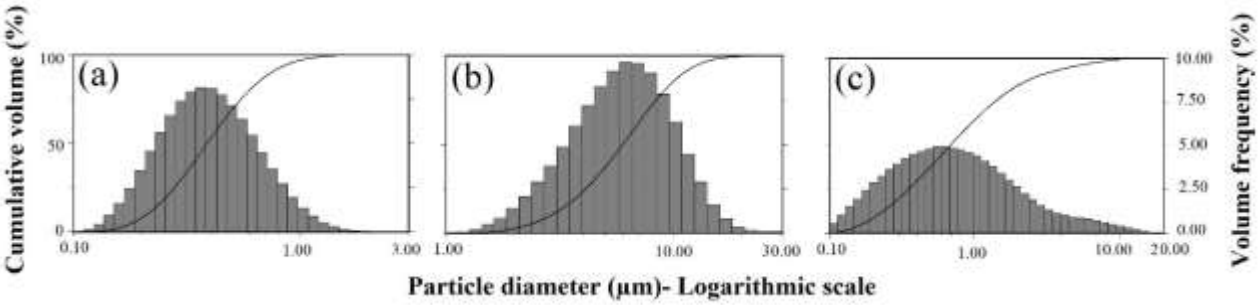

Figure 7. 2 Particle size distribution of the suspensions: (a) TiO_2: d10=0.2 μm, d50=0.39 μm, d90=0.75 μm, (b) Cu_2O: d10=2.9 μm, d50=5.9 μm, d90=11 μm, (c) TiO_2- Cu_2O: d_{10}=0.2 μm, d_{50}=0.68 μm, d_{90}=2.8 μm, to deposit T1-SPS / T5-SHVOF, C-SPS, and TC-SPS coatings, respectively.

Furthermore, TiO_2-Al_2O_3 composite coatings were manufactured by APS techniques. Two feedstock powders containing different quantities of the TiO_2 (40% and 13%) were used to evaluate the role of TiO_2 content on the antiviral activity of the coatings.

7.2.2 Characterization and evaluation

The morphology of the powder, surface of the coatings, and polished cross-section of the coatings were observed with a field emission scanning electron microscope (FESEM JSM 7600TFE, JEOL, Japan) in secondary electron and backscattered electron modes. The surface roughness of the coatings was measured with a confocal laser microscope (LEXT OLS4000 Olympus, Toronto, Canada), and the arithmetic average surface roughness (Ra) has been reported. The phase analysis of the coatings was carried out by the X-ray diffraction (XRD) technique (X'Pert pro, PANalytical, Philips, Netherlands) in a range of 10−75° with Cu Kα radiation and a step size of 0.02°. The phase content was quantified by the tabulated reference intensity ratio using DIFFRACT.EVA software (Bruker, USA) and PDF-2 database (international center for diffraction data).

7.2.2.1 Antiviral activity measurements

The antiviral performance of selected coatings was assessed in a containment level 2 bio lab under UVA light (Fisher Scientific, Canada), ambient light, and dark conditions. Two UVA (λ = 365 nm) lamps with a power of 15 W each were used. The intensity of UVA light was reduced by decreasing the transmission to eliminate the impact of UVA illumination killing the virus

directly. Therefore, the intensity of the UVA lights was decreased using 2.0 OD UV-NIR Neutral Density Filters (88-275, Edmund Optics Inc., U.S.), allowing only 1% transmission. The distance between the surface of the samples and UVA lights was around 7 cm, and the distance between the surface of the samples and the UV-NIR filters was around 2 cm, allowing a normal air circulation over the surface of the samples. The ambient light was provided using white LED lights, generally used to illuminate inside the fume hood. The intensity of the ambient light was measured at around 500 lux using a light meter (LANTEX LM-50KL, ON, Canada).

The antiviral activity of the coatings was assessed using the HCov-229E-Luc virus as a surrogate for the SARS-CoV-2 virus [155]. The HCov-229E-Luc virus contains a Luciferase reporter gene allowing quantification of the relative amount of the viable virus in terms of Relative Luminescence Unit (RLU), determined by measuring the luminescence signal using a Luciferase assay [156].

HCoV-229E-Luc stocks containing 1000 Plaque Forming Units (PFU) were prepared in Dulbecco's Modified Eagle Medium (DMEM) containing 2% Fetal Bovine Serum (FBS). A 50 µl of the virus solution was put on the surface of the coatings. The coatings were exposed to ambient/UVA light or kept in the dark. The virus was recollected from the coating surface by pipetting 100 µL of media (Dulbecco's Modified Eagle Medium) at the coatings' surface at three-time points, 0 min, 10 min, and 20 min after exposure. A fresh coating was used for the test at each time point. The retrieved virus was then used to infect Huh7 cells in triplicates. Huh7 cells are a human epithelial liver cell line derived from hepatoma tissue, which supports HCoV-229E replication. A Renilla-Glo Luciferase Assay System (catalogue number E2720, Promega), with Perkin Elmer plate reader (Ensight, Perkin Elmer), was used to quantify the virus infection. Furthermore, a copper plate (Cu), with high antiviral activity, and a stainless steel 304 plate (S.S.) with no antiviral activity were used as positive and negative control samples, respectively [157][158]. The schematic of the antiviral activity assessment process is shown in Fig. 7.3.

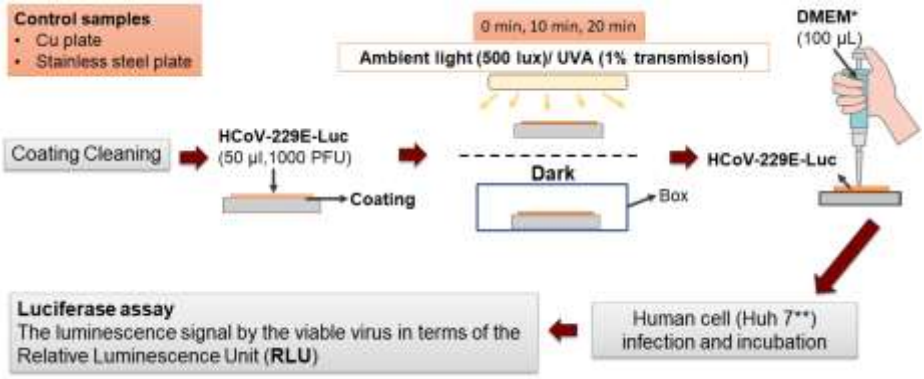

Figure 7. 3 Schematic of the antiviral activity assessment process.

7.3 Results and discussion

7.3.1 The phase composition and oxygen vacancy presence

XRD patterns and the derived information of TiO_2 and Cu_2O, TiO_2- Cu_2O and TiO_2-Al_2O_3 coatings are shown in Fig. 7.4 and Table 7.3. According to the results, various ranges of anatase phase contents were produced in TiO_2 coatings, while T1-SPS and T5-SHVOF coatings presented the highest anatase content.

XRD patterns (Fig. 7.4) show Cu_2O, CuO, and Cu phases for C-SPS coating and anatase, rutile, Cu_2O, and Cu phases for TC-SPS coating. According to the literature, copper (Cu) and Cu_2O are considered antibacterial/ antiviral materials by direct contact mechanism [91][236][237]. On the other hand, the inferior antiviral activity of CuO phase might be related to the less potential of CuO phase to adsorb and denature proteins [91]. In TiO_2-Al_2O_3 coatings, some part of the active TiO_2 phase was transformed into $TiAl_2O_5$ phase, as shown in Fig. 7.4 and Table 7.3. The formation of the aluminum titanate phase could be detrimental to the photoactivity of the coatings.

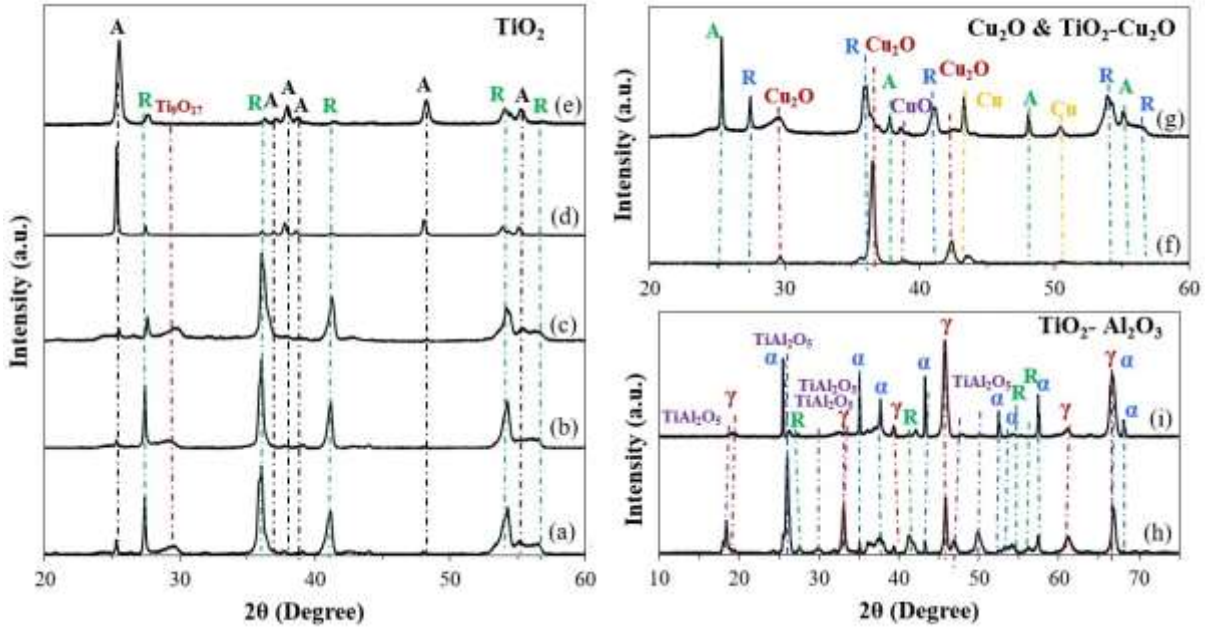

Figure 7. 4 XRD patterns of coatings as (a) T2- APS, (b) T3- APS, (c) T4- APS, (d) T1- SPS, (e) T5- SHVOF, and (f) C-SPS, (g) TC-SPS, (h) A40%T-APS, (i) A13%T-APS, which A denotes anatase phase, R rutile phase, α is α-Al_2O_3, and γ is γ-Al_2O_3.

Table 7. 3 Phase content of the coatings derived from Fig. 7.4.

Sample	%Anatase	%Rutile	%Ti_9O_{17}	%Cu_2O	%CuO	%Cu	%α-Al_2O_3	%γ-Al_2O_3	%$TiAl_2O_5$
T1-SPS	83	17	-	-	-	-	-	-	-
T2-APS	9.5	64.5	26	-	-	-	-	-	-
T3-APS	6	67.5	26.5	-	-	-	-	-	-
T4-APS	28	72	-	-	-	-	-	-	-
T5-SHVOF	82	18	-	-	-	-	-	-	-
C-SPS	-	-	-	65.1	18.2	16.7	-	-	-
TC-SPS	42	19	-	34	-	5	-	-	-
A40%T-APS	-	6	-	-	-	-	32.5	37	24.5
A13%T-APS	-	2	-	-	-	-	55	32	11

7.3.2 Coating microstructures and morphology

3-D maps of the top surfaces of the coatings taken by a confocal laser microscope are presented in Fig. 7.5. Based on the results, different surface roughnesses were produced using different thermal spray processes. T5-SHVOF coating showed the smoothest surface (R_a~1.8 µm), and the roughest surface was observed in TC-SPS coating (R_a~9.2 µm).

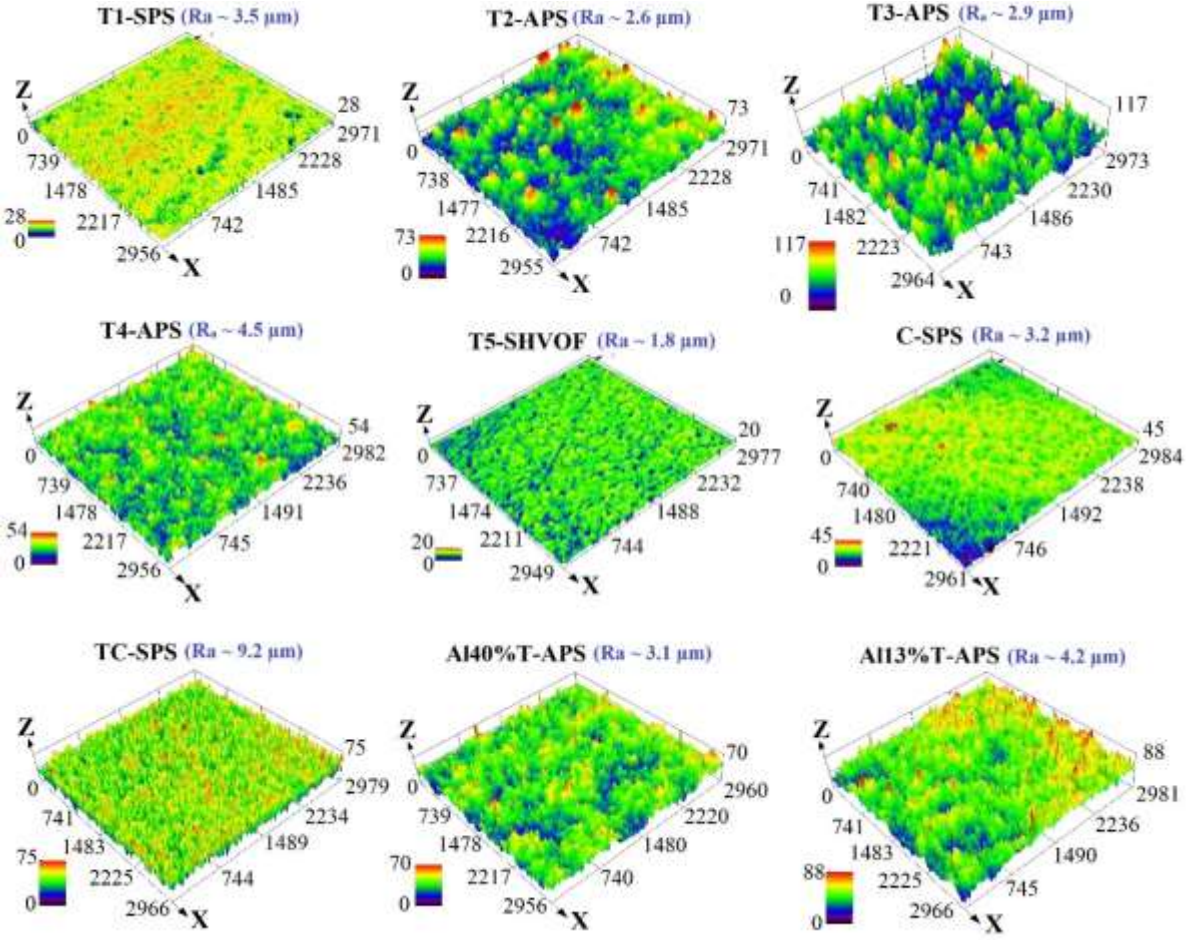

Figure 7. 5 Top surface 3D images of the coatings provided by the confocal laser microscope.

The SEM micrographs of the coating cross-sections and top surfaces are shown in Figs. 7.6 - 7.10. Cross-sectioned SEM images of TiO_2 coatings (Fig. 7.6) showed mechanically stable coatings firmly bonded to the surface. According to the top surface images of TiO_2 coatings, T1-SPS and T5-SHVOF coatings presented higher fine porosities, as shown in Fig. 7.7. At higher magnification (Fig. 7.8), un-melted agglomerated particles and re-solidified particles were observed in the coatings produced by suspension as the feedstock material.

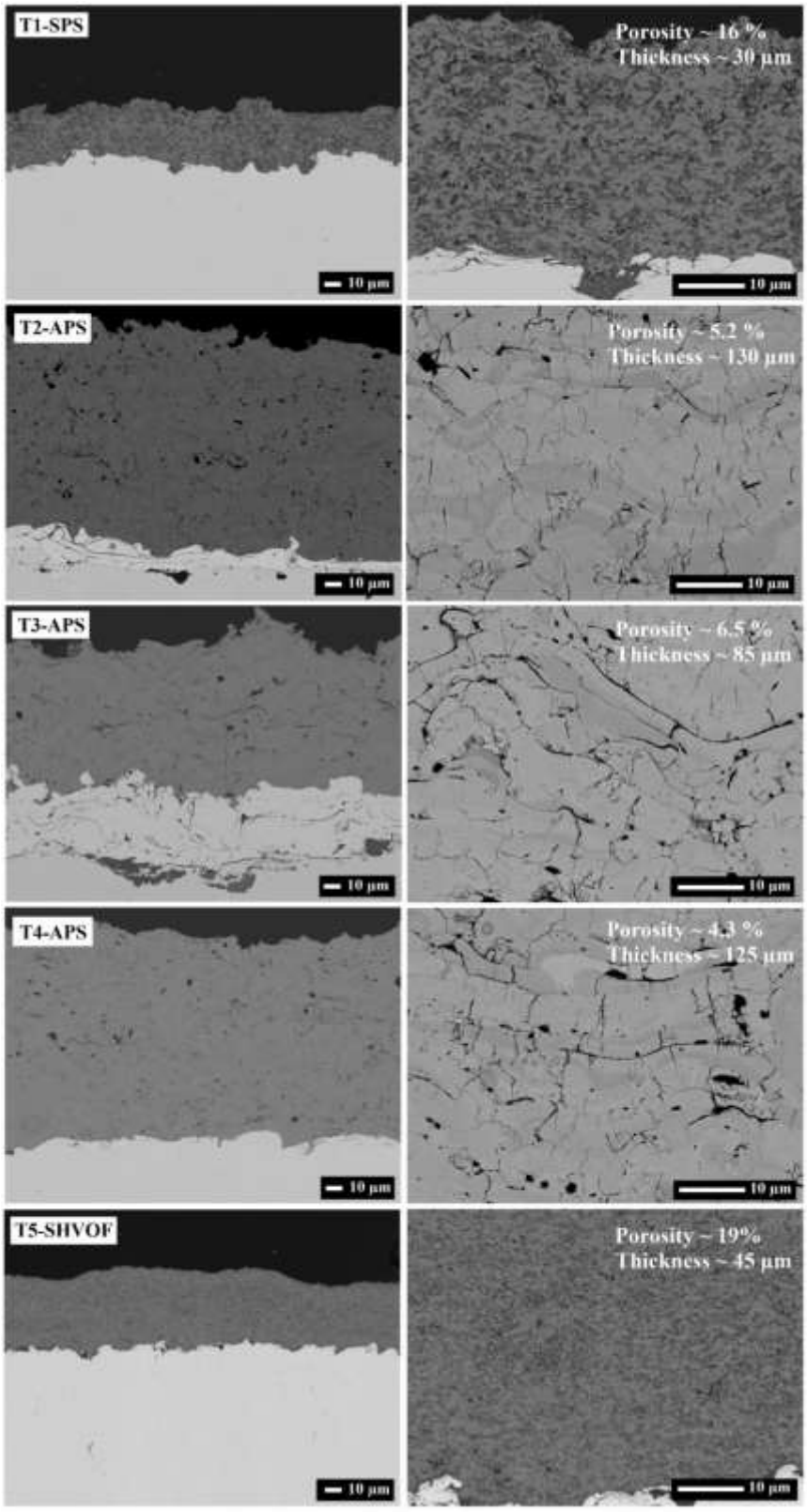

Figure 7. 6 BSE FESEM micrographs of TiO_2 coatings' cross-sections at two magnifications.

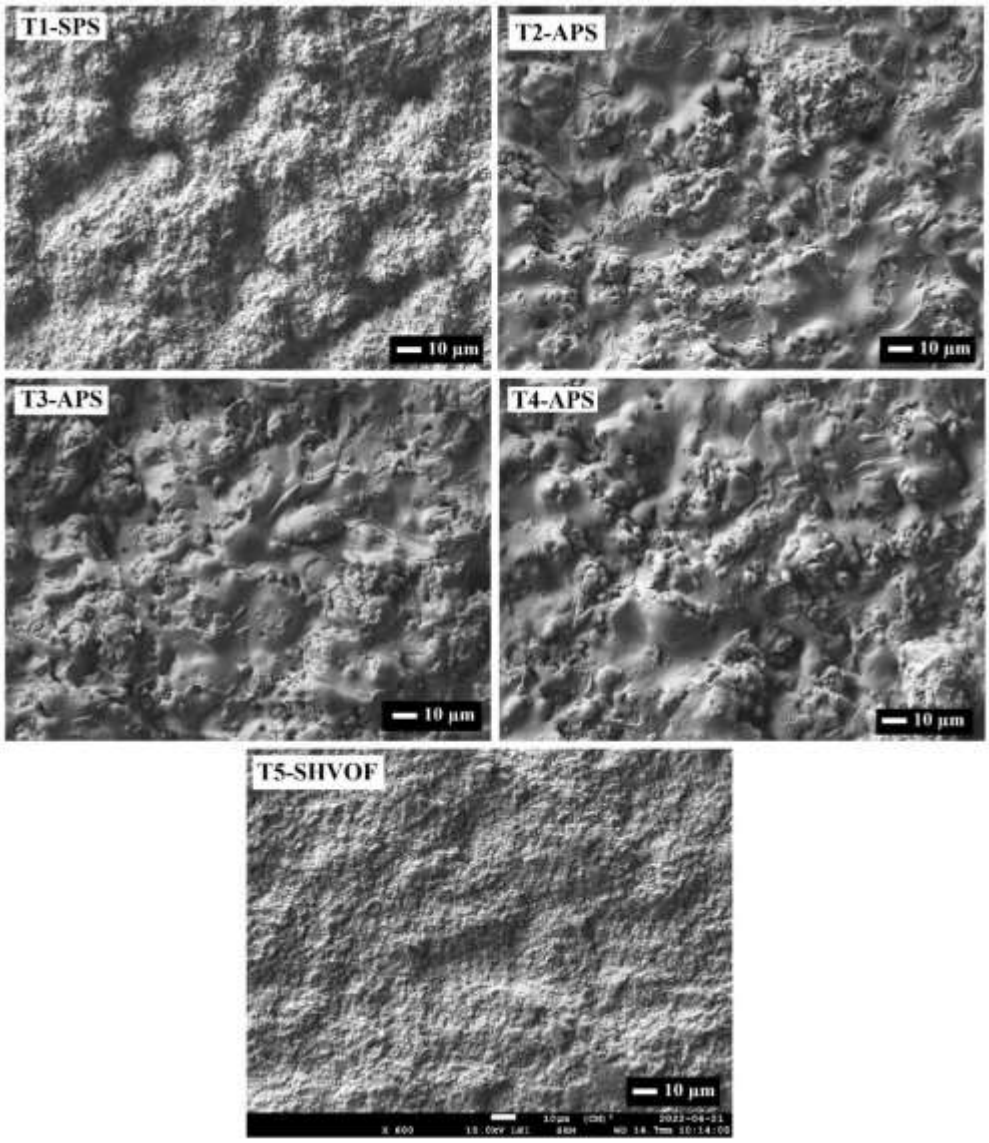

Figure 7. 7 Top surface SE FESEM micrographs of TiO_2 coatings.

Sub-micron particles used for preparing the suspension for SPS and S-HVOF processes would travel within the colder fringe of the plasma plume with lower thermal energy. Moreover, the relatively high vaporization enthalpy of water as the solvent in the suspension would cool down the plasma jet and increase the un-melted ratio in the suspension sprayed coatings compared to APS coatings. Re-solidification of the melted particles before impacting the substrate might form re-solidified particles [212][183][44]. The presence of agglomerated un-melted particles and re-solidified particles is of great importance for increasing the specific surface area of the photocatalyst and, hence improving its activity.

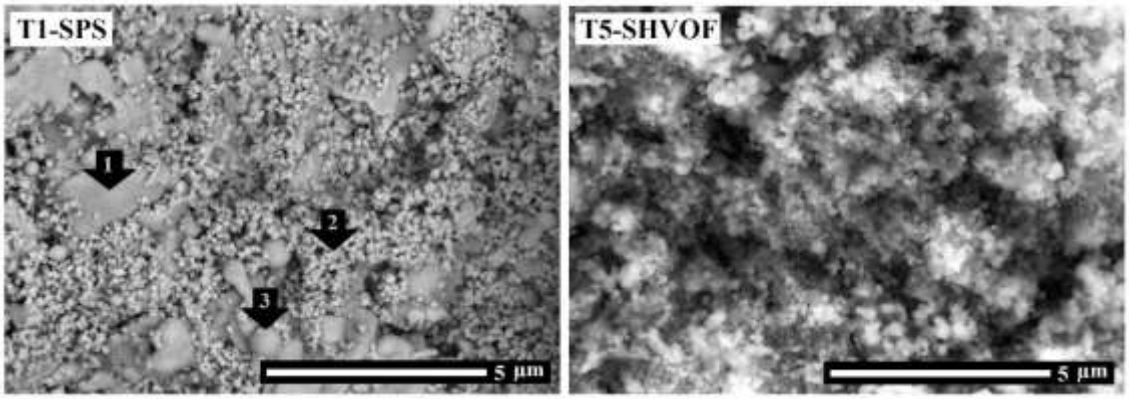

Figure 7. 8 Top surface SE FESEM micrographs of T1-SPS and T5-SHVOF at high magnification, where (1) fully melted particles, (2) un-melted agglomerated particles, and (3) re-solidified particles.

SEM micrographs of Cu_2O, and TiO_2 composites with Cu_2O and Al_2O_3 are shown in Figs. 7.9 and 7.10. The lower deposition efficiency of Cu_2O and TiO_2- Cu_2O coatings might be related to the plasma processing parameters and, specifically plasma power. To maintain Cu_2O phase, a low plasma power was applied by using He and a low H_2 flow rate as the secondary gas for Cu_2O and TiO_2- Cu_2O coatings, respectively.

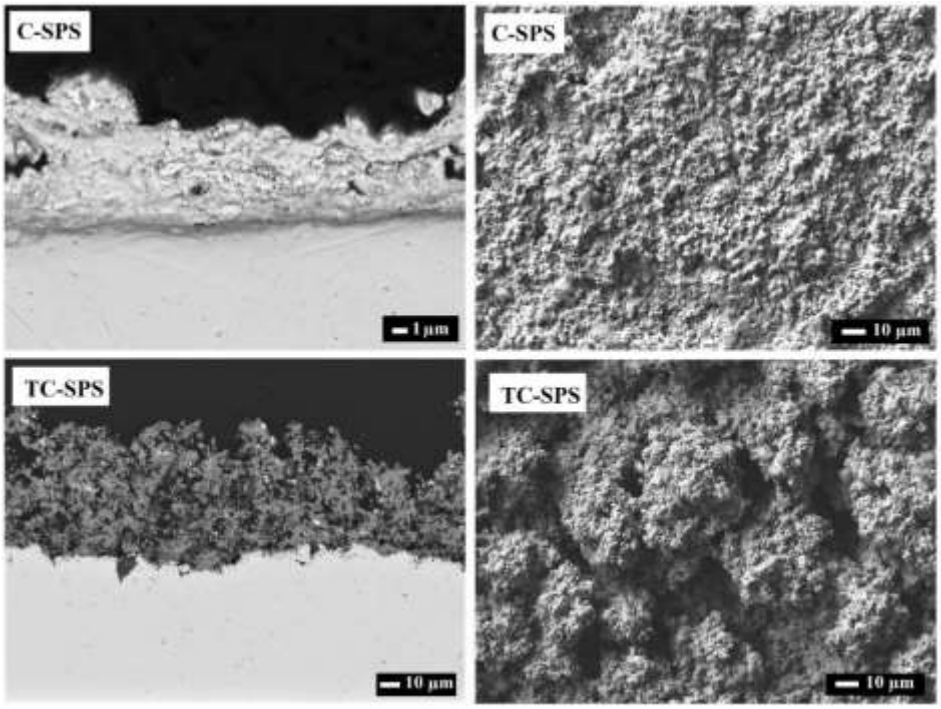

Figure 7. 9 FESEM micrographs of Cu_2O and TiO_2-Cu_2O coatings, left side: BSE cross-sectioned, Right side: S.E. top surface images.

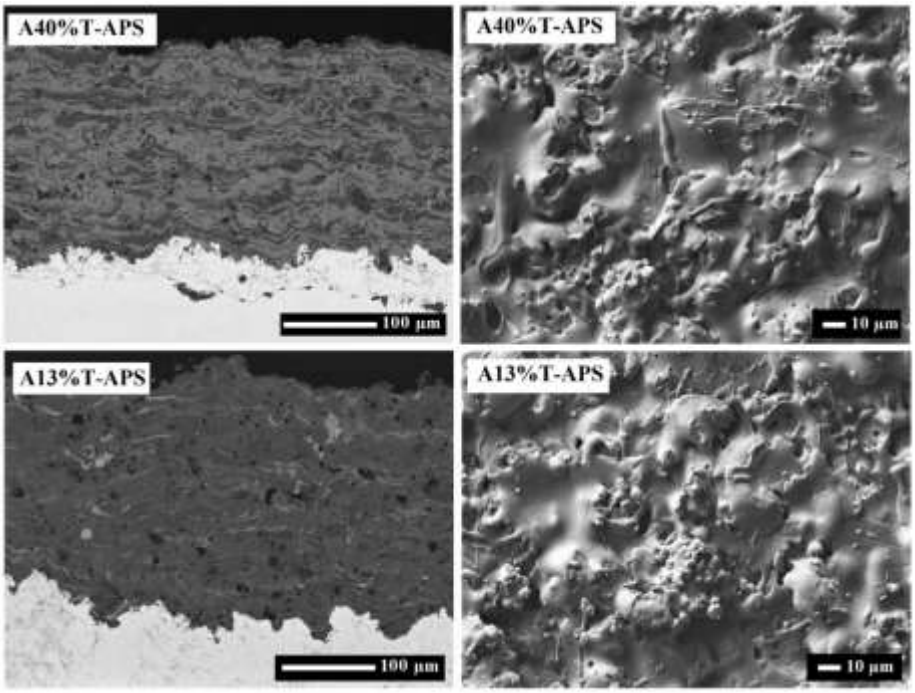

Figure 7. 10 FESEM micrographs of TiO_2-Al_2O_3 coatings, left side: BSE cross-sectioned, Right side: S.E. top surface images.

Energy dispersive spectroscopy (EDS) measurements were performed on TiO_2 composite coatings to investigate the second phase distribution through the coatings, as shown in Fig. 7.11. According to the EDS mapping results, Al_2O_3 phase in both TiO_2-Al_2O_3 coatings enclosed a significant portion of the composite coatings.

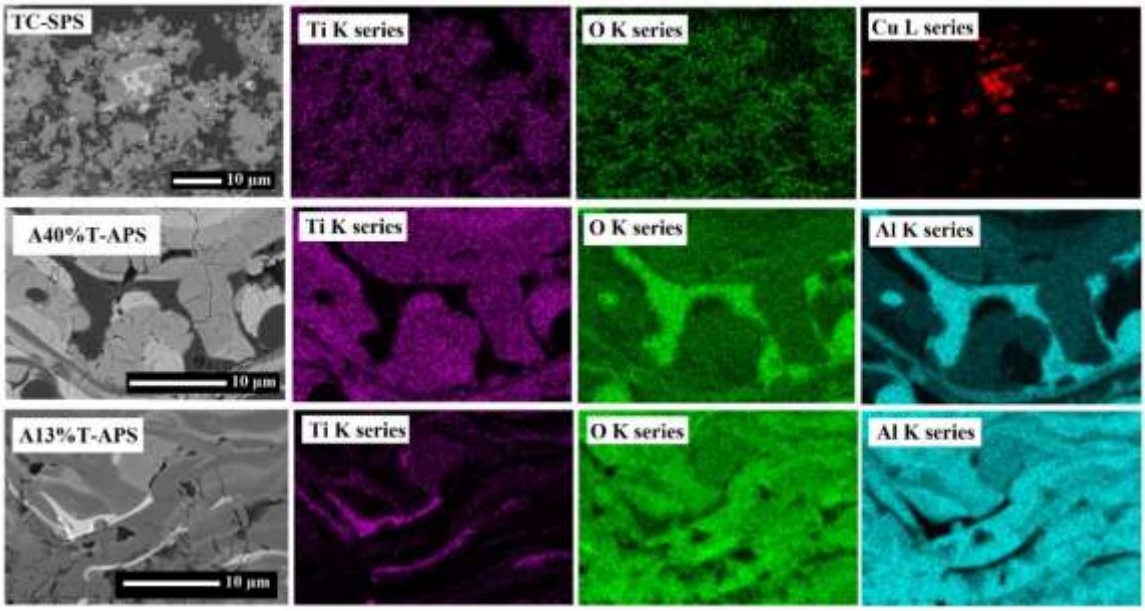

Figure 7. 11 FESEM-EDX mapping of the cross-sectional view of TiO_2-Cu_2O and TiO_2-Al_2O_3 coatings.

7.3.3 Antiviral activity assessment

7.3.3.1 Al_2O_3-TiO_2 coatings

Figure 7.12 shows the antiviral activity of A40%T-APS and A13%T-APS coatings under UVA and ambient light. The coatings showed almost no antiviral activity in both cases, similar to the stainless-steel control sample. The antiviral activity of TiO_2 is due to the photocatalytic oxidation property [99]. When TiO_2 is exposed to photons with energy more than its bandgap, an electron (e^-) is excited from the valence band (VB) to the conduction band (CB), and a hole (h^+) is generated in the valence band. At the surface of the photocatalyst, these charge carriers interact with oxygen and water to produce highly reactive oxygen species (ROS) such as hydroxyl radicals ($^{\cdot}HO$), $O_2^{\cdot -}$, $HO_2^{\cdot}$, H_2O_2, etc. [238]. Equations 7.1 to 7.5 show the mechanisms of producing some ROS [238].

$$TiO_2 + hv \rightarrow TiO_2\,(e^- + h^+) \quad (7.1)$$
$$TiO_2\,(h^+) + H_2O \rightarrow TiO_2 + {}^{\cdot}HO + H \quad (7.2)$$
$$TiO_2\,(e^-) + O_2 \rightarrow TiO_2 + O_2^{\cdot -} \quad (7.3)$$
$$O_2^{\cdot -} + H^+ \rightarrow HO_2^{\cdot} \quad (7.4)$$
$$O_2^{\cdot -} + HO_2^{\cdot} \rightarrow {}^{\cdot}HO + O_2 + H_2O_2 \quad (7.5)$$

ROS such as $^{\cdot}HO$, $O_2^{\cdot -}$, $HO_2^{\cdot}$, H_2O_2 has been suggested to be responsible for the degradation of viruses [99][238]. These ROS could damage the lipid membrane of the virus and degrade the capsid proteins or the envelope of the virus. Consequently, nucleic acid leakage occurs following virus destruction due to the decomposition of its genetic material [238][239].

Generally, the photogenerated electron-hole pairs in TiO_2 are produced under UV illumination due to their 3-3.2 eV bandgap energy [43]. However, thermal sprayed coatings show photocatalytic activity under visible light due to the presence of oxygen vacancy and Ti^{3+} ions in the coatings [150][240][241]. In Al_2O_3-TiO_2 coatings, as mentioned in section 7.3.1, most of the TiO_2 in the feedstock was transformed into $TiAl_2O_5$ in the coatings. Furthermore, EDS images of Al_2O_3-TiO_2 coatings in Fig. 7.12 showed the photocatalically active surface of TiO_2 covered with inert Al_2O_3 resulting in suppression of the photocatalytic activity in these coatings.

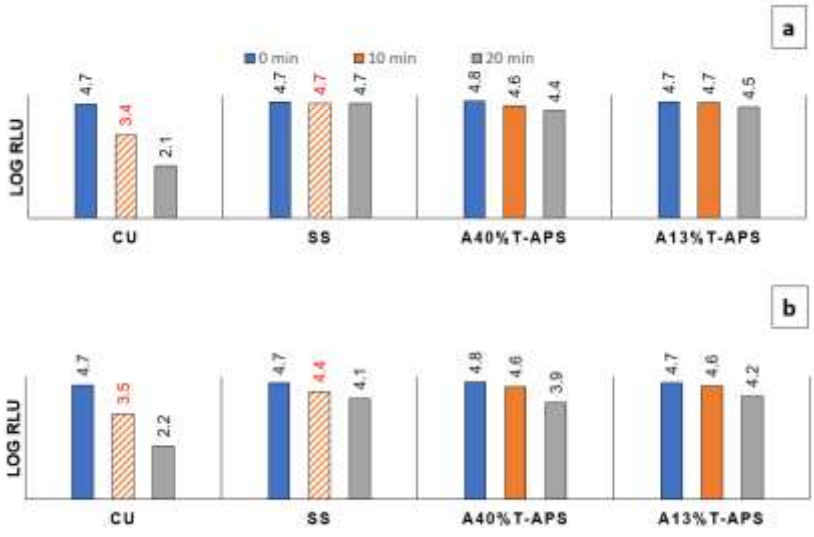

Figure 7. 12 Antiviral activity assessment of Al_2O_3-TiO_2 Coatings under (a) ambient light, (b) UVA light. Cu-10 min and SS-10 min were calculated by linear interpolation.

7.3.3.2 TiO_2 coatings

Figure 7.13 shows the antiviral activity of the TiO_2 coatings produced with SPS, APS, and S-HVOF processes under UVA and ambient light. The antiviral activity of the coatings is rather similar under UVA and ambient light. Interestingly, the antiviral activity of the coatings under UVA and ambient light, regardless of the thermal spray production process, is almost as high as the copper sample. After 20 min, 99.7% of the virus on the copper sample was killed under UVA and ambient light. Despite the minor fluctuation, which could correspond to the specific surface characteristics of the samples in this work, a consistent trend can be observed in the results.

In general, anatase content in TiO_2 is believed to be the most promising factor for photocatalytic activity [19][22][38]. However, other parameters, such as oxygen vacancy and surface morphology, could also play a critical role in the photocatalytic performance of thermally sprayed coatings [212][43].

It can be seen that samples T1-SPS and T5-SHVOF, with around 80% anatase, show slightly higher antiviral activity than copper under both ambient and UVA illuminations. Notably, the Log RLU value of these two samples at 0 min, which determines the amount of the re-collectible virus from the coatings' surface, is lower than the other coatings and the dense control samples. A relatively high porosity on the surface of T1-SPS and T5-SHVOF, shown in Fig. 7.8, results in the penetration of a fraction of the virus through the coatings almost immediately after being put on the surface. This sponge-like feature is not necessarily undesirable since coronaviruses have a limited chance of survival that can last up to a few days [242]. Therefore, the virus removed below the touchable section of the surface cannot be transmitted to a host to create an infection and eventually decomposes. In addition, the high porosity and asperities on the surface create a larger photocatalytically reactive surface area, which, combined with the anatase content, could lead to a more efficient photocatalytic performance. Thus, in porous TiO_2 coatings, the antiviral activity depends on the combined effect of the efficient photocatalytic oxidation on the surface and displacement of the virus from the surface.

Likewise, in samples T2-APS, T3-APS, and T4-APS, the antiviral activity could be explained through a combined effect of several parameters. Figure 7.14 shows the color of the TiO_2 coatings produced with different thermal spray processes. It can be seen that the APS coatings are much darker than SPS and S-HVOF coatings. It was shown previously that the darker the sub-stoichiometric TiO_{2-x} coating in SPS coatings, the higher the oxygen vacancy content[212][150]. Furthermore, the level of darkness in sub-stoichiometric coatings is related to the concentration of the Ti^{3+} ions [63][64][136].

In the thermal spray process, a high-temperature heat source is utilized to melt and accelerate feedstock material (such as powder or suspension) to form the coating. Oxygen vacancy could form during the intense heating of the particles, and its quantity is associated with the temperature of the in-flight particles. Notably, the presence of hydrogen as a reductive gas could promote the formation of oxygen vacancy [92][45][134]. Therefore, Ti^{4+} could be reduced to Ti^{3+} by accepting electrons from the reducing gas, and oxygen vacancies, or even by receiving the photogenerated electrons under UVA and ambient lights [161]. Oxygen vacancies and Ti^{3+} ions generate new energy levels below the conduction band, inhibiting charge carrier recombination and enhancing photocatalytic activity [66].

Consequently, the dark APS coatings may include higher levels of oxygen vacancy and Ti^{3+} ions resulting in the enhancement of antiviral performance. On the other hand, the lighter

color in SPS and HVOF coatings could be due to a lower level of oxygen vacancy. Using water-based suspension feedstock for T1-SPS and T5-SHVOF would cool down the plasma jet due to the high vaporization enthalpy of water (2.3×10^6 J kg^{-1}), decreasing the chance of producing oxygen vacancy in the coatings.

Finally, it is worth mentioning that the synergetic effect between anatase and rutile in TiO_2 coatings may also promote photocatalytic reactivity by decreasing the recombination rate of the charge carriers [66].

An almost similar antiviral activity for TiO_2 coatings under both UVA and ambient light could propose a more sustainable solution for indoor applications by using the commonly used visible light systems and for outdoor applications where the sunlight consists of around 53% visible light [243].

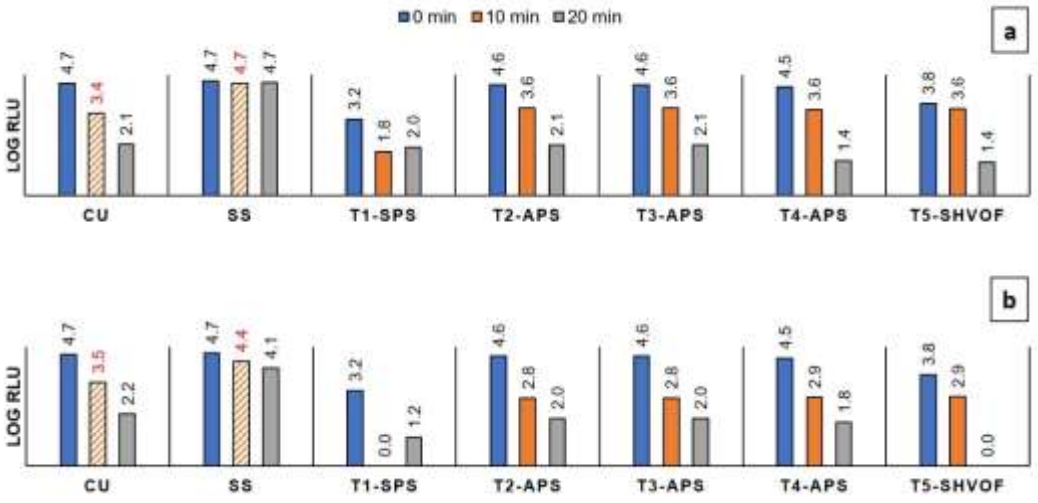

Figure 7. 13 Antiviral activity assessment of TiO_2 Coatings under a) ambient light, b) UVA light. Cu-10 min and SS-10 min were calculated by linear interpolation.

Figure 7. 14 The color difference between TiO_2 coatings produced by various thermal spray processes.

7.3.3.3 TiO_2-Cu_2O coatings

The suggested mechanism for virus deactivation by Cu_2O is the direct contact of the virus with solid-state Cu_2O compounds through valence-state Cu(I) species resulting in the denaturation or degradation of its biomolecules. Therefore, Cu_2O shows antiviral activity independent of optical absorption and in the dark environment [91][244]. The drawback lies in the oxidation of Cu(I) to Cu(II) under ambient conditions, which does not show significant antiviral activity [244]. In TiO_2-Cu_2O composite, a combination of copper species with photogenerated holes in the valence band of TiO_2 under light irradiation can cause membrane damage, followed by protein oxidation and DNA degradation [90][98]. Furthermore, it was suggested that the photogenerated electrons in TiO_2 could be received by Cu(II), suppressing the self-oxidation of Cu(I) and ensuring a sustainable antiviral property of Cu_2O [244].

Figure 7.15 shows the antiviral activity of the Cu_2O and TiO_2-Cu_2O coatings produced with SPS processes under UVA, ambient light, and dark.

In Figs. 7.15 (a) and (b), Cu_2O and TiO_2-Cu_2O coatings show a relatively similar antiviral activity under both UVA and ambient lights, almost as well as that of the pure copper control sample. The Log RLU value of TiO_2- Cu_2O coating at 0 min shows that the quantity of re-collected virus was lower than Cu_2O coating. The lower quantity of re-collected virus is due to the high porosity observed on the surface of TiO_2- Cu_2O coating shown in Fig. 7.9. Therefore, the antiviral performance in TiO_2-Cu_2O could be linked to the combined effect of photocatalytic reactivity of TiO_2, removal of the virus from the top surface of the coating due to porosity, and direct contact of Cu_2O. However, looking at Fig. 7.11, it can be seen that the Cu species are enveloped by TiO_2, which might have limited the antiviral activity due to the direct contact with solid-state Cu_2O.

Figure 7.15 (c) shows the antiviral activity of Cu_2O and TiO_2-Cu_2O coatings in dark conditions. The antiviral activity of Cu_2O coating in the dark is not significantly different from that under UVA and ambient light. This outcome was not unexpected since the direct-contact virus-killing mechanism in Cu_2O is independent of photon energy [91][244].

Interestingly, the TiO_2-Cu_2O coating in dark conditions shows a significant decrease in the quantity of the viable virus, close to that of the copper sample. However, the Log RLU values for TiO_2-Cu_2O coating at 0, 10, and 20 min are somewhat similar. As mentioned earlier, this close similarity in Log RLU values indicates that the observed antiviral activity could correspond to penetration of the virus through the porous structure of the coating and its removal from the top surface. Additionally, the effect of the direct-contact virus-killing mechanism of Cu_2O could be suppressed probably due to the covering of Cu species by TiO_2, as shown in Fig. 7.11. It can be assumed that optimizing the proportion of Cu_2O in TiO_2-Cu_2O coating might probably be advantageous in terms of increasing the efficiency of antiviral activity in the dark.

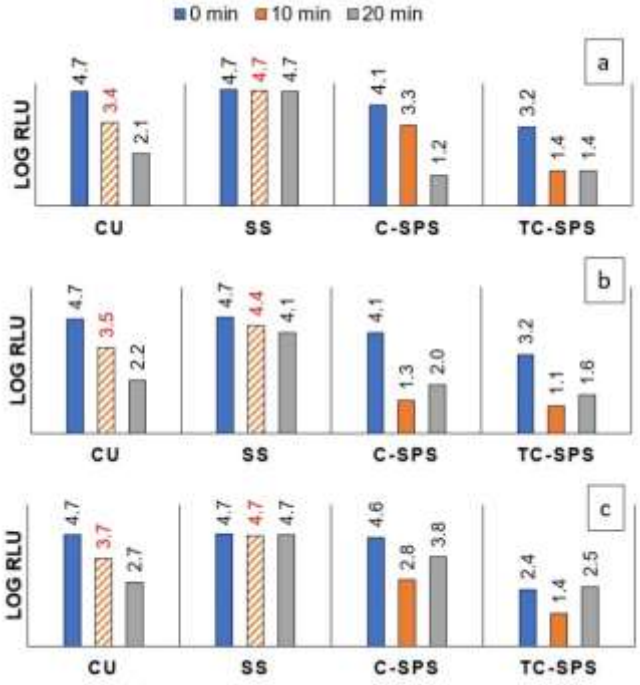

Figure 7. 15 Antiviral activity assessment of TiO_2-Cu_2O Coatings under a) ambient light, b) UVA light, and c) dark. Cu-10 min and SS-10 min were calculated by linear interpolation.

7.4 Conclusion

This study confirms the possibility of producing antiviral coatings using thermal spray technologies. The antiviral activity of thermally sprayed coatings was assessed under ambient light, UVA, and dark conditions. TiO_2, Cu_2O, TiO_2-Cu_2O, and Al_2O_3-TiO_2 coatings were produced by APS, SPS, and S-HVOF processes. Regardless of the coating fabrication process, the antiviral performance of TiO_2 and TiO_2-Cu_2O coatings was as well as pure copper under UVA and ambient light. Furthermore, Cu_2O coating showed antiviral activity in dark conditions close to that of copper. Copper is antiviral upon direct contact with the virus. However, its activity would not last long if the surface became oxidized or contaminated by organic molecules and virus residues. In comparison, TiO_2 is a stable material with an inherently self-cleaning characteristic. Moreover, the price of pure copper compared to TiO_2 coating is one of the important parameters that should be considered for industrial application. Results showed that the antiviral performance of the coatings corresponded to the collective influence of various parameters, including the photocatalytic activity of TiO_2, direct contact of Cu_2O components, and surface properties of the coatings, such as porosity and roughness. The surface porosity resulted in the transportation of a significant quantity of the virus beneath the touchable surface of the coatings, hindering its potential to cause infection. Although the regular cleaning processes of touched surfaces with high roughness and porosity could be challenging, an optimized level of surface properties could be beneficial to the total antiviral performance of the coatings through the combined effect of killing the virus and removing the virus from the surface.

Our results show that thermally sprayed coatings can introduce a potentially cost-effective solution to produce efficient antiviral high-touch coatings for indoor applications under ambient light, in the dark, and outdoor applications under sunlight.

Acknowledgement

This study was financially supported by the Natural Sciences and Engineering Research Council of Canada (NSERC) and Mitacs. Additionally, the authors extend their appreciation to Dr. David Kwan and Dr. Lan Huong Nguyen from Concordia University, Dr. Maurice Ringuette form University of Toronto, Dr. Maniya Aghasibeig and Dr. Bruno M. H. Guerreiro from National Research Council Canada, Murray Pearson from Hatch, Alan Burgess from Sprywerx, Adam Truchon, and Alexandre Gonçalves Andrade from Metal 7.

Chapter 8. Conclusion and future works

8.1 Summary and conclusion

The main objective of this work was to develop scalable photoactive TiO_2 coatings with acceptable efficiency under visible light for water treatment and antiviral application. Thermal spray processes are ideal for coating large surfaces due to their ability to operate in atmospheric conditions, scalability, and capability to deposit various engineering ceramics and metals.

In the first step, the role of the crystalline phase on the photocatalytic activity of suspension plasma sprayed (SPS) TiO_2 coatings was systematically investigated. According to the literature, crystalline phase is one of the most important parameters affecting the photocatalytic efficiency of TiO_2 coatings, and anatase is the most favorable phase. Based on the results, plasma spraying conditions and, more importantly, hydrogen flow rates could significantly affect coatings 'properties like crystalline phases, oxygen vacancies, and morphologies confirmed by various characterization tests. Hydrogen is a reducing gas that could increase temperature and velocity of particles. Based on the results, oxygen vacancy content was increased in the coatings produced at higher H_2 flow rates. The higher deposition efficiency of the coatings produced at higher power may be related to the higher total gas flow rate which could favor suspension atomization. All as-sprayed coatings were polished and heat-treated to reach the same roughness and oxygen content, while no significant phase changes were observed after heat treatment. Photocatalytic activity results showed that all the coatings exhibited remarkable photocatalytic activity. However, the performance of as-sprayed coatings was significantly better than that of polished heat-treated counterparts, which might stem from the combination of phase composition and other influencing factors. While for as-sprayed coatings, no direct correlation between anatase content and their photocatalytic activity was ascertained, TiO_2 coating with the highest amount of anatase content presented the best activity after polishing and heat treatment.

Subsequently, the optical and photocatalytic performance of TiO_2 coatings produced by suspension plasma spray (SPS) were investigated with a focus on the effects of oxygen deficiency and Ti^{3+} ions. By varying the annealing temperature of the as-sprayed samples (400-550 ºC), coatings with different oxygen levels were produced. The higher the heat treatment temperature, the more oxygen was recaptured in the coating while the initial crystalline phase was maintained. The optical properties of sub-stoichiometric TiO_{2-x} were found to vary along with its stoichiometry. Introducing oxygen vacancies and Ti^{3+} ions to the TiO_2 lattice sites resulted in a significant decrease in the bandgap energy and a shift of the absorption edge to visible light due to the formation of $[Ov \cdot Ti^{3+}]^+$ between the valence and conduction bands.

Additionally, the presence of energy levels between the bandgap could act as traps, promoting the separation of photo-generated electrons and holes, thus improving the photocatalytic response of the sub-stoichiometric TiO_{2-x} under visible light. Based on the

photocatalytic activity results, the rate constant for methylene blue (MB) degradation of the as-sprayed TiO_2 coating with the highest oxygen deficiency was 3.8×10^{-2} min^{-1}, while the heat-treated coating with the lowest oxygen deficiency had a rate constant of 1.3×10^{-2} min^{-1}. This study showcased the development of efficient sub-stoichiometric TiO_{2-x} photocatalyst coatings, which could be used to reduce the environmental impact of the textile industry.

In the next step, the role of the CeO_2 compositing and cerium dopant were investigated on the coatings produced by SPS and hybrid suspension (SPS) and solution precursor plasma spraying (SPPS) approach. The presence of cerium doping was verified through EDS mapping, XRD peaks, Raman peak shifting, and XPS analysis. The XPS analysis, in particular, revealed the presence of a combination of Ce^{3+} and Ce^{4+} ions, suggesting a higher concentration of oxygen vacancies in Ce-doped and CeO_2 composite coatings. Cerium dopant introduces e new band states below the conduction band of TiO_2 that could reduce the recombination rate by trapping charge carriers. Moreover, it will reduce the bandgap and shift the light absorption to the visible range. The UV-Vis experiments showed that doping TiO_2 with cerium or forming a composite with CeO_2 shifted the absorbance edge of TiO_2 coatings toward the visible range. However, pure TiO_2 (SPS) presented superior photocatalytic activity. The addition of sub-micron CeO_2 particles to the composite matrix covering the active surface of TiO_2 particles has been found to reduce the photocatalytic efficiency of the coatings. This decreased activity of Ce-doped TiO_2 can be attributed to the generation of deep-level point defects, such as oxygen vacancy, due to an inadequate dosage of dopant, which results in an increased rate of recombination of photogenerated charge carriers. The SPS-SPPS method has proven to be a promising technique for doping TiO_2; however, further analysis is needed to determine the ideal amount of dopant needed to maximize the material's photoactivity.

In the last step, the antiviral activity of TiO_2, Cu_2O, TiO_2-Cu_2O and TiO_2-Al_2O_3 coatings was investigated under ambient light, UVA, and dark conditions. These coatings were produced by different thermal spray processes, including atmospheric plasma spray (APS), suspension plasma spray (SPS), and suspension high-velocity oxygen fuel (S-HVOF). Regardless of the fabrication process, the antiviral performance of TiO_2 and TiO_2-Cu_2O coatings was comparable to that of pure copper when exposed to UVA and ambient light. Additionally, Cu_2O coating was almost as effective as copper in dark conditions. The antiviral efficiency of the coatings was determined by the combination of various factors, including the photocatalytic activity of TiO_2, the direct contact of Cu_2O components, and the surface morphology of the coatings. The porous surface enabled the virus to go beneath the reachable surface of the coatings, reducing the risk of infection. While regular cleaning of rough and porous surfaces may be difficult, a tailored level of surface features can improve the antiviral performance of the coatings by both killing the virus and eliminating it from the surface. Our findings suggest that thermally sprayed coatings could be a viable, cost-effective method of producing antiviral high-touch coatings for both indoor and outdoor applications.

Based on the results and conclusions provided, it can be seen that, SPS TiO_2 have unique properties that can be tailored for different applications. This highlights the importance of comprehending the correlation between spray parameters and coating properties, as the coatings demonstrated effective photoactivity for water purification and antiviral applications. These results suggest the potential for further application of these coatings in hydrogen production.

8.2 Contributions

The main contributions of this research can be summarized as follows.

- A systematic procedure was established to understand the influential role of anatase phase on the photocatalytic activity of TiO_2 coatings obtained by suspension plasma spraying. Based on the results, there is no direct correlation between anatase phase content and photocatalytic activity of as-sprayed coatings due to their unique microstructure and the existence of oxygen vacancies. At the same time, anatase phase plays an important role in post-treated coatings with similar coating characteristics and oxygen contents.
- A systematic work was performed to present the influential role of oxygen vacancies on the optical properties and photocatalytic activity of sub-stoichiometric TiO_{2-x} coatings obtained by suspension plasma spraying. A method based on TGA analysis was proposed to monitor the oxygen concentration of photocatalytic coatings as a function of SPS deposition parameters. Based on the result, the more the hydrogen flow rate was, the more oxygen vacancy was produced in the coatings, which could be both sub-stoichiometric anatase and rutile. While after heat treatment at 550 ºC, all coatings re-oxidized to stoichiometric TiO_2. Sub-stoichiometric titania (TiO_{2-x}) coatings showed remarkable photocatalytic activity for water purification with MB.
- SPS-SPPS method has shown a promising technique for doping TiO_2 while the optimum amount of the dopant is needed to reach the highest photoactivity. Moreover, TiO_2-CeO_2 composite was produced using SPS process. Although, Sub-micron CeO_2 particles decreased the photocatalytic activity of TiO_2 coatings by covering its active surface area.
- Thermally sprayed TiO_{2-x} coatings have emerged as a viable solution for indoor applications to decrease viral transmission through highly touched surfaces. It can be used in ventilation systems as well.
- This research shows the impressive capability of suspension plasma spraying to produce highly active TiO_2 coatings for photocatalytic activity and antiviral applications. Furthermore, the versatile and scalable thermal spray technology makes it compatible with industrial production.

8.3 Future work

Based on the results of the present research study, the following suggestions are proposed for future research to enhance the photoactivity of the coatings:

- Investigating the role of the other influencing parameters on the thermally sprayed TiO_2 coatings, such as surface roughness.
- Optimize the cerium dopant amount by depositing coatings containing a higher and lower dosage than the current dosage we used.
- Producing TiO_2-CeO_2 composite using SPPS process to create nanostructured composite coatings.
- Testing the antiviral activity of the coating on highly touched surfaces under real-life conditions and HVAC systems.
- Performing long-term experiments using modified photocatalysts to explore the stability and deactivation behavior of the coatings when exposed to light irradiation.
- Testing the performance of developed photocatalysts under a flowing water system.

References

[1] E. Kampa, Marilena; Castanas, Human health effects of air pollution, Environ. Pollut. 151 (2008) 362–367. https://doi.org/10.1016/j.jaci.2004.08.030.

[2] J. Yu, X. Zhao, Q. Zhao, Photocatalytic activity of nanometer TiO_2 thin films prepared by the sol-gel method, Mater. Chem. Phys. 69 (2001) 25–29. https://doi.org/10.1016/S0254-0584(00)00291-1.

[3] M.A. Rauf, M.A. Meetani, S. Hisaindee, An overview on the photocatalytic degradation of azo dyes in the presence of TiO_2 doped with selective transition metals, Desalination. 276 (2011) 13–27. https://doi.org/10.1016/j.desal.2011.03.071.

[4] A.L. Ahmad, S.W. Puasa, Reactive dyes decolourization from an aqueous solution by combined coagulation/micellar-enhanced ultrafiltration process, Chem. Eng. J. 132 (2007) 257–265. https://doi.org/10.1016/j.cej.2007.01.005.

[5] S. Zodi, O. Potier, F. Lapicque, J.P. Leclerc, Treatment of the industrial wastewaters by electrocoagulation: Optimization of coupled electrochemical and sedimentation processes, Desalination. 261 (2010) 186–190. https://doi.org/10.1016/j.desal.2010.04.024.

[6] M.J. Martin, A. Artola, M.D. Balaguer, M. Rigola, Activated carbons developed from surplus sewage sludge for the removal of dyes from dilute aqueous solutions, Chem. Eng. J. 94 (2003) 231–239. https://doi.org/10.1016/S1385-8947(03)00054-8.

[7] N. Nasuha, B.H. Hameed, A.T.M. Din, Rejected tea as a potential low-cost adsorbent for the removal of methylene blue, J. Hazard. Mater. 175 (2010) 126–132. https://doi.org/10.1016/j.jhazmat.2009.09.138.

[8] G. Kampf, D. Todt, S. Pfaender, E. Steinmann, Persistence of coronaviruses on inanimate surfaces and their inactivation with biocidal agents, J. Hosp. Infect. 104 (2020) 246–251. https://doi.org/10.1016/j.jhin.2020.01.022.

[9] World Health Organization, COVID-19 Weekly Epidemiological Update, World Heal. Organ. (2022) 1–33. https://www.who.int/publications/m/item/weekly-epidemiological-update-on-covid-19---2-november-2022.

[10] C.M. So, M.Y. Cheng, J.C. Yu, P.K. Wong, Degradation of azo dye Procion Red MX-5B by photocatalytic oxidation, Chemosphere. 46 (2002) 905–912. https://doi.org/10.1016/S0045-6535(01)00153-9.

[11] C. Di Valentin, E. Finazzi, G. Pacchioni, A. Selloni, S. Livraghi, M.C. Paganini, E. Giamello, N-doped TiO_2: Theory and experiment, Chem. Phys. 339 (2007) 44–56. https://doi.org/10.1016/j.chemphys.2007.07.020.

[12] A. Fujishima, X. Zhang, D.A. Tryk, TiO_2 photocatalysis and related surface phenomena, Surf. Sci. Rep. 63 (2008) 515–582. https://doi.org/10.1016/j.surfrep.2008.10.001.

[13] M.I. Badawy, E.M. Souaya, T.A. Gad-Allah, M.S. Abdel-Wahed, M. Ulbricht, Fabrication of Ag/TiO_2 photocatalyst for the treatment of simulated hospital wastewater under sunlight, Environ. Prog. Sustain. Energy. 33 (2014) 886–894. https://doi.org/10.1002/ep.

[14] H. Qin, G. Gu, S. Liu, Preparation of nitrogen-doped titania using sol–gel technique and its photocatalytic activity, Mater. Chem. Phys. 112 (2008) 346–352. https://doi.org/10.1016/j.matchemphys.2008.05.059.

[15] D. Reyes-Coronado, G. Rodr´ıguez-Gattorno, M.E. Espinosa-Pesqueira, C. Cab, R. de Coss, G. Oskam, Phase-pure TiO_2 nanoparticles : anatase , brookite and rutile, Nanotechnology. 19 (2008) 145605. https://doi.org/10.1088/0957-4484/19/14/145605.

[16] C. Zhang, Y. Li, D. Shuai, Y. Shen, D. Wang, Progress and challenges in photocatalytic disinfection of waterborne Viruses: A review to fill current knowledge gaps, Chem. Eng. J. 355 (2019) 399–415. https://doi.org/10.1016/j.cej.2018.08.158.

[17] H. Cui, J. Jiang, W. Gu, C. Sun, D. Wu, T. Yang, G. Yang, Photocatalytic inactivation efficiency of anatase nano-TiO_2 sol on the H9N2 avian influenza virus, Photochem. Photobiol. 86 (2010) 1135–1139. https://doi.org/10.1111/j.1751-1097.2010.00763.x.

[18] Y. Kikuchi, K. Sunada, T. Iyoda, K. Hashimoto, A. Fujishima, Photocatalytic bactericidal effect of TiO_2 thin films: Dynamic view of the active oxygen species responsible for the effect, J. Photochem. Photobiol. A Chem. 106 (1997) 51–56. https://doi.org/10.1016/S1010-6030(97)00038-5.

[19] J. Prakash, J. Cho, Y.K. Mishra, Photocatalytic TiO_2 nanomaterials as potential antimicrobial and antiviral agents: Scope against blocking the SARS-COV-2 spread, Micro Nano Eng. 14 (2022) 100100. https://doi.org/10.1016/j.mne.2021.100100.

[20] A. Fujishima, T.N. Rao, D.A. Tryk, Titanium dioxide photocatalysis, J. Photochem. Photobiol. C Photochem. Rev. 1 (2000) 1–21. https://doi.org/https://doi.org/10.1016/S1389-5567(00)00002-2.

[21] H. Dong, G. Zeng, L. Tang, C. Fan, C. Zhang, X. He, Y. He, An overview on limitations of TiO_2-based

particles for photocatalytic degradation of organic pollutants and the corresponding countermeasures, Water Res. 79 (2015) 128–146. https://doi.org/10.1016/j.watres.2015.04.038.
[22] T. Luttrell, S. Halpegamage, J. Tao, A. Kramer, E. Sutter, M. Batzill, Why is anatase a better photocatalyst than rutile? - Model studies on epitaxial TiO_2 films, Sci. Rep. 4, 4043 (2014) 1–8. https://doi.org/10.1038/srep04043.
[23] O.A. Krysiak, P.J. Barczuk, K. Bienkowski, T. Wojciechowski, J. Augustynski, The photocatalytic activity of rutile and anatase TiO_2 electrodes modified with plasmonic metal nanoparticles followed by photoelectrochemical measurements, Catal. Today. 321–322 (2019) 52–58. https://doi.org/10.1016/j.cattod.2018.01.007.
[24] R. Jaiswal, N. Patel, D.C. Kothari, A. Miotello, Improved visible light photocatalytic activity of TiO_2 co-doped with Vanadium and Nitrogen, Appl. Catal. B Environ. 126 (2012) 47–54. https://doi.org/10.1016/j.apcatb.2012.06.030.
[25] M. Rochkind, S. Pasternak, Y. Paz, Using dyes for evaluating photocatalytic properties: A critical review, Molecules. 20 (2015) 88–110. https://doi.org/10.3390/molecules20010088.
[26] N.M. Mahmoodi, M. Arami, N.Y. Limaee, N.S. Tabrizi, Kinetics of heterogeneous photocatalytic degradation of reactive dyes in an immobilized TiO_2 photocatalytic reactor, J. Colloid Interface Sci. 295 (2006) 159–164. https://doi.org/10.1016/j.jcis.2005.08.007.
[27] C.C. Wang, C.K. Lee, M. Du Lyu, L.C. Juang, Photocatalytic degradation of C.I. Basic Violet 10 using TiO_2 catalysts supported by Y zeolite: An investigation of the effects of operational parameters, Dye. Pigment. 76 (2008) 817–824. https://doi.org/10.1016/j.dyepig.2007.02.004.
[28] A. Hernández-Ramírez, I. Medina-Ramírez, Photocatalytic semiconductors: Synthesis, characterization, and environmental applications, in: Springer Int. Pu, 2016. https://doi.org/10.1007/978-3-319-10999-2.
[29] M.R. Hoffmann, S.T. Martin, W. Choi, D.W. Bahnemann, Environmental Applications of Semiconductor Photocatalysis, Chem. Rev. 95 (1995) 69–96. https://doi.org/10.1021/cr00033a004.
[30] T. Hisatomi, J. Kubota, K. Domen, Recent advances in semiconductors for photocatalytic and photoelectrochemical water splitting, Chem. Soc. Rev. 43 (2014) 7520–7535. https://doi.org/10.1039/c3cs60378d.
[31] S.H.S. Chan, T.Y. Wu, J.C. Juan, C.Y. Teh, Recent developments of metal oxide semiconductors as photocatalysts in advanced oxidation processes (AOPs) for treatment of dye waste-water, J. Chem. Technol. Biotechnol. 86 (2011) 1130–1158. https://doi.org/10.1002/jctb.2636.
[32] A.B. Djurišić, Y.H. Leung, A.M. Ching Ng, Strategies for improving the efficiency of semiconductor metal oxide photocatalysis, Mater. Horizons. 1 (2014) 400–410. https://doi.org/10.1039/c4mh00031e.
[33] M.M. Khan, S.F. Adil, A. Al-Mayouf, Metal oxides as photocatalysts, J. Saudi Chem. Soc. 19 (2015) 462–464. https://doi.org/10.1016/j.jscs.2015.04.003.
[34] A.L. Linsebigler, G. Lu, J.T. Yates, Photocatalysis on TiO_2 Surfaces: Principles, Mechanisms, and Selected Results, Chem. Rev. 95 (1995) 735–758. https://doi.org/10.1021/cr00035a013.
[35] H. Khatibnezhad, M.A. Faghihi Sani, Preparation and characterization of nanostructured TiO_2 thin film codoped with nitrogen and vanadium on glass surface by sol–gel dip-coating method, Res. Chem. Intermed. 41 (2015) 7349–7361. https://doi.org/10.1007/s11164-014-1816-1.
[36] F.L. Toma, L.M. Berger, I. Shakhverdova, B. Leupolt, A. Potthoff, K. Oelschlägel, T. Meissner, J.A.I. Gomez, Y. de Miguel, Parameters influencing the photocatalytic activity of suspension-sprayed TiO_2 coatings, J. Therm. Spray Technol. 23 (2014) 1037–1053. https://doi.org/10.1007/s11666-014-0090-5.
[37] D.A.H. Hanaor, C.C. Sorrell, Review of the anatase to rutile phase transformation, J. Mater. Sci. 46 (2011) 855–874. https://doi.org/10.1007/s10853-010-5113-0.
[38] J. Zhang, P. Zhou, J. Liu, J. Yu, New understanding of the difference of photocatalytic activity among anatase, rutile and brookite TiO_2, Phys. Chem. Chem. Phys. 16 (2014) 20382–20386. https://doi.org/10.1039/c4cp02201g.
[39] A. Sclafani, J.M. Herrmann, Comparison of the photoelectronic and photocatalytic activities of various anatase and rutile forms of titania in pure liquid organic phases and in aqueous solutions, J. Phys. Chem. 100 (1996) 13655–13661. https://doi.org/10.1021/jp9533584.
[40] M. Xu, Y. Gao, E.M. Moreno, M. Kunst, M. Muhler, Y. Wang, H. Idriss, C. Wöll, Photocatalytic activity of bulk TiO_2 anatase and rutile single crystals using infrared absorption spectroscopy, Phys. Rev. Lett. 106 (2011) 1–4. https://doi.org/10.1103/PhysRevLett.106.138302.
[41] G. Odling, N. Robertson, Why is anatase a better photocatalyst than rutile? the importance of free hydroxyl radicals, ChemSusChem. 8 (2015) 1838–1840. https://doi.org/10.1002/cssc.201500298.
[42] G. Mauer, A. Guignard, R. Vaßen, Plasma spraying of efficient photoactive TiO_2 coatings, Surf. Coatings

Technol. 220 (2013) 40–43. https://doi.org/10.1016/j.surfcoat.2012.08.042.
[43] S. Kozerski, F.L. Toma, L. Pawlowski, B. Leupolt, L. Latka, L.M. Berger, Suspension plasma sprayed TiO_2 coatings using different injectors and their photocatalytic properties, Surf. Coatings Technol. 205 (2010) 980–986. https://doi.org/10.1016/j.surfcoat.2010.04.068.
[44] E. Alebrahim, F. Tarasi, M.S. Rahaman, A. Dolatabadi, C. Moreau, Fabrication of titanium dioxide filtration membrane using suspension plasma spray process, Surf. Coatings Technol. 378 (2019) 124927. https://doi.org/10.1016/j.surfcoat.2019.124927.
[45] J.R. Colmenares-Angulo, V. Cannillo, L. Lusvarghi, A. Sola, S. Sampath, Role of process type and process conditions on phase content and physical properties of thermal sprayed TiO_2 coatings, J. Mater. Sci. 44 (2009) 2276–2287. https://doi.org/10.1007/s10853-008-3044-9.
[46] M.N. Chong, B. Jin, C.W.K. Chow, C. Saint, Recent developments in photocatalytic water treatment technology: A review, Water Res. 44 (2010) 2997–3027. https://doi.org/10.1016/j.watres.2010.02.039.
[47] R. Saravanan, F. Gracia, A. Stephen, Basic Principles, Mechanism, and Challenges of Photocatalysis, in: Springer Ser. Polym. Compos. Mater. Springer, Cham, 2017: pp. 19–41. https://doi.org/10.1007/978-3-319-62446-4.
[48] S. Malato, P. Fernández-Ibáñez, M.I. Maldonado, J. Blanco, W. Gernjak, Decontamination and disinfection of water by solar photocatalysis: Recent overview and trends, Catal. Today. 147 (2009) 1–59. https://doi.org/10.1016/j.cattod.2009.06.018.
[49] T. Tachikawa, M. Fujitsuka, T. Majima, Mechanistic insight into the TiO_2 photocatalytic reactions: Design of new photocatalysts, J. Phys. Chem. C. 111 (2007) 5259–5275. https://doi.org/10.1021/jp069005u.
[50] A. Zaleska, Doped-TiO2: A Review, Recent Patents Eng. 2 (2008) 157–164. https://doi.org/10.2174/187221208786306289.
[51] M. Ni, M.K.H. Leung, D.Y.C. Leung, K. Sumathy, A review and recent developments in photocatalytic water-splitting using TiO_2 for hydrogen production, Renew. Sustain. Energy Rev. 11 (2007) 401–425. https://doi.org/10.1016/j.rser.2005.01.009.
[52] R. Daghrir, P. Drogui, D. Robert, Modified TiO2 for environmental photocatalytic applications: a review, Ind. Eng. Chem. Res. 52 (2013) 3581–3599. https://doi.org/10.1021/ie303468t.
[53] V. Štengl, S. Bakardjieva, N. Murafa, Preparation and photocatalytic activity of rare earth doped TiO_2 nanoparticles, Mater. Chem. Phys. 114 (2009) 217–226. https://doi.org/10.1016/j.matchemphys.2008.09.025.
[54] A. Makdee, P. Unwiset, K. Chayakul, Effects of Ce addition on the properties and photocatalytic activity of TiO_2, investigated by X-ray absorption spectroscopy, Mater. Chem. Phys. 213 (2018) 431–443. https://doi.org/10.1016/j.matchemphys.2018.04.016.
[55] S.M. Chang, W.S. Liu, The roles of surface-doped metal ions (V, Mn, Fe, Cu, Ce, and W) in the interfacial behavior of TiO_2 photocatalysts, Appl. Catal. B Environ. 156–157 (2014) 466–475. https://doi.org/10.1016/j.apcatb.2014.03.044.
[56] N. Yan, Z. Zhu, J. Zhang, Z. Zhao, Q. Liu, Preparation and properties of ce-doped TiO_2 photocatalyst, Mater. Res. Bull. 47 (2012) 1869–1873. https://doi.org/10.1016/j.materresbull.2012.04.077.
[57] J. Xie, D. Jiang, M. Chen, D. Li, J. Zhu, X. Lü, C. Yan, Preparation and characterization of monodisperse Ce-doped TiO_2 microspheres with visible light photocatalytic activity, Colloids Surfaces A Physicochem. Eng. Asp. 372 (2010) 107–114. https://doi.org/10.1016/j.colsurfa.2010.09.037.
[58] S. Rehman, R. Ullah, A.M. Butt, N.D. Gohar, Strategies of making TiO_2 and ZnO visible light active, J. Hazard. Mater. 170 (2009) 560–569. https://doi.org/10.1016/j.jhazmat.2009.05.064.
[59] W. Ren, Z. Ai, F. Jia, L. Zhang, X. Fan, Z. Zou, Low temperature preparation and visible light photocatalytic activity of mesoporous carbon-doped crystalline TiO_2, Appl. Catal. B Environ. 69 (2007) 138–144. https://doi.org/10.1016/j.apcatb.2006.06.015.
[60] X. Shao, W. Lu, R. Zhang, F. Pan, Enhanced photocatalytic activity of TiO_2 -C hybrid aerogels for methylene blue degradation, Sci. Rep. 3 (2013) 1–9. https://doi.org/10.1038/srep03018.
[61] Q. Chen, D. Jiang, W. Shi, D. Wu, Y. Xu, Visible-light-activated Ce-Si co-doped TiO_2 photocatalyst, Appl. Surf. Sci. 255 (2009) 7918–7924. https://doi.org/10.1016/j.apsusc.2009.04.167.
[62] I. Justicia, G. Garcia, G.A. Battiston, R. Gerbasi, F. Ager, M. Guerra, J. Caixach, J.A. Pardo, J. Rivera, A. Figueras, Photocatalysis in the visible range of sub-stoichiometric anatase films prepared by MOCVD, Electrochim. Acta. 50 (2005) 4605–4608. https://doi.org/10.1016/j.electacta.2004.10.096.
[63] I. Justicia, P. Ordejón, G. Canto, J.L. Mozos, J. Fraxedas, G.A. Battiston, R. Gerbasi, A. Figueras, Designed self-doped titanium oxide thin films for efficient visible-light photocatalysis, Adv. Mater. 14 (2002) 1399–1402. https://doi.org/https://doi.org/10.1002/1521-4095(20021002)14:19<1399::AID-ADMA1399>3.0.CO;2-C.

[64] F.J. Ager, I. Justicia, R. Gerbasi, G.A. Battiston, N. McSporran, A. Figueras, RBS analysis of substoichiometric TiO_2-anatase thin films for visible-light photocatalysis, Nucl. Instruments Methods Phys. Res. Sect. B Beam Interact. with Mater. Atoms. 249 (2006) 490–492. https://doi.org/10.1016/j.nimb.2006.03.037.
[65] I. Justicia, G. Garcia, L. Vázquez, J. Santiso, P. Ordejón, G. Battiston, R. Gerbasi, A. Figueras, Self-doped titanium oxide thin films for efficient visible light photocatalysis An example: Nonylphenol photodegradation, Sensors Actuators B Chem. 109 (2005) 52–56. https://doi.org/10.1016/j.snb.2005.03.021.
[66] F. Amano, M. Nakata, A. Yamamoto, T. Tanaka, Rutile titanium dioxide prepared by hydrogen reduction of Degussa P25 for highly efficient photocatalytic hydrogen evolution, Catal. Sci. Technol. 6 (2016) 5693–5699. https://doi.org/10.1039/c6cy00296j.
[67] F. Amano, M. Nakata, High-temperature calcination and hydrogen reduction of rutile TiO_2: A method to improve the photocatalytic activity for water oxidation, Appl. Catal. B Environ. 158–159 (2014) 202–208. https://doi.org/10.1016/j.apcatb.2014.04.025.
[68] V. Subramanian, E. Wolf, P. V. Kamat, Semiconductor-metal composite nanostructures. To what extent do metal nanoparticles improve the photocatalytic activity of TiO_2 films?, J. Phys. Chem. B. 105 (2001) 11439–11446. https://doi.org/10.1021/jp011118k.
[69] Z. Fan, F. Meng, J. Gong, H. Li, Y. Hu, D. Liu, Enhanced photocatalytic activity of hierarchical flower-like CeO_2/TiO_2 heterostructures, Mater. Lett. 175 (2016) 36–39. https://doi.org/10.1016/j.matlet.2016.03.136.
[70] B. Jiang, S. Zhang, X. Guo, B. Jin, Y. Tian, Preparation and photocatalytic activity of CeO_2 /TiO_2 interface composite film, Appl. Surf. Sci. 255 (2009) 5975–5978. https://doi.org/10.1016/j.apsusc.2009.01.049.
[71] F. Kılıç Dokan, M. Kuru, A new approach to optimize the synthesis parameters of TiO_2 microsphere and development of photocatalytic performance, J. Mater. Sci. Mater. Electron. 32 (2021) 640–655. https://doi.org/10.1007/s10854-020-04845-y.
[72] J. Prakash, S. Sun, H.C. Swart, R.K. Gupta, Noble metals-TiO_2 nanocomposites: From fundamental mechanisms to photocatalysis, surface enhanced Raman scattering and antibacterial applications, Appl. Mater. Today. 11 (2018) 82–135. https://doi.org/10.1016/j.apmt.2018.02.002.
[73] J.H. Hsieh, R.B. Yu, Y.K. Chang, C. Li, Structural analysis of TiO_2 and TiO_2-Ag thin films and their antibacterial behaviors, J. Phys. Conf. Ser. 339 (2012) 1–5. https://doi.org/10.1088/1742-6596/339/1/012012.
[74] A. Houas, H. Lachheb, M. Ksibi, E. Elaloui, C. Guillard, J.M. Herrmann, Photocatalytic degradation pathway of methylene blue in water, Appl. Catal. B Environ. 31 (2001) 145–157. https://doi.org/10.1016/S0926-3373(00)00276-9.
[75] T. Zhang, T. Oyama, A. Aoshima, H. Hidaka, J. Zhao, N. Serpone, Photooxidative N-demethylation of methylene blue in aqueous TiO_2 dispersions under UV irradiation, J. Photochem. Photobiol. A Chem. 140 (2001) 163–172. https://doi.org/10.1016/S1010-6030(01)00398-7.
[76] S. Komtchou, N. Delegan, A. Dirany, P. Drogui, D. Robert, M.A. El Khakani, Photo-electrocatalytic oxidation of atrazine using sputtured deposited TiO_2: WN photoanodes under UV/visible light, Catal. Today. 340 (2020) 323–333. https://doi.org/10.1016/j.cattod.2019.04.067.
[77] S. Komtchou, A. Dirany, P. Drogui, N. Delegan, P. Lafrance, D. Robert, M.A. El Khakani, Degradation of atrazine in aqueous solution with electrophotocatalytic process using TiO_{2-x} photoanode, Chemosphere. 157 (2016) 79–88. https://doi.org/10.1016/j.chemosphere.2016.05.022.
[78] R. Daghrir, P. Drogui, N. Delegan, M.A. El Khakani, Electrochemical degradation of chlortetracycline using N-doped Ti/TiO_2 photoanode under sunlight irradiations, Water Res. 47 (2013) 6801–6810. https://doi.org/10.1016/j.watres.2013.09.011.
[79] A. Mills, An overview of the methylene blue ISO test for assessing the activities of photocatalytic films, Appl. Catal. B Environ. 128 (2012) 144–149. https://doi.org/10.1016/j.apcatb.2012.01.019.
[80] L. Zhang, T. Kanki, N. Sano, A. Toyoda, Development of TiO_2 photocatalyst reaction for water purification, Sep. Purif. Technol. 31 (2003) 105–110. https://doi.org/10.1016/S1383-5866(02)00157-0.
[81] Z. Shayegan, C.S. Lee, F. Haghighat, TiO2 photocatalyst for removal of volatile organic compounds in gas phase – A review, Chem. Eng. J. 334 (2018) 2408–2439. https://doi.org/10.1016/j.cej.2017.09.153.
[82] Z. Shayegan, F. Haghighat, C.S. Lee, Carbon-doped TiO2film to enhance visible and UV light photocatalytic degradation of indoor environment volatile organic compounds, J. Environ. Chem. Eng. 8 (2020) 104162. https://doi.org/10.1016/j.jece.2020.104162.
[83] Z. Shayegan, F. Haghighat, C.S. Lee, A. Bahloul, M. Huard, Effect of surface fluorination of P25-TiO_2 on adsorption of indoor environment volatile organic compounds, Chem. Eng. J. 346 (2018) 578–589. https://doi.org/10.1016/j.cej.2018.04.043.
[84] Z. Shayegan, F. Haghighat, C.S. Lee, Photocatalytic oxidation of volatile organic compounds for indoor

environment applications: Three different scaled setups, Chem. Eng. J. 357 (2019) 533–546. https://doi.org/10.1016/j.cej.2018.09.167.
[85] Z. Shayegan, C.S. Lee, F. Haghighat, Effect of surface fluorination of P25-TiO_2 coated on nickel substrate for photocatalytic oxidation of methyl ethyl ketone in indoor environments, J. Environ. Chem. Eng. 7 (2019) 103390. https://doi.org/10.1016/j.jece.2019.103390.
[86] J.S. Dalton, P.A. Janes, N.G. Jones, J.A. Nicholson, K.R. Hallam, G.C. Allen, Photocatalytic oxidation of NO_x gases using TiO_2: A surface spectroscopic approach, Environ. Pollut. 120 (2002) 415–422. https://doi.org/10.1016/S0269-7491(02)00107-0.
[87] F.L. Toma, G. Bertrand, D. Klein, C. Coddet, C. Meunier, Nanostructured photocatalytic titania coatings formed by suspension plasma spraying, J. Therm. Spray Technol. 15 (2006) 587–592. https://doi.org/10.1361/105996306X147234.
[88] F.L. Toma, S. Guessasma, D. Klein, G. Montavon, G. Bertrand, C. Coddet, Neural computation to predict TiO_2 photocalytic efficiency for nitrogen oxides removal, J. Photochem. Photobiol. A Chem. 165 (2004) 91–96. https://doi.org/10.1016/j.jphotochem.2004.03.004.
[89] V. Binas, D. Venieri, D. Kotzias, G. Kiriakidis, Modified TiO_2 based photocatalysts for improved air and health quality, J. Mater. 3 (2017) 3–16. https://doi.org/10.1016/j.jmat.2016.11.002.
[90] X. Qiu, M. Miyauchi, K. Sunada, M. Minoshima, M. Liu, Y. Lu, D. Li, Y. Shimodaira, Y. Hosogi, Y. Kuroda, K. Hashimoto, Hybrid Cu_xO/TiO_2 nanocomposites as risk-reduction materials in indoor environments, ACS Nano. 6 (2012) 1609–1618. https://doi.org/10.1021/nn2045888.
[91] K. Sunada, M. Minoshima, K. Hashimoto, Highly efficient antiviral and antibacterial activities of solid-state cuprous compounds, J. Hazard. Mater. 235–236 (2012) 265–270. https://doi.org/10.1016/j.jhazmat.2012.07.052.
[92] N. George, M. Mahon, A. McDonald, Bactericidal performance of flame-sprayed nanostructured titania-copper composite coatings, J. Therm. Spray Technol. 19 (2010) 1042–1053. https://doi.org/10.1007/s11666-010-9503-2.
[93] M. Versoza, W. Jung, M.L. Barabad, S. Ko, M. Kim, D. Park, Reduction of Escherichia coli using metal plates with the influenced of applied low current and physical barrier of filter layers, Int. J. Environ. Res. Public Health. 16 (2019) 3887. https://doi.org/10.3390/ijerph16203887.
[94] J.R. Scully, The COVID-19 Pandemic, Part 1: Can Antimicrobial Copper-Based Alloys Help Suppress Infectious Transmission of Viruses Originating from Human Contact with High-Touch Surfaces?, CORROSION. 76 (2020) 523–527.
[95] P. Hajkova, P. Spatenka, J. Horsky, I. Horska, A. Kolouch, Photocatalytic effect of TiO_2 films on viruses and bacteria, Plasma Process. Polym. 4 (2007) 397–401. https://doi.org/10.1002/ppap.200731007.
[96] G. Borkow, S.S. Zhou, T. Page, J. Gabbay, A novel anti-influenza copper oxide containing respiratory face mask, PLoS One. 5 (2010). https://doi.org/10.1371/journal.pone.0011295.
[97] G. Borkow, Safety of Using Copper Oxide in Medical Devices and Consumer Products, Curr. Chem. Biol. 6 (2012) 86–92. https://doi.org/10.2174/2212796811206010086.
[98] M. Liu, K. Sunada, K. Hashimoto, M. Miyauchi, Visible-light sensitive Cu(ii)-TiO_2 with sustained anti-viral activity for efficient indoor environmental remediation, J. Mater. Chem. A. 3 (2015) 17312–17319. https://doi.org/10.1039/c5ta03756e.
[99] N. Bono, F. Ponti, C. Punta, G. Candiani, Effect of UV irradiation and TiO_2-photocatalysis on airborne bacteria and viruses: An overview, Materials (Basel). 14 (2021) 1075. https://doi.org/10.3390/ma14051075.
[100] T. Terlouw, C. Bauer, R. McKenna, M. Mazzotti, Large-scale hydrogen production via water electrolysis: a techno-economic and environmental assessment, Energy Environ. Sci. (2022) 3583–3602. https://doi.org/10.1039/d2ee01023b.
[101] M. Tahir, S. Tasleem, B. Tahir, Recent development in band engineering of binary semiconductor materials for solar driven photocatalytic hydrogen production, Int. J. Hydrogen Energy. 45 (2020) 15985–16038. https://doi.org/10.1016/j.ijhydene.2020.04.071.
[102] S.S. Tak, O. Shetye, O. Muley, H. Jaiswal, S.N. Malik, Emerging technologies for hydrogen production from wastewater, Int. J. Hydrogen Energy. (2022) 1–20. https://doi.org/10.1016/j.ijhydene.2022.06.225.
[103] B. Kim, Y. Jung, B.J. Park, G. Das, H.H. Yoon, Y.S. Yoon, Photo-assisted electrolysis of urea using Ni-modified WO_3/g-C_3N_4 as a bifunctional catalyst, Int. J. Hydrogen Energy. 47 (2022) 5797–5806. https://doi.org/10.1016/j.ijhydene.2021.11.237.
[104] M.R. Gholipour, C.T. Dinh, F. Béland, T.O. Do, Nanocomposite heterojunctions as sunlight-driven photocatalysts for hydrogen production from water splitting, Nanoscale. 7 (2015) 8187–8208. https://doi.org/10.1039/c4nr07224c.

[105] Z. Wang, L. Wang, Photoelectrode for water splitting: Materials, fabrication and characterization, Sci. China Mater. 61 (2018) 806–821. https://doi.org/10.1007/s40843-018-9240-y.
[106] A. Naldoni, M. Altomare, G. Zoppellaro, N. Liu, Š. Kment, R. Zbořil, P. Schmuki, Photocatalysis with reduced TiO_2 : From Black TiO_2 to cocatalyst-free hydrogen production, ACS Catal. 9 (2019) 345–364. https://doi.org/10.1021/acscatal.8b04068.
[107] S. Chen, T. Liu, Z. Zheng, M. Ishaq, G. Liang, P. Fan, T. Chen, J. Tang, Recent progress and perspectives on Sb_2Se_3-based photocathodes for solar hydrogen production via photoelectrochemical water splitting, J. Energy Chem. 67 (2022) 508–523. https://doi.org/10.1016/j.jechem.2021.08.062.
[108] Q. Chen, G. Fan, H. Fu, Z. Li, Z. Zou, Tandem photoelectrochemical cells for solar water splitting, Adv. Phys. X. 3 (2018) 863–884. https://doi.org/10.1080/23746149.2018.1487267.
[109] J.H. Kim, H. Kaneko, T. Minegishi, J. Kubota, K. Domen, J.S. Lee, Overall Photoelectrochemical Water Splitting using Tandem Cell under Simulated Sunlight, ChemSusChem. 9 (2016) 61–66. https://doi.org/10.1002/cssc.201501401.
[110] J. Brillet, J.H. Yum, M. Cornuz, T. Hisatomi, R. Solarska, J. Augustynski, M. Graetzel, K. Sivula, Highly efficient water splitting by a dual-absorber tandem cell, Nat. Photonics. 6 (2012) 824–828. https://doi.org/10.1038/nphoton.2012.265.
[111] Purifics Water Inc, (n.d.). https://www.purifics.com/photo-cat.
[112] A. Mills, A. Lepre, N. Elliott, S. Bhopal, I.P. Parkin, S.A. O'Neill, Characterisation of the photocatalyst Pilkington Activ™: A reference film photocatalyst?, J. Photochem. Photobiol. A Chem. 160 (2003) 213–224. https://doi.org/10.1016/S1010-6030(03)00205-3.
[113] S. Tek, Comparative study of optically activated nanocomposites with photocatalytic TiO_2 and ZnO nanoparticles for massive environmental decontamination, J. Nanophotonics. 1 (2007) 011685. https://doi.org/10.1117/1.2828851.
[114] L. Du, T.W. Coyle, K. Chien, L. Pershin, T. Li, M. Golozar, Titanium dioxide coating prepared by use of a suspension-solution plasma-spray process, J. Therm. Spray Technol. 24 (2015) 915–924. https://doi.org/10.1007/s11666-015-0251-1.
[115] J.R. Davis, Handbook of Thermal Spray Technology - Google Books, ASM Int. (2004).
[116] S. Amin, H. Panchal, A. Professor, A Review on Thermal Spray Coating Processes, Int. J. Curr. Trends Eng. Res. 2 (2016) 556–563. http://www.ijcter.com.
[117] A.S.M. Thermal, S. Society, Overview of Thermal Spray Technology, Therm. Spray Technol. (2022) 1–9. https://doi.org/10.31399/asm.tb.tstap.t56040001.
[118] P.L. Fauchais, M.I. Heberlein, Joachim V.R.Boulos, Thermal Spray Fundamentals, Springer Science & Business Media, 2014. https://doi.org/10.1007/978-3-030-70672-2.
[119] H. Herman, S. Sampath, R. Mccune, T hermal Spray : Current Status and Future Trends, MRS Bull. 17 (2000) 17–25.
[120] A. Feuerstein, J. Knapp, T. Taylor, A. Ashary, A. Bolcavage, N. Hitchman, Technical and economical aspects of current thermal barrier coating systems for gas turbine engines by thermal spray and EBPVD: A review, J. Therm. Spray Technol. 17 (2008) 199–213. https://doi.org/10.1007/s11666-007-9148-y.
[121] A. Vardelle, C. Moreau, J. Akedo, H. Ashrafizadeh, C.C. Berndt, J.O. Berghaus, M. Boulos, J. Brogan, A.C. Bourtsalas, A. Dolatabadi, M. Dorfman, T.J. Eden, P. Fauchais, G. Fisher, F. Gaertner, M. Gindrat, R. Henne, M. Hyland, E. Irissou, E.H. Jordan, K.A. Khor, A. Killinger, Y.C. Lau, C.J. Li, L. Li, J. Longtin, N. Markocsan, P.J. Masset, J. Matejicek, G. Mauer, A. McDonald, J. Mostaghimi, S. Sampath, G. Schiller, K. Shinoda, M.F. Smith, A.A. Syed, N.J. Themelis, F.L. Toma, J.P. Trelles, R. Vassen, P. Vuoristo, The 2016 Thermal Spray Roadmap, J. Therm. Spray Technol. 25 (2016) 1376–1440. https://doi.org/10.1007/s11666-016-0473-x.
[122] P. Fauchais, M. Vardelle, S. Goutier, Latest Researches Advances of Plasma Spraying: From Splat to Coating Formation, J. Therm. Spray Technol. 25 (2016) 1534–1553. https://doi.org/10.1007/s11666-016-0435-3.
[123] A. Vardelle, C. Moreau, N.J. Themelis, C. Chazelas, A Perspective on Plasma Spray Technology, Plasma Chem. Plasma Process. 35 (2015) 491–509. https://doi.org/10.1007/s11090-014-9600-y.
[124] P. Fauchais, R. Etchart-Salas, C. Delbos, M. Tognonvi, V. Rat, J.F. Coudert, T. Chartier, Suspension and solution plasma spraying of finely structured layers: potential application to SOFCs, J. Phys. D. Appl. Phys. 40 (2007) 2394–2406. https://doi.org/10.1088/0022-3727/40/8/S19.
[125] N. Sharifi, M. Pugh, C. Moreau, A. Dolatabadi, Developing hydrophobic and superhydrophobic TiO_2 coatings by plasma spraying, Surf. Coatings Technol. 289 (2016) 29–36. https://doi.org/10.1016/j.surfcoat.2016.01.029.
[126] P. Fauchais, V. Rat, J.F. Coudert, N. Caron, P. Fauchais, V. Rat, J.F. Coudert, Parameters Controlling Liquid

Plasma Spraying : Solutions , Sols , or Suspensions, J. Therm. Spray Technol. 17 (2008) 31–59. https://doi.org/10.1007/s11666-007-9152-2.
[127] N. Curry, K. VanEvery, T. Snyder, J. Susnjar, S. Bjorklund, Performance testing of suspension plasma sprayed thermal barrier coatings produced with varied suspension parameters, Coatings. 5 (2015) 338–356. https://doi.org/10.3390/coatings5030338.
[128] J.O. Oberste Berghaus, J.G. Legoux, C. Moreau, F. Tarasi, T. Chráska, Mechanical and thermal transport properties of suspension thermal-sprayed alumina-zirconia composite coatings, J. Therm. Spray Technol. 17 (2008) 91–104. https://doi.org/10.1007/s11666-007-9146-0.
[129] M. Jadidi, M. Mousavi, S. Moghtadernejad, A. Dolatabadi, A Three-Dimensional Analysis of the Suspension Plasma Spray Impinging on a Flat Substrate, J. Therm. Spray Technol. 24 (2014) 11–23. https://doi.org/10.1007/s11666-014-0166-2.
[130] A. Ganvir, Design of Suspension Plasma Sprayed Thermal Barrier Coatings, Doctoral dissertation, University West, 2018. http://www.diva-portal.org/smash/get/diva2:1209589/FULLTEXT01.pdf.
[131] K. Vanevery, M.J.M. Krane, R.W. Trice, H. Wang, W. Porter, M. Besser, D. Sordelet, J. Ilavsky, J. Almer, Column formation in suspension plasma-sprayed coatings and resultant thermal properties, J. Therm. Spray Technol. 20 (2011) 817–828. https://doi.org/10.1007/s11666-011-9632-2.
[132] R. Jaworski, L. Pawlowski, F. Roudet, S. Kozerski, A. Le Maguer, Influence of Suspension Plasma Spraying Process Parameters on TiO_2 Coatings Microstructure, J. Therm. Spray Technol. 17 (2007) 73–81. https://doi.org/10.1007/s11666-007-9147-z.
[133] F.L. Toma, G. Bertrand, D. Klein, C. Meunier, S. Begin, Development of photocatalytic active TiO_2 surfaces by thermal spraying of nanopowders, J. Nanomater. 58 (2008). https://doi.org/10.1155/2008/384171.
[134] F.L. Toma, D. Sokolov, G. Bertrand, D. Klein, C. Coddet, C. Meunier, Comparison of the photocatalytic behavior of TiO_2 coatings elaborated by different thermal spraying processes, Proc. Int. Therm. Spray Conf. 15 (2006) 576–581. https://doi.org/10.1361/105996306X147225.
[135] I. Burlacov, J. Jirkovský, M. Müller, R.B. Heimann, Induction plasma-sprayed photocatalytically active titania coatings and their characterisation by micro-Raman spectroscopy, Surf. Coatings Technol. 201 (2006) 255–264. https://doi.org/10.1016/j.surfcoat.2005.11.117.
[136] P. Vu, N. Otto, A. Vogel, F. Kern, A. Killinger, R. Gadow, Efficiently quantifying the anatase content and investigating its effect on the photocatalytic activity of titania coatings by suspension plasma spraying, Surf. Coatings Technol. (2018). https://doi.org/10.1016/j.surfcoat.2018.07.064.
[137] J.H. Huang, M.S. Wong, Structures and properties of titania thin films annealed under different atmosphere, Thin Solid Films. 520 (2011) 1379–1384. https://doi.org/10.1016/j.tsf.2011.08.094.
[138] W. Fang, M. Xing, J. Zhang, A new approach to prepare Ti^{3+} self-doped TiO_2 via $NaBH_4$ reduction and hydrochloric acid treatment, Appl. Catal. B Environ. 160–161 (2014) 240–246. https://doi.org/10.1016/j.apcatb.2014.05.031.
[139] S. Wang, J. Cai, J. Mao, S. Li, J. Shen, S. Gao, J. Huang, X. Wang, I.P. Parkin, Y. Lai, Defective black Ti^{3+} self-doped TiO_2 and reduced graphene oxide composite nanoparticles for boosting visible-light driven photocatalytic and photoelectrochemical activity, Appl. Surf. Sci. 467–468 (2019) 45–55. https://doi.org/10.1016/j.apsusc.2018.10.138.
[140] F.L. Toma, G. Bertrand, S.O. Chwa, D. Klein, H. Liao, C. Meunier, C. Coddet, Microstructure and photocatalytic properties of nanostructured TiO_2 and TiO_2-Al coatings elaborated by HVOF spraying for the nitrogen oxides removal, Mater. Sci. Eng. A. 417 (2006) 56–62. https://doi.org/10.1016/j.msea.2005.09.112.
[141] P. Fauchais, M. Vardelle, S. Goutier, A. Vardelle, Key Challenges and Opportunities in Suspension and Solution Plasma Spraying, Plasma Chem. Plasma Process. 35 (2015) 511–525. https://doi.org/10.1007/s11090-014-9594-5.
[142] S.T. Aruna, A. Vismaya, N. Balaji, Photocatalytic behavior of titania coatings fabricated by suspension and solution precursor plasma spray processes, Mater. Manuf. Process. 36 (2021) 868–875. https://doi.org/10.1080/10426914.2020.1866188.
[143] D. Tejero-martin, Z. Pala, S. Rushworth, T. Hussain, Splat formation and microstructure of solution precursor thermal sprayed Nb-doped titanium oxide coatings, Ceram. Int. 46 (2020) 5098–5108. https://doi.org/10.1016/j.ceramint.2019.10.253.
[144] K. Vanevery, M.J.M. Krane, R.W. Trice, W. Porter, H. Wang, M. Besser, D. Sordelet, J. Ilavsky, J. Almer, In-flight alloying of nanocrystalline Yttria-stabilized zirconia using suspension spray to produce ultra-low thermal conductivity thermal barriers, Int. J. Appl. Ceram. Technol. 8 (2011) 1382–1392. https://doi.org/10.1111/j.1744-7402.2010.02593.x.
[145] S. Gong, K. VanEvery, H. Wang, R.W. Trice, Microstructure and thermal properties of inflight rare-earth

doped thermal barriers prepared by suspension plasma spray, J. Eur. Ceram. Soc. 34 (2014) 1243–1253. https://doi.org/10.1016/j.jeurceramsoc.2013.11.016.
[146] M. Oksa, E. Turunen, T. Suhonen, T. Varis, S.P. Hannula, Optimization and characterization of high velocity oxy-fuel sprayed coatings: Techniques, materials, and applications, Coatings. 1 (2011) 17–52. https://doi.org/10.3390/coatings1010017.
[147] G. Bolelli, V. Cannillo, R. Gadow, A. Killinger, L. Lusvarghi, J. Rauch, Properties of High Velocity Suspension Flame Sprayed (HVSFS) TiO_2 coatings, Surf. Coatings Technol. 203 (2009) 1722–1732. https://doi.org/10.1016/j.surfcoat.2009.01.006.
[148] S. Zimmermann, G. Mauer, K.H. Rauwald, J. Schein, Characterization of an Axial-Injection Plasma Spray Torch, J. Therm. Spray Technol. 30 (2021) 1724–1736. https://doi.org/10.1007/s11666-021-01235-6.
[149] Thermal Spray & Multiphase Flow Laboratory facilities, Concordia University, (n.d.). https://users.encs.concordia.ca/~dolat/tsmf/static/facilities/.
[150] H. Khatibnezhad, F. Ambriz-Vargas, F. Ben Ettouil, C. Moreau, An investigation on the photocatalytic activity of sub-stoichiometric TiO_{2-x} coatings produced by suspension plasma spray, J. Eur. Ceram. Soc. (2020) 0–1. https://doi.org/10.1016/j.jeurceramsoc.2020.08.017.
[151] Y. Lu, M. Hirohashi, K. Sato, Thermoelectric properties of non-stoichiometric titanium dioxide TiO_{2-x} fabricated by reduction treatment using carbon powder, Mater. Trans. 47 (2006) 1449–1452. https://doi.org/10.2320/matertrans.47.1449.
[152] H. Lee, S.J. Han, R.C. Seshadri, S. Sampath, Thermoelectric properties of in-situ plasma spray synthesized sub-stoichiometry TiO_{2-x}, Sci. Rep. 6 (2016) 1–11. https://doi.org/10.1038/srep36581.
[153] H. Lee, R.C. Seshadri, Z. Pala, S. Sampath, Optimizing thermoelectric properties of in situ plasma-spray-synthesized sub-stoichiometric TiO_{2-x} deposits, J. Therm. Spray Technol. 27 (2018) 968–982. https://doi.org/10.1007/s11666-018-0731-1.
[154] B. Xu, J. Ding, L. Feng, Y. Ding, F. Ge, Z. Cai, Self-cleaning cotton fabrics via combination of photocatalytic TiO_2 and superhydrophobic SiO_2, Surf. Coatings Technol. 262 (2015) 70–76. https://doi.org/10.1016/j.surfcoat.2014.12.017.
[155] T. Meunier, L. Desmarets, S. Bordage, M. Bamba, K. Hervouet, Y. Rouillé, N. François, M. Decossas, V. Sencio, F. Trottein, F.H.T. Bi, O. Lambert, J. Dubuisson, S. Belouzard, S. Sahpaz, K. Séron, A Photoactivable Natural Product with Broad Antiviral Activity against Enveloped Viruses, Including Highly Pathogenic Coronaviruses, Antimicrob. Agents Chemother. 66 (2022). https://doi.org/10.1128/AAC.01581-21.
[156] S.T. Smale, Luciferase assay, Cold Spring Harb. Protoc. 5 (2010) 2010–2013. https://doi.org/10.1101/pdb.prot5421.
[157] J.O. Noyce, H. Michels, C.W. Keevil, Inactivation of influenza A virus on copper versus stainless steel surfaces, Appl. Environ. Microbiol. 73 (2007) 2748–2750. https://doi.org/10.1128/AEM.01139-06.
[158] S. Mehtar, I. Wiid, S.D. Todorov, The antimicrobial activity of copper and copper alloys against nosocomial pathogens and Mycobacterium tuberculosis isolated from healthcare facilities in the Western Cape: an in-vitro study, J. Hosp. Infect. 68 (2008) 45–51. https://doi.org/10.1016/j.jhin.2007.10.009.
[159] F.N.I. Sari, D.T.K. Yen, J.M. Ting, Enhanced photocatalytic performance of TiO_2 through a novel direct dual Z-scheme design, Appl. Surf. Sci. 533 (2020) 147506. https://doi.org/10.1016/j.apsusc.2020.147506.
[160] S. Banerjee, S.C. Pillai, P. Falaras, K.E. O'shea, J.A. Byrne, D.D. Dionysiou, New insights into the mechanism of visible light photocatalysis, J. Phys. Chem. Lett. 5 (2014) 2543–2554. https://doi.org/10.1021/jz501030x.
[161] L.B. Xiong, J.L. Li, B. Yang, Y. Yu, Ti^{3+} in the surface of titanium dioxide: Generation, properties and photocatalytic application, J. Nanomater. 2012 (2012). https://doi.org/10.1155/2012/831524.
[162] T. Zhang, Y. Liu, Y. Rao, X. Li, D. Yuan, S. Tang, Q. Zhao, Enhanced photocatalytic activity of TiO_2 with acetylene black and persulfate for degradation of tetracycline hydrochloride under visible light, Chem. Eng. J. 384 (2020) 123350. https://doi.org/10.1016/j.cej.2019.123350.
[163] Y.Y. Zaw, D. Channei, T. Threrujirapapong, W. Khanitchaidecha, A. Nakaruk, Effect of anatase/rutile phase ratio on the photodegradation of methylene blue under uv irradiation, Mater. Sci. Forum. 998 MSF (2020) 78–83. https://doi.org/10.4028/www.scientific.net/MSF.998.78.
[164] A. Nakaruk, D. Ragazzon, C.C. Sorrell, Anatase-rutile transformation through high-temperature annealing of titania films produced by ultrasonic spray pyrolysis, Thin Solid Films. 518 (2010) 3735–3742. https://doi.org/10.1016/j.tsf.2009.10.109.
[165] N. Wetchakun, B. Incessungvorn, K. Wetchakun, S. Phanichphant, Influence of calcination temperature on anatase to rutile phase transformation in TiO_2 nanoparticles synthesized by the modified sol-gel method, Mater. Lett. 82 (2012) 195–198. https://doi.org/10.1016/j.matlet.2012.05.092.
[166] M. Wagstaffe, H. Noei, A. Stierle, Elucidating the Defect-Induced Changes in the Photocatalytic Activity of

TiO_2, J. Phys. Chem. C. 124 (2020) 12539–12547. https://doi.org/10.1021/acs.jpcc.0c02809.
[167] M. Mehta, N. Kodan, S. Kumar, A. Kaushal, L. Mayrhofer, M. Walter, M. Moseler, A. Dey, S. Krishnamurthy, S. Basu, A.P. Singh, Hydrogen treated anatase TiO_2: A new experimental approach and further insights from theory, J. Mater. Chem. A. 4 (2016) 2670–2681. https://doi.org/10.1039/c5ta07133j.
[168] A. Kleiman, J.M. Meichtry, D. Vega, M.I. Litter, A. Márquez, Photocatalytic activity of TiO_2 films prepared by cathodic arc deposition: Dependence on thickness and reuse of the photocatalysts, Surf. Coatings Technol. 382 (2020) 125154. https://doi.org/10.1016/j.surfcoat.2019.125154.
[169] R.C. Tucker Jr, Introduction to Coating Design and Processing, 2013. https://doi.org/10.31399/asm.hb.v05a.a0005725.
[170] J.F. Li, C.X. Ding, Crystalline orientation of plasma-sprayed TiO_2 coatings, J. Mater. Sci. Lett. 17 (1998) 1747–1749. https://doi.org/10.1023/A:1006647807208.
[171] M. Bai, R. Khammas, L. Guan, J.W. Murray, T. Hussain, Suspension high velocity oxy-fuel spraying of a rutile TiO_2 feedstock: Microstructure, phase evolution and photocatalytic behaviour, Ceram. Int. 43 (2017) 15288–15295. https://doi.org/10.1016/j.ceramint.2017.08.068.
[172] E. Bannier, G. Darut, E. Sánchez, A. Denoirjean, M.C. Bordes, M.D. Salvador, E. Rayón, H. Ageorges, Microstructure and photocatalytic activity of suspension plasma sprayed TiO2 coatings on steel and glass substrates, Surf. Coatings Technol. 206 (2011) 378–386. https://doi.org/10.1016/j.surfcoat.2011.07.039.
[173] M. Bozorgtabar, M. Rahimipour, M. Salehi, Effect of thermal spray processes on anatase-rutile phase transformation in nano-structured TiO_2 photo-catalyst coatings, Surf. Eng. 26 (2010) 422–427. https://doi.org/10.1179/174329409X446278.
[174] Z. Yi, J. Liu, W. Wei, J. Wang, S.W. Lee, Photocatalytic performance and microstructure of thermal-sprayed nanostructured TiO_2 coatings, Ceram. Int. 34 (2008) 351–357. https://doi.org/10.1016/j.ceramint.2006.10.023.
[175] D. Chen, F. Li, A.K. Ray, External and internal mass transfer effect on photocatalytic degradation, Catal. Today. 66 (2001) 475–485. https://doi.org/10.1016/S0920-5861(01)00256-5.
[176] D. Chen, F. Li, A.K. Ray, Effect of mass transfer and catalyst layer thickness on photocatalytic reaction, AIChE J. 46 (2000) 1034–1045. https://doi.org/10.1002/aic.690460515.
[177] F.L. Toma, L. Berger, C.C. Stahr, T. Naumann, S. Langner, Microstructures and Functional Properties of Suspension-Sprayed Al_2O_3 and TiO_2 Coatings : An Overview, J. Therm. Spray Technol. 19 (2010) 262–274. https://doi.org/10.1007/s11666-009-9417-z.
[178] G. Bertrand, N. Berger-keller, C. Meunier, C. Coddet, Evaluation of metastable phase and microhardness on plasma sprayed titania coatings, Surf. Coatings Technol. 200 (2006) 5013–5019. https://doi.org/10.1016/j.surfcoat.2005.05.016.
[179] V.H. Castrejón-Sánchez, E. Camps, M. Camacho-López, Quantification of phase content in TiO_2 thin films by Raman spectroscopy, Superf. y Vacio. 27 (2014) 88–92.
[180] T.D. Robert, L.D. Laude, V.M. Geskin, R. Lazzaroni, Micro-Raman spectroscopy study of surface transformations induced by excimer laser irradiation of TiO_2, Thin Solid Films. 440 (2003) 268–277. https://doi.org/10.1016/S0040-6090.
[181] C. Lee, H. Choi, C. Lee, H. Kim, Photocatalytic properties of nano-structured TiO_2 plasma sprayed coating, Surf. Coatings Technol. 173 (2003) 192–200. https://doi.org/10.1016/S0257-8972(03)00509-7.
[182] H. Okamoto, O-Ti (Oxygen-Titanium), J. Phase Equilibria Diffus. 32 (2011) 473–474. https://doi.org/10.1007/s11669-011-9935-5.
[183] F.L. Toma, G. Bertrand, S. Begin, C. Meunier, O. Barres, D. Klein, C. Coddet, Microstructure and environmental functionalities of TiO_2-supported photocatalysts obtained by suspension plasma spraying, Appl. Catal. B Environ. 68 (2006) 74–84. https://doi.org/10.1016/j.apcatb.2006.07.009.
[184] J. Zhang, Q. Xu, Z. Feng, M. Li, C. Li, Importance of the Relationship between Surface Phases and Photocatalytic Activity of TiO_2, Angew. Chemie. 120 (2008) 1790–1793. https://doi.org/10.1002/ange.200704788.
[185] F. Millot, M.G. Blanchin, R. Tétot, J.F. Marucco, B. Poumellec, C. Picard, B. Touzelin, High temperature nonstoichiometric rutile TiO_{2-x}, Prog. Solid State Chem. 17 (1987) 263–293. https://doi.org/10.1016/0079-6786(87)90004-5.
[186] K. Szot, M. Rogala, W. Speier, Z. Klusek, A. Besmehn, R. Waser, TiO_2 - A prototypical memristive material, Nanotechnology. 22 (2011) 254001. https://doi.org/10.1088/0957-4484/22/25/254001.
[187] C. Zhao, Y. Yang, L. Luo, S. Shao, Y. Zhou, Y. Shao, F. Zhan, J. Yang, Y. Zhou, γ-ray induced formation of oxygen vacancies and Ti^{3+} defects in anatase TiO_2 for efficient photocatalytic organic pollutant degradation, Sci. Total Environ. 747 (2020) 141533. https://doi.org/10.1016/j.scitotenv.2020.141533.

[188] A. Sarkar, G.G. Khan, The formation and detection techniques of oxygen vacancies in titanium oxide-based nanostructures, Nanoscale. 11 (2019) 3414–3444. https://doi.org/10.1039/c8nr09666j.
[189] I. Tsuyumoto, H. Uchikawa, New orthorhombic titanium oxide, $TiO_{1.94}$, J. Mater. Sci. Lett. 19 (2000) 2075–2076. https://doi.org/10.1023/A:1026733617500.
[190] A. Richter, L.M. Berger, Y.J. Sohn, S. Conze, K. Sempf, R. Vaßen, Impact of Al_2O_3-40 wt.% TiO_2 feedstock powder characteristics on the sprayability, microstructure and mechanical properties of plasma sprayed coatings, J. Eur. Ceram. Soc. 39 (2019) 5391–5402. https://doi.org/10.1016/j.jeurceramsoc.2019.08.026.
[191] W.D. Callister, D.G. Rethwisch, Chapter 21: Optical Properties, in: Mater. Sci. Eng. An Introd., 2013: pp. 838–867.
[192] D.O. Scanlon, C.W. Dunnill, J. Buckeridge, S.A. Shevlin, A.J. Logsdail, S.M. Woodley, C.R.A. Catlow, M.J. Powell, R.G. Palgrave, I.P. Parkin, G.W. Watson, T.W. Keal, P. Sherwood, A. Walsh, A.A. Sokol, Band alignment of rutile and anatase TiO_2, Nat. Mater. 12 (2013) 798–801. https://doi.org/10.1038/nmat3697.
[193] N.T. Nolan, D.W. Synnott, M.K. Seery, S.J. Hinder, A. Van Wassenhoven, S.C. Pillai, Effect of N-doping on the photocatalytic activity of sol–gel TiO_2, J. Hazard. Mater. 212 (2012) 88–94. https://doi.org/10.1016/j.jhazmat.2011.08.074.
[194] C. Wu, Y. Yue, X. Deng, W. Hua, Z. Gao, Investigation on the synergetic effect between anatase and rutile nanoparticles in gas-phase photocatalytic oxidations, Catal. Today. 93–95 (2004) 863–869. https://doi.org/10.1016/j.cattod.2004.06.087.
[195] F.L. Toma, L.M. Berger, D. Jacquet, D. Wicky, I. Villaluenga, Y.R. de Miguel, J.S. Lindeløv, Comparative study on the photocatalytic behaviour of titanium oxide thermal sprayed coatings from powders and suspensions, Surf. Coatings Technol. 203 (2009) 2150–2156. https://doi.org/10.1016/j.surfcoat.2008.10.022.
[196] H. Zhang, M. Yu, X. Qin, Photocatalytic activity of TiO_2 nanofibers: The surface crystalline phase matters, Nanomaterials. 9 (2019) 535. https://doi.org/10.3390/nano9040535.
[197] M. Gardon, C. Fernández-Rodríguez, D. Garzón Sousa, J.M. Doña-Rodríguez, S. Dosta, I.G. Cano, J.M. Guilemany, Photocatalytic Activity of Nanostructured Anatase Coatings Obtained by Cold Gas Spray, J. Therm. Spray Technol. 23 (2014) 1135–1141. https://doi.org/10.1007/s11666-014-0087-0.
[198] Y. Yu, J.C. Yu, J. Yu, Y. Kwok, Y. Che, J. Zhao, L. Ding, W. Ge, P. Wong, Enhancement of photocatalytic activity of mesoporous TiO_2 by using carbon nanotubes, Appl. Catal. A Gen. 289 (2005) 186–196. https://doi.org/10.1016/j.apcata.2005.04.057.
[199] R.D. Shannon, J.A. Pask, Kinetic of the anatase-rutile transformation, J. Am. Ceram. Soc. 48 (1965) 391–398.
[200] G. Bao, L. Wang, Multiple cracking in functionally graded ceramic/metal coatings, Int. J. Solids Struct. 32 (1995) 2853–2871. https://doi.org/10.1016/0020-7683(94)00267-Z.
[201] S. Numata, N. Kinjo, D. Makino, Chemical structures and properties of low thermal expansion coefficient polyimides, Polym. Eng. Sci. 28 (1988) 906–911. https://doi.org/10.1002/pen.760281405.
[202] X.Q. Cao, R. Vassen, D. Stoever, Ceramic materials for thermal barrier coatings, J. Eur. Ceram. Soc. 24 (2004) 1–10. https://doi.org/10.1016/S0955-2219(03)00129-8.
[203] Z. Pala, E. Shaw, J.W. Murray, N. Senin, T. Hussain, Suspension high velocity oxy-fuel spraying of TiO_2: A quantitative approach to phase composition, J. Eur. Ceram. Soc. 37 (2017) 801–810. https://doi.org/10.1016/j.jeurceramsoc.2016.08.030.
[204] Z. El Koura, M. Cazzanelli, N. Bazzanella, N. Patel, R. Fernandes, G.E. Arnaoutakis, A. Gakamsky, A. Dick, A. Quaranta, A. Miotello, Synthesis and characterization of Cu and N codoped RF-sputtered TiO_2 films: photoluminescence dynamics of charge carriers relevant for water splitting, J. Phys. Chem. C. 120 (2016) 12042−12050.
[205] J.C. Parker, R.W. Siegel, Calibration of the Raman spectrum to the oxygen stoichiometry of nanophase TiO_2, Appl. Phys. Lett. 57 (1990) 943–945. https://doi.org/10.1063/1.104274.
[206] A. Turkovic, M. Ivanda, A. Drasner, V. Vranesa, M. Persin, Raman spectroscopy of thermally annealed TiO_2 thin films, Thin Solid Films. 198 (1991) 199–205.
[207] J.C. Parker, R.W. Siegel, Raman microprobe study of nanophase TiO_2 and oxidation-induced spectral changes, J. Mater. Res. 5 (1990) 1246–1252. https://doi.org/10.1557/JMR.1990.1246.
[208] M. Alijani, B.K. Kaleji, S. Rezaee, Improved visible light photocatalytic activity of TiO_2 nano powders with metal ions doping for glazed ceramic tiles, Opt. Quantum Electron. 49 (2017) 1–13. https://doi.org/10.1007/s11082-017-1064-x.
[209] J. Ananpattarachai, P. Kajitvichyanukul, S. Seraphin, Visible light absorption ability and photocatalytic oxidation activity of various interstitial N-doped TiO_2 prepared from different nitrogen dopants, J. Hazard. Mater. 168 (2009) 253–261. https://doi.org/10.1016/j.jhazmat.2009.02.036.
[210] M.R. Gholipour, F. Béland, T.O. Do, Graphitic carbon nitride-titanium dioxide nanocomposite for

photocatalytic hydrogen production under visible light, Int. J. Chem. React. Eng. 14 (2016) 851–858. https://doi.org/10.1515/ijcre-2015-0094.
[211] N.N. Ilkhechi, M. Alijani, B.K. Kaleji, Optical and structural properties of TiO_2 nanopowders with Co/Ce doping at various temperature, Opt. Quantum Electron. 48 (2016) 1–9. https://doi.org/10.1007/s11082-016-0435-z.
[212] H. Khatibnezhad, F. Ambriz-Vargas, F. Ben Ettouil, C. Moreau, Role of phase content on the photocatalytic performance of TiO_2 coatings deposited by suspension plasma spray, J. Eur. Ceram. Soc. 42 (2022) 2905–2920. https://doi.org/10.1016/j.jeurceramsoc.2022.02.010.
[213] M. Janczarek, E. Kowalska, On the origin of enhanced photocatalytic activity of copper-modified titania in the oxidative reaction systems, Catalysts. 7 (2017) 317. https://doi.org/10.3390/catal7110317.
[214] J. wen Shi, J. tang Zheng, P. Wu, Preparation, characterization and photocatalytic activities of holmium-doped titanium dioxide nanoparticles, J. Hazard. Mater. 161 (2009) 416–422. https://doi.org/10.1016/j.jhazmat.2008.03.114.
[215] A.S.M. Nur, M. Sultana, A. Mondal, S. Islam, F.N. Robel, A. Islam, M.S.A. Sumi, A review on the development of elemental and codoped TiO_2 photocatalysts for enhanced dye degradation under UV–vis irradiation, J. Water Process Eng. 47 (2022) 102728. https://doi.org/10.1016/j.jwpe.2022.102728.
[216] A. Mehtab, J. Ahmed, S.M. Alshehri, Y. Mao, T. Ahmad, Rare earth doped metal oxide nanoparticles for photocatalysis: A perspective, Nanotechnology. 33 (2022) 142001. https://doi.org/10.1088/1361-6528/ac43e7.
[217] E. Cerrato, E. Gaggero, P. Calza, M.C. Paganini, The role of Cerium, Europium and Erbium doped TiO2 photocatalysts in water treatment: A mini-review, Chem. Eng. J. Adv. 10 (2022) 100268. https://doi.org/10.1016/j.ceja.2022.100268.
[218] M. Alijani, B.K. Kaleji, Optical and structural properties of TiO_2 nanopowders with Ce/Sn doping at various calcination temperature and time, Opt. Quantum Electron. 49 (2017) 1–16. https://doi.org/10.1007/s11082-016-0851-0.
[219] P. GOUGEON, A new Sensor for on-line Diagnostics of Particles under Thermal Spraying Conditions., Adv. Proc. Tech. 6 (1994). https://cir.nii.ac.jp/crid/1571417124050802816.bib?lang=en (accessed August 16, 2022).
[220] P. Lewis, S. Micklethwaite, J. Harrington, M. Dixon, R. Brydson, N. Hondow, Exploring backscattered imaging in low voltage FE-SEM, J. Phys. Conf. Ser. 644 (2015). https://doi.org/10.1088/1742-6596/644/1/012019.
[221] Y. Li, T. Ishigaki, Thermodynamic analysis of nucleation of anatase and rutile from TiO_2 melt, J. Cryst. Growth. 242 (2002) 511–516. https://doi.org/10.1016/S0022-0248(02)01438-0.
[222] G.B. Vieira, H.J. José, M. Peterson, V.Z. Baldissarelli, P. Alvarez, R. de F.P.M. Moreira, CeO_2 / TiO_2 nanostructures enhance adsorption and photocatalytic degradation of organic compounds in aqueous suspension, "Journal Photochem. Photobiol. A Chem. 353 (2018) 325–336. https://doi.org/10.1016/j.jphotochem.2017.11.045.
[223] P. Gu, X. Zhu, H. Wu, J. Li, D. Yang, Influence of oxygen vacancy on the response properties of TiO_2 ultraviolet detectors, J. Alloys Compd. 779 (2019) 821–830. https://doi.org/10.1016/j.jallcom.2018.11.283.
[224] B. Kartha, K. Thanikachalam, N. Vijayakumar, N.S. Alharbi, S. Kadaikunnan, J.M. Khaled, K. Gopinath, M. Govindarajan, Synthesis and characterization of Ce-doped TiO_2 nanoparticles and their enhanced anticancer activity in Y79 retinoblastoma cancer cells, Green Process. Synth. 11 (2022) 143–149. https://doi.org/10.1515/gps-2022-0011.
[225] M.J. Muñoz-Batista, M.N. Gómez-Cerezo, A. Kubacka, D. Tudela, M. Fernández-García, Role of interface contact in CeO_2-TiO_2 photocatalytic composite materials, ACS Catal. 4 (2014) 63–72. https://doi.org/10.1021/cs400878b.
[226] E. Paparazzo, On the curve-fitting of XPS Ce(3d) spectra of cerium oxides, Mater. Res. Bull. 46 (2011) 323–326. https://doi.org/10.1016/j.materresbull.2010.11.009.
[227] E.J. Haas, F.J. Angulo, J.M. McLaughlin, E. Anis, S.R. Singer, F. Khan, N. Brooks, M. Smaja, G. Mircus, K. Pan, J. Southern, D.L. Swerdlow, L. Jodar, Y. Levy, S. Alroy-Preis, Impact and effectiveness of mRNA BNT162b2 vaccine against SARS-CoV-2 infections and COVID-19 cases, hospitalisations, and deaths following a nationwide vaccination campaign in Israel: an observational study using national surveillance data, Lancet. 397 (2021) 1819–1829. https://doi.org/10.1016/S0140-6736(21)00947-8.
[228] L. Morawska, J. Cao, Airborne transmission of SARS-CoV-2: The world should face the reality, Environ. Int. 139 (2020) 105730. https://doi.org/10.1016/j.envint.2020.105730.
[229] S.L. Warnes, Z.R. Little, C.W. Keevil, Human coronavirus 229E remains infectious on common touch surface

materials, MBio. 6 (2015) 1–10. https://doi.org/10.1128/mBio.01697-15.
[230] P.D. Rakowska, M. Tiddia, N. Faruqui, C. Bankier, Y. Pei, A.J. Pollard, J. Zhang, I.S. Gilmore, Antiviral surfaces and coatings and their mechanisms of action, Commun. Mater. 2 (2021). https://doi.org/10.1038/s43246-021-00153-y.
[231] A. Bregnocchi, R. Jafari, G. Momen, Design strategies for antiviral coatings and surfaces: A review, Appl. Surf. Sci. Adv. 8 (2022) 100224. https://doi.org/10.1016/j.apsadv.2022.100224.
[232] T. Matsunaga, R. Tomoda, T. Nakajima, H. Wake, Photoelectrochemical sterilization of microbial cells by semiconductor powders, FEMS Microbiol. Lett. 29 (1985) 211–214. https://doi.org/10.1111/j.1574-6968.1985.tb00864.x.
[233] V. Stengl, H. Ageorges, P. Ctibor, N. Murafa, Atmospheric plasma sprayed (APS) coatings of Al_2O_3-TiO_2 system for photocatalytic application, Photochem. Photobiol. Sci. 8 (2009) 733–738. https://doi.org/10.1039/b817199h.
[234] H. Choi, E. Stathatos, D.D. Dionysiou, Sol-gel preparation of mesoporous photocatalytic TiO_2 films and TiO_2/Al_2O_3 composite membranes for environmental applications, Appl. Catal. B Environ. 63 (2006) 60–67. https://doi.org/10.1016/j.apcatb.2005.09.012.
[235] B. Jeffery, M. Peppler, R.S. Lima, A. McDonald, Bactericidal effects of HVOF-sprayed nanostructured TiO_2 on pseudomonas aeruginosa, J. Therm. Spray Technol. 19 (2010) 344–349. https://doi.org/10.1007/s11666-009-9369-3.
[236] V. Selvamani, A. Zareei, A. Elkashif, M.K. Maruthamuthu, S. Chittiboyina, D. Delisi, Z. Li, L. Cai, V.G. Pol, M.N. Seleem, R. Rahimi, Hierarchical Micro/Mesoporous Copper Structure with Enhanced Antimicrobial Property via Laser Surface Texturing, Adv. Mater. Interfaces. 7 (2020) 1901890. https://doi.org/10.1002/admi.201901890.
[237] M. Vincent, R.E. Duval, P. Hartemann, M. Engels-Deutsch, Contact killing and antimicrobial properties of copper, J. Appl. Microbiol. 124 (2018) 1032–1046. https://doi.org/10.1111/jam.13681.
[238] M. Gong, S. Xiao, X. Yu, C. Dong, J. Ji, D. Zhang, M. Xing, Research progress of photocatalytic sterilization over semiconductors, RSC Adv. 9 (2019) 19278–19284. https://doi.org/10.1039/c9ra01826c.
[239] R. Han, J.D. Coey, C. O'Rourke, C.G.G. Bamford, A. Mills, Flexible, disposable photocatalytic plastic films for the destruction of viruses, J. Photochem. Photobiol. B Biol. 235 (2022) 112551. https://doi.org/10.1016/j.jphotobiol.2022.112551.
[240] Y. Fu, Y. Liu, H. Li, Onion-like carbon-modified TiO_2 coating by suspension plasma spray with enhanced photocatalytic performances, J. Nanoparticle Res. 21 (2019) 1–12. https://doi.org/10.1007/s11051-019-4633-z.
[241] E. Alebrahim, M.S. Rahaman, C. Moreau, TiO2 Photocatalytic Ultrafiltration Membrane Developed with Suspension Plasma Spray Process, Coatings 2022, Vol. 12, Page 1764. 12 (2022) 1764. https://doi.org/10.3390/COATINGS12111764.
[242] L. Fiorillo, G. Cervino, M. Matarese, C. D'amico, G. Surace, V. Paduano, M.T. Fiorillo, A. Moschella, A. La Bruna, G.L. Romano, R. Laudicella, S. Baldari, M. Cicciù, COVID-19 surface persistence: A recent data summary and its importance for medical and dental settings, Int. J. Environ. Res. Public Health. 17 (2020) 3132. https://doi.org/10.3390/ijerph17093132.
[243] Yamasaki RS, Intensity variations of ultraviolet, visible, and near infrared bands of terrestrial solar radiation, J Paint Technol. 43 (1971) 75–83.
[244] M. Miyauchi, K. Sunada, K. Hashimoto, Antiviral effect of visible light-sensitive Cu_xO/TiO_2 photocatalyst, Catalysts. 10 (2020) 1–19. https://doi.org/10.3390/catal10091093.